











Library and  
Archives Canada

Bibliothèque et  
Archives Canada

Published Heritage  
Branch

Direction du  
Patrimoine de l'édition

395 Wellington Street  
Ottawa ON K1A 0N4  
Canada

395, rue Wellington  
Ottawa ON K1A 0N4  
Canada

*Your file* *Votre référence*  
*ISBN: 978-0-494-33444-7*  
*Our file* *Notre référence*  
*ISBN: 978-0-494-33444-7*

#### NOTICE:

The author has granted a non-exclusive license allowing Library and Archives Canada to reproduce, publish, archive, preserve, conserve, communicate to the public by telecommunication or on the Internet, loan, distribute and sell theses worldwide, for commercial or non-commercial purposes, in microform, paper, electronic and/or any other formats.

The author retains copyright ownership and moral rights in this thesis. Neither the thesis nor substantial extracts from it may be printed or otherwise reproduced without the author's permission.

#### AVIS:

L'auteur a accordé une licence non exclusive permettant à la Bibliothèque et Archives Canada de reproduire, publier, archiver, sauvegarder, conserver, transmettre au public par télécommunication ou par l'Internet, prêter, distribuer et vendre des thèses partout dans le monde, à des fins commerciales ou autres, sur support microforme, papier, électronique et/ou autres formats.

L'auteur conserve la propriété du droit d'auteur et des droits moraux qui protègent cette thèse. Ni la thèse ni des extraits substantiels de celle-ci ne doivent être imprimés ou autrement reproduits sans son autorisation.

---

In compliance with the Canadian Privacy Act some supporting forms may have been removed from this thesis.

Conformément à la loi canadienne sur la protection de la vie privée, quelques formulaires secondaires ont été enlevés de cette thèse.

While these forms may be included in the document page count, their removal does not represent any loss of content from the thesis.

Bien que ces formulaires aient inclus dans la pagination, il n'y aura aucun contenu manquant.

  
**Canada**



# **Tide Modelling in the Northwest Atlantic**

**By**

**© Shastri Paturi**

**A thesis submitted to the school of Graduate Studies in partial fulfillment of the requirements for the degree of Master of Science**

**Department of Physics and Physical Oceanography**

**Memorial University of Newfoundland**

**August, 2007**

**St. John's**

**Newfoundland**

**Canada**

“In loving memory of my mother who passed away on April 23, 1988 ...”

# Table of Contents

<b>Abstract.....</b>	<b>v</b>
<b>Acknowledgement .....</b>	<b>vii</b>
<b>List of Figures.....</b>	<b>viii</b>
<b>List of Tables .....</b>	<b>xiii</b>
<b>List of Symbols .....</b>	<b>xv</b>
<b>1. Introduction .....</b>	<b>1</b>
1.1. Ocean tides – Description and Overview.....	1
1.2. Earth & Load Tides.....	3
1.3. Observations of Tides .....	4
1.4. Modelling Ocean Tides.....	5
1.5. Objectives.....	8
1.6. Outline of Thesis .....	9
<b>2. Hydrodynamic Equations .....</b>	<b>10</b>
2.1. Basic Equations .....	10
2.2. Horizontal and Vertical Mixing Coefficients.....	14
2.3. The Vertically Integrated Equations .....	18
2.4. Model Domain.....	20
2.5. Model Grid .....	23
2.6. Boundary Conditions .....	25
2.7. The Equilibrium, Earth and Load tides.....	30
2.8. Assimilation Methods .....	32
<b>3. Model Runs and Analysis Methods .....</b>	<b>36</b>
3.1. Model Runs .....	36
3.1.1. Barotropic Run .....	36
3.1.2. Barotropic Data Assimilation.....	37
3.1.3. Diagnostic Run .....	37
3.1.4. Diagnostic Data Assimilation.....	37
3.2. Harmonic Analysis .....	37
3.3. Error Measures .....	38
<b>4. Observational Data.....</b>	<b>39</b>
4.1. Tidal and Pressure Gauge Data .....	39
4.2. Current Meter Data.....	40
4.3. Altimeter Data .....	42
4.4. Hydrography Data .....	45
4.5. Comparison of Altimeter Data with Observations .....	48
<b>5. Barotropic Results.....</b>	<b>54</b>
5.1. Unassimilated .....	54
5.1.1. Tidal Elevations.....	54
5.1.2. Tidal Currents.....	65
5.2. Assimilation Run .....	71
5.2.1. Tidal Elevation .....	71
5.2.2. Tidal Currents.....	87

5.2.3.	Vertical Structure of Model Tidal Currents .....	103
<b>6.</b>	<b>Diagnostic Results.....</b>	<b>106</b>
6.1.	Unassimilated .....	106
6.2.	Assimilation Run .....	107
6.2.1.	Tidal Elevations.....	107
6.2.2.	Tidal Currents.....	107
6.2.3.	Vertical Structure of Model Tidal Currents .....	114
<b>7.</b>	<b>Discussion and Summary .....</b>	<b>117</b>
7.1.	Key Results .....	118
7.2.	Future Work .....	121
	<b>References.....</b>	<b>122</b>
	<b>Appendix.....</b>	<b>129</b>
A.	Names and locations of Tide and Bottom Pressure Gauges .....	129
B.	Station by Station Comparison .....	132
C.	Co-range and Co-phase charts of Equilibrium, Earth & Load Tides .....	135
D.	Elevation data for the North Atlantic Model .....	141
E.	Station-wise error estimates of tidal elevations for the barotropic runs.....	149
F.	Co-range and co-phase charts for $M_2$ constituent from a single constituent run. ..	158

## Abstract

A three dimensional tidal model for the northwest Atlantic was developed including the 8 leading semi-diurnal ( $M_2$ ,  $S_2$ ,  $N_2$  and  $K_2$ ) and diurnal ( $K_1$ ,  $O_1$ ,  $P_1$ , &  $Q_1$ ) constituents. Altimetric tides from TOPEX/Poseidon, TOPEX Tandem Mission, JASON-1, ENVISAT, and GFO missions were assimilated into the model. The model was a primitive equation, sigma coordinate system in the vertical, finite difference Princeton Ocean Model (POM). The model used a horizontal rectilinear grid of  $1/12^\circ$  X  $1/12^\circ$  resolution. The vertical eddy viscosity is computed using the Mellor and Yamada (1982) level 2.5 turbulence model. The model domain covers the region from  $75^\circ$ W to  $42^\circ$ W and  $36^\circ$ N to  $66^\circ$ N. The model is forced at the boundaries with elevations and depth-averaged currents for the 8 semidiurnal and diurnal constituents extracted from a North Atlantic Model (Egbert and Erofeeva, 2002). We carried out experiments with homogeneous and stratified (summer-diagnostic) fluid, with and without assimilation, and their results are compared.

The model reproduced the  $M_2$ ,  $S_2$ ,  $N_2$ ,  $K_1$  and  $O_1$  tidal elevations to an accuracy of 2.1 cm, 1.6 cm, 0.9 cm 1.2 cm & 0.9 cm respectively excluding the Bay of Fundy and Gulf of Maine region. Including the Bay of Fundy and Gulf of Maine region, the accuracy is 10.7 cm, 2.8 cm, 2.5 cm, 1.3 cm and 1.1 cm respectively. Assimilation improved the model tidal elevation by a factor of 40-60%. The semi-diurnal tidal currents agreed to better than the diurnal constituents with observations. The agreement was best for the Georges Bank region indicating the model's capability to handle strong tidal current variability well. Assimilation improved the model tidal currents by roughly 20-30%. An enhancement of the  $K_1$  and  $O_1$  tidal elevation and currents at the shelf edge of Labrador is found in the model, in agreement with theory and observations.

Inclusion of horizontally and vertically varying stratification indicates that stratification has a significant influence on the vertical profile of currents in the shallow areas. Tidal currents decrease in the bottom boundary, increase significantly in the rest of the bottom layer, and decrease in the upper and middle water column. Stratification improves the  $K_1$  and  $O_1$  currents very slightly by  $\sim 5\%$ . Bottom friction and vertical eddy viscosity both played an important role in the shallow areas, especially in the Bay of Fundy, Gulf of Maine, Georges Bank and Scotian Shelf.

## **Acknowledgement**

I would like to thank Dr. Guoqi Han and Dr. Brad de Young for offering me this opportunity to participate in a challenging and exciting research project as part of my graduate degree program. I am grateful for their patience, insight, guidance and financial support during the course of this thesis.

Thanks are also due to Chris Stevenson for providing the necessary computational support which helped me finish my experiments in time.

A special mention of my wife, Sudha Paturi, without whose support I would not have been able to accomplish this.

This project was supported by the New Initiative Funds and the Federal Program for Energy, Research and Development.

## List of Figures

Figure 2-1. The sigma coordinate system. The vertical coordinate $\sigma$ ranges from $\sigma = 0$ at $z = \eta$ to $\sigma = -1$ at $z \cong H$ (Source: POM User Guide, 2004).....	11
Figure 2-2. Map of the model domain (75 °W to 42 °W and 36 °N to 66 °N), showing the location of major features and regions, bathymetry (200 and 3000m). The open boundaries are depicted as green dashed lines. Map projection is based on cylindrical coordinate system, which will be used in all other map figures in this thesis. ....	21
Figure 2-3. ETOPO2 elevation data. Scale at right shows the depth in metres.....	24
Figure 2-4. The bottom topography contours, from ETOPO2 and a finite element model provided by G. Han (PC, 2006) interpolated onto the model grid. The 50-, 200-, 1000, 3000- & 5000m contours are labeled and shown in red, blue, yellow, cyan & magenta colours respectively.....	25
Figure 2-5. Elevation open boundary values (amplitude and phase) for $M_2$ (this page) and $K_1$ (next page) constituents from North Atlantic Model and altimeter data (interpolated on to the model grid), in the East-West and North-South domain. The red circles are the altimeter data values and the blue asterix (*) are the values from the North Atlantic Model. The gaps in the plots are for the closed boundaries. The amplitudes are in cm and phases are in degrees.....	28
Figure 4-1. Locations of tide and bottom pressure gauges (with 200m isobath – red solid line). The legend inside the figure describes the markers used to define the different locations of the tide and bottom pressure gauges. The figure has been expanded in for clarity of locations for the tide and bottom pressure gauges. ....	40
Figure 4-2. Location of current meters used for comparison with model data (with 200- (solid red line), 1000- (solid blue line) & 3000m (solid green line) isobaths). The text inside the figure is the names of locations where the vertical structure of currents is examined. The legend figure describes the markers used to define the six different locations of the current meters. The figure has been zoomed in for clarity of locations.....	42
Figure 4-3. Tracks of the multi-mission altimeter data used for data assimilation in the model. ....	44
Figure 4-4. Climatological monthly-mean Surface (upper panel) and bottom (lower panel) temperature (°C) and salinity for the august, interpolated onto the model grid. ....	47
Figure 4-5. Model grid $\sigma$ , difference (bottom –surface). The values are in $\text{kg/m}^3$ . ....	48

Figure 4-6. Scatter diagrams of amplitudes and phases of the altimeter observations (vertical axis) and in-situ data (horizontal axis) for $M_2$ , $S_2$ & $N_2$ . The markers correspond to the 4 different regions, excluding BoFGoM as described in Figure 4-1. The solid line along the centre of each graph indicates where all points should lie if the agreement were perfect. Amplitudes are in centimeters and phases in degrees. The range of phases is defined from $0^\circ$ to $360^\circ$ .....	50
Figure 4-7. Same as Figure (4-6), but for $K_1$ & $O_1$ .....	51
Figure 5-1. Model computed Co-range (a) and Co-phase (b) charts for $M_2$ constituent. The amplitude is in m and phases are in degrees. The contours are co-range (a) and co-phase (b) lines scaled to show the proper distribution of amplitude and phase respectively. ....	56
Figure 5-2. Model computed Co-range (a) and Co-phase (b) charts for $K_1$ constituent. The amplitude is in m and phases are in degrees. The contours are co-range (a) and co-phase (b) lines scaled to show the proper distribution of amplitude and phase respectively. ....	57
Figure 5-3. Scatter diagrams of amplitudes and phases of the model results from the Bu run (vertical axis) and in-situ data (horizontal axis) for $M_2$ , $S_2$ & $N_2$ . The markers correspond to the 4 different regions, excluding BoFGoM as described in Figure 4-1. The solid line along the centre of each graph indicates where all points should lie if the agreement were perfect. Amplitudes are in centimeters and phases in degrees. The range of phases is defined from $0^\circ$ to $360^\circ$ .....	63
Figure 5-4 .Same as Figure (5-3), but for $K_1$ & $O_1$ .....	64
Figure 5-5. Scatter diagrams for the amplitude phase between the model (horizontal axis) and in situ observed currents (vertical axis) for $M_2$ constituent from the Bu run. The top panel is for the zonal (U, eastward) and the bottom panel is the meridional (V, northward) components in the whole model domain. The markers correspond to the 6 different regions as described in Figure 4-2. The solid line along the centre of each graph indicates where all points should lie if the agreement were perfect. The amplitudes are in cm/s and phases in degrees. The range of phases is defined from $0^\circ$ to $360^\circ$ .....	69
Figure 5-6. Same as Figure 5-5 but for $K_1$ . ....	70
Figure 5-7. Model computed Co-range (a) and Co-phase (b) charts for $M_2$ constituent from Ba run. The amplitude is in m and phases are in degrees. The contours are co-range (a) and co-phase (b) lines scaled to show the proper distribution of amplitude and phase respectively. ....	75
Figure 5-8. Model computed Co-range (a) and Co-phase (b) charts for $S_2$ constituent from Ba run. The amplitude is in m and phases are in degrees. The contours are co-range (a) and co-phase (b) lines scaled to show the proper distribution of amplitude and phase respectively. ....	76

Figure 5-9. Model computed Co-range (a) and Co-phase (b) charts for N <sub>2</sub> constituent from Ba run. The amplitude is in m and phases are in degrees. The contours are co-range (a) and co-phase (b) lines scaled to show the proper distribution of amplitude and phase respectively.....	77
Figure 5-10. Model computed Co-range (a) and Co-phase (b) charts for K <sub>1</sub> constituent from Ba run. The amplitude is in m and phases are in degrees. The contours are co-range (a) and co-phase (b) lines scaled to show the proper distribution of amplitude and phase respectively.....	78
Figure 5-11. Model computed Co-range (a) and Co-phase (b) charts for O <sub>1</sub> constituent from Ba run. The amplitude is in m and phases are in degrees. The contours are co-range (a) and co-phase (b) lines scaled to show the proper distribution of amplitude and phase respectively.....	79
Figure 5-12. Scatter diagrams of amplitudes and phases of the model computed elevation (horizontal) and observation (vertical) for the Semi-diurnal constituents (M <sub>2</sub> , S <sub>2</sub> & N <sub>2</sub> ) from Ba run. The markers correspond to the 4 different regions, excluding BoFGoM as described in Figure 4-1. The solid line along the centre of each graph indicates where all points should lie if the agreement were perfect. Amplitudes are in centimeters and phases in degrees. The range of phases is defined from 0° to 360°.83	
Figure 5-13. Same as Figure 5-12, but for K <sub>1</sub> and O <sub>1</sub> .....	84
Figure 5-14. Sub-sampled M <sub>2</sub> current ellipses (a) at the surface and (b) at a near bottom level ( $\sigma = -0.95$ ), from Ba run. The radial lines in ellipses indicate common time. The 200-, 1000- & 3000m isobaths are displayed in red, green and magenta colors respectively. ....	90
Figure 5-15. Sub-sampled K <sub>1</sub> current ellipses at the surface, from Ba run. The radial lines in ellipses indicate common time. The 200-, 1000- & 3000m isobaths are displayed in red, green and magenta colors respectively. ....	92
Figure 5-16. Sub-sampled O <sub>1</sub> current ellipses at the surface, from Ba run. The radial lines in ellipses indicate common time. The 200-, 1000- & 3000m isobaths are displayed in red, green and magenta colors respectively. ....	93
Figure 5-17. Scatter diagrams of the M <sub>2</sub> model tidal current amplitude and phase (top Panel) and the zonal (U, eastward) & meridional (V, northward) components (lower panel), from Ba run. ....	98
Figure 5-18. Same as Figure 5-17, but for S <sub>2</sub> . ....	99
Figure 5-19. Same as Figure 5-17, but for N <sub>2</sub> . ....	100
Figure 5-20. Same as Figure5-17, but for K <sub>1</sub> . ....	101
Figure 5-21. Same as Figure 5-17, but for O <sub>1</sub> . ....	102

Figure 5-22. Computed vertical profiles of $M_2$ currents at S01, S02, NF01, NF02, GB01 and GB02 for the Ba Experiment (blue solid line) and Bu experiment (green dashed line). The red asterix (*) are the observed values. The locations are shown in Figure 4-2.....	105
Figure 6-1. Sub-sampled $K_1$ current ellipses at the surface, from Da run. The radial lines in ellipses indicate common time. The 200-, 1000- & 3000m isobaths are displayed in red, green and magenta colors respectively. ....	111
Figure 6-2. Computed vertical profiles of $M_2$ currents at S01, S02, NF01, NF02, GB01 and GB02 for the Da Experiment (blue solid line) and Du experiment (green dashed line). The red asterix (*) are the observed values. The locations are shown in Figure 4-2.....	116
Figure B-1. Location of assigned Station Numbers of Bottom Pressure gauges in the Labrador Sea & Shelf.....	132
Figure B-2. Location of assigned Station Numbers of tide gauges in the Coastal Nova Scotia.....	133
Figure B-3. Location of assigned Station Numbers of tide and bottom pressure gauges in the Super Stations.....	133
Figure B-4. Location of assigned Station Numbers of tide gauges in the Coastal Island of Newfoundland.....	134
Figure B-5. Location of assigned Station Numbers of tide gauges in the Bay of Fundy & Gulf of Maine.....	134
Figure C-1. Co-range (top) and Co-phase (bottom) charts for $M_2$ equilibrium, earth & load tide. The amplitude is in mm and phases are in degrees. The contours are scaled to show proper distribution of amplitude and phase respectively.....	136
Figure C-2. Co-range (top) and Co-phase (bottom) charts for $S_2$ equilibrium, earth & load tide. The amplitude is in mm and phases are in degrees. The contours are scaled to show proper distribution of amplitude and phase respectively.....	137
Figure C-3. Co-range (top) and Co-phase (bottom) charts for $N_2$ equilibrium, earth & load tide. The amplitude is in mm and phases are in degrees. The contours are scaled to show proper distribution of amplitude and phase respectively.....	138
Figure C-4. Co-range (top) and Co-phase (bottom) charts for $K_1$ equilibrium, earth & load tide. The amplitude is in mm and phases are in degrees. The contours are scaled to show proper distribution of amplitude and phase respectively.....	139
Figure C-5. Co-range (top) and Co-phase (bottom) charts for $O_1$ equilibrium, earth & load tide. The amplitude is in mm and phases are in degrees. The contours are scaled to show proper distribution of amplitude and phase respectively.....	140

Figure F-1. Model computed Co-range (top) and Co-phase (bottom) charts for  $M_2$  constituent from single constituent unassimilated run. The amplitude is in m and phases are in degrees. The contours are co-range (top) and co-phase (bottom) lines scaled to show the proper distribution of amplitude and phase respectively. .... 159

## List of Tables

Table 1-1. Principal Tidal Constituents.....	2
Table 2-1. Love numbers, $k_n$ and $h_n$ , and tidal potential amplitudes, $H_n$ , used in calculating the Earth tides (from Foreman et al. 1995).....	32
Table 3-1. Numerical experiments mentioned in this study.....	36
Table 4-1. The number of available comparisons for current meter observations, including different depths at each location, made for model current data.....	41
Table 4-2. Statistics for amplitude and phase between the Altimeter derived and in-situ observed tides for the five major semi-diurnal and diurnal constituents in the 5 different regions, excluding BoFGoM and for all locations (5 regions combined). The locations are defined in Figure 4-1.....	52
Table 5-1. Statistics of model computed elevation from Bu run for semi-diurnal and diurnal constituents compared with observations at Tide and Pressure Gauge Sites for the Baseline (Bu) run for all the five regions, excluding BoFGoM and all locations. The locations are defined in Figure 4-1.....	60
Table 5-2. Statistics of model computed currents for semi-diurnal and diurnal constituents compared with observations at moored current meter sites for six sub-regions (a-f) of the model domain and the whole model domain (g) for the Bu run. The location and names of the sub-regions are as described in Figure 4-2.....	67
Table 5-3. Statistics of model computed elevation for semi-diurnal and diurnal constituents compared with observations at Tide and Bottom Pressure Gauge Sites for the Ba run. The locations are defined in Figure 4-1.....	85
Table 5-4. Statistics of model computed currents for semi-diurnal and diurnal constituents compared with observations at moored current meter Sites for six sub regions (a-f) of the model domain and the whole model domain (g) for the Baseline run with assimilation (Ba) using multi-mission altimeter data.....	96
Table 6-1. Statistics of model computed elevation for semi-diurnal and diurnal constituents compared with observations at Tide and Bottom Pressure Gauge Sites for the Diagnostic run with assimilation using multi-mission altimeter data.....	109
Table 6-2. Statistics of model computed currents for semi-diurnal and diurnal constituents compared with observations at moored current meter sites for six sub regions (a-f) of the model domain and the whole model domain (g) for the diagnostic run with assimilation (Da) using multi-mission altimeter data.....	112

Table A-1. List of Tide and Bottom pressure gauge locations including the length of the record used for comparing the model elevation solutions. ....	129
Table D-1. Statistics of model computed elevation for semi-diurnal and diurnal constituents compared with observations at Tide and Bottom Pressure Gauge Sites for the North Atlantic Model. ....	141
Table D-2. Summary of observed and computed semidiurnal tidal elevations at Tide and Bottom Pressure gauge sites for the North Atlantic Model. AO, amplitude (cm) observed; PO, phase (degree) observed; AMO, difference of model amplitudes from observations; PMO, model-observation phase difference. ....	143
Table D-3. Same as Table D-2, but for diurnal constituents. ....	146
Table E-1. Summary of observed and computed semidiurnal tidal elevations at Tide and Bottom Pressure gauge sites from Ba experiment. AO, amplitude (cm) observed; PO, phase (degree) observed; AMO, difference of model amplitudes from observations; PMO, model-observation phase difference. ....	149
Table E-2. Same as Table E-1, but for diurnal constituents. ....	152
Table E-3. Summary of observed and computed $M_2$ and $K_1$ tidal elevations at Tide and Bottom Pressure gauge sites from Bu experiment. AO, amplitude (cm) observed; PO, phase (degree) observed; AMO, difference of model amplitudes from observations; PMO, model-observation phase difference. ....	155

## List of Symbols

C	the coefficient of the Smagorinsky diffusivity
$\kappa$	von Karman's constant = 0.4
$\sigma$	sigma coordinate which spans the domain, $z = 0$ (surface) to $z = -1$ (bottom)
$\eta$	the free surface elevation (m)
$\zeta_b$	elevation of sea bed above its undisturbed level
$\bar{\zeta}$	the equilibrium tide
H	the bottom depth (m)
$A_M$	horizontal kinematic viscosity ( $m^2 s^{-1}$ )
$A_H$	horizontal heat diffusivity
l	turbulence length scale
$K_M$	vertical kinematic viscosity ( $m^2 s^{-1}$ )
$K_H$	vertical diffusivity ( $m^2 s^{-1}$ )
R	short wave radiation flux ( $ms^{-1}K$ ).
$q^2$	twice the turbulence kinetic energy ( $m^2 s^{-2}$ )
$q^{2l}$	$q^2$ x the turbulence length scale ( $m^3 s^{-2}$ )
T	potential temperature (K)
S	salinity (psu)
U	east-component of horizontal velocities ( $m s^{-1}$ )
V	north-component of horizontal velocities ( $m s^{-1}$ )
$\omega$	sigma coordinate vertical velocity ( $m s^{-1}$ )

# 1. Introduction

## 1.1. Ocean tides – Description and Overview

Ocean tides are a result of the gravitational forces primarily from the Moon, Sun but to a lesser degree from other planets in the Solar system. The gravitational forces that cause tides depend on the mass of the heavenly body and that of the Earth and inversely on the square of the distance between the two bodies. Tides due to other planetary bodies are negligible (the contribution of Venus, the planet nearest to the Earth is  $5.4 \times 10^{-5}$  times that of the Moon).

If water covered the globe, then water would move instantly in response to this force (equilibrium tide approximation). There would be a bulge facing the Moon and another at the opposite side, and flattening at points away from the moon. A rotating Earth under these bulges would produce two bulges and two accompanying lows to an observer on the surface of the Earth, whose period would be 12 hr (half of Earth's rotation). Since the Moon is also rotating, the effective period of the bulges is one half lunar days, 12.421 hours ( $M_2$  tide). Since the Moon's orbital plane is inclined with respect to the Earth's equatorial plane, the north-south symmetry with respect to the equator cannot be expected. Therefore, the high tides will appear larger if the Moon travels directly overhead. This inequality depends on latitude of the observation point and the fraction of the lunar month, and can be represented as a superposition of the semidiurnal tide,  $M_2$  with a diurnal component. The diurnal component is composed of two subcomponents,  $K_1$  (with contribution from the Sun) and  $O_1$ . The eccentricity of the Moon's orbit (0.0549) produces the  $N_2$  tide. The Earth and the Sun rotate about a common center once a year and the gravitational force between them creates two bulges along the Earth-Sun axis,

leading to the semidiurnal tide  $S_2$  of exactly 12 hr period (as the Sun is stationary) and the diurnal equality contribution to  $K_1$  from the Sun, due to the inclination of the elliptic plane to the earth's equatorial plane. Since the declination of the Moon has a period of one tropical (sidereal) month (27.3217 days) and also because of the annual period of the declination of the Sun, the overall effect is to produce a lunar potential with semidiurnal, diurnal, fortnightly and monthly components. The orbital tilt is responsible for producing both the diurnal and long-period tides. Long period lunar (and solar) tides are also called declinational tides. Table 1-1 lists the names and periods of the major lunar and solar tidal frequencies.

Table 1-1. Principal Tidal Constituents

<b>TIDAL SPECIES</b>	<b>NAME</b>	<b>PERIOD (HR)</b>
<b>Semidiurnal</b>		
Principal Lunar	$M_2$	12.4206
Principal Solar	$S_2$	12.0000
Lunar Elliptic	$N_2$	12.6584
Lunisolar	$K_2$	11.9673
<b>Diurnal</b>		
Lunisolar	$K_1$	23.9344
Principal Lunar	$O_1$	25.8194
Principal Solar	$P_1$	24.0659
Elliptic Lunar	$Q_1$	26.8684
<b>Long Period</b>		
Fortnightly	$M_f$	327.85
Monthly	$M_m$	661.31
Semiannual	$S_{sa}$	4383.05

When the lunar and solar tractive forces reinforce each other, or when the Sun and the Moon are on the same or opposite sides of the Earth (full Moon and the new moon), the tides are the largest and are called spring tides. When they counteract each other, they are  $90^\circ$  to each other or in quadrature, the tides are low and are called neap tides. For spring tides,  $M_2$  and  $S_2$  reinforce each other but are opposed during neap tides. Since the tidal

tractive force due to the Sun is roughly half of that of the Moon, the ratio of spring to neap tides is roughly three to one (Cartwright, 1997).

Tides in different locations are classified based on the predominant amplitudes of the tide using a function called the form ratio

$$F = \frac{K_1 + O_1}{M_2 + S_2}$$

This F ratio measures the relative strength of the diurnal and semi-diurnal tides.

F > 3	Diurnal	1 High, 1 Low per day
0.25 < F < 3	Mixed	2 Highs, 2 lows per day, but of mixed strength
F > 0.25	Semidiurnal	2 Highs, 2 Lows per day, similar strength

The most important semidiurnal tide in the global ocean is  $M_2$ , the lunar tide, and the most important diurnal one is  $K_1$ , a declinational tide with contributions from both the Moon and the Sun. The natural period of oscillation of the Atlantic Ocean is close to 12.5 hours making it resonant to the semi-diurnal components and so the tides in the ocean are mainly semi-diurnal unlike the Pacific, whose natural period of oscillation is closer to 25 hours, where the tidal regime is predominantly diurnal. Nevertheless, both lunar and solar tides occur in both oceans and their relative importance can vary locally.

## 1.2. Earth & Load Tides

It is not only the ocean that responds to tidal forcing but also the solid Earth, as an elastic body. Earth tides are the displacements of the Earth's crust in response to the gravitational attraction of the Moon and the Sun. Their effect on oceanic tides is primarily to reduce the amplitude of the equilibrium tides the ocean feels, since the Earth deforms in the

same direction as the oceans under the influence of the tidal forcing by the Moon and the Sun. The response of the solid Earth to tidal forcing is nearly instantaneous so that the spatial distribution of the Earth's body tides is the same as that of the tidal forcing because the natural frequencies are an order of magnitude larger than tidal frequencies. The oceanic tide also affects the earth below. The loading due to the oceanic tide deforms it elastically. These ocean tides that induce solid earth tides are load tides. Ocean-tide loading is the displacement of the Earth's crust in response to the ocean tides. The loading effects also extend to continents.

### **1.3. Observations of Tides**

In the last two decades, many observations have been made on the eastern continental shelves of North America. The five principal constituents ( $M_2$ ,  $S_2$ ,  $N_2$ ,  $K_1$  &  $O_1$ ) were compiled by Moody et al. (1984) for the North American Continental shelf between Cape Hatteras and Laurentian Channel and account for more than 93% of variance of sea-surface elevation for periods shorter than 33 hours. Methods for observing tides have evolved from the simple and straightforward local measurement hundreds and thousands of years ago to the modern use of satellite sensors:

#### **Tides**

- Classical method – rod with scale – height recorded hourly by visual observations.
- Float type recorders. Stilling well (to reduce effects of waves and wind) with a float on a lever arm. Arm connected to analog recording device like a chart recorder.
- Pressure sensors. Pressure recorded at a fixed depth (say 10 m or ocean bottom) is converted to an equivalent sea level using the hydrostatic equation.

- Radar altimetry. Measures variations in distance from an orbiting satellite to the surface of the ocean and use satellite altitude to infer sea level .

## **Tidal Currents**

- Drifters and dyes. Eulerian flow of current speed and directions measured on nautical charts.
- Rotor current meters. Measure current speed by counting the rate of rotation of a propeller or similar device suspended in the flow. A magnet within the instrument indicates current direction relative to magnetic north.
- Acoustic travel-time meters. Acoustic Doppler Current Profiler (measure the travel time in both directions of an acoustic pulse between a pair of transducers).
- Electromagnetic methods. Measure the rate of movement of the seawater conductor (voltage gradient is produced across the direction of the flow).

### **1.4. Modelling Ocean Tides**

Numerical models have been used to study tides for several decades and are of particular interest in the coastal regions where the tidal behaviour on the shelf and shelf-break regions are of particular interest. Finite element models have been used to simulate the circulation and hydrography of different regions of the Northwest Atlantic. Xu et al. (2001) used the FUNDY5 model in the Newfoundland and Southern Labrador shelves. Lynch and Naimie (1993) used a Finite Element Model on the outer banks of the Gulf of Maine. Han and Loder (2003) used QUODDY4 on the eastern Scotian Shelf.

One of the most widely used finite difference model for shelf circulation studies involving tides is the Princeton Ocean Model (POM). The POM has been widely and extensively used for simulation of tides in shelf and open ocean region around the world.

Holloway (1996) applied a 2-D version of POM to the Australian North-west shelf. Cummins et al. (1997) applied a fully prognostic 3-D version to study tidal simulations of the northern coastal waters of British Columbia. In the Northwest Atlantic, Han (2000) used a version of POM (ECOM-si) to study the 3D tidal currents and mixing quantities over the Newfoundland shelf for five primary constituents.

To date, however, models of open coastlines have been concerned almost exclusively with barotropic tidal modelling (Foreman et. al 1995). While baroclinic models in three dimensions have been applied to embayments and channels of limited extent (Matsuyama 1985; Wang 1989), baroclinic tidal studies of open coastlines have been limited to applications of two-dimensional, cross-shelf models (e.g., Craig 1988; Sherwin and Taylor 1990). Results, particularly  $M_2$  baroclinic energy fluxes, were highly sensitive to the specification of the cross-shelf topographic section. To date, significant progress has been made in the determination of tidal elevation and currents using numerical models for world's continental shelves, some of which are 3-dimensional (e.g., Davies and Jones, 1992; Lynch and Namie, 1993).

Numerical modelling studies of the Scotian shelf have primarily focused on particular flow components such as tidal rectification (e.g. Greenberg 1983; Tee et al. 1993), baroclinic circulation (e.g., Hannah et al. 1996; Sheng and Thompson 1996), wind-driven flow and barotropic through flow (e.g. Schwing 1992; Greenberg et al. 1997) and seasonal and low-frequency circulation due to combined forcing (e.g., Griffin and Thompson 1996; Han et al. 1997). On the Grand Banks, non-tidal components account for only about 9% of the total variance of the sea-surface elevation (Petrie et al., 1987). Tidal models have made significant improvements to tidal charts of this region (Godin, 1980; Moody et al., 1984; Petrie et al., 1987; de Margerie and Lank, 1986). In the Grand

Banks of Newfoundland, tides exhibit considerable spatial variability especially in amplitude (Godin, 1980; Petrie et al., 1987; Han et al., 1996). Tidal components account for ~91% of the total variance of the sea surface height in the Grand Banks region. Petrie (1987) has also shown that the tidal band accounts for 51% of the current variance for periods longer than 12 hours and is an important part of the current spectrum over the outer Grand Banks. There are other features, such as inertial current oscillations (de Young and Tang, 1990), which can dominate the current variance, particularly during winter. Saucier and Chasse (2000) have investigated the action of tides on density-driven circulation, internal gravity waves and mixing in the St. Lawrence Estuary.

Satellite altimetry produces unique global measurements of instantaneous sea-surface heights over periods of several years. The availability of such data with regular spatial and temporal distribution offers a bright prospect for precisely mapping the open-ocean tides on a worldwide basis. A number of methods such as harmonic analysis (Han et al., 1993; Ma et al., 1994), response analysis (Cartwright and Ray, 1990; Woodworth and Thomas, 1990; Anderson, 1994), and inverse methods (Mazegga and Berge 1994), have been used to extract ocean tides from Altimeter data. The TOPEX/Poseidon (TP) altimeter data (Fu et al., 1994) have a high measurement precision (~ 3cm) and a low orbit error (~5 cm). These data have been widely used in previous tidal studies (e.g, Anderson, 1994; Ma et. al., 1994; Mazegga and Berge, 1994). Analysis of altimeter data for shallow-water oceanic tides have been performed by Woodworth and Thomas (1990) and Mazegga and Berge (1994).

In general, tides cannot be derived directly from altimetric measurements within a few tens of kilometres of the coastline where reliable altimeter measurements are lacking (Han et al., 1996). In fact many users of altimeter data have simply excluded data over

the continental shelf (e.g. Kantha, 1995). To date, most tidal applications of altimeter data have focused on deep ocean tides, however there are many exceptions: Woodworth and Thomas (1990), Han et al. (1993, 1996) and Mazegga and Berge (1994). Woodworth and Thomas (1990) and Mazegga and Berge (1994) combined altimeter data with tide gauge data to produce empirical regional tidal charts. An alternative approach is to assimilate altimeter-derived tides into regional models. The usefulness of such assimilation models has been demonstrated by Han and Ikeda (1995) using a direct insertion method in a shelf model, by Egbert et al. (1994) and le Provost et al. (1998) using an inverse method and by Kantha (1995) using a weighted insertion method in global tidal models.

Han et al. (2000) only considered the  $M_2$  constituent and assimilated TP data directly into the interior of the POM model using a nudging technique. Xu et al. (2001) assimilated TP data along with current elevation observational data in FUNDY5 tidal model using a direct inverse method for the Newfoundland and south Labrador shelves. Dupont et al. (2002) assimilated TP data into a Finite element model for the five constituents ( $M_2$ ,  $S_2$ ,  $N_2$ ,  $K_1$  &  $O_1$ ) for the Northwest Atlantic region. Lu et al. (2001) have assimilated tidal heights from observations around the Gulf of St. Lawrence using CANDIE model through incremental approach.

## **1.5. Objectives**

The goal of this study is to develop a 3D tidal model to accurately calculate tidal elevations and currents for the Northwest Atlantic. Our domain of interest includes the Hudson Strait, the Labrador Sea and Shelf, the Newfoundland and Scotian Shelf, Georges Bank including the Bay of Fundy and the Gulf of Maine. We will apply a Finite difference model by implementing complete tidal dynamics (including the equilibrium, Earth and Load tide) and assimilating altimeter data. This study is an extension of Dupont

et al. (2002) but is a new contribution for three reasons: 1) the first of the regional studies applied to the Northwest Atlantic that provides 3-dimensional solutions for tidal currents, in particular, 2) including 8 major constituents and 3) assimilating multi-mission altimeter data. The results are to be used for forecasting tides and tidal currents in these regions with the shelf regions in particular, detiding altimeter data for future data assimilation studies to better understand sub-tidal shelf circulation and also detiding vessel mounted ADCP currents.

## **1.6. Outline of Thesis**

Chapter 2 describes the major topographical features and tidal regimes of the study region and its associated sub-regions; the model resolution; the bottom topography used; the open boundary conditions employed and the assimilation methods for the data assimilation. The list of experiments, the harmonic analysis and the method for computing the error estimates are detailed in chapter 3. Chapter 4 presents the observational data for tidal elevation and currents used for comparing the model results, the hydrography data used to initialize the model for diagnostic studies and the altimeter data used for assimilation of data into the model. The model results and comparison with observations from barotropic simulation for the 8 major tidal constituents, unassimilated and assimilated, are presented in chapter 5. Chapter 6 presents the diagnostic model results with temperature and salinity fields representative of August, for unassimilated and assimilated, compared with observations. Chapter 7 offers a summary and discussion of the results.

## 2. Hydrodynamic Equations

### 2.1. Basic Equations

The numerical model used for this study is the widely used Princeton Ocean Model (POM), (Blumberg and Mellor, 1987)). It is a sigma coordinate, free surface, primitive equation ocean model. The model contains an embedded second moment turbulence closure sub-model to provide vertical mixing coefficients. Sigma coordinates are used in the vertical, with scaling based on the water depth. The model has curvilinear orthogonal coordinates and an “Arakawa C” grid in the horizontal. As a special case, rectilinear coordinate system can also be easily implemented.

The horizontal time differencing is explicit whereas the vertical differencing is implicit. The latter determines time constraints for the vertical coordinate and permits the use of fine vertical resolution in the surface and bottom layers. The model has a free surface and a split time step. The external mode portion of the model is two-dimensional and uses a time step based on the Courant-Friedrichs-Levy (CFL) condition and the external wave speed. The internal mode is three-dimensional and uses a time step based on the CFL condition and internal wave speed. Complete thermodynamics are implemented. The 2D (external mode) portion of the model can be run *cum sole*. In this case, the bottom shear stress, normally a consequence of the 3-D calculation and the turbulence mixing coefficient, is replaced by a quadratic drag relation. It also runs in a diagnostic mode where the thermodynamic properties are invariant in time.

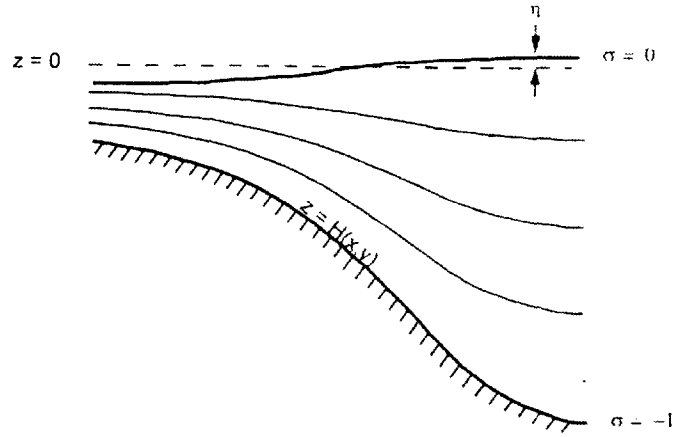


Figure 2-1. The sigma coordinate system. The vertical coordinate  $\sigma$  ranges from  $\sigma = 0$  at  $z = \eta$  to  $\sigma = -1$  at  $z \cong H$  (Source: POM User Guide, 2004).

The basic equations are represented in a bottom following, sigma coordinate system which is illustrated in Figure 2-1. The reader is referred to Phillips (1957); Blumberg and Mellor (1980, 1987) for a derivation of the sigma coordinate equations which are based on the transformation,

$$x^* = x \tag{2-1a}$$

$$y^* = y \tag{2-1b}$$

$$\sigma = \frac{z - \eta}{H + \eta} \tag{2-1c}$$

$$t^* = t \tag{2-1d}$$

where  $x, y, z$  are the conventional cartesian coordinates;  $D \equiv H + \eta$ , where  $H(x, y)$  is the bottom topography and  $\eta(x, y, t)$  is the surface elevation. The vertical coordinate  $\sigma$  ranges from  $\sigma = 0$  at  $z = \eta$  to  $\sigma = -1$  at  $z \cong H$ . After conversion to sigma coordinates and removal of the asterisks, the basic equations are written (in horizontal cartesian coordinates) as,

$$\frac{\partial DU}{\partial x} + \frac{\partial DV}{\partial y} + \frac{\partial \omega}{\partial \sigma} + \frac{\partial \eta}{\partial t} = 0 \quad (2-2)$$

$$\begin{aligned} \frac{\partial UD}{\partial t} + \frac{\partial U^2 D}{\partial x} + \frac{\partial UV D}{\partial y} + \frac{\partial U \omega}{\partial \sigma} - fVD + gD \frac{\partial}{\partial x} (\eta + \zeta_b - \bar{\zeta}) \\ + \frac{gD^2}{\rho_0} \int_{\sigma}^0 \left[ \frac{\partial \rho'}{\partial x} - \frac{\sigma'}{D} \frac{\partial D}{\partial x} \frac{\partial \rho'}{\partial \sigma'} \right] d\sigma' = \frac{\partial}{\partial \sigma} \left[ \frac{K_M}{D} \frac{\partial U}{\partial \sigma} \right] + F_x \end{aligned} \quad (2-3)$$

$$\begin{aligned} \frac{\partial VD}{\partial t} + \frac{\partial UV D}{\partial x} + \frac{\partial V^2 D}{\partial y} + \frac{\partial V \omega}{\partial \sigma} + fUD + gD \frac{\partial}{\partial y} (\eta + \zeta_b - \bar{\zeta}) + \\ \frac{gD^2}{\rho_0} \int_{\sigma}^0 \left[ \frac{\partial \rho'}{\partial y} - \frac{\sigma'}{D} \frac{\partial D}{\partial y} \frac{\partial \rho'}{\partial \sigma'} \right] d\sigma' = \frac{\partial}{\partial \sigma} \left[ \frac{K_M}{D} \frac{\partial V}{\partial \sigma} \right] + F_y \end{aligned} \quad (2-4)$$

$$\frac{\partial TD}{\partial t} + \frac{\partial TUD}{\partial x} + \frac{\partial TVD}{\partial y} + \frac{\partial T \omega}{\partial \sigma} = \frac{\partial}{\partial \sigma} \left[ \frac{K_H}{D} \frac{\partial T}{\partial \sigma} \right] + F_T + fUD - \frac{\partial R}{\partial z} \quad (2-5)$$

$$\frac{\partial SD}{\partial t} + \frac{\partial SUD}{\partial x} + \frac{\partial SV D}{\partial y} + \frac{\partial S \omega}{\partial \sigma} = \frac{\partial}{\partial \sigma} \left[ \frac{K_H}{D} \frac{\partial S}{\partial \sigma} \right] + F_S \quad (2-6)$$

$$\begin{aligned} \frac{\partial q^2 D}{\partial t} + \frac{\partial U q^2 D}{\partial x} + \frac{\partial V q^2 D}{\partial y} + \frac{\partial \omega q^2}{\partial \sigma} = \frac{\partial}{\partial \sigma} \left[ \frac{K_q}{D} \frac{\partial q^2}{\partial \sigma} \right] \\ + \frac{2K_M}{D} \left[ \left( \frac{\partial U}{\partial \sigma} \right)^2 - \left( \frac{\partial V}{\partial \sigma} \right)^2 \right] + \frac{2g}{\rho_0} K_H \frac{\partial \tilde{\rho}}{\partial \sigma} - \frac{2Dq^3}{B_1 l} + F_q \end{aligned} \quad (2-7)$$

$$\begin{aligned} \frac{\partial q^2 l D}{\partial t} + \frac{\partial U q^2 l D}{\partial x} + \frac{\partial V q^2 l D}{\partial y} + \frac{\partial \omega q^2 l}{\partial \sigma} = \frac{\partial}{\partial \sigma} \left[ \frac{K_q}{D} \frac{\partial q^2 l}{\partial \sigma} \right] \\ + E_1 l \left( \frac{K_M}{D} \left[ \left( \frac{\partial U}{\partial \sigma} \right)^2 + \left( \frac{\partial V}{\partial \sigma} \right)^2 \right] + E_3 \frac{g}{\rho_0} K_H \frac{\partial \tilde{\rho}}{\partial \sigma} \right) - \frac{Dq^3}{B_1} \tilde{W} + F_l \end{aligned} \quad (2-8)$$

$\omega$  is the transformed vertical velocity; physically,  $\omega$  is the velocity component normal to sigma surfaces. The transformation to the Cartesian vertical velocity is

$$W = \omega + U \left( \sigma \frac{\partial D}{\partial x} + \frac{\sigma \eta}{\partial x} \right) + V \left( \sigma \frac{\partial D}{\partial y} + \frac{\sigma \eta}{\partial y} \right) + \sigma \frac{\partial D}{\partial t} + \frac{\sigma \eta}{\partial t} \quad (2-9)$$

The term multiplying  $q^3/B_1$  in equation (2-8) is a wall proximity function inserted empirically to assure log-law behavior near solid boundaries prescribed according to

$$\tilde{W} = 1 + E_2(l/kL) \quad (2-10a)$$

and  $L$  is given by

$$L^{-1} = (\eta - z)^{-1} + (H - z)^{-1}. \quad (2-10b)$$

also  $\partial\tilde{\rho}/\partial\sigma \equiv \partial\rho/\partial\sigma - c_s^{-2} \partial\rho/\partial\sigma$ , where  $c_s$  is the speed of sound.  $T$  is potential temperature. In equations (2-3) and (2-4),  $c_s$  is subtracted from  $\rho$  to form  $\rho'$  before the integration is carried out.  $\rho_{MEAN}$  is generally the initial density field which is area averaged on  $z$ -levels and then transferred to sigma coordinates in the exact same way as the initial density field.

The horizontal viscosity and diffusion terms are defined according to:

$$F_x \equiv \frac{\partial}{\partial x}(H\tau_{xx}) + \frac{\partial}{\partial y}(H\tau_{xy}) \quad (2-11a)$$

$$F_y \equiv \frac{\partial}{\partial x}(H\tau_{xy}) + \frac{\partial}{\partial y}(H\tau_{yy}) \quad (2-11b)$$

where

$$\tau_{xx} = 2A_M \frac{\partial U}{\partial x} \quad (2-12a)$$

$$\tau_{xy} = \tau_{yx} = A_M \left( \frac{\partial U}{\partial y} + \frac{\partial V}{\partial x} \right) \quad (2-12b)$$

$$\tau_{yy} = 2A_M \frac{\partial V}{\partial y} \quad (2-12c)$$

also,

$$F_\phi \equiv \frac{\partial}{\partial x}(Hq_x) + \frac{\partial}{\partial y}(Hq_y) \quad (2-13)$$

where

$$q_x \equiv A_H \frac{\partial \phi}{\partial x} \quad (2-14a)$$

$$q_y \equiv A_H \frac{\partial \phi}{\partial y} \quad (2-14b)$$

and where  $\phi$  represents  $T, S, q^2$  or  $q^2 l$ .

The inclusion of equations (2-11a,b), (2-12a,b), (2-13) and (2-14a,b) allows for a realistic treatment of bottom boundary layers. The bottom boundary layer is important in tidally driven regions, in wind driven coastal regions and according to Mellor and Wang (1996), in deep ocean basins. All variables are defined in the List of Symbols.

## 2.2. Horizontal and Vertical Mixing Coefficients

### a) The Smagorinsky Diffusivity

The horizontal mixing coefficients for momentum (viscosity), and tracers (diffusivity), are calculated by Smagorinsky diffusivity for horizontal diffusion although a constant or biharmonic diffusion can and has been used instead.

The Smagorinsky formula (Smagorinsky et al., 1965) is,

$$A_M = C \Delta x \Delta y \left[ \left( \frac{\partial U}{\partial x} \right)^2 + \frac{1}{2} \left( \frac{\partial V}{\partial x} + \frac{\partial U}{\partial y} \right)^2 + \left( \frac{\partial V}{\partial y} \right)^2 \right]^{1/2} \quad (2-15)$$

The Smagorinsky diffusivity coefficient ( $C$ ), can vary in range, from 0.10 to 0.20. Those values seem to work well, but, if the grid spacing is small enough (Oey et al, 1985a,b),  $C$  can be nil.  $A_H$  is prescribed as a function of the inverse turbulent Prandtl number,  $A_H / A_M$ . An advantage of the Smagorinsky relation is that  $C$  is non-dimensional; related advantages are that  $A_M$  decreases as resolution improves and that is small if velocity

gradients are small. This kind of empirical formulation helps to adjust the horizontal diffusivity in the problem areas without affecting the overall model domain and results.

### b) 2.5 Turbulence Closure Model

Vertical mixing coefficients  $K_M$  and  $K_H$  in the fully turbulent mixed layers at the surface and the bottom are obtained by second order closure model of turbulence based on the work of Mellor and Yamada (1974, 1982) and Galperin et al. (1988). The turbulence in this so-called level 2.5 model is characterized by two quantities, the turbulence kinetic energy  $q^2/2$  and the turbulence macro scale  $l$ . This two-equation model of turbulence is governed by (2-7) and (2-8).

The second order closure (Galperin et al., 1988) relates the vertical mixing coefficients,  $K_M$ ,  $K_H$  and  $K_q$  to the turbulent quantities  $q$  and  $l$ , that are defined according to

$$K_M = qlS_M \quad (2-16a)$$

$$K_H = qlS_H \quad (2-16b)$$

$$K_q = qlS_q \quad (2-16c)$$

where  $S_M$ ,  $S_H$  and  $S_q$  are stability functions determined from algebraic relations derived analytically from simplifications made to the full second moment closure model. The coefficients,  $S_M$  and  $S_H$  are functions of the Richardson number and are given by

$$S_H [1 - (3A_2B_2 + 18A_1A_2)G_H] = A_2 [1 - 6A_1 / B_1] \quad (2-17a)$$

$$S_M [1 - 9A_1A_2G_H] - S_H [(18A_1^2 + A_1A_2)G_H] = A_1 [1 - 3C_1 - 6A_1 / B_1] \quad (2-17b)$$

and

$$S_q = 0.2 \quad (2-17c)$$

$$\text{where } G_H = \frac{l^2}{q^2} \frac{g}{\rho_0} \left[ \frac{\partial \rho}{\partial z} - \frac{1}{c_s^2} \frac{\partial p}{\partial z} \right] \quad (2-17d)$$

is a Richardson number.  $S_M$  and  $S_H$  are also functions of  $G_H$ , which is in turn a function of the buoyancy gradient described by  $N$  which is the Brunt-Vaisala frequency indicative of the stability of the fluid column given by  $N^2 = - \left[ \frac{g}{\rho_0} \frac{\partial \rho}{\partial z} - \frac{g^2}{c_s^2} \right]$ .  $A_1, A_2, B_1$  and  $B_2$  are

constants that determine the ratios of various turbulence length scales to the turbulence macroscale  $\bar{l}$ . The turbulence closure assumes that all turbulence length scales are proportional to one another. Terms  $C_1, E_1, E_2$  and  $E_3$  are empirical constants determined by appealing to well-known laboratory experiments on turbulence, as are constants  $A_1, A_2, B_1$  and  $B_2$ . The five constants in (2-17a,b) are evaluated from neutral homogeneous and near surface turbulence (law-of-the-wall region) and are found (Mellor and Yamada, 1982) to be  $(A_1, B_1, A_2, B_2, C_1) = (0.92, 16.6, 0.74, 10.1, 0.08)$ . The values for constants  $E_1, E_2, E_3$  are 1.8, 1.8 and 1.33 respectively. The stability functions limit to infinity as  $G_H$  approaches the value, 0.0288, a value larger than one expects in the nature. The quantity,  $c_s^2$  in the square brackets of (2-15c) is the speed of the sound, squared. The vertical pressure gradient is obtained from the hydrostatic relation. The density is taken as a constant, i.e.,  $\partial \rho / \partial z = -\rho_0 z$ .

### c) Vertical Boundary conditions

The vertical boundary conditions for (2-2) are

$$\omega(0) = \omega(-1) = 0 \quad (2-18a,b)$$

However, if there is to be a surface throughflow of (usually fresh) water,  $\omega(0) \neq 0$ .

The surface boundary conditions for (2-3) and (2-4) are

$$\frac{K_M}{D} \left( \frac{\partial U}{\partial \sigma}, \frac{\partial V}{\partial \sigma} \right) = -(\langle wu(0) \rangle, \langle wv(0) \rangle), \sigma \rightarrow 0 \quad (2-18a,b)$$

where the right hand side of the equation is the input values for the surface turbulence momentum flux (the stress components are of opposite sign). The bottom boundary conditions are

$$\frac{K_M}{D} \left( \frac{\partial U}{\partial \sigma}, \frac{\partial V}{\partial \sigma} \right) = C_z [U^2 + V^2] (U, V), \sigma \rightarrow -1 \quad (2-18c,d)$$

where

$$C_z = \text{MAX} \left[ \frac{\kappa^2}{[\ln \{(1 + \sigma_{kb-1}) H / z_0\}]^2}, 0.0025 \right] \quad (2-18e)$$

Here,  $\kappa = 0.4$  is the von Karman constant that occurs in the log-law governing the velocity profile adjacent to a boundary in a turbulent boundary layer,  $z_0$  is the roughness parameter and  $C_z$  is the bottom friction coefficient (max value =1.0). Equations (2-18c,d,e) are derived by matching the numerical solution to the “law of the wall”. Numerically they are applied to the grid points nearest to the bottom. Where the bottom is not well resolved,  $(1 + \sigma_{kb-1}) H / z_0$  is large and (2-15e) reverts a constant drag coefficient, 0.0025. The boundary conditions on (2-5) and (2-6) are

$$\frac{K_H}{D} \left( \frac{\partial T}{\partial \sigma}, \frac{\partial S}{\partial \sigma} \right) = (\langle w\theta(0) \rangle), \sigma \rightarrow 0 \quad (2-19a,b)$$

$$\frac{K_H}{D} \left( \frac{\partial T}{\partial \sigma}, \frac{\partial S}{\partial \sigma} \right) = 0, \sigma \rightarrow -1 \quad (2-19c,d)$$

The boundary conditions for (2-7) and (2-8) are

$$(q^2(0), q^2l(0)) = (B_1^{2/3} u_r^2(0), 0) \quad (2-20a,b)$$

$$(q^2(-1), q^2l(-1)) = (B_1^{2/3} u_r^2(-1), 0) \quad (2-20c,d)$$

where  $u_r$  is the friction velocity at the top or bottom. This formulation helps reduce numerical noise in the shallow shelf regions, especially in the vicinity of Hudson Strait.

### 2.3. The Vertically Integrated Equations

The equations governing the dynamics of coastal circulation contain fast moving external gravity waves and slow moving internal gravity waves. To conserve computational resources and reduce computing time, the vertically integrated equations (external) are separated from the vertical structure equations (internal mode). This technique, known as mode-splitting (Simons, 1974; Madala and Piacsek, 1977) permits the calculation of the free surface elevation by solving the vertical transport separately from the three-dimensional calculation of the velocity and the thermodynamic properties.

The velocity external mode equations are obtained by integrating the internal mode equations over depth, thereby eliminating all vertical structure. Thus, by integrating (2-2) from  $\sigma \rightarrow -1$  to  $\sigma = 0$  and using the boundary conditions (2-14a,b), an equation for the surface elevation can be written as

$$\frac{\partial \eta}{\partial t} + \frac{\partial \bar{U}D}{\partial x} + \frac{\partial \bar{V}D}{\partial y} = 0 \quad (2-21)$$

After integration, the momentum equations (2-3) and (2-4), become

$$\begin{aligned} \frac{\partial \bar{U}D}{\partial t} + \frac{\partial \bar{U}^2 D}{\partial x} + \frac{\partial \bar{U}\bar{V}D}{\partial y} - \tilde{F}_x - f\bar{V}D + gD \frac{\partial \eta}{\partial x} = -\langle wu(0) \rangle + \langle wu(-1) \rangle \\ + G_x - \frac{gD}{\rho_0} \int_{-1}^0 \int_{\sigma}^0 \left[ D \frac{\partial \rho'}{\partial x} - \frac{\partial D}{\partial x} \sigma' \frac{\partial \rho'}{\partial \sigma} \right] d\sigma' d\sigma \end{aligned} \quad (2-22)$$

$$\frac{\partial \bar{V}D}{\partial t} + \frac{\partial \bar{U}\bar{V}D}{\partial x} + \frac{\partial \bar{V}^2 D}{\partial y} + -\tilde{F}_y - f\bar{U}D + gD \frac{\partial \eta}{\partial y} = -\langle wu(0) \rangle + \langle wu(-1) \rangle$$

$$+G_y - \frac{gD}{\rho_0} \int_{-1}^0 \int_{\sigma}^0 \left[ D \frac{\partial \rho'}{\partial y} - \frac{\partial D}{\partial y} \sigma' \frac{\partial \rho'}{\partial \sigma} \right] d\sigma' d\sigma \quad (2-23)$$

The overbars denote vertically integrated velocities such as

$$\bar{U} \equiv \int_{-1}^0 U d\sigma \quad (2-24)$$

The wind stress components are  $-\langle wu(0) \rangle$  and  $-\langle wv(0) \rangle$ , and the bottom stress components are  $-\langle wu(-1) \rangle$  and  $-\langle wv(-1) \rangle$ . The quantities  $\tilde{F}_x$  and  $\tilde{F}_y$  are defined according to

$$\tilde{F}_x = \frac{\partial}{\partial x} \left[ H2\bar{A}_M \frac{\partial \bar{U}}{\partial x} \right] + \frac{\partial}{\partial y} \left[ H\bar{A}_M \left( \frac{\partial \bar{U}}{\partial y} + \frac{\partial \bar{V}}{\partial x} \right) \right] \quad (2-25a)$$

and

$$\tilde{F}_y = \frac{\partial}{\partial y} \left[ H2\bar{A}_M \frac{\partial \bar{V}}{\partial y} \right] + \frac{\partial}{\partial x} \left[ H\bar{A}_M \left( \frac{\partial \bar{U}}{\partial y} + \frac{\partial \bar{V}}{\partial x} \right) \right] \quad (2-25b)$$

The dispersion terms are defined according to

$$G_x = \frac{\partial \bar{U}^2 D}{\partial x} + \frac{\partial \bar{U} \bar{V} D}{\partial y} - \tilde{F}_x - \frac{\partial \bar{U}^2 D}{\partial x} - \frac{\partial \bar{U} \bar{V}}{\partial y} + \bar{F}_x \quad (2-26a)$$

$$G_y = \frac{\partial \bar{U} \bar{V} D}{\partial x} + \frac{\partial \bar{V}^2 D}{\partial y} - \tilde{F}_y - \frac{\partial \bar{U} \bar{V} D}{\partial x} - \frac{\partial \bar{V}^2}{\partial y} + \bar{F}_y \quad (2-26b)$$

If  $A_M$  is constant in the vertical, then the “F” terms in (2-25a) and (2-25b) cancel. The Samogorinsky diffusivity allows us to account for vertical variability in the horizontal diffusivity, which is important in studying the tidal variability in shelf regions as shallow water depth strongly, influences the vertical structure of currents.

All terms on the right hand side of (2-22) and (2-23) are evaluated at each internal time step and then held constant throughout the many external time steps. If the external mode is executed *cum sole*, then  $G_x = G_y = 0$ .

## 2.4. Model Domain

The model domain is from 42°W to 75°W and 36°N to 66°N (Figure 2-2). The domain includes both coastal and deep ocean regime. The coastal ocean can be broadly divided into six regions (Loder et al. 1998). Starting from north, the Labrador Shelf is relatively long, straight and rugged, extending from Hudson Strait to the Strait of Belle Isle. There it adjoins the Newfoundland Shelf, which extends around the seaward coast of Newfoundland to Cabot Strait and the Laurentian Channel, and includes the Grand Banks and the offshore Flemish Cap. To the West of Newfoundland lies the Gulf of St. Lawrence, a nearly enclosed shallow sea which receives the freshwater discharge of the St. Lawrence River system and whose principal connection to the open shelf is through Cabot Strait. The open shelf continues with the relatively short, straight and rugged Scotian Shelf, which off southwestern Nova Scotia, connects to the Gulf of Maine, a tidally energetic semi- enclosed shallow sea encompassing the Bay of Fundy and Georges Bank. The segment is completed with the Mid Atlantic Bight, which has a long, smooth and narrowing shelf extending from Cape Cod to Cape Hatteras. The northeastern North American coastal ocean is the setting for a range of important interdisciplinary scientific and management issues. Generally high phytoplankton production supports important marine ecosystems and commercial fisheries, which were the incentives for coastal settlement by Europeans several centuries ago.

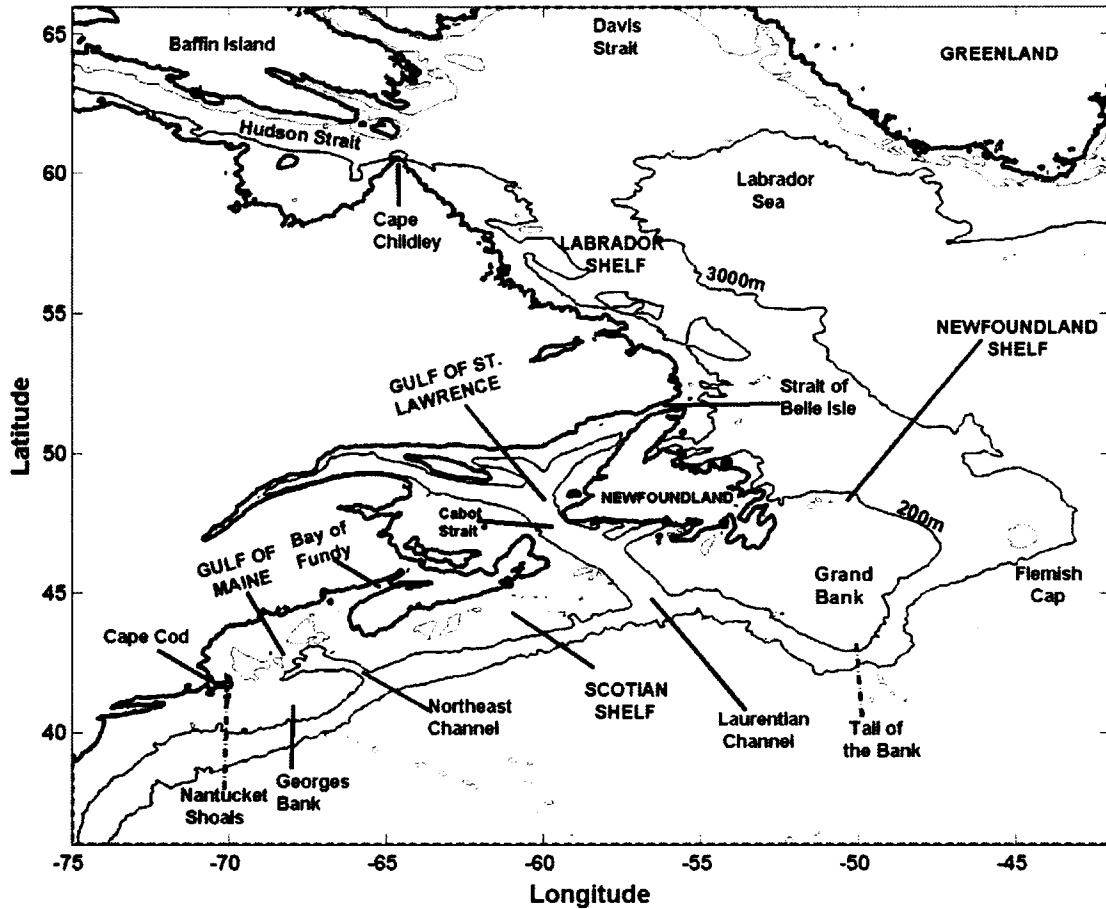


Figure 2-2. Map of the model domain (75 °W to 42 °W and 36 °N to 66 °N), showing the location of major features and regions, bathymetry (200 and 3000m). The open boundaries are depicted as green dashed lines. Map projection is based on cylindrical coordinate system, which will be used in all other map figures in this thesis.

The Gulf of Maine (GoM), located on the North American continental shelf between Cape Code and Nova Scotia, is a semi-enclosed basin opening to the North Atlantic Ocean. The geometry of the GoM is characterized by several deep basins and shallow submarine banks. On the seaward flank of the GoM is Georges Bank (GB), which is separated from the Nantucket Shoals to the west by the Great South Channel (GSC) and from the Scotian Shelf to the east by the Northeast Channel. The bank is roughly elliptical in plan view with a length of about 200 km along the major axis and a width of about 150 km along the minor axis. The GSC runs approximately north-south, with a sill

depth of about 50 m located near 40 degree and 45' to separate the mid and outer continental shelf to the south from the deeper GoM to the north with depths in exceed of 150 m. The deep connection between the GoM and the open ocean is mainly through Northeast Channel where the sill depth is about 230 m. A special feature of the Gulf of Maine is its strong barotropic resonance at semidiurnal frequencies (Lynch et. al., 1992). The dominant  $M_2$  tide, present seaward of Georges Bank at roughly 0.5m amplitude, grows monotonously to 4m in the Bay of Fundy and exceeds 6 m in its farthest extremity, the Minas Basin. This resonance results in strong gradients in elevation amplitude (0.5 m) and phase ( $90^\circ$ ) over the banks; these elevation gradients are further enhanced in the velocity response by the shallow bank topography – tidal currents reach 1 m/s atop Georges Bank. Hudson Strait, connecting Hudson Bay and Foxe Basin with the Labrador Sea, is a region characterized by high tides and strong residual flows. Tidal sea-level elevations typically vary in the range between 3-6m and in certain locations exceeding 9m (Easton, 1972). Tidal currents are strong with amplitudes generally of 0.2 to 1 m/s but reaching 2 m/s in the vicinity of the eastern entrance (Chandler et al., 1985; Osborn et al., 1978). The topography of the Eastern Scotian Shelf is characterized by shallow outer banks, deep inner basins, and cross shelf channels (Han and Loder, 2003). This complex geometry, together with the confluence of Gulf of St. Lawrence outflow through Cabot Strait (CS), the Labrador Current extension along the shelf break and the cyclonic gyre over the continental slope, results in pronounced spatial and temporal structure in the region's circulation pattern. On the shelf scale the region has variable inflows of relatively saline offshore Slope Water. On the topographic (bank/basin/channel) scale, the structure and variability of circulation features is characterized by partial gyres and cross-shelf flows.

## 2.5. Model Grid

The governing equations of the model are solved over a horizontal rectilinear grid. The model resolution was fixed at  $1/12^{\circ} \times 1/12^{\circ}$  in the horizontal. The grid has a meridional spacing of 9.3 km and a zonal spacing that varies from 7.5 km at  $36^{\circ}\text{N}$  to 3.8 km at  $66^{\circ}\text{N}$ . In all four cases (see Table 2-2), there are 16 unequally spaced levels ( $\sigma=0$  at the sea surface and  $\sigma=-1$  at the bottom) in the vertical. For the baseline cases (Bu,Ba), following is the distribution:  $\sigma = (0, -0.025, -0.05, -0.1, -0.2, -0.3, -0.4, -0.5, -0.6, -0.7, -0.8, -0.9, -0.95, -0.975, -0.9875, -1)$ . The resolution is increased near the bottom boundary layers (the last four near to the bottom), to be able to resolve properly the tidal features in the shelf region. For the diagnostic cases (Du and Da), the number of layers in the vertical are increased to properly interpolate and represent the surface temperature and salinity from the monthly-mean hydrography data (Geshelin et al., 1999) which is on a regular z-level (0, 10, 20, 30, 50, 75, 100, 125, 150, 200, 250, 300, 400, 500, 600, 700, 800, 900, 1000, 1100, 1200, 1300, 1400, 1500, 1750, 2000, 2500, 3000, 3500, 4000, 4500). In the Arakawa-C grid formulation, the scalar quantities are defined at the centre of the grid point, in the vertical and the horizontal. The vertical level distribution is as follows:  $\sigma = (0, -0.0078, -0.0156, -0.0313, -0.0625, -0.125, -0.25, -0.5, -0.75, -0.875, -0.9375, -0.9688, -0.9844, -0.9922, -0.9961, -1)$ .

Bottom topography was derived from ETOPO2 elevation data (Figure 2-3). The ETOPO2 elevation data was cleaned up to remove artificial islands especially in the Hudson strait area, the Newfoundland shelf and the Gulf of St. Lawrence. The bathymetry from a finite element model [G. Han, personal communication 2006], was incorporated into the model for the region including the Labrador region and below  $58^{\circ}\text{N}$  and Sable Island was added. A 5-point Laplacian smoother was used to smooth the elevation data in the

Hudson Strait to conserve volume in the adjacent grid points. To minimize the pressure gradient errors, the bottom topography in the model (Figure 2-4) has been smoothed such that the difference of the depths of the adjacent grid points divided by their mean is less than 0.1 in the Northern part of the model (58 °N to 66 °N) and 0.4 for the rest of the model (Mellor et al., 1994). The adjustment is made so as to conserve the combined volume of the adjacent grid points. The maximum ocean depth in the model is 5600m and the minimum depth is 10m.

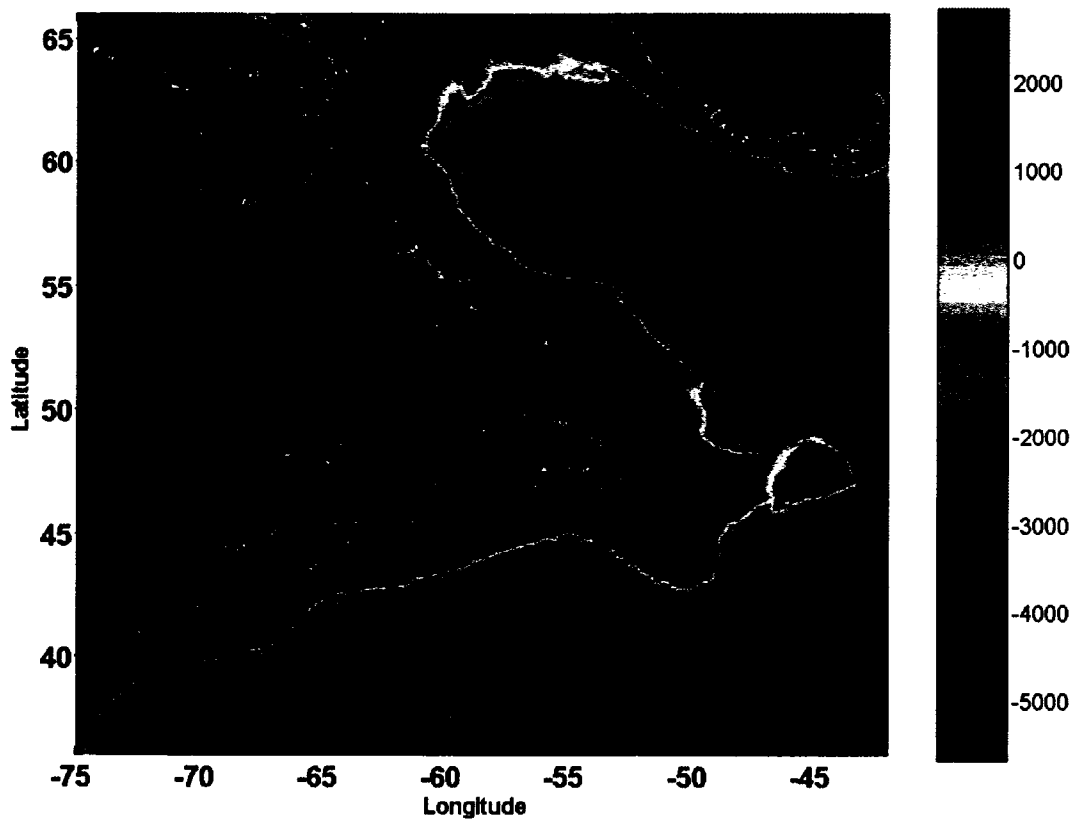


Figure 2-3. ETOPO2 elevation data. Scale at right shows the depth in metres.

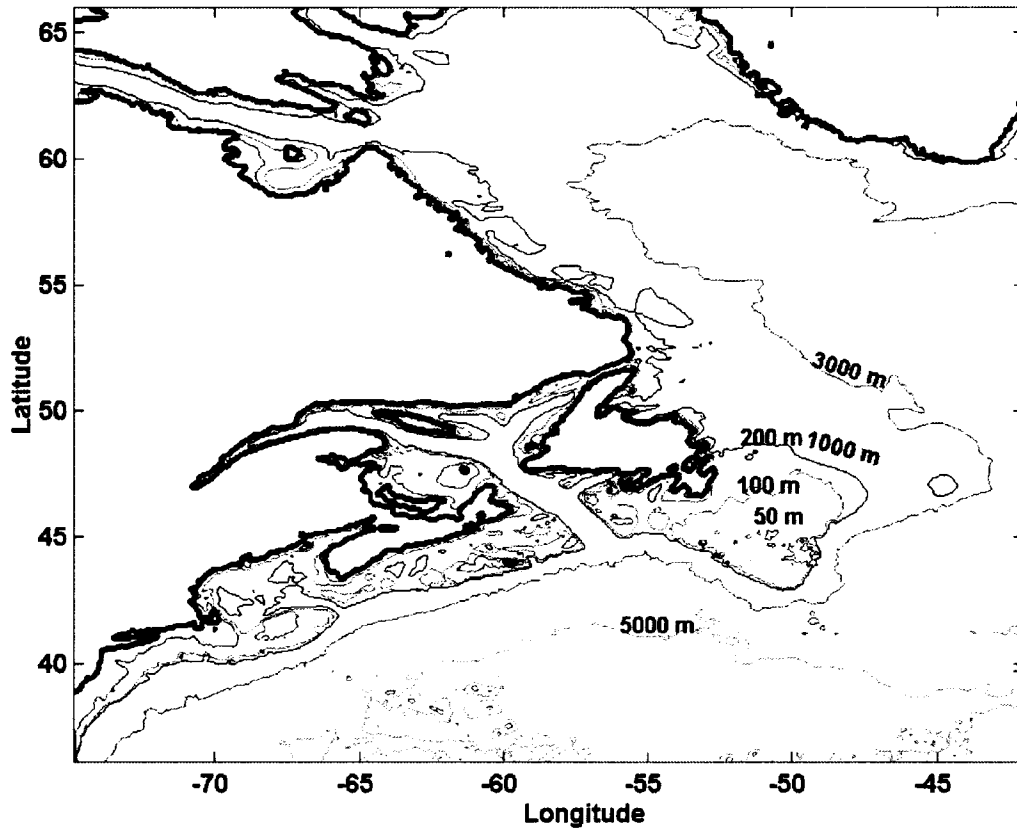


Figure 2-4. The bottom topography contours, from ETOPO2 and a finite element model provided by G. Han (PC, 2006) interpolated onto the model grid. The 50-, 200-, 1000, 3000- & 5000m contours are labeled and shown in red, blue, yellow, cyan & magenta colours respectively.

## 2.6. Boundary Conditions

### i) Elevation

Elevation is specified as

$$\eta = \hat{\zeta} \quad (2-27)$$

where  $\hat{\zeta}$  is a prescribed function of position and time

### ii) Depth-averaged Current

A simple gravity-wave radiation condition (Flather, 1987)

$$q = \hat{q} + \frac{c}{H}(\eta - \hat{\zeta}) \quad (2-28)$$

where  $c = (gH)^{1/2}$ , and  $\hat{\zeta}$  and  $\hat{q}$ , respectively the input elevation and current, are prescribed as functions of position and time.

The gravity-wave condition treats any internally generated deviations from the prescribed elevation and current at the boundary as free progressive waves propagating outward across it.

The prescribed input elevation ( $\hat{\zeta}$ ) and current ( $\hat{q}$ ) for the multi-constituent runs are of the form

$$\hat{\zeta} = \sum_{i=1}^{i=8} \zeta_{ai} \cos(\omega_i t + \phi_i) \quad (2-29a)$$

$$U = \sum_{i=1}^{i=8} U_{ai} \cos(\omega_i t + \phi_i) \quad (2-29b)$$

$$V = \sum_{i=1}^{i=8} V_{ai} \cos(\omega_i t + \phi_i) \quad (2-29c)$$

where  $\zeta_{ai}$ ,  $U_{ai}$  &  $V_{ai}$  are the amplitudes of the elevation and zonal and meridional components of the prescribed elevation and current respectively,  $\omega_i$  is the angular frequency of the tidal constituent  $i$  and  $\phi_i$  is the phase lag of the tidal constituent  $i$  calculated at the Greenwich Meridian.

### iii) 3-D current

A radiation boundary condition for the internal mode variables on the lateral open boundaries are prescribed as (POM user guide, 2004)

$$\frac{\partial U}{\partial t} + c_i \frac{\partial U}{\partial x} = 0 \quad (2-30a)$$

$$\frac{\partial V}{\partial t} + c_i \frac{\partial V}{\partial y} = 0 \quad (2-30b)$$

for the meridional and zonal components respectively.

A zero normal velocity is imposed at the lateral land boundary, while the normal gradient of the tangential velocity component is set to zero at the open boundary. At the sea-surface a zero stress boundary condition is applied, with the absence of wind stress. Correspondingly, the flux of turbulent kinetic energy is set to zero.

The reliability and confidence level of the elevation open boundary values for  $M_2$  and  $K_1$  constituents from a North Atlantic Model (Egbert and Erofeeva, 2002) are evaluated against the altimeter data. Figure 2-5 shows the elevation open boundary values for  $M_2$  and  $K_1$  constituents from the North Atlantic Model compared with the multi-mission altimeter data (interpolated onto the model grid) used for assimilation. It is clear from the figure that the model's open boundary values derived from the North Atlantic Model agree well with the altimeter data with an error estimate of 2.1 cm in amplitude and 4.4 deg in phase for  $M_2$  constituent and 4.1 cm in amplitude and 7.8 deg in phase for the  $K_1$  constituent.

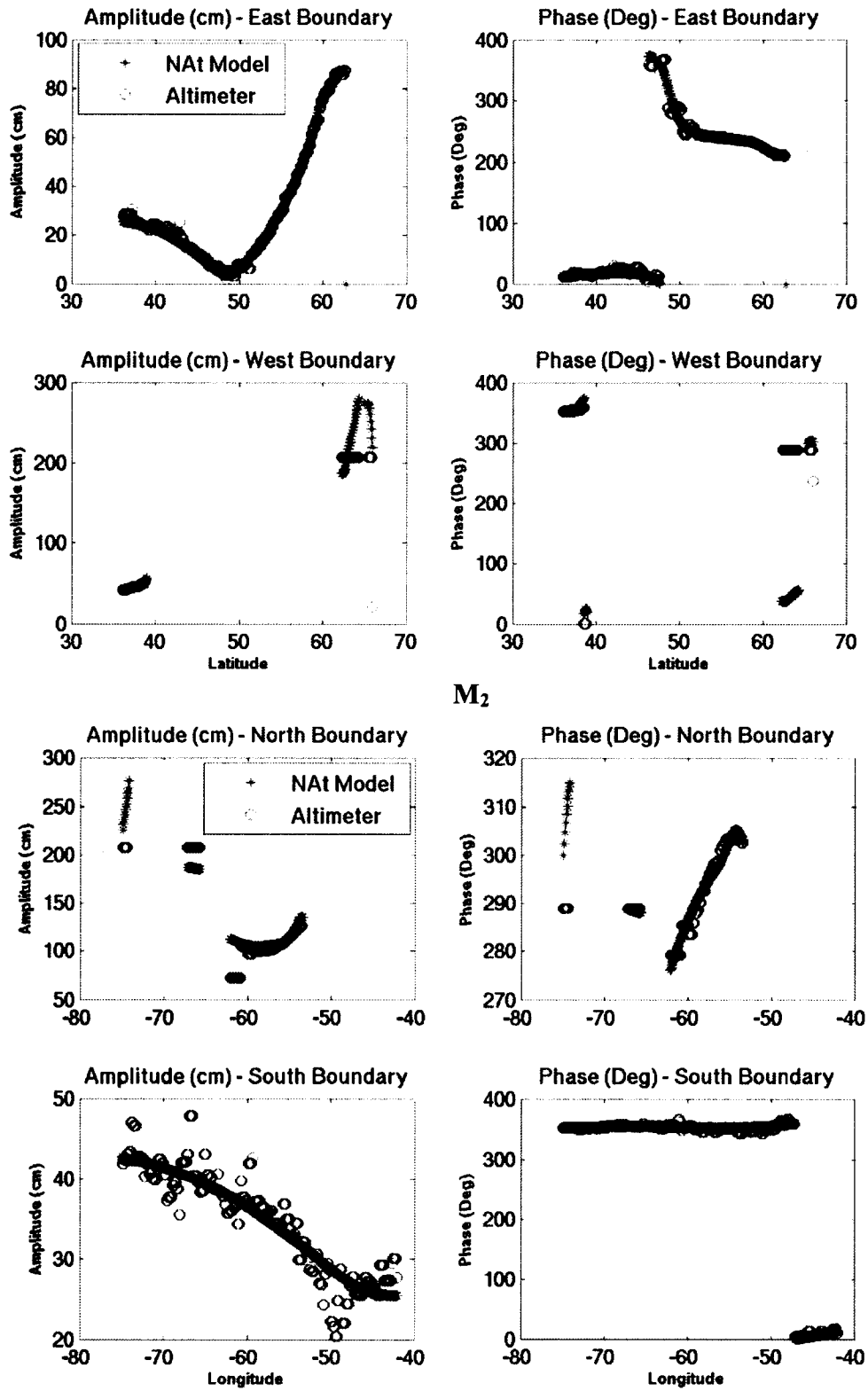


Figure 2-5. Elevation open boundary values (amplitude and phase) for  $M_2$  (this page) and  $K_1$  (next page) constituents from North Atlantic Model and altimeter data (interpolated on to the model grid), in the East-West and North-South domain. The red circles are the altimeter data values and the blue asterisk (\*) are the values from the North Atlantic Model. The gaps in the plots are for the closed boundaries. The amplitudes are in cm and phases are in degrees.

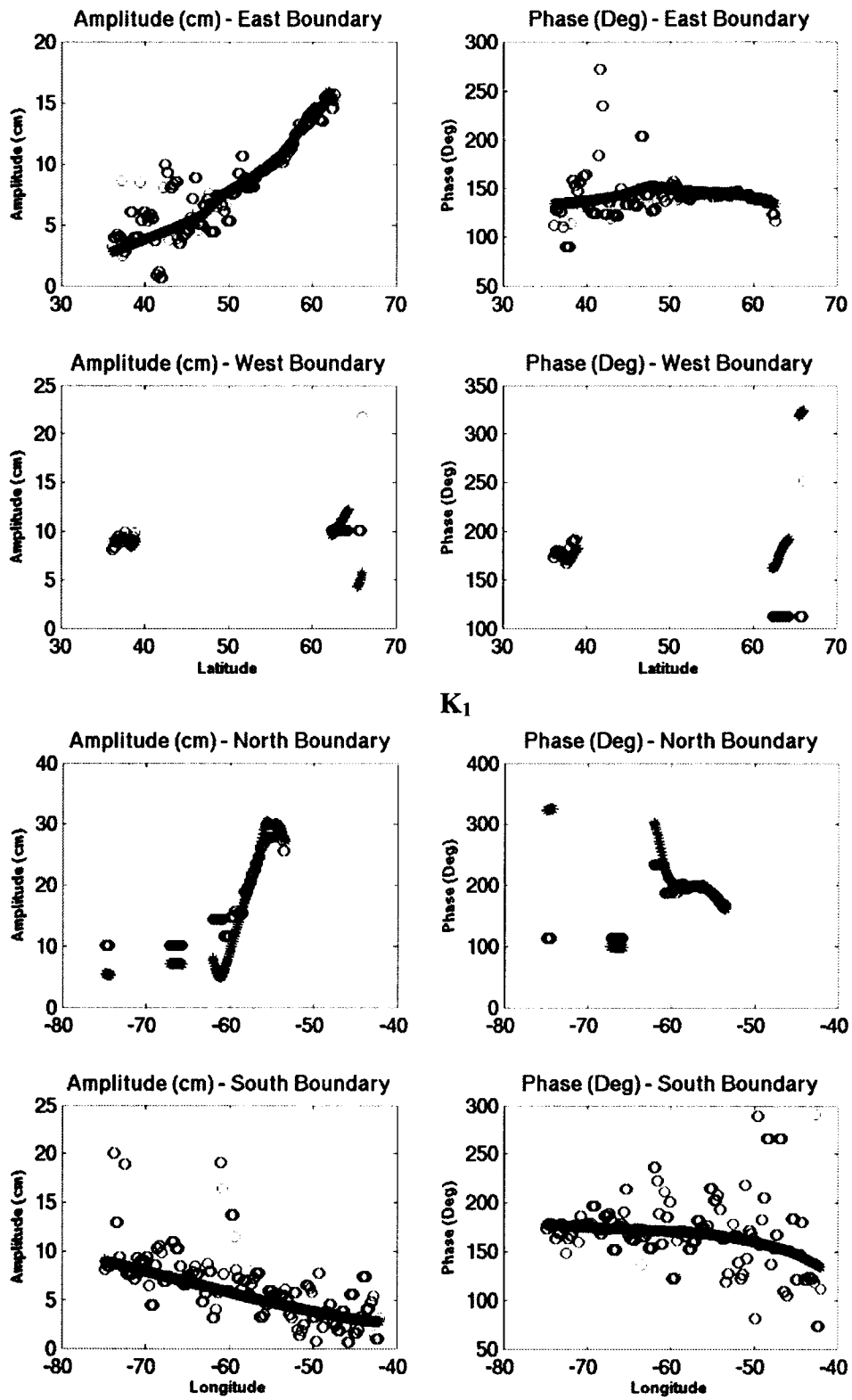


Figure 2-5. (Continued).

## 2.7. The Equilibrium, Earth and Load tides

Considering the specifications of  $\zeta_b$  and  $\bar{\zeta}$  in (2-3) and (2-4), the assumptions available are as follows:

a) Simplest is that the earth is rigid, so that  $\zeta_b = 0$ , and that the influence of the tide-generating potential is negligible, so that  $\bar{\zeta} = 0$ . Then the motion is driven entirely by the oscillation on the open boundaries prescribed by (2-27) & (2-28), and the co-oscillating tide results.

b) Retaining the influence of tide generating potential and assuming the earth to be elastic gives

$$\bar{\zeta}_n - \zeta_{bn} = (1 + k_n - h_n) \bar{\zeta}_{0n} \quad (2-31)$$

Where  $\bar{\zeta}_{0n} = \Phi_n / g$  the unperturbed equilibrium tide produced by the tide-generating potential  $\Phi_n$  and  $k_n$  and  $h_n$  are Love numbers relating the body earth tide and associated perturbations to the potential. Subscript n denotes the tidal constituent.

c) The most complete description of earth tide influence is obtained by including the load tide (the deformation of the elastic Earth due to the redistribution of mass in the ocean tide) and associated perturbations.

The next section describes the method used for calculating the Equilibrium, Earth and load tides.

As a crude approximation, if  $\zeta$  is the oceanic tide, the load tide can be taken as  $0.007 \zeta$  in magnitude and exactly in anti-phase with the oceanic tide, and the gravitational potential due to it is  $0.05g\zeta$  (Cartwright, 1993). However, a more accurate method is to calculate equivalent load love numbers, using a Green's function approach and an Earth model. Farrell (1972) developed a method for computing the ocean tide loading which

involves the calculation of a convolution integral around the whole oceanic globe for each point where the tide loading effect is evaluated. Subsequently, Francis & Mazegga (1990) used this method and the tidal model of Schwiderski (1980a,b) to produce global charts of the ocean-tide loading. With the advent of TP global tide models, these calculations were upgraded by various researchers (e.g., Matsumoto et al., 1995) and loadings at 0.5 degree intervals around the whole globe are available in Anon. (1996).

Francis & Mazegga (1990) and Ray (1998) show that the ocean-tide loading for tidal constituent  $n$  at latitude  $\phi$  ( $^{\circ}$ N) and longitude  $\chi$  ( $^{\circ}$ E) is given by

$$\zeta_{bn}(\phi, \chi) = \rho_w R^2 \iint_{\Omega} G(\alpha) \eta_n \partial \Omega \quad (2-32)$$

where  $\rho_w$  is the density of sea water,  $R$  is the radius of the earth,  $\eta_n$  is the ocean tide,  $\alpha$  is the angle between the point under consideration and the integration point, and  $\Omega$  is the domain of integration. The kernel function,  $G(\alpha)$ , is a Green's function and is tabulated for various Earth models by Farrell (1972).

Earth tides are calculated from the astronomical tide-generating potential  $\Phi$ , given by (e.g., Foreman et al. 1995):

$$\Phi_n = gH_n \cos^2 \phi \cos(\omega t + 2\chi + V_n) \quad (2-33a)$$

for semi-diurnal tides and

$$\Phi_n = gH_n \sin 2\phi \cos(\omega t + \chi + V_n) \quad (2-33b)$$

for diurnal tides, where the subscript  $n$  denotes the tidal constituent of angular frequency  $\omega_n$ ,  $g$  is the acceleration due to gravity,  $H_n$  is the amplitude (Table 2-1) and  $V_n$  is an argument which is the same as that used for tidal predictions and relates to the state

of the tide at the tide datum (typically this is 0 h UT, 1 January 1900). The Earth tide,  $\eta E_n$ , is related to the astronomical tide-generating potential by (Ray, 1998):

$$\eta E_n = \frac{h_n \Phi_n}{g} \quad (2-34)$$

Where  $h_n$  is the Love number (Wahr 1981) given in the Table 2-1.

Table 2-1. Love numbers,  $k_n$  and  $h_n$ , and tidal potential amplitudes,  $H_n$ , used in calculating the Earth tides (from Foreman et al. 1995)

Constituent	$k_n$	$h_n$	$H_n$ (mm)
M <sub>2</sub>	0.302	0.609	0.24408
S <sub>2</sub>	0.302	0.609	0.11355
N <sub>2</sub>	0.302	0.609	0.04674
K <sub>2</sub>	0.302	0.609	0.03090
K <sub>1</sub>	0.256	0.520	0.14246
O <sub>1</sub>	0.298	0.603	0.10128
P <sub>1</sub>	0.287	0.581	0.04713
Q <sub>1</sub>	0.298	0.603	0.01940

## 2.8. Assimilation Methods

All models of physical and other processes are only approximations to the “truth”. Each and every numerical model has some kind of built-in bias which could result from errors in initial condition, prescribed open boundary conditions, etc. To obtain a realistic model data output, it is necessary to employ actual observations of physical processes into the model. The process of employing observed data from the real ocean, to keep the modeled ocean realistic, is called data assimilation.

The following section describes a few available and employed assimilation methods, which also includes the one that has been employed in the study.

### a) Data insertion

In this method, the model predicted values are simply replaced by observed values at grid points, where observations are available. The implicit assumption is that the data are accurate and the model errors are large. The main disadvantage is that the continuity equations are not satisfied and the focus is mainly on the particular variable which is being replaced. The *Blending* estimate is a scalar linear combination of the forecast and data values at all data points, with user-assigned weights.

### b) Nudging

The *Nudging* or *Newtonian Relaxation Scheme* "relaxes" the dynamical model towards the observations. To do so, terms proportional to the difference between the data and state variables (i.e. data residuals) are added to the dynamical model. The coefficients in the relaxation can vary in time but cannot be too large to avoid model disruptions. They should be related to dynamical scales and *a priori* estimates of model and data errors. It is also possible to use nudging techniques in which appropriate Newtonian damping terms that damp the variable to the observed value with a predetermined timescale are introduced into the governing equations. In this method the model is slowly nudged (or coaxed) toward observations at each time step in the model via a Newtonian damping term in the prognostic equation for the variable:

$$\frac{\partial X}{\partial t} = -\frac{(X - X_0)}{T_d} \quad (2-35)$$

where the model variable  $X$  is nudged toward a reference value  $X_0$  (the value to be assimilated) at a timescale  $T_d$ .  $X_0$  can itself be a function of time. The smaller the value of  $T_d$ , the more rapidly it is nudged towards the reference value, since as  $T_d \rightarrow 0, X \rightarrow X_0$ . The larger the value of  $T_d$  compared to the characteristic timescale of

variability in the prognostic variable, the weaker the influence of assimilated data. The value of  $T_d$  encodes the confidence in the assimilated value versus the model value. For tidal applications the values for  $T_d$  can be the period of the tidal constituent more pronounced in the area of the study and  $X_0$  is typically the sea surface elevation.

### c) Optimal Interpolation

*Optimal interpolation* (OI), also referred to as *statistical interpolation* in meteorology, is a simplification of the Kalman Filter. The data-forecast melding or analysis step is still a linear combination of the dynamical forecast with the data residuals, but in the OI scheme, the matrix weighting these residuals or gain matrix is empirically assigned. In the Kalman Filter, the gain is computed and updated internally. If the assigned OI gain is diagonal, the OI and above nudging scheme can be equivalent. However, the OI gain is usually not diagonal, but a function of empirical correlation and error matrices. Han et al. (2000) used an assimilation scheme that uses a blending approach based on optimal linear interpolation (White et al., 1990). The method involves a forcing term equal to the smoothed difference between the model elevation and the interior observations imposed at regular intervals (in this case, 6 model time steps).

### d) Direct Inverse Method

Xu et al. (2001) have used a direct inverse method wherein the elevation vector  $\xi$  is splitted into a part  $\zeta$  defined on the boundary nodes and a part defined on the interior nodes, and splitting the stiffness matrix  $A$  into boundary and interior parts ( $A_{bc}$  and  $A_{in}$ ). For more details the readers are referred to the above mentioned paper. It works only for linear cases.

**e) Other Methods**

There are more complex and expensive methods such as Kalman filters (Gelb, 1988), which blend the model and observed values optimally, take into account the model error and observational error statistics and variational methods (e.g., Derber and Rosati, 1989 & Thacker and Long, 1987)).

### 3. Model Runs and Analysis Methods

#### 3.1. Model Runs

The numerical experiments of this study are listed in Table 3-1. Most of the discussion is focused on a comparison of the first two cases with special focus on the second case, but mention is also made of the other two runs.

Table 3-1. Numerical experiments mentioned in this study.

<i>Experiment</i>	<i>Stratification Profile</i>	<i>Comments</i>
Bu	None	Homogeneous fluid case
Ba	None	Homogeneous fluid case with assimilation using altimeter data
Du	August	Diagnostic case
Da	August	Diagnostic case with assimilation using altimeter data

For all the four model runs, the model was forced at the open boundaries (Figure 2-2) with elevation and depth-averaged velocity for  $M_2$ ,  $S_2$ ,  $N_2$ ,  $K_2$ ,  $K_1$ ,  $O_1$ ,  $P_1$  and  $Q_1$  derived from a North Atlantic Model (Egbert and Erofeeva, 2002). The model was integrated for 39 days of simulated time. Hourly elevation and current fields from the last 30 days were subjected to a harmonic analysis to separate the response at the 8 constituent frequencies. This analysis period is sufficient for the harmonic analysis to separate the response within the diurnal and semi-diurnal frequency bands. The initial spin up time of 9 days is sufficient to establish a dynamically equilibrium state.

##### 3.1.1. Barotropic Run

This experiment, also referred to as Baseline unassimilated, is a control run in which a homogeneous unstratified fluid is specified. An external time step of 6 seconds and an

internal time step of 180 seconds are chosen. Tidal elevations and currents are computed by integrating forward the model in time from a state of rest.

### **3.1.2. Barotropic Data Assimilation**

The multi-mission altimeter data was assimilated at every external time-step into the model using a nudging method (see section 2.8 (b)), the time scale,  $T_d$ , was 12.42 hours (time period of  $M_2$  tidal cycle).

### **3.1.3. Diagnostic Run**

A horizontally and vertically varying climatological monthly mean fixed summer density profile (see section 4.4) was used to initialize the model for this experiment. The baroclinic pressure gradients are turned off to disallow baroclinic (internal) tides being generated in the model solutions. In any case, the diagnostic run does not generate baroclinic tides. The baroclinic tides are barotropically forced in a stratified ocean with variable bathymetry. Tidal elevations and currents are computed by integrating forward the model in time from a state of rest. An external time step of 2 seconds and an internal time step of 60 seconds are chosen.

### **3.1.4. Diagnostic Data Assimilation**

The multi-mission altimeter data was assimilated at every external time-step into the model using a nudging method (see section 2.8 (b)), the time scale,  $T_d$ , was 24 hours (~ time period of  $K_1$  tidal cycle).

## **3.2. Harmonic Analysis**

A harmonic analysis package (Pawlowicz et al., 2002) was used to analyze the time-series for the model elevation and current output.

### 3.3. Error Measures

The error in a tidal constituent at an observation point was computed by interpolating the model solution for the tidal constituent to the observation point. To provide a quantitative assessment of the model solution (for the tidal elevation and current), three methods were employed:

- a. The Root Mean Square (RMS) Error of the difference between the Observed value and model solution for each constituent are calculated for amplitude and phase.
- b. Averages of the absolute RMS error (AbsErr),  $L^{-1} \sum_L D$ , and the relative RMS error (RelErr),  $L^{-1} \sum_L D / A_o$ , are computed for semi-diurnal and diurnal constituents at each location of the observed value. The averaging is based on the total number (=L) of in-situ observations for Tide & Bottom pressure gauges and the Current Meter moorings. D is the RMS difference over a tidal cycle between model and observations, given by

$$D = \left[ \frac{1}{2} (A_o^2 + A_m^2) - A_o A_m \cos(\phi_o - \phi_m) \right]^{1/2} \quad (3.1)$$

where  $A$  and  $\phi$  are amplitudes and phases for a given constituent, and subscripts  $m$  and  $o$  refer to model and observations respectively.

- c. The Root Sum Square (RSS) value for all the five major constituents, used for comparison with the observed values, is calculated for each region, excluding BoFGoM and for all the regions.

## 4. Observational Data

### 4.1. Tidal and Pressure Gauge Data

The observational dataset comprising of the five major semi-diurnal ( $M_2$ ,  $S_2$  &  $N_2$ ) and diurnal constituents ( $K_1$  &  $O_1$ ) is widely distributed over the study region. The in-situ elevations are taken from coastal tide gauge and bottom pressure gauge locations (Figure 4-1). The observational dataset, comprising a total of 101 locations, is divided into 5 regions: coastal island of Newfoundland, coastal Nova Scotia, Bay of Fundy and Gulf of Maine (BoFGoM), Labrador Sea & Shelf and Super Stations (Newfoundland Grand Banks and off the coast of Nova Scotia). Tidal parameters are determined using the standard BIO tidal analysis package.

The coastal tide gauge constituents at 55 locations are extracted from the database provided by Canadian Hydrographic Service, covering the region of coastal island of Newfoundland, coastal Nova Scotia and Bay of Fundy and Gulf of Maine (BoFGoM). The typical length of the record varies from 29 to 365 days with a median length of 55 days. The phases are corrected with respect to Greenwich. An additional 22 observations from bottom pressure gauges in the region of Labrador Sea and Shelf are obtained from Wright et al. (1988, 1991). Apart from 5 locations, 837, 838, 840, 791 and 790 where the length of the record is 1000, 2500, 3560, and 1007 and 2480 days respectively, the median length of the record excluding the 5 locations listed above is 200 days. The observations, totaling 24, for the Super Stations are collected from Han et al. (1996). The median length of the record for the 8 offshore locations (8-15) is 171 days. The observational uncertainty in amplitude was estimated to be of the order of 1 cm for the  $M_2$  and 0.3 cm for the other constituents. The phase error was estimated to range from about  $1^\circ$  to  $3^\circ$  (de Margerie and Lank, 1986). Table A-1 lists the locations of the tide and

bottom pressure gauges along with the length of the record for all the regions in the model domain.

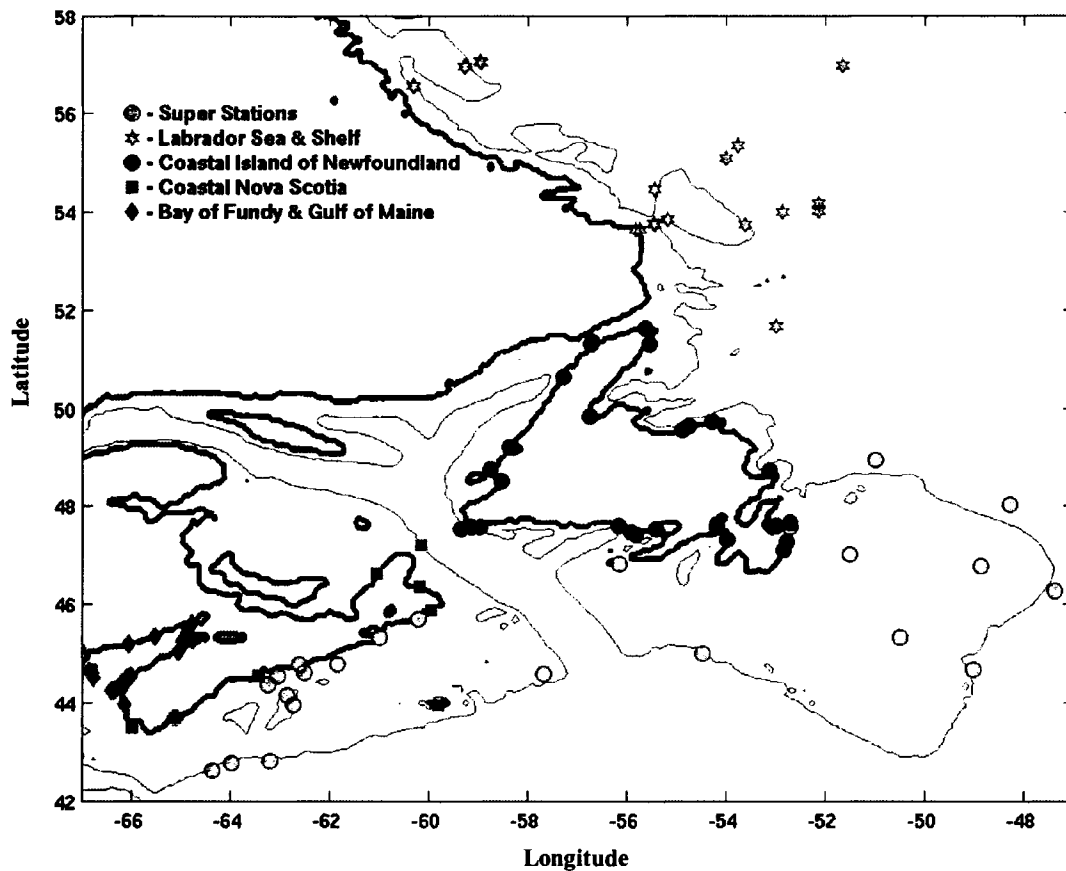


Figure 4-1. Locations of tide and bottom pressure gauges (with 200m isobath – red solid line). The legend inside the figure describes the markers used to define the different locations of the tide and bottom pressure gauges. The figure has been expanded in for clarity of locations for the tide and bottom pressure gauges.

#### 4.2. Current Meter Data

The tidal current velocity data is obtained from the Northwest Atlantic tidal current database (Drozowski et al. 2002). The total number of stations available are 267 and it covers the region from the Georges Bank to the Labrador Shelf excluding the Gulf of St. Lawrence and includes the 5 major tidal constituents ( $M_2$ ,  $S_2$ ,  $N_2$ ,  $K_1$  &  $O_1$ ), the locations of which are shown in Figure 4-2. The number of observations for each constituent

varies. Table 4-1 lists the total number of comparisons available for each constituent including the different depths of data recorded at each observation location. For a detailed description of the database and the data, the reader can go through the report by Drozdowski et al. (2002).

The velocity data are divided into 6 regions: the Labrador Shelf – (18 comparisons), the Newfoundland Shelf (including the North Avalon Channel) – (41 comparisons), the Scotian Shelf - (145 comparisons), Georges Bank – (22 comparisons), Bay of Fundy & Gulf of Maine (BoFGoM) – (9 comparisons) and Channel (comprising of Great South Channel, Nantucket Shoals, New England Shelf & North East Channel) – (32 comparisons). The database consists of tidal current velocity data stored as east (U) and north (V) components of amplitude and phase lag (Degrees Greenwich). The data were collected from 1978 to 1993.

Table 4-1. The number of available comparisons (records) for current meter observations, including different depths at each location, made for model current data.

<b>Constituent</b>	<b>BoFGoM</b>	<b>Channel</b>	<b>GB</b>	<b>Lab</b>	<b>NFShelf</b>	<b>ScoShelf</b>	<b>Total</b>
<b>M<sub>2</sub></b>	<b>13</b>	<b>63</b>	<b>60</b>	<b>47</b>	<b>76</b>	<b>348</b>	<b>607</b>
<b>S<sub>2</sub></b>	<b>12</b>	<b>48</b>	<b>61</b>	<b>49</b>	<b>75</b>	<b>319</b>	<b>564</b>
<b>N<sub>2</sub></b>	<b>13</b>	<b>55</b>	<b>57</b>	<b>49</b>	<b>74</b>	<b>308</b>	<b>556</b>
<b>K<sub>1</sub></b>	<b>13</b>	<b>56</b>	<b>61</b>	<b>23</b>	<b>64</b>	<b>302</b>	<b>519</b>
<b>O<sub>1</sub></b>	<b>14</b>	<b>53</b>	<b>61</b>	<b>44</b>	<b>66</b>	<b>305</b>	<b>543</b>

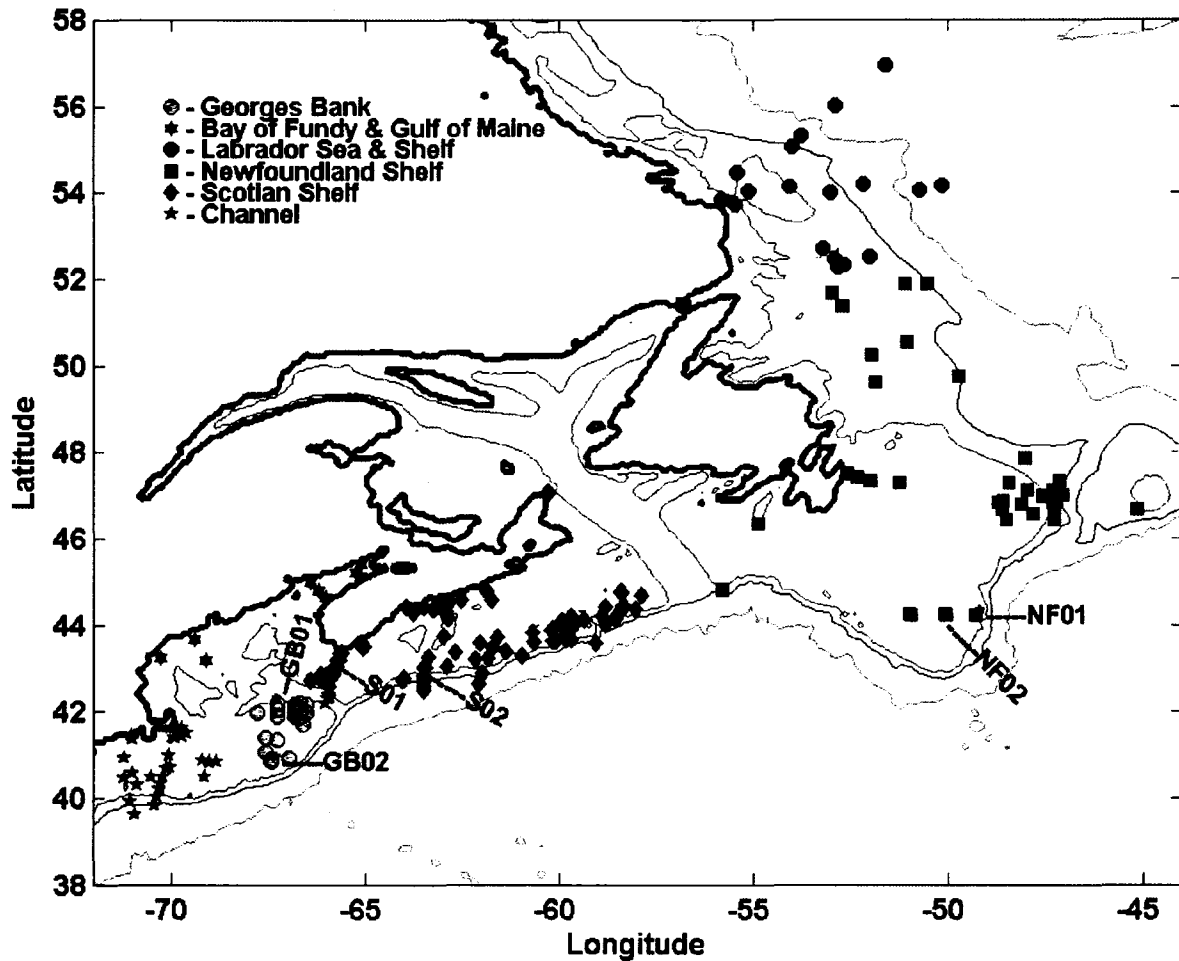


Figure 4-2. Location of current meters used for comparison with model data (with 200- (solid red line), 1000- (solid blue line) & 3000m (solid green line) isobaths). The text inside the figure is the names of locations where the vertical structure of currents is examined. The legend figure describes the markers used to define the six different locations of the current meters. The figure has been zoomed in for clarity of locations.

### 4.3. Altimeter Data

Satellite altimeter data of T/P, TOPEX Tandem Mission, JASON-1, ENVISAT, and GFO missions were used to derive the 8 short period tides namely  $M_2$ ,  $S_2$ ,  $N_2$ ,  $K_2$ ,  $K_1$ ,  $O_1$ ,  $P_1$  &  $Q_1$  [Y. Yi and C.K. Shum, personal communication, 2006]. TOPEX GDR data (no POSEIDON data) on original tracks for T/P cycles 4-364 spanning 11/92-8/02, TOPEX Tandem Mission GDR for T/P cycles 369-479 (9/02-9/05), JASON GDR cycles 1-135

(1/02-9/05), GFO GDR cycles 37-168 (1/00-3/06) and ENVISAT GDR cycles 10-38 (10/02-7/05) are used in the study.

NASA (National Aeronautics and Space Administration, USA) currently has two satellite missions that measure Ocean Surface Topography (OST). TP was launched in 1992, and Jason was launched in 2001, which continues the measurements made by TP. These missions use radar altimeter systems specially designed to make extremely accurate and precise measurements of the ocean surface. These measurements give long-term information about the world's oceans and currents. Both measure the height of the sea surface with an accuracy of 4 to 5 centimeters (less than 2 inches) relative to the center of the Earth, and collect data over nearly all of Earth's ice-free oceans every 10 days. The European Space Agency (ESA) launched ENVISAT spacecraft from Kourou in French Guyana on the night of 28 February 2002. This satellite measures atmosphere, ocean, land and ice over a five-year period. The GEOSAT Follow-on (GFO) program is the US Navy's initiative to develop an operational series of radar altimeter satellites to maintain continuous ocean observation from the GEOSAT Exact Repeat Orbit. GFO is the follow-on to the highly successful GEOSAT-A and was launched in February 1998. On 29 November 2000, the Navy accepted the satellite as operational. The 5-year GEOSAT mission objective to measure the dynamic topography of the Western Boundary currents and their associated rings and eddies, to provide sea surface height data for assimilation into numerical models, and to map the progression of El Nino in the equatorial Pacific. TOPEX Tandem Mission is a maneuver to move TP to a new Tandem Mission orbit that places TOPEX/Poseidon in an orbital position halfway between that of Jason-1. The two satellites increase global data coverage twofold.

The altimetric tides were provided by Y. Yi and C.K. Shum (personal communication, 2006) on a 1/4 x 1/4 degrees grid for the Northwest Atlantic, bounded by 34N & 71N parallels and 284E & 330E meridians, excluding the Hudson Strait area. Annual, semi-annual,  $M_2$ , and  $M_4$  long-period tides were solved for simultaneously in this tidal analysis. There are numerous grid points at which the tidal solution is not available because of a lack of nearby radar altimeter data. The available altimeter data was bilinearly interpolated on to the model grid, which is 1/12 x 1/12 degree. The altimeter data for the 8 constituents are available in amplitude (cm) and phase (degrees, relative to Greenwich). The amplitude and phase values are converted into cosine and sine components, for each tidal constituent, for assimilation into the model. The broad coverage of the altimeter elevation data allows a crude display of the spatial pattern of all leading 8 tidal constituents without application of a dynamical model. Figure 4-3 shows the tracks of the individual mission altimeter data mentioned in the section.

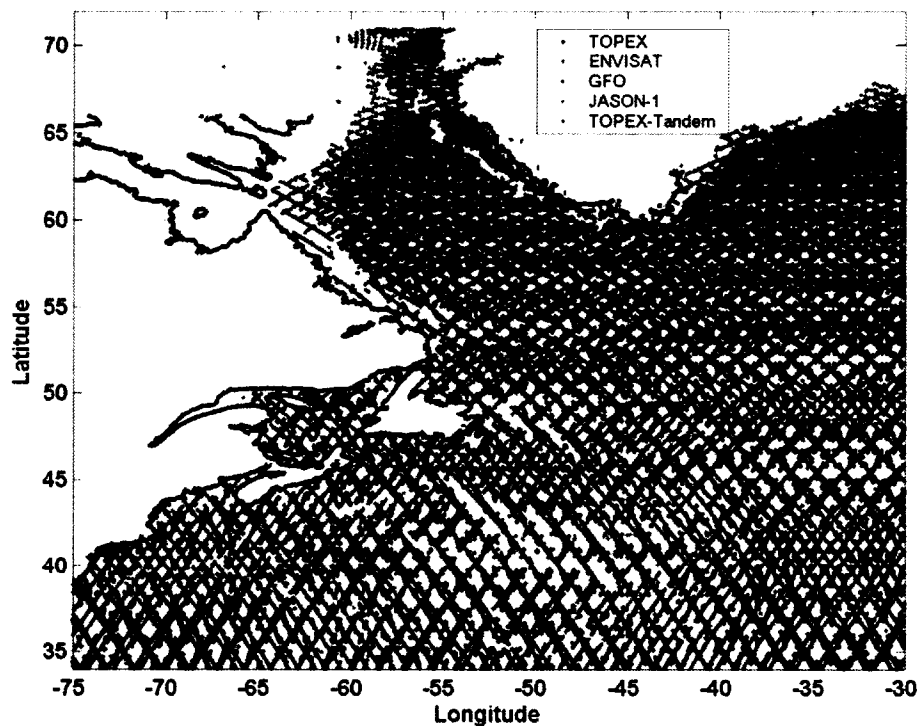


Figure 4-3. Tracks of the multi-mission altimeter data used for data assimilation in the model.

#### **4.4. Hydrography Data**

The monthly-mean temperature and salinity data was obtained from Geshelin et al. (1999). The data were available on  $1/6^\circ \times 1/6^\circ$  grid for all the 12 months. The temperature and salinity are provided at standard z-level depths (0, 10, 20, 30, 50, 75, 100, 125, 150, 200, 250, 300, 400, 500, 600, 700, 800, 900, 1000, 1100, 1200, 1300, 1400, 1500, 1750, 2000, 2500, 3000, 3500, 4000, 4500). The temperature and salinity data are interpolated on to model sigma grid using a bilinear interpolation method.

The summer surface (bottom) temperature (and salinity) field is shown in Figure 4-4. Large contrasts in the sea surface temperature between the near shore shelf waters and the Gulf Stream occur at narrow boundaries called fronts, close to the Southern boundary of the model domain in the Scotian Shelf region. Offshore a sharp front separates the shelf water from slope water (yellow/orange), which is created by mixing shelf and Gulf Stream water (red). In the eastern part of the domain close to the Flemish Cap, a tongue of warm water (yellow) from the North Atlantic Current (NAC) is seen being mixed in the Labrador Sea where the branch of the cold Labrador current is seen entering into the Strait of Belle Isle and the Newfoundland Shelf. The northern waters of the Gulf of St. Lawrence are cooled by the inflow of the Labrador water and by upwelling of cold deep water in the St. Lawrence estuary. Maximum surface temperatures occur over the shallow southwestern portion of the gulf where solar heating warms the entire water column. The Labrador Current remains distinct to the southern tip of Newfoundland Grand Banks where it meets and mixes with the Gulf Stream. The cold Labrador water separates a warm zone over the shallow southeastern bank from the warm water of the NAC offshore. A less-distinct branch of the Labrador Current is seen inshore along the Newfoundland coast. The summer bottom temperature field shows cold temperatures

across the whole domain with warmer temperatures occurring in the shallow areas of the tail of the Grand Bank, the region around Prince Edward Island and the region along the Middle and the South Atlantic Bight where the seafloor protrudes into the seasonally heated layer.

The summer salinity field clearly shows the influences of the annual cycle of river discharge, with the relatively freshwater from the spring discharge peak spreading offshore into the Gulf of St. Lawrence and onto the Eastern Scotian Shelf (ESS). The spatial pattern is quantitatively consistent with the known seaward flow into the western gulf, and with the greatest freshwater discharge being into Lower St. Lawrence Estuary. There is a well-defined plume extending along the western sides of Cabot Strait and the Laurentian Channel with a bifurcation onto the inner Scotian shelf, reflecting the passage of the annual salinity minimum through Cabot Strait in late summer (September; Sutcliffe et al. 1976). The low salinity areas along the shelf regions from Labrador shelf to Newfoundland shelf are because of the snowmelt. In contrast, the bottom salinity shows the effects of the topographic regime.

The model interpolated density difference (Figure 4-5, bottom-surface) plot shows that the stratification is stronger in the Laurentian channel extending into St. Lawrence Estuary, at the edge of the Newfoundland Grand Bank region and offshore of the Scotian shelf.

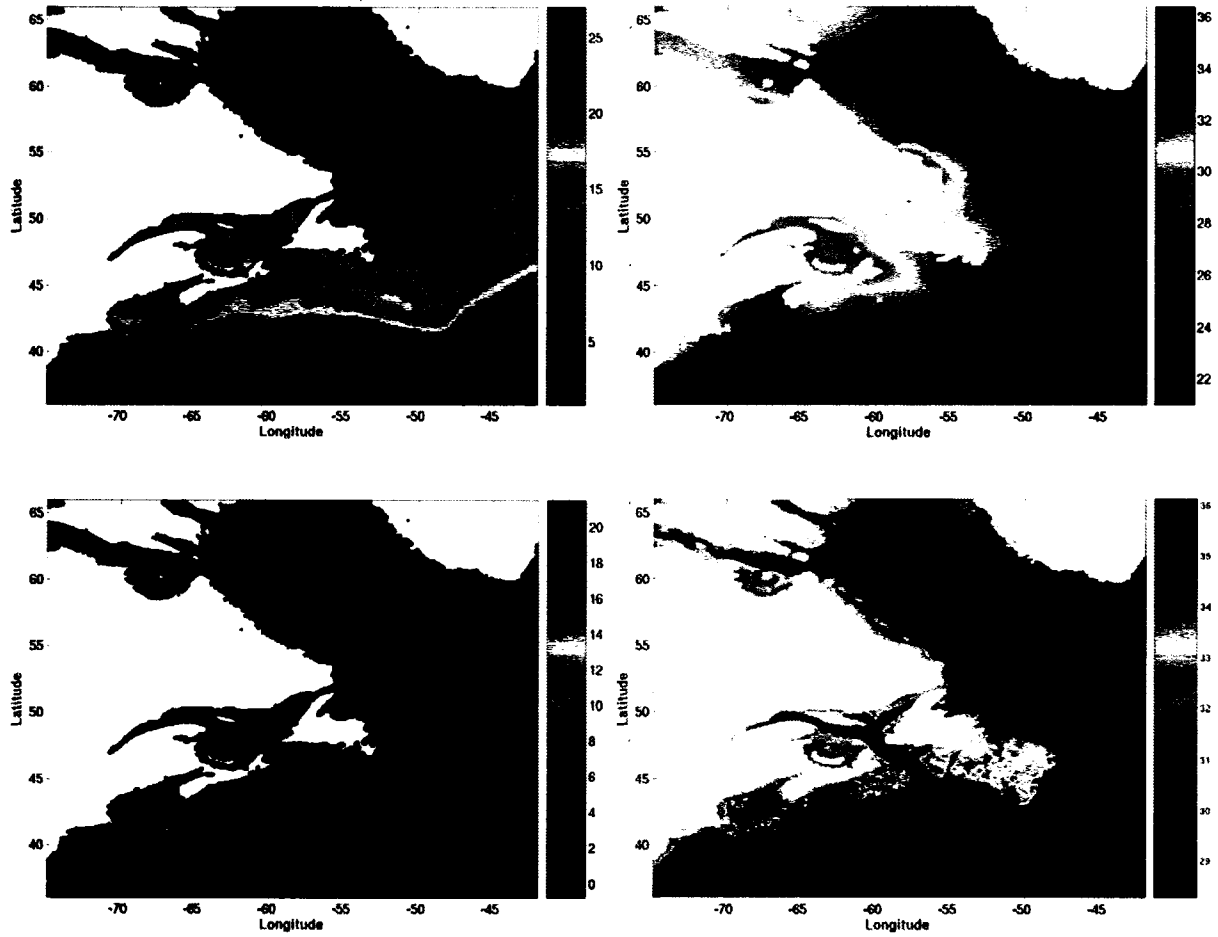


Figure 4-4. Climatological monthly-mean Surface (upper panel) and bottom (lower panel) temperature ( $^{\circ}\text{C}$ ) and salinity for the august, interpolated onto the model grid.

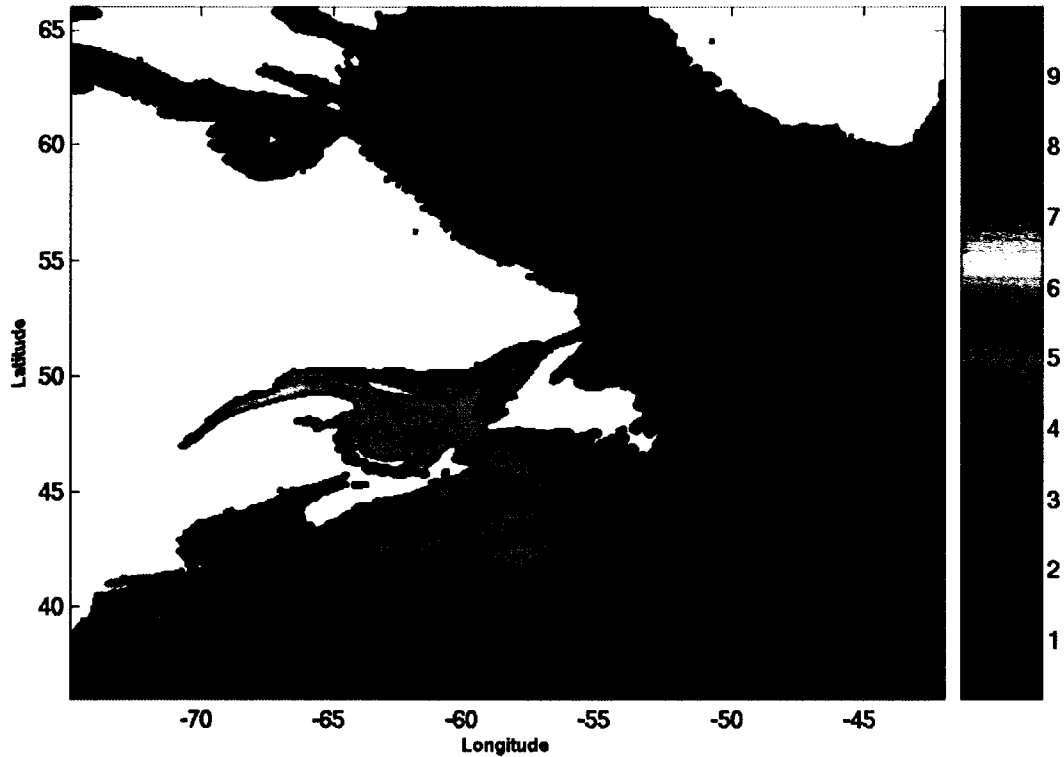


Figure 4-5. Model grid  $\sigma_t$  difference (bottom - surface). The values are in  $\text{kg/m}^3$ .

#### 4.5. Comparison of Altimeter Data with Observations

The quality of the altimeter data that is subsequently used for data assimilation into the POM model is evaluated by comparing the amplitude and phase with in-situ observations from tide and bottom pressure gauges. Separate comparisons for semi-diurnal ( $M_2$ ,  $S_2$ ,  $N_2$ ) and diurnal constituents ( $K_1$ ,  $O_1$ ), were made. Scatter plots with altimetric-derived versus in-situ observed values of semi-diurnal and diurnal constituents are shown in Figures 4-6 & 4-7 respectively. The scatter plots for  $M_2$  show good overall agreement between the altimeter and observed data, except at two locations for the island of Newfoundland where the altimeter data seems to over estimate.

The RMS amplitude & phase differences and the absolute & relative error for the 5 major constituents in the five different regions are presented in Table 4-2. The RSS value for

Super Stations is 2.5 cm for amplitude and 3.0 cm for absolute error (AbsErr) for all the five constituents. Around the Coastal Island of Newfoundland, the values are 4.5 cm and 4.7 cm respectively. The errors are: 5.2 cm in amplitude and 8.1 cm in absolute error for the coastal Nova Scotia region. The smallest error was for the Labrador Sea and Shelf region, 1.7 cm in amplitude and 2.4 cm in absolute value. The errors are the maximum in the BoFGoM region with values of 38.8 cm and 38.9 cm with the maximum value contributed by the  $M_2$  constituent, whose RMS amplitude difference is 36.5 cm and the AbsErr is 36.0 cm as compared to 16.2 cm and 40.0 cm respectively for the North Atlantic Model (see Table D-1). The North Atlantic model is able to resolve the resonant  $M_2$  amplitude in the BoFGoM region to within 5%.

The total value of RSS, including all the 5 regions, is 10.1 cm for the RMS amplitude difference and 11.1 cm for the AbsErr. The RMS phase differences for semidiurnals range from 3.7 to 8.8 degrees and those of diurnals vary from 8.1 to 9.9 degrees. The poor agreement for diurnal constituent can be attributed partly to the existence of the amphidromic points near the eastern Scotian Shelf and the resulting signal-to-noise ratio (Han et al., 1996).

The higher relative percentage error indicates that the altimeter data overestimates the elevations. The reason for the overestimation can be a result of the altimeter data quality deteriorates severely crossing the land sea boundary because the radar return may be dominated by reflection from the solid earth than from sea surface (Han et al., 1996), especially in the Bay of Fundy region, owing to the presence of the narrow channel. The mean error estimates give an indication that the multi-mission altimeter data is reliable except in the BoFGoM region.

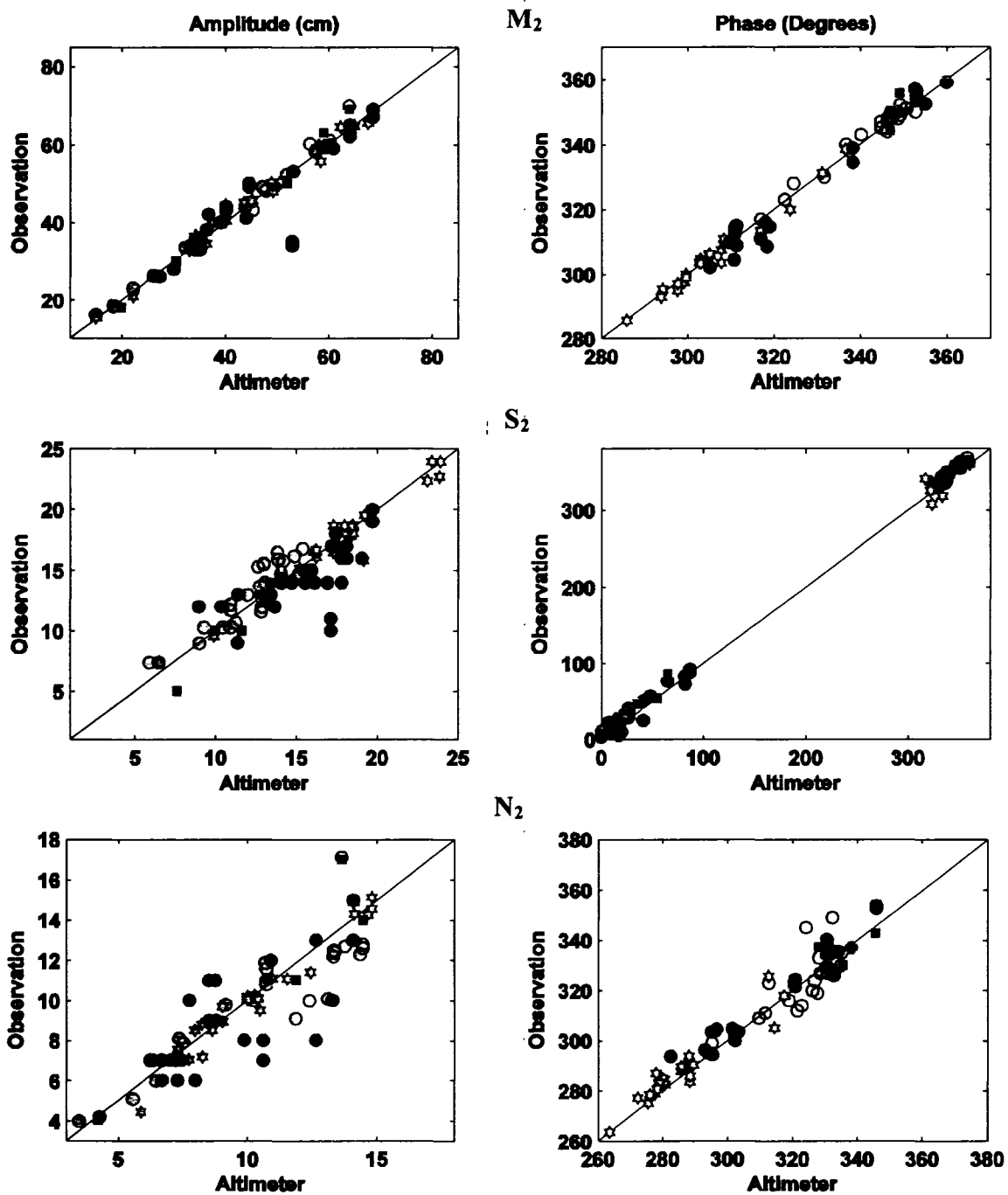


Figure 4-6. Scatter diagrams of amplitudes and phases of the altimeter observations (vertical axis) and in-situ data (horizontal axis) for  $M_2$ ,  $S_2$  &  $N_2$ . The markers correspond to the 4 different regions, excluding BoFGoM as described in Figure 4-1. The solid line along the centre of each graph indicates where all points should lie if the agreement were perfect. Amplitudes are in centimeters and phases in degrees. The range of phases is defined from  $0^\circ$  to  $360^\circ$ .

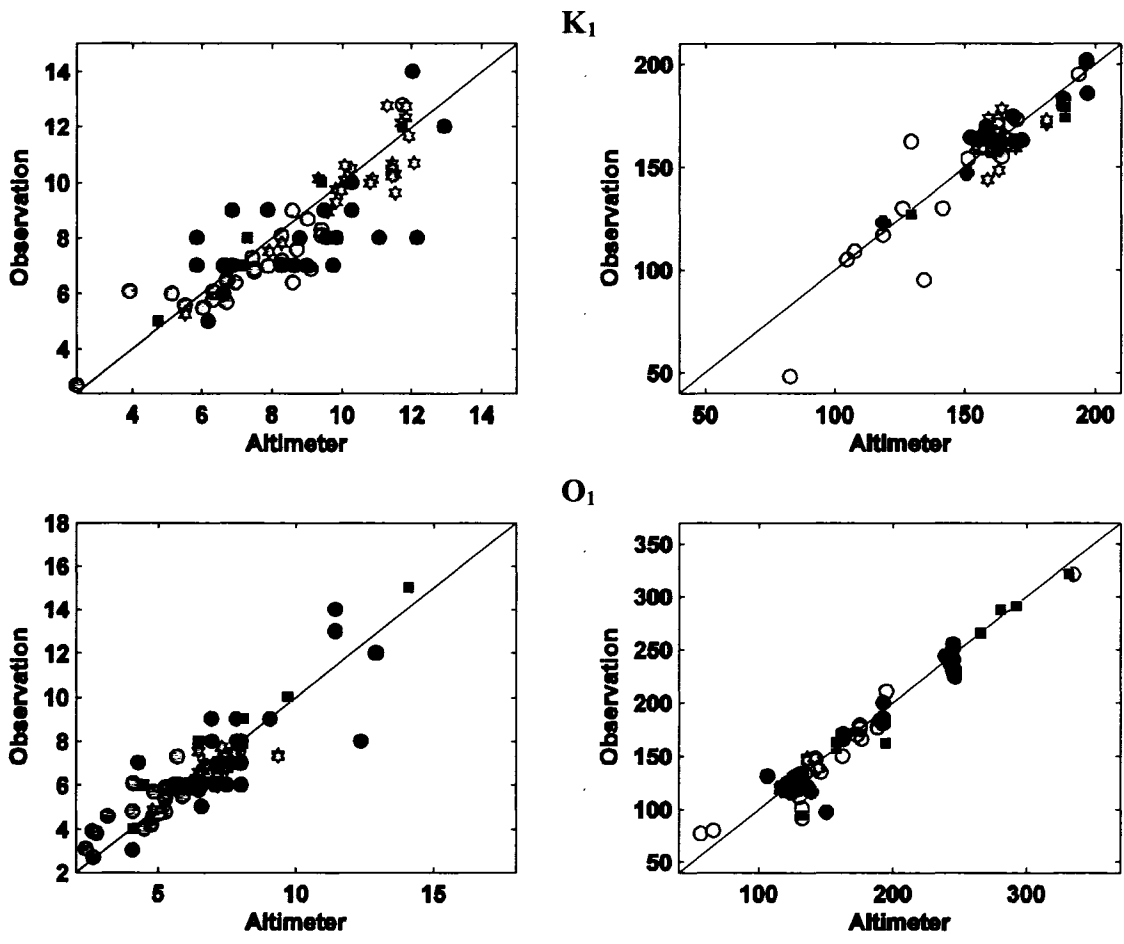


Figure 4-7. Same as Figure (4-6), but for  $K_1$  &  $O_1$ .

Table 4-2. Statistics for amplitude and phase between the Altimeter derived and in-situ observed tides for the five major semi-diurnal and diurnal constituents in the 5 different regions, excluding BoFGoM and for all locations (5 regions combined). The locations are defined in Figure 4-1.

<b>Constituent</b>	<b>RMS Amplitude Difference (cm)</b>	<b>RMS Phase Difference (Degrees)</b>	<b>AbsErr (cm)</b>	<b>RelErr (%)</b>
<b>Super Stations</b>				
<b>M<sub>2</sub></b>	<b>1.3</b>	<b>1.8</b>	<b>1.5</b>	<b>3.3</b>
<b>S<sub>2</sub></b>	<b>1.2</b>	<b>8.3</b>	<b>1.7</b>	<b>12.9</b>
<b>N<sub>2</sub></b>	<b>1.1</b>	<b>5.4</b>	<b>1.1</b>	<b>11.6</b>
<b>K<sub>1</sub></b>	<b>0.8</b>	<b>8.6</b>	<b>1.0</b>	<b>15.4</b>
<b>O<sub>1</sub></b>	<b>0.7</b>	<b>12.9</b>	<b>0.9</b>	<b>19.9</b>
<b>RSS</b>	<b>2.5</b>		<b>3.0</b>	
<b>Coastal Island of Newfoundland</b>				
<b>M<sub>2</sub></b>	<b>3.2</b>	<b>3.9</b>	<b>3.4</b>	<b>8.6</b>
<b>S<sub>2</sub></b>	<b>1.8</b>	<b>7.1</b>	<b>2.0</b>	<b>14.9</b>
<b>N<sub>2</sub></b>	<b>1.3</b>	<b>8.0</b>	<b>1.4</b>	<b>16.7</b>
<b>K<sub>1</sub></b>	<b>1.8</b>	<b>9.7</b>	<b>1.8</b>	<b>20.9</b>
<b>O<sub>1</sub></b>	<b>1.3</b>	<b>10.0</b>	<b>1.4</b>	<b>19.4</b>
<b>RSS</b>	<b>4.5</b>		<b>4.7</b>	
<b>Coastal Nova Scotia</b>				
<b>M<sub>2</sub></b>	<b>2.9</b>	<b>5.1</b>	<b>6.8</b>	<b>8.1</b>
<b>S<sub>2</sub></b>	<b>3.0</b>	<b>10.2</b>	<b>3.3</b>	<b>23.2</b>
<b>N<sub>2</sub></b>	<b>0.8</b>	<b>5.4</b>	<b>1.3</b>	<b>9.0</b>
<b>K<sub>1</sub></b>	<b>3.0</b>	<b>8.6</b>	<b>2.6</b>	<b>23.5</b>
<b>O<sub>1</sub></b>	<b>0.7</b>	<b>13.2</b>	<b>1.1</b>	<b>19.5</b>
<b>RSS</b>	<b>5.2</b>		<b>8.1</b>	
<b>Labrador Sea &amp; Shelf</b>				
<b>M<sub>2</sub></b>	<b>1.2</b>	<b>1.3</b>	<b>1.2</b>	<b>2.8</b>
<b>S<sub>2</sub></b>	<b>0.7</b>	<b>6.1</b>	<b>1.6</b>	<b>8.8</b>
<b>N<sub>2</sub></b>	<b>0.5</b>	<b>3.6</b>	<b>0.6</b>	<b>7.1</b>
<b>K<sub>1</sub></b>	<b>0.7</b>	<b>5.4</b>	<b>0.9</b>	<b>9.1</b>
<b>O<sub>1</sub></b>	<b>0.5</b>	<b>3.4</b>	<b>0.5</b>	<b>7.3</b>
<b>RSS</b>	<b>1.7</b>		<b>2.4</b>	

<b>Constituent</b>	<b>RMS Amplitude Difference (cm)</b>	<b>RMS Phase Difference (Degrees)</b>	<b>AbsErr (cm)</b>	<b>RelErr (%)</b>
<b>BoFGoM</b>				
<b>M<sub>2</sub></b>	<b>36.5</b>	<b>6.5</b>	<b>36.0</b>	<b>12.5</b>
<b>S<sub>2</sub></b>	<b>7.5</b>	<b>12.2</b>	<b>10.2</b>	<b>22.9</b>
<b>N<sub>2</sub></b>	<b>10.2</b>	<b>8.0</b>	<b>9.8</b>	<b>17.9</b>
<b>K<sub>1</sub></b>	<b>3.2</b>	<b>9.8</b>	<b>3.4</b>	<b>21.7</b>
<b>O<sub>1</sub></b>	<b>2.1</b>	<b>6.4</b>	<b>1.8</b>	<b>17.3</b>
<b>RSS</b>	<b>38.8</b>		<b>38.9</b>	
<b>Excluding BoFGoM</b>				
<b>M<sub>2</sub></b>	<b>2.1</b>	<b>3.0</b>	<b>3.2</b>	<b>5.7</b>
<b>S<sub>2</sub></b>	<b>1.7</b>	<b>7.9</b>	<b>2.1</b>	<b>14.9</b>
<b>N<sub>2</sub></b>	<b>0.9</b>	<b>5.6</b>	<b>1.1</b>	<b>11.1</b>
<b>K<sub>1</sub></b>	<b>1.6</b>	<b>8.1</b>	<b>1.5</b>	<b>17.2</b>
<b>O<sub>1</sub></b>	<b>0.8</b>	<b>9.9</b>	<b>1.0</b>	<b>16.5</b>
<b>RSS</b>	<b>3.4</b>		<b>4.4</b>	
<b>At all Locations</b>				
<b>M<sub>2</sub></b>	<b>9.0</b>	<b>3.7</b>	<b>9.8</b>	<b>7.1</b>
<b>S<sub>2</sub></b>	<b>2.9</b>	<b>8.8</b>	<b>3.7</b>	<b>16.5</b>
<b>N<sub>2</sub></b>	<b>2.8</b>	<b>6.1</b>	<b>2.9</b>	<b>12.5</b>
<b>K<sub>1</sub></b>	<b>1.9</b>	<b>8.4</b>	<b>1.9</b>	<b>18.1</b>
<b>O<sub>1</sub></b>	<b>1.1</b>	<b>9.2</b>	<b>1.1</b>	<b>16.7</b>
<b>Total RSS</b>	<b>10.1</b>		<b>11.1</b>	

Table 4-2 (continued).

## 5. Barotropic Results

Background on the major semi-diurnal and diurnal tidal elevation and currents in the Northwest Atlantic can be found in the work of Moody et al. (1984), de Margerie and Lank (1986), Han et al. (1996), Han et al. (1997) and Han and Loder (2002) for the Eastern & Western Scotian Shelf, Lu et al. (2000) and Saucier and Chasse (2000) in the Gulf of St. Lawrence, Petrie et al. (1987), Xu et al. (2001), Han (2000) for the Newfoundland & Southern Labrador shelves, Lynch and Naimie (1993) for the Gulf of Maine and Dupont et al. (2002) for the entire study region.

### 5.1. Unassimilated

The tidal elevations and currents (U & V components), computed from the last 30 days of the model run (Bu experiment), are harmonically analysed to extract the amplitude and phase for the 8 constituents.

#### 5.1.1. Tidal Elevations

##### a) *Co-range and Co-phase charts:*

Figures 5-1 and 5-2 show the computed amplitude and phases for the  $M_2$  and  $K_1$  constituent respectively. The results are in broad agreement with the global Oregon State University (OSU) TP solution (Egbert et al., 1994; Egbert and Erofeeva, 2002) in the whole domain excepting the region of the Gulf of St. Lawrence (the OSU solution is downloadable from [www.coas.oregonstate.edu/research/po/research/tide](http://www.coas.oregonstate.edu/research/po/research/tide)), where there is no amphidromic point for  $M_2$  constituent (Figure 5-1a), the stronger tidal signal in the BoFGoM region for  $M_2$  tide (Figure 5-1), with the amplitude being overestimated by ~40 cm and a phase error of ~20 deg, and faster propagation of  $M_2$  tide in the Labrador Sea

and shelf region (Figure 5-1b). The reason for the amphidromic point not generated by the model seems to be related to of topography. Figure E-1a,b show the co-range and co-phase plots with an amphidromic point generated in the Gulf of St. Lawrence (shifted to the west as compared to previously published results, e.g. Godin, 1980) from the single  $M_2$  constituent run when Egbert and Erofeeva (2002) topography was used.

The model  $K_1$  tide (Figure 5-2a,b) indicates the presence of an amphidromic point in the Laurentian Channel which is consistent with the North Atlantic Model (Egbert et al. 1994; Han 1996). Godin (1980) has reported the traditional location near Sable Island. A secondary amphidromic point is seen to the west of Baffin Island and the diurnal intensification (amplitude maxima of 28 cm) on the shelf break, east of Davis Strait, northern model domain.

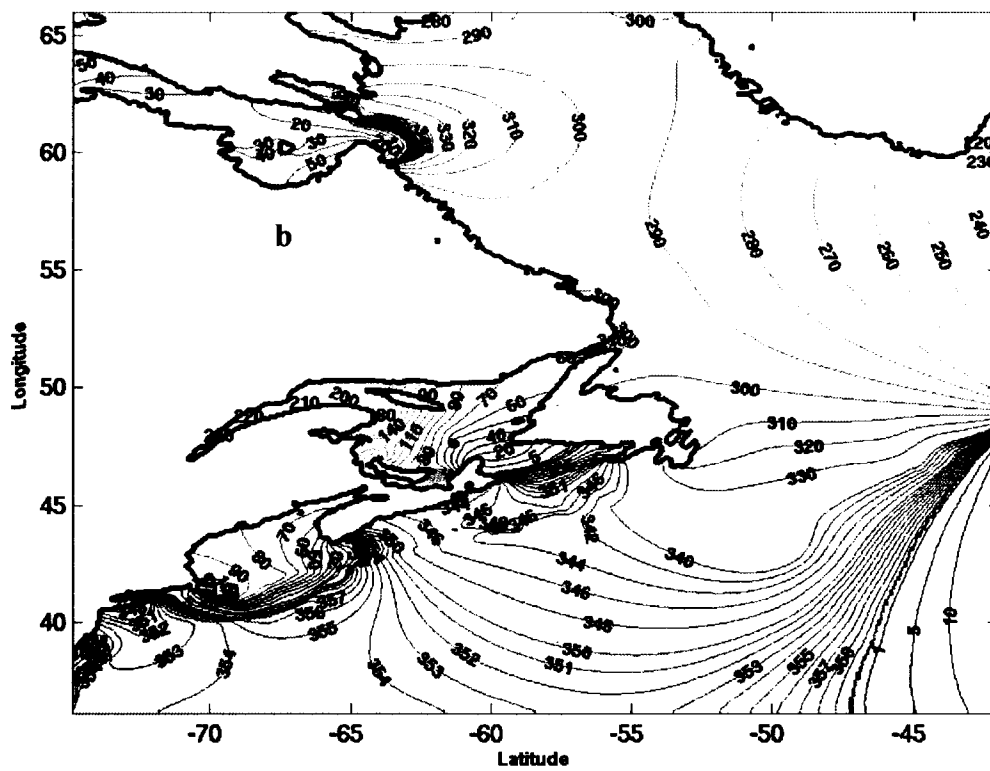
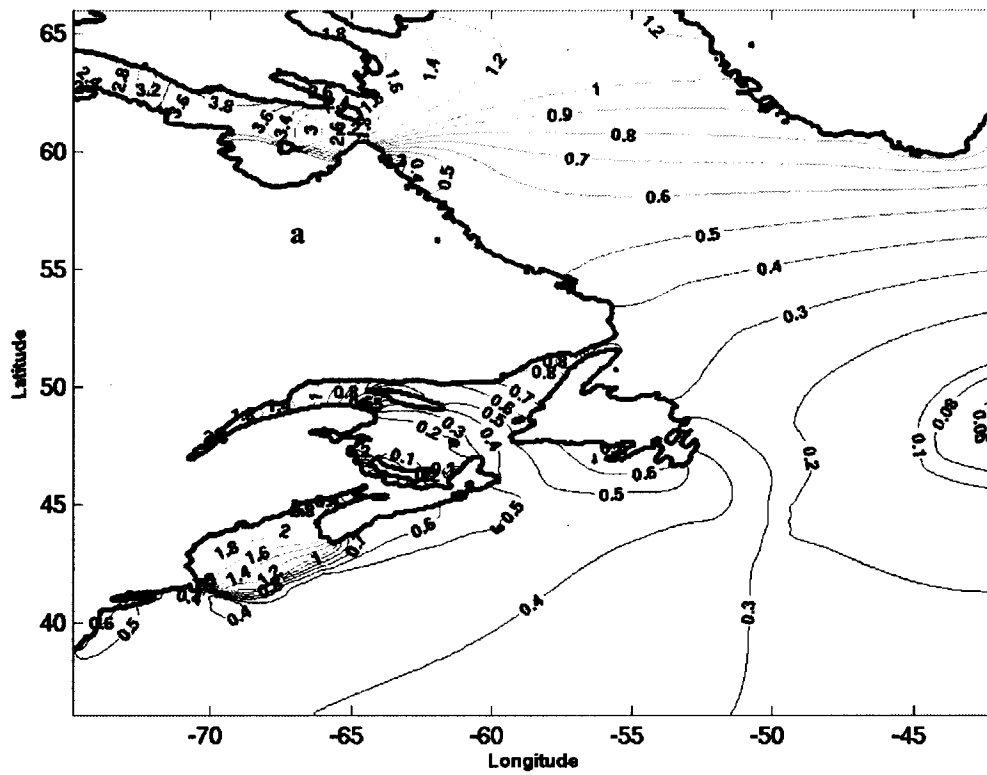


Figure 5-1. Model computed Co-range (a) and Co-phase (b) charts for  $M_2$  constituent. The amplitude is in m and phases are in degrees. The contours are co-range (a) and co-phase (b) lines scaled to show the proper distribution of amplitude and phase respectively.

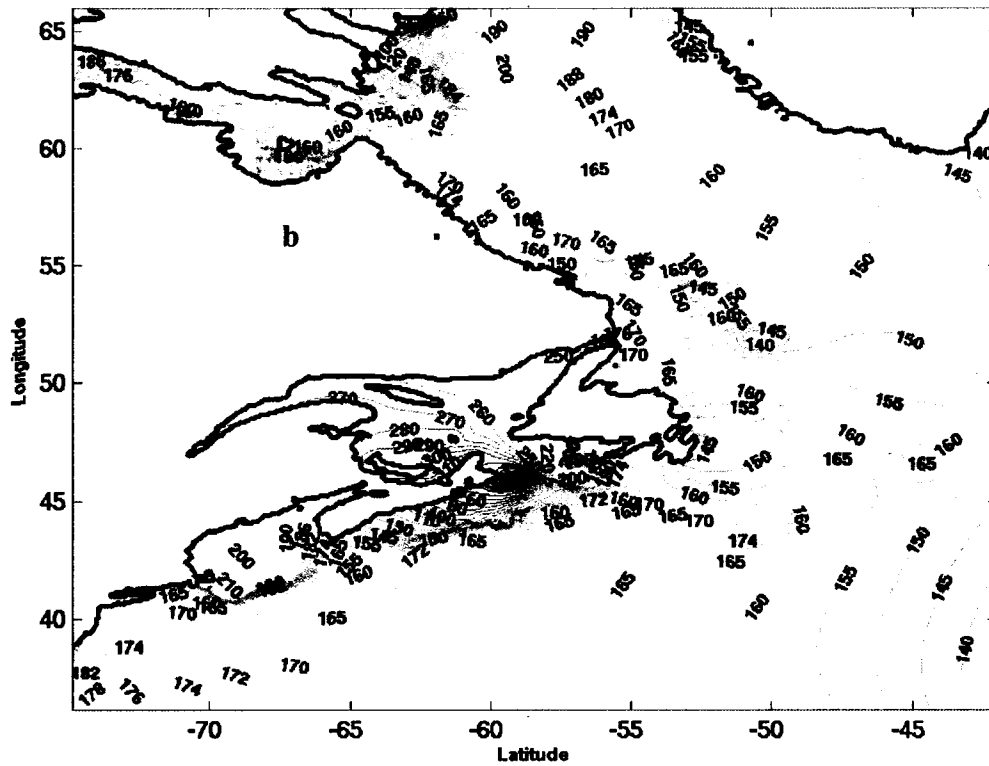
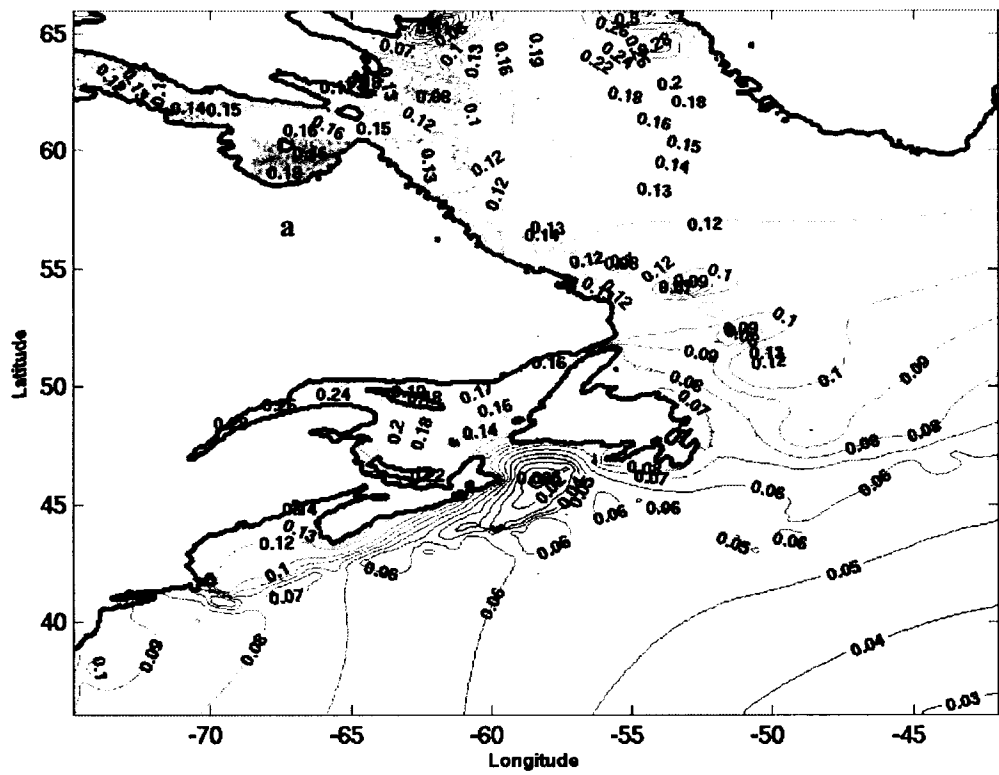


Figure 5-2. Model computed Co-range (a) and Co-phase (b) charts for  $K_1$  constituent. The amplitude is in m and phases are in degrees. The contours are co-range (a) and co-phase (b) lines scaled to show the proper distribution of amplitude and phase respectively.

## **b) Comparison with observations**

The model computed major semi-diurnal ( $M_2$ ,  $S_2$ , and  $N_2$ ) and diurnal constituents ( $K_1$  &  $O_1$ ) are compared with observed elevation amplitude and phase at coastal tide gauges and offshore bottom pressure gauge locations for the 5 regions.

Table 5-1 lists the mean RMS difference errors for amplitude and phase and the mean absolute and relative error for all the five constituents in the five different regions considered. The RSS value for the combined five constituents is also presented in the table to assess the performance of the model in reproducing the tidal elevations. A look at the mean error for the individual constituents at each region suggests that for the semi-diurnal constituents the mean absolute errors are in the range 0.9 to 2.5 cm for the Super Stations (See Table A-1) and for the diurnals, the errors are 1.3 cm for  $K_1$  and 0.9 cm for  $O_1$  constituent.

In the coastal regions of Newfoundland and Nova Scotia, the errors for  $M_2$  are large and are 6.3 cm and 10.2 cm respectively. The amplitude errors are larger than the phase errors suggesting that the model overestimates the  $M_2$  tidal signal in the shallow shelf regions, especially in the Nova Scotia region where it is characterized by shallow embayment.

The RSS errors in the Labrador region are 4.7 cm for amplitude, 16.9 deg error in phase with an absolute error of 5.8 cm. The RMS error reported by Dupont et al. (2002) for  $M_2$  constituent is 7.88 cm which is almost double (4.1 cm) to what we have achieved. The inclusion of the effect of the tidal potential and loading, changes the amplitude in the region.

For the diurnal constituents, the AbsErr is 1.6 cm & 18.8 cm for  $K_1$  and 1.1 cm & 4.6 cm in the coastal stations of Newfoundland and Nova Scotia respectively. The mean AbsErr for all locations is smaller than the semi-diurnal constituents.

A detailed comparison between the computed and observed elevation amplitude and phase of  $M_2$  and  $K_1$  tidal constituents at coastal tide gauge and bottom pressure gauges is given in Table E-3. The reader is referred to Appendix B for detailed locations of the tide and pressure gauges with station numbers. The amplitude difference is 1-5 cm for the Super Stations except for station ST-6 where the error is 9.7 cm. The phase difference is 1-10 deg. In the Bay of Fundy and Gulf of Maine region, the amplitude errors are in the range 50-70 cm, except at one location (BG-11) where the amplitude error is 1.9 cm. The smallest amplitude errors (5-8 cm) are seen at stations BG-5, BG-7 & BG-8.

The computed elevation parameters for the  $K_1$  tide show negligible biases with the largest errors in the BoFGoM region. At most of the sites the amplitude error is < 3cm and the phase difference is within 25 deg. Han (2000) has reported errors of 1.8 cm for amplitude and 3.6 deg for phase for semi-diurnals and <1 cm and 11 deg.

Table 5-1. Statistics of model computed elevation from Bu run for semi-diurnal and diurnal constituents compared with observations at Tide and Pressure Gauge Sites for the Baseline (Bu) run for all the five regions, excluding BoFGoM and all locations. The locations are defined in Figure 4-1.

<b>Constituent</b>	<b>RMS Amplitude Difference (cm)</b>	<b>RMS Phase Difference (Degrees)</b>	<b>AbsErr (cm)</b>	<b>RelErr (%)</b>
<b>Super Stations</b>				
<b>M2</b>	<b>1.9</b>	<b>3.8</b>	<b>2.5</b>	<b>5.8</b>
<b>S2</b>	<b>1.6</b>	<b>7.5</b>	<b>1.8</b>	<b>13.3</b>
<b>N2</b>	<b>0.7</b>	<b>5.4</b>	<b>0.9</b>	<b>9.2</b>
<b>K1</b>	<b>1.5</b>	<b>7.3</b>	<b>1.3</b>	<b>18.7</b>
<b>O1</b>	<b>1.0</b>	<b>6.6</b>	<b>0.9</b>	<b>20.2</b>
<b>RSS</b>	<b>3.1</b>		<b>3.5</b>	
<b>Coastal Island of Newfoundland</b>				
<b>M2</b>	<b>7.2</b>	<b>4.8</b>	<b>6.3</b>	<b>15.0</b>
<b>S2</b>	<b>2.0</b>	<b>12.4</b>	<b>2.7</b>	<b>20.6</b>
<b>N2</b>	<b>1.4</b>	<b>5.7</b>	<b>1.3</b>	<b>15.7</b>
<b>K1</b>	<b>1.6</b>	<b>11.5</b>	<b>1.8</b>	<b>22.4</b>
<b>O1</b>	<b>1.2</b>	<b>6.8</b>	<b>1.1</b>	<b>15.4</b>
<b>RSS</b>	<b>7.9</b>		<b>7.3</b>	
<b>Coastal Nova Scotia</b>				
<b>M2</b>	<b>11.3</b>	<b>8.9</b>	<b>10.2</b>	<b>16.3</b>
<b>S2</b>	<b>6.4</b>	<b>15.2</b>	<b>5.8</b>	<b>39.0</b>
<b>N2</b>	<b>2.0</b>	<b>6.4</b>	<b>1.8</b>	<b>13.7</b>
<b>K1</b>	<b>2.1</b>	<b>5.5</b>	<b>1.6</b>	<b>19.1</b>
<b>O1</b>	<b>5.5</b>	<b>9.0</b>	<b>4.9</b>	<b>22.0</b>
<b>RSS</b>	<b>14.4</b>		<b>12.9</b>	
<b>Labrador Sea &amp; Shelf</b>				
<b>M2</b>	<b>4.1</b>	<b>6.1</b>	<b>4.6</b>	<b>9.4</b>
<b>S2</b>	<b>1.6</b>	<b>11.8</b>	<b>3.1</b>	<b>15.9</b>
<b>N2</b>	<b>0.5</b>	<b>3.4</b>	<b>0.6</b>	<b>5.7</b>
<b>K1</b>	<b>1.2</b>	<b>9.7</b>	<b>1.6</b>	<b>16.0</b>
<b>O1</b>	<b>0.6</b>	<b>2.5</b>	<b>0.5</b>	<b>7.3</b>
<b>RSS</b>	<b>4.7</b>		<b>5.8</b>	

Table 5-1. (continued)

<b>Constituent</b>	<b>RMS Amplitude Difference (cm)</b>	<b>RMS Phase Difference (Degrees)</b>	<b>AbsErr (cm)</b>	<b>RelErr (%)</b>
<b>BoFGoM</b>				
<b>M2</b>	<b>36.8</b>	<b>18.4</b>	<b>82.3</b>	<b>28.0</b>
<b>S2</b>	<b>42.7</b>	<b>13.3</b>	<b>32.0</b>	<b>79.0</b>
<b>N2</b>	<b>9.8</b>	<b>14.3</b>	<b>14.1</b>	<b>24.4</b>
<b>K1</b>	<b>1.3</b>	<b>3.8</b>	<b>1.3</b>	<b>8.1</b>
<b>O1</b>	<b>2.1</b>	<b>14.0</b>	<b>2.6</b>	<b>24.1</b>
<b>RSS</b>	<b>57.2</b>		<b>89.4</b>	
<b>Excluding BoFGoM</b>				
<b>M2</b>	<b>6.1</b>	<b>5.9</b>	<b>5.9</b>	<b>11.6</b>
<b>S2</b>	<b>2.9</b>	<b>11.7</b>	<b>3.3</b>	<b>22.2</b>
<b>N2</b>	<b>1.2</b>	<b>5.2</b>	<b>1.1</b>	<b>11.1</b>
<b>K1</b>	<b>1.6</b>	<b>8.5</b>	<b>1.6</b>	<b>19.0</b>
<b>O1</b>	<b>2.1</b>	<b>6.2</b>	<b>1.8</b>	<b>16.2</b>
<b>RSS</b>	<b>7.4</b>		<b>7.3</b>	
<b>At all Locations</b>				
<b>M2</b>	<b>12.3</b>	<b>8.4</b>	<b>21.2</b>	<b>14.9</b>
<b>S2</b>	<b>10.9</b>	<b>12.0</b>	<b>9.1</b>	<b>33.6</b>
<b>N2</b>	<b>2.9</b>	<b>7.0</b>	<b>3.7</b>	<b>13.7</b>
<b>K1</b>	<b>1.5</b>	<b>7.6</b>	<b>1.5</b>	<b>16.8</b>
<b>O1</b>	<b>2.1</b>	<b>7.8</b>	<b>2.0</b>	<b>17.8</b>
<b>RSS</b>	<b>16.8</b>		<b>23.5</b>	

The computed magnitudes and phases of elevation semi-diurnals (Figure 5-3) and diurnals (Figure 5-4) are compared with observations. The scatter diagrams for  $M_2$  constituent show overall good agreement. For higher amplitudes, the model overestimates, especially at locations around the Coastal Island of Newfoundland (red circles) by 5-10cm. The model is very sensitive to sharp changes in topography. For  $S_2$ , the model computed magnitudes are overestimated by a factor of 2-5 cm in the coastal regions of Newfoundland (red circles). For diurnal constituents, the model overestimates the magnitude by ~2-5 cm but mostly in phase with the observations.

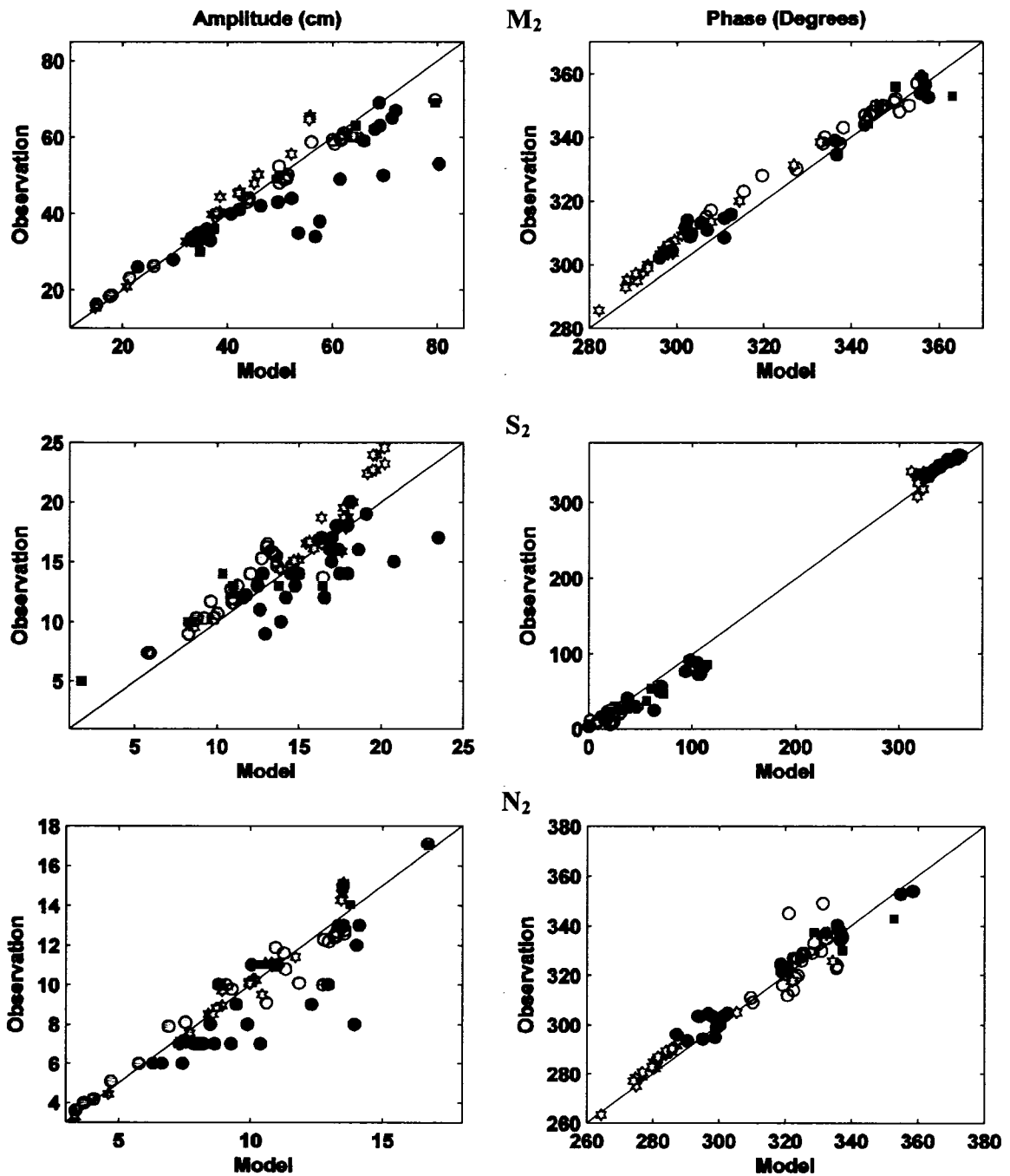


Figure 5-3. Scatter diagrams of amplitudes and phases of the model results from the Bu run (vertical axis) and in-situ data (horizontal axis) for M<sub>2</sub>, S<sub>2</sub> & N<sub>2</sub>. The markers correspond to the 4 different regions, excluding BoFGoM as described in Figure 4-1. The solid line along the centre of each graph indicates where all points should lie if the agreement were perfect. Amplitudes are in centimeters and phases in degrees. The range of phases is defined from 0° to 360°.

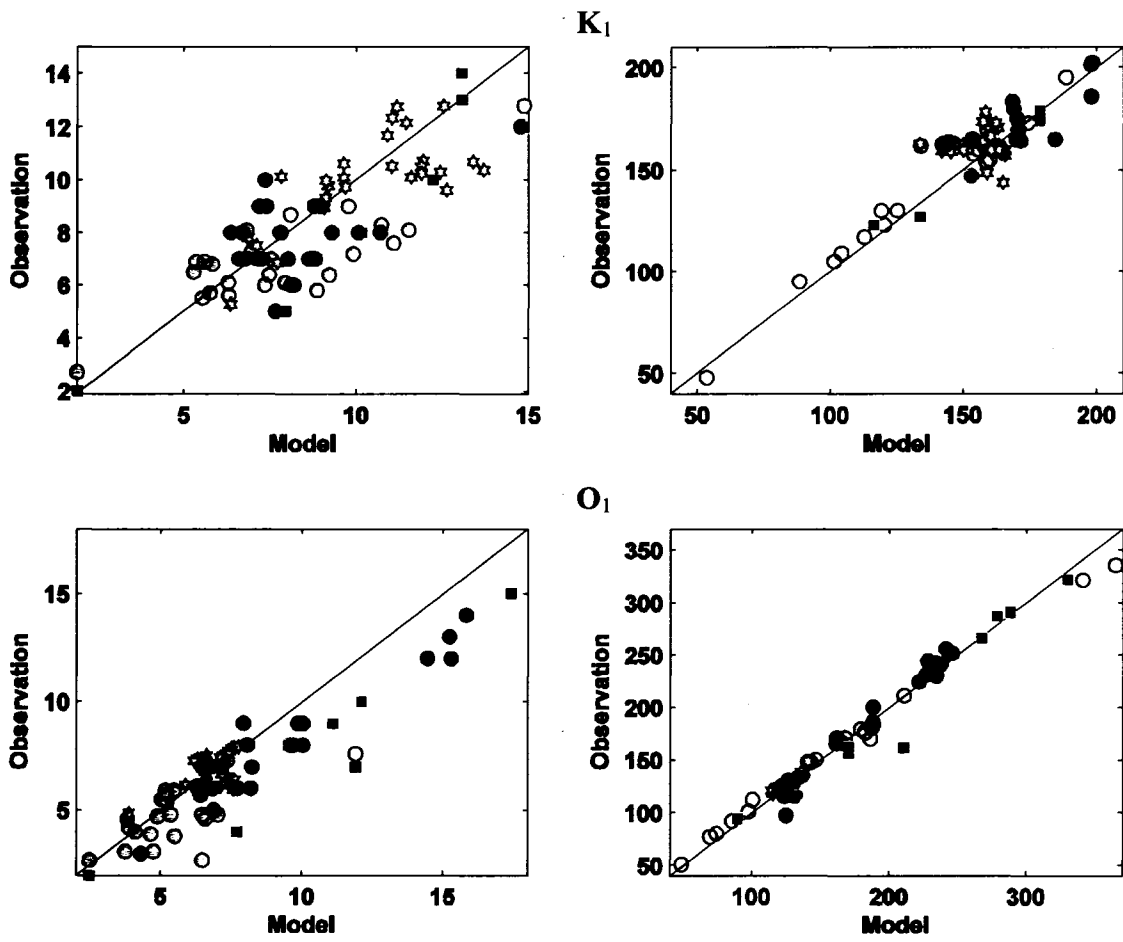


Figure 5-4 .Same as Figure (5-3), but for  $K_1$  &  $O_1$ .

### 5.1.2. Tidal Currents

#### a) *Tidal current ellipses*

The spatial distribution of computed tidal currents is similar that from the Ba experiment and is discussed in detail in section 5.2.2.

#### b) *Comparison with observations:*

Since the model also calculates tidal currents, the comparison of those against observations provides another source of independent verification. Table 5-2 lists the RMS errors and absolute and relative errors for all 5 major tidal constituents, region-wise and for all locations. An overall assessment of the model RMS errors shows that the model performs better for  $M_2$  constituent compared to the entire 5 major constituents.  $M_2$  is the largest constituent in terms of amplitude of tidal currents in the whole model domain. Inter-comparison between semi-diurnal and diurnal constituents shows that the model reproduces the semi-diurnal currents better than the diurnal currents. The mean relative error for  $M_2$  and  $N_2$  constituents is <60% except for  $S_2$  whose relative error is around 85%. The relative error for diurnal constituents is close to 100% for the meridional component and around 75% for the zonal component.

Only the major semi-diurnal ( $M_2$ ) and diurnal ( $K_1$ ) constituents are discussed in this section as the major focus is on the results from the assimilated experiment. The region-wise comparison suggests that the agreement of the model results with observations is better for  $M_2$  in all the 6 regions among the 5 major tidal constituents. In the Bay of Fundy and Gulf of Maine, the model has underestimated the amplitude of currents for both the components (Figure 5-8; red hexagons), which is evident from the RMS and absolute errors while it seems to be in phase with the observations. The large errors can be because of localized resonance effects in the Bay of Fundy region. In the

Newfoundland shelf region the RMS error for the  $M_2$  constituent are 2.48cm/s in amplitude and 36 deg in phase. Han (2000) has reported RMS errors as 2.3cm/s and 28 deg. Han (2000) combined the 5 major tidal constituents into a model whose domain was smaller than the horizontal scale of tidal elevation amplitudes specified at the lateral open boundaries. In the Scotian shelf, the relative errors lie between 60-120% for all the 5 constituents. This can be because this region is characterized by very shallow topography marked with bays and embayments (Figure 1) and some of the errors seem however to be localized to a few places. The model has overestimated the currents for U-component (Figure 5-8; top left; green diamond) in this region and also by double in a couple of places.

Table 5-2. Statistics of model computed currents for semi-diurnal and diurnal constituents compared with observations at moored current meter sites for six sub-regions (a-f) of the model domain and the whole model domain (g) for the Bu run. The location and names of the sub-regions are as described in Figure 4-2.

**a) Bay of Fundy and Gulf of Maine**

Constituent	RMS U		RMS V		AbsErr U	RelErr U	AbsErr V	RelErr V
	Amp (cm/s)	Phase (Deg)	Amp (cm/s)	Phase (Deg)	(cm/s)	(%)	(cm/s)	(%)
<b>M<sub>2</sub></b>	22.1	26.8	10.8	37.9	19.3	54.9	15.2	59.1
<b>S<sub>2</sub></b>	1.2	34.1	3.3	35.7	1.9	95.6	2.8	84.4
<b>N<sub>2</sub></b>	4.8	25.8	2.3	35.8	4.1	45.6	3.1	53.6
<b>K<sub>1</sub></b>	0.4	25.4	0.3	32.0	0.4	45.5	0.5	65.1
<b>O<sub>1</sub></b>	0.3	26.2	0.2	56.3	0.4	46.2	0.3	88.6

**b) Georges Bank**

Constituent	RMS U		RMS V		AbsErr U	RelErr U	AbsErr V	RelErr V
	Amp (cm/s)	Phase (Deg)	Amp (cm/s)	Phase (Deg)	(cm/s)	(%)	(cm/s)	(%)
<b>M<sub>2</sub></b>	14.1	20.6	19.7	26.5	17.8	50.8	24.8	54.4
<b>S<sub>2</sub></b>	7.7	33.9	8.4	34.0	6.8	142.5	7.9	123.7
<b>N<sub>2</sub></b>	2.9	23.9	3.9	33.7	3.8	49.5	6.0	58.8
<b>K<sub>1</sub></b>	1.3	32.9	1.8	21.0	1.6	56.1	2.0	59.3
<b>O<sub>1</sub></b>	1.2	54.2	1.5	38.3	1.3	122.6	1.6	136.4

**c) Channel**

Constituent	RMS U		RMS V		AbsErr U	RelErr U	AbsErr V	RelErr V
	Amp (cm/s)	Phase (Deg)	Amp (cm/s)	Phase (Deg)	(cm/s)	(%)	(cm/s)	(%)
<b>M<sub>2</sub></b>	11.0	28.8	11.0	23.6	11.2	62.3	12.8	45.6
<b>S<sub>2</sub></b>	3.1	44.6	4.4	63.4	3.0	100.5	4.1	102.1
<b>N<sub>2</sub></b>	2.0	37.9	2.6	28.8	2.6	58.6	3.1	47.8
<b>K<sub>1</sub></b>	2.5	39.9	2.4	29.5	2.4	59.7	2.2	62.2
<b>O<sub>1</sub></b>	1.3	39.2	1.3	42.7	1.4	53.0	1.3	67.2

**d) Labrador**

Constituent	RMS U	RMS U	RMS V	RMS V	AbsErr U	RelErr U	AbsErr V	RelErr V
	Amp (cm/s)	Phase (Deg)	Amp (cm/s)	Phase (Deg)	(cm/s)	(%)	(cm/s)	(%)
<b>M<sub>2</sub></b>	1.1	37.4	1.7	64.0	1.9	52.1	2.5	57.1
<b>S<sub>2</sub></b>	0.5	41.8	0.7	59.0	0.8	55.6	0.8	60.0
<b>N<sub>2</sub></b>	0.4	40.2	0.4	61.0	0.6	60.4	0.5	60.1
<b>K<sub>1</sub></b>	0.5	79.7	0.3	30.3	0.7	109.9	0.4	54.6
<b>O<sub>1</sub></b>	0.4	54.3	0.4	71.4	0.5	74.1	0.5	89.4

**e) Newfoundland & North Avalon Channel**

Constituent	RMS U	RMS U	RMS V	RMS V	AbsErr U	RelErr U	AbsErr V	RelErr V
	Amp (cm/s)	Phase (Deg)	Amp (cm/s)	Phase (Deg)	(cm/s)	(%)	(cm/s)	(%)
<b>M<sub>2</sub></b>	1.8	17.2	1.7	31.6	1.7	38.4	2.1	47.0
<b>S<sub>2</sub></b>	1.3	42.0	1.0	51.6	2.3	100.1	2.4	81.1
<b>N<sub>2</sub></b>	0.6	36.1	0.6	50.6	0.8	58.3	0.8	67.9
<b>K<sub>1</sub></b>	1.4	54.5	1.1	53.4	1.6	114.0	1.6	106.9
<b>O<sub>1</sub></b>	1.1	57.2	0.9	54.6	1.2	122.3	1.2	94.7

**f) Scotian Shelf**

Constituent	RMS U	RMS U	RMS V	RMS V	AbsErr U	RelErr U	AbsErr V	RelErr V
	Amp (cm/s)	Phase (Deg)	Amp (cm/s)	Phase (Deg)	(cm/s)	(%)	(cm/s)	(%)
<b>M<sub>2</sub></b>	9.9	27.4	6.1	37.5	9.5	52.6	6.9	62.3
<b>S<sub>2</sub></b>	4.5	51.3	2.2	53.3	4.3	97.2	2.8	91.5
<b>N<sub>2</sub></b>	2.3	31.4	1.6	44.0	2.4	61.4	1.9	72.5
<b>K<sub>1</sub></b>	3.3	44.0	2.5	58.8	3.8	76.0	3.1	120.0
<b>O<sub>1</sub></b>	3.2	37.3	2.3	62.8	3.6	74.8	2.9	116.3

g) At all Locations

Constituent	RMS U		RMS V		AbsErr U	RelErr U	AbsErr V	RelErr V
	Amp (cm/s)	Phase (Deg)	Amp (cm/s)	Phase (Deg)	(cm/s)	(%)	(cm/s)	(%)
M <sub>2</sub>	9.0	26.4	7.2	36.3	9.1	51.6	8.5	57.4
S <sub>2</sub>	3.9	46.1	2.8	51.3	3.9	94.1	3.2	90.0
N <sub>2</sub>	2.0	32.5	1.7	43.6	2.2	59.0	2.2	66.5
K <sub>1</sub>	2.5	44.7	2.1	48.6	2.9	77.3	2.5	100.7
O <sub>1</sub>	2.3	42.2	1.7	57.5	2.5	79.5	2.1	102.9

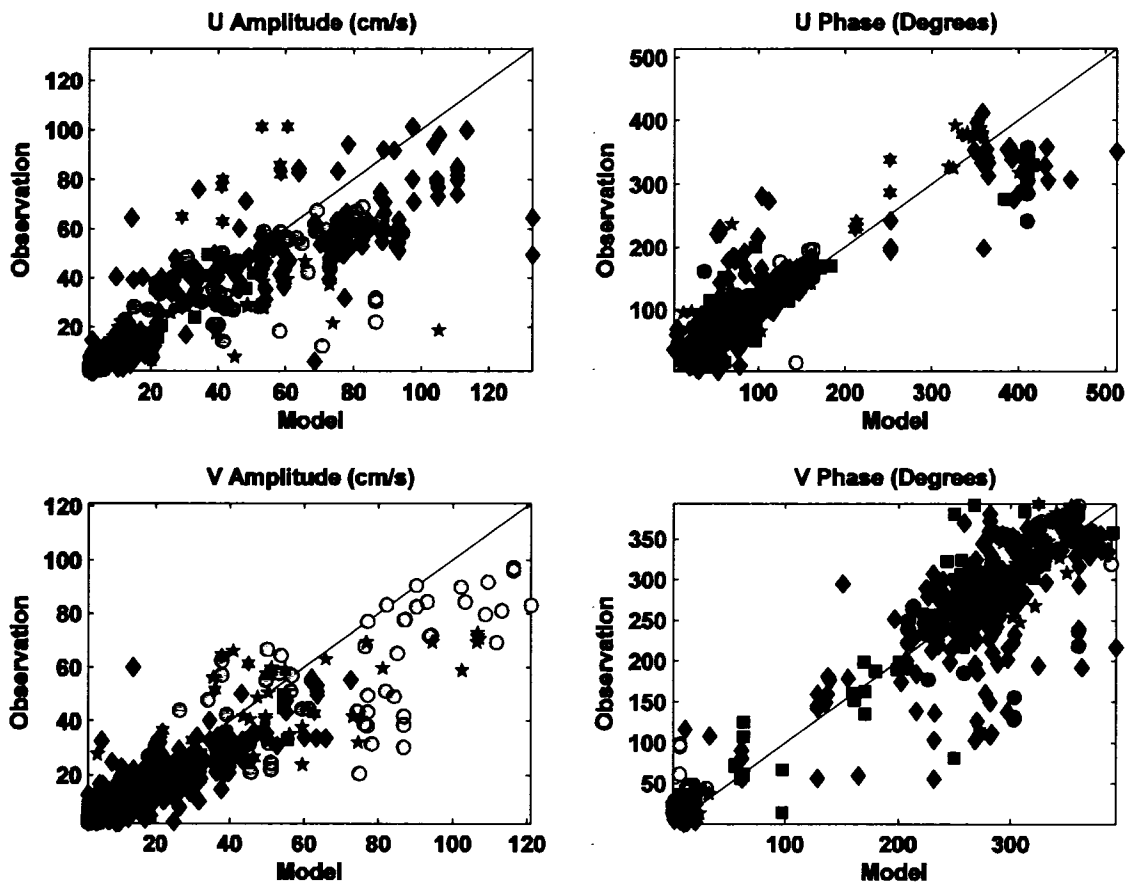


Figure 5-5. Scatter diagrams for the amplitude phase between the model (horizontal axis) and in situ observed currents (vertical axis) for M<sub>2</sub> constituent from the Bu run. The top panel is for the zonal (U, eastward) and the bottom panel is the meridional (V, northward) components in the whole model domain. The markers correspond to the 6 different regions as described in Figure 4-2. The solid line along the centre of each graph indicates where all points should lie if the agreement were perfect. The amplitudes are in cm/s and phases in degrees. The range of phases is defined from 0° to 360°.

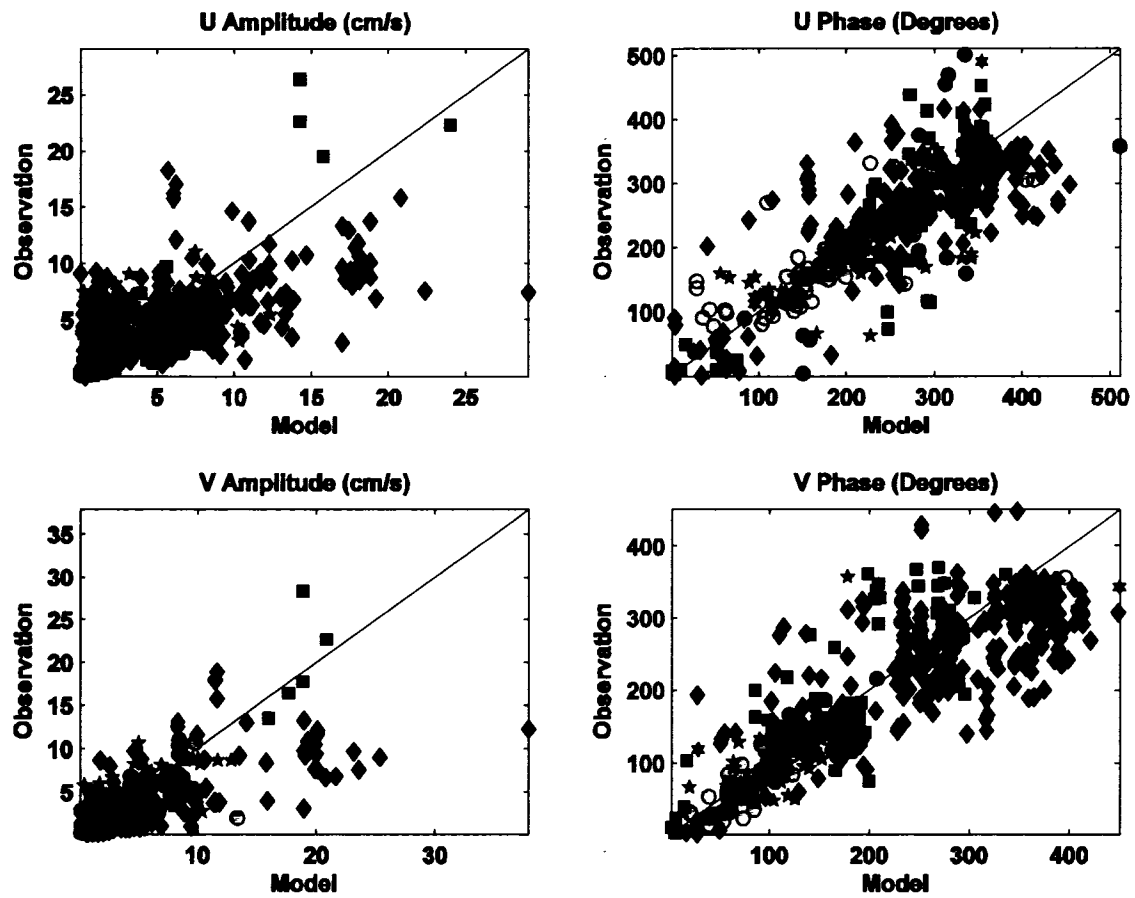


Figure 5-6. Same as Figure 5-5 but for K<sub>1</sub>.

## 5.2. Assimilation Run

The results in this section are drawn mainly from experiment Ba, with homogeneous fluid and data assimilation using multi-mission altimeter data. A nudging method is used to assimilate the elevation data from the altimeter data with a nudging time-period ( $T_d$ ) of  $M_2$  tidal cycle (12.42 hrs). As shown later in this section, the assimilation has significantly improved the model solutions. Therefore the spatial distribution of tidal elevation and currents for the five major semi-diurnal ( $M_2$ ,  $S_2$  and  $N_2$ ) and diurnal ( $K_1$  and  $O_1$ ) constituents is discussed in detail in this section.

### 5.2.1. Tidal Elevation

#### a) Co-range and co-phase charts

The co-range and co-phase charts of the 5 leading major semidiurnal and diurnal constituents are shown in Figures 5-7 (a,b), 5-8 (a,b), 5-9 (a,b), 5-10 (a,b) and 5-11 (a,b). The model computed  $M_2$  tide (Figure 5-7a,b) propagates southeastward with the amplitude increasing toward Newfoundland coast and the north of the domain towards Labrador shelf and Davis Strait, consistent with an amphidromic point located east of the Newfoundland Shelf in deep North Atlantic (Schwiderski, 1980). In the north portion of the domain, an amplitude minimum occurs southeast of Cape Chidley, where the tide propagates in an anticlockwise direction entering into Hudson Strait. There the maximum amplitudes of 5-6m are seen in Ungava Bay. Easton (1972) has reported tidal sea-level variations in the range of 3 to 6m and in certain locations exceed 9m. Along the coastline around Newfoundland, the amplitude is nearly doubled from north to west of Avalon Peninsula. The Amplitude increases from the Northern Newfoundland shelf to the southwestern Scotian shelf, ranging from 20 to 80 cm. The amplitude ranges from 15 cm

to 70cm in the Placentia Bay consistent with previous descriptions of the regional  $M_2$  tide (e.g., Petrie et al. 1987; Han 2000). The  $M_2$  phase indicates southward propagation from the northern Newfoundland shelf. It travels westward over the southwestern Newfoundland shelf, and subsequently into the Gulf of St. Lawrence through the Cabot Strait, with a well-formed amphidromic point to the west of Magdalen Island and a secondary amphidrome just to the west of the Prince Edward Island (PEI) (Godin 1980; Lu et al. 2001). The amplitude increases from 20 cm on the northern shelf to 50 cm on the southwestern shelf and then decreases to 40 cm at Cabot Strait. The  $M_2$  tidal oscillations on the eastern and middle Scotian Shelf seem to be in phase. There are rapid phase and amplitude changes over the western Scotian Shelf because of resonance in the adjacent Bay of Fundy (Greenberg, 1990), with amplitudes increasing to a maximum of ~4m in the northern edge and a phase shift of approximately 90 degrees in the Georges Bank. There is phase error of 10 degrees for the  $M_2$  tide in the Gulf of Maine including the Bay of Fundy in comparison to previously published results (Godin 1980; Lynch and Naimie 1992). Such changes were also seen in the models of de Margerie and Lank (1986). The amplitude near resonance is limited by friction, which is particularly strong in shallow water regions.

The  $S_2$  tide (Figure 5-8a,b) presents similar tendencies with regards to the  $M_2$  tide, with the amplitude minimum on the eastern Cape Chidley developing into a well-defined amphidromic point. The amphidromic point in the Gulf of St. Lawrence is shifted to the east of Northumberland Strait. The amplitude of the  $S_2$  tide is 33% to that of the  $M_2$  tide.

The  $N_2$  tide (Figure 5-9a,b) presents similar tendencies as that of  $M_2$  tide, with the presence of an amphidromic point in the Gulf of St. Lawrence. Since the period of  $N_2$

(12.66 hrs) tide is very close to the  $M_2$  (12.42 hrs) tide, the phase distribution is quite similar to it. The  $N_2$  tide is 21.5% of the  $M_2$  tide.

The diurnal ( $K_1$  and  $O_1$ ) tidal waves off the Canadian Atlantic coastal waters propagate along the continental margin equatorward, each with a mid-ocean amphidrome (e.g., Le Provost et al., 1994). Local amphidromic on the Canadian Atlantic Shelf are generated along the irregular coastline with various inland seas and embayments. For example, amphidromes west of the southwestern Newfoundland Shelf (Godin, 1980; Han et al., 1996) are associated with an estuarine interaction between the shelf diurnal regime and the diurnal response in the Gulf of St. Lawrence. Flather (1988) carried out a numerical experiment that demonstrated the significant influences of diurnal tidal flow in Juan de Fuca Strait on the diurnal tide over the nearby Vancouver Shelf. The model diurnal charts show significantly different spatial pattern compared with the  $M_2$  cotidal chart over the entire model domain. Some diurnal intensification over the outer shelf and shelf break due to a shelf wave resonance can be seen from the co-range and co-phase charts of the diurnal constituents ( $K_1$  and  $O_1$ ).

The model  $K_1$  tide (Figure 5-10a,b) indicates the presence of an amphidromic point in the Laurentian Channel which is consistent with the North Atlantic Model (Egbert et al. 1994; Han 1996). Godin (1980) has reported the traditional location near Sable Island. A secondary amphidromic point is seen to the west of Baffin Island and the diurnal intensification (amplitude maxima of 28 cm) on the shelf break, east of Davis Strait, northern model domain.

The  $O_1$  tide (Figure 5-11a,b) propagates northward and southward from the northern Newfoundland shelf and then westward from northern Newfoundland shelf with amplitude decreasing away from the coast, characteristic of a Kelvin wave propagating

along the coastline. An amphidromic point appears inshore of the Sable Island. The maximum amplitude of 19 cm occurs at the mouth of the St. Lawrence Estuary.

Assimilation has had a greater effect on the semi-diurnal constituents than on the diurnal constituents.



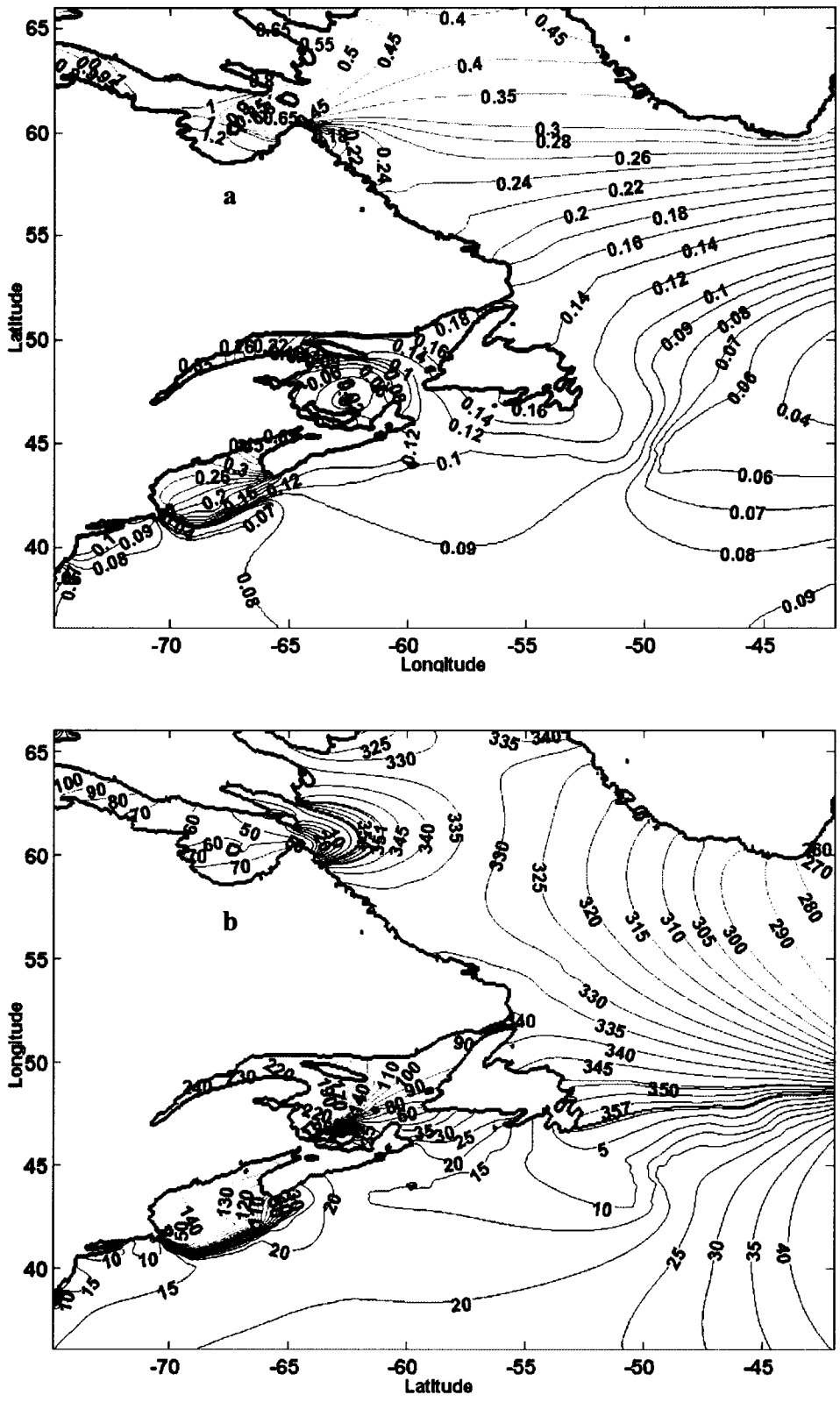


Figure 5-8. Model computed Co-range (a) and Co-phase (b) charts for  $S_2$  constituent from Ba run. The amplitude is in m and phases are in degrees. The contours are co-range (a) and co-phase (b) lines scaled to show the proper distribution of amplitude and phase respectively.

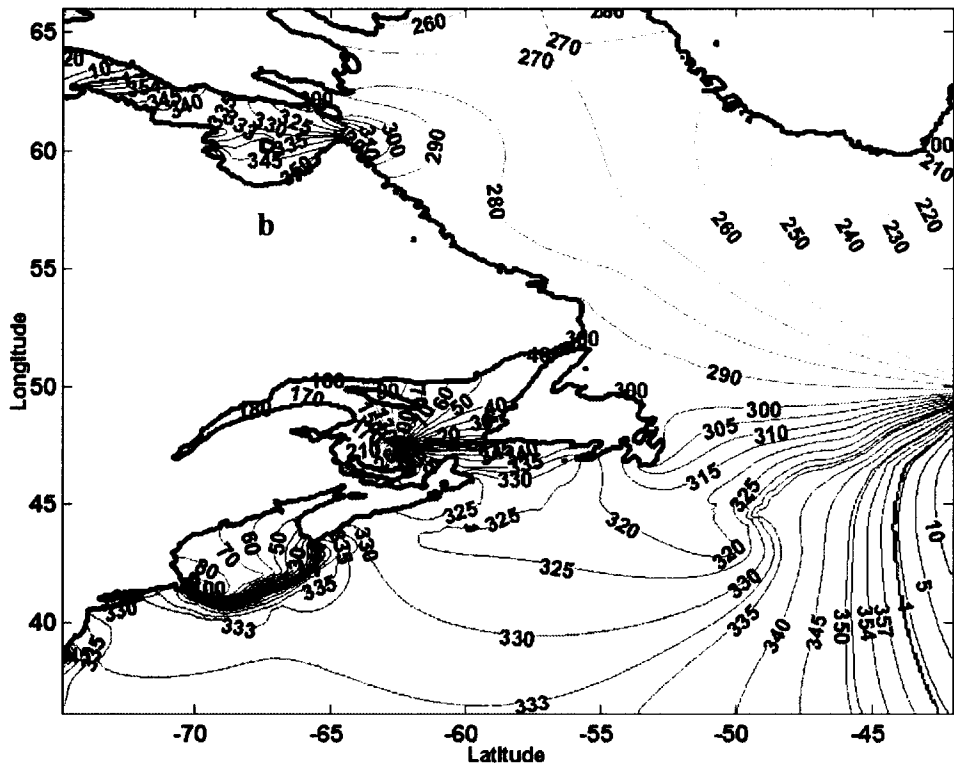
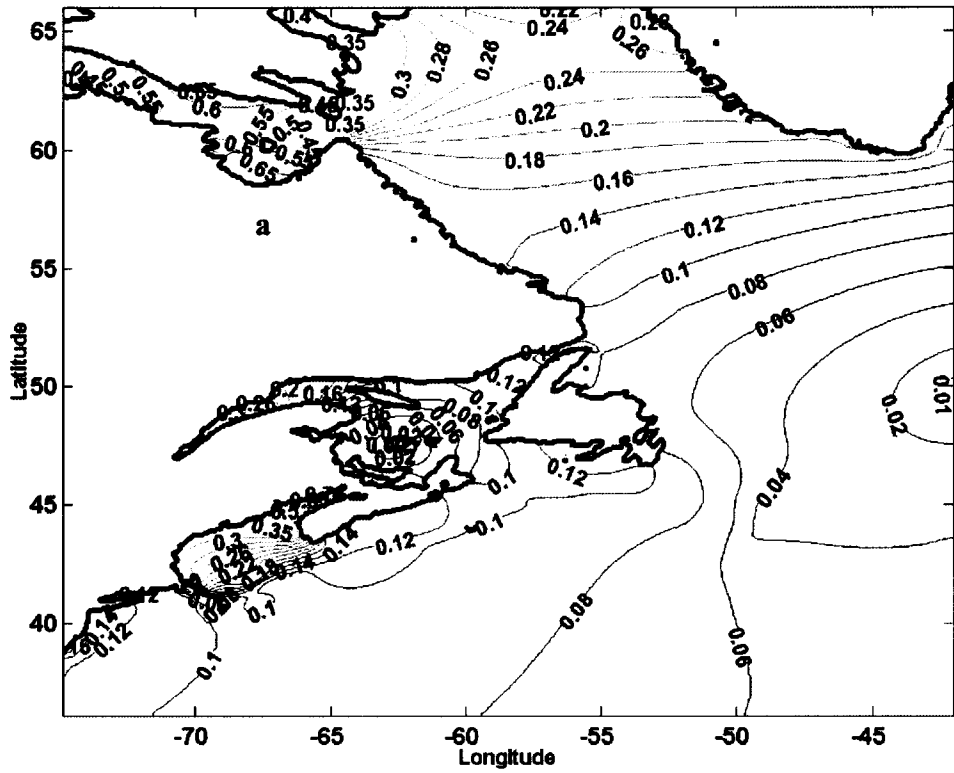


Figure 5-9. Model computed Co-range (a) and Co-phase (b) charts for  $N_2$  constituent from Ba run. The amplitude is in m and phases are in degrees. The contours are co-range (a) and co-phase (b) lines scaled to show the proper distribution of amplitude and phase respectively.

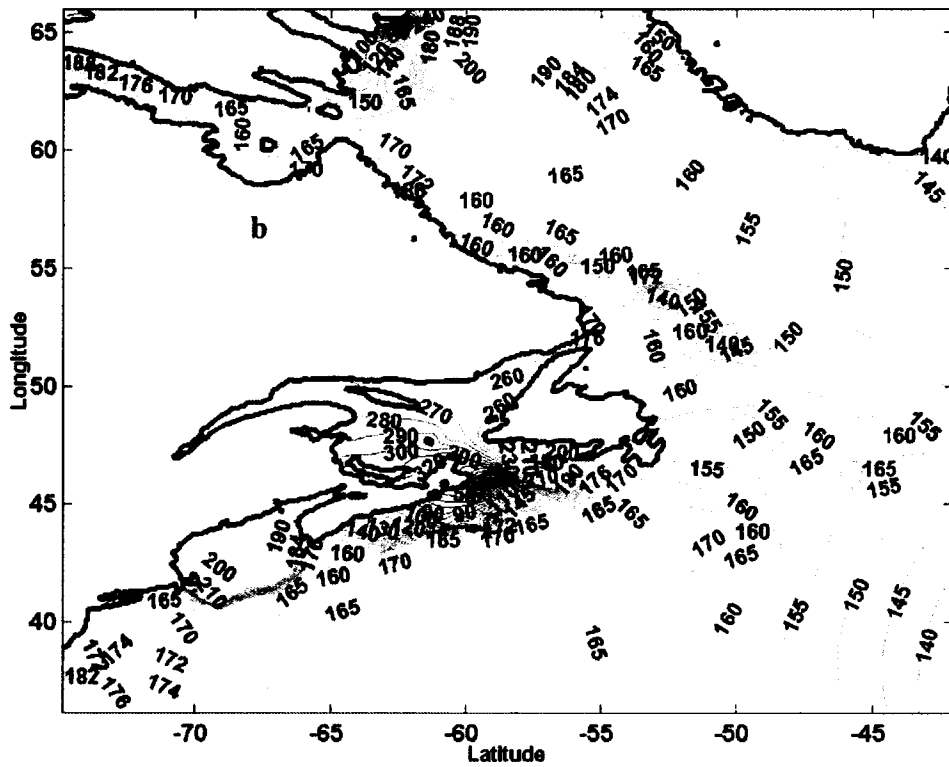
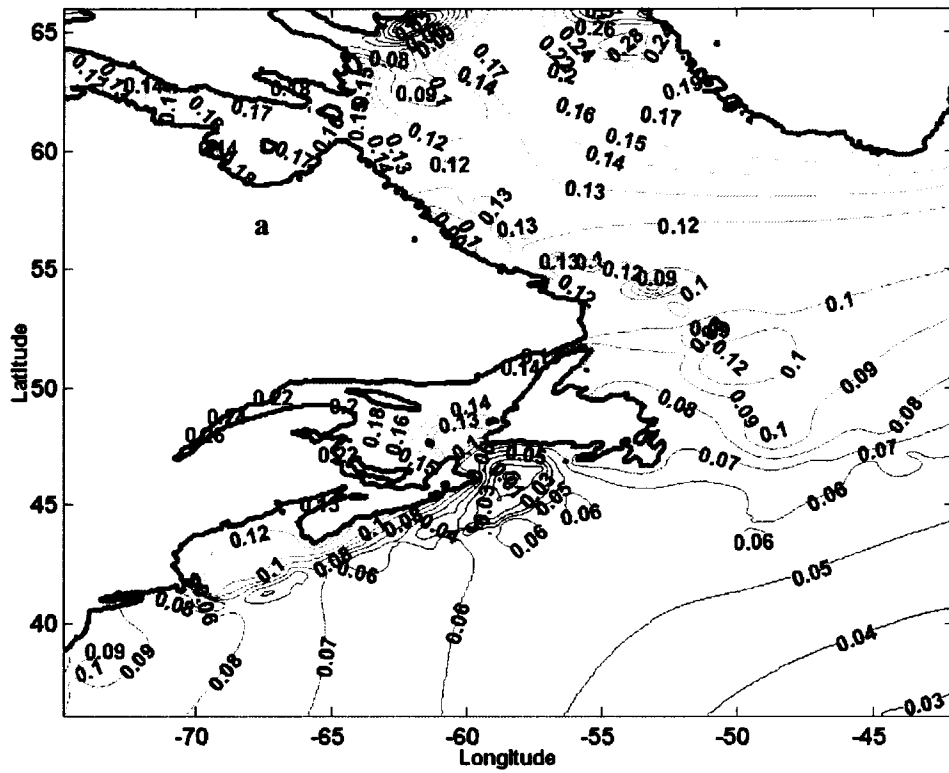


Figure 5-10. Model computed Co-range (a) and Co-phase (b) charts for  $K_1$  constituent from Ba run. The amplitude is in m and phases are in degrees. The contours are co-range (a) and co-phase (b) lines scaled to show the proper distribution of amplitude and phase respectively.

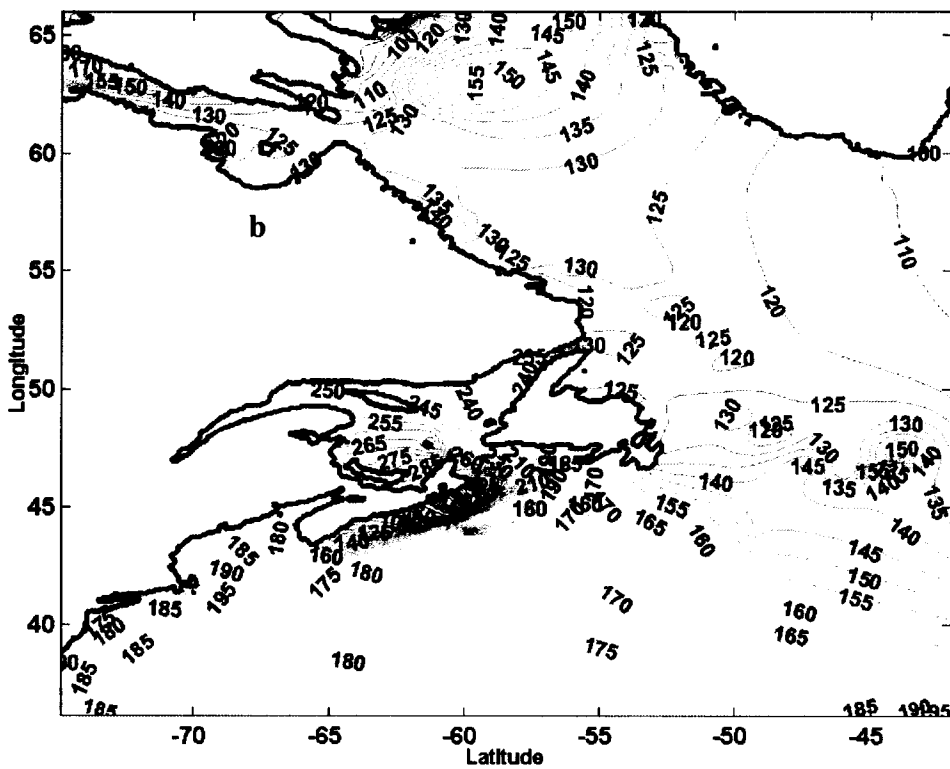
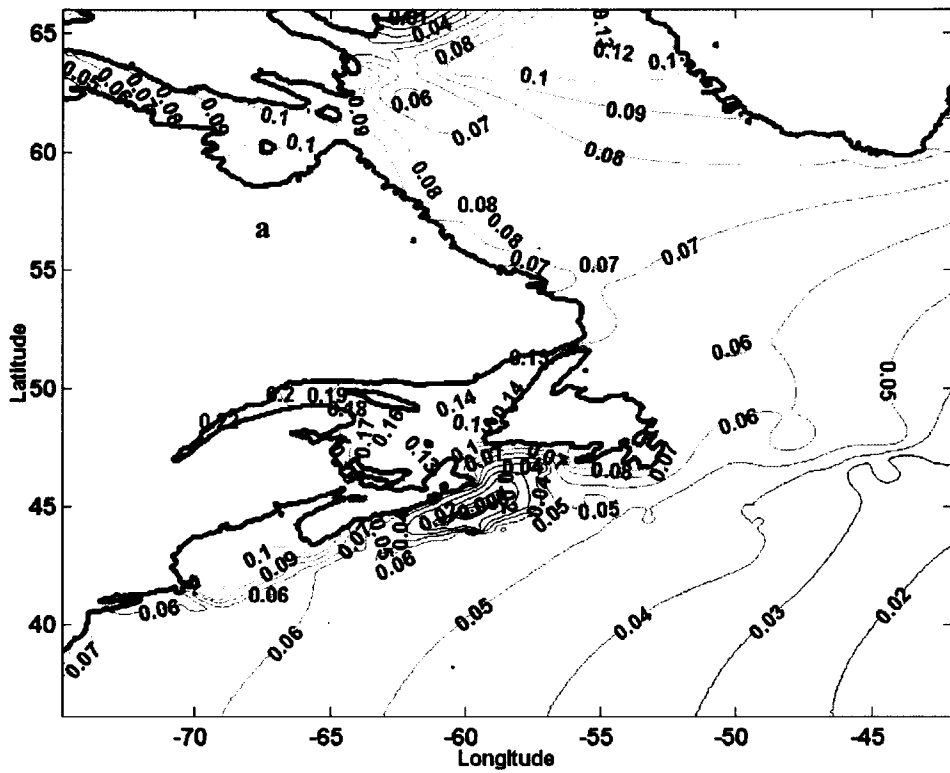


Figure 5-11. Model computed Co-range (a) and Co-phase (b) charts for O<sub>1</sub> constituent from Ba run. The amplitude is in m and phases are in degrees. The contours are co-range (a) and co-phase (b) lines scaled to show the proper distribution of amplitude and phase respectively.

### **b) Comparison with observations**

Figure 5-12 and Figure 5-13 show the scatter plots of the model computed elevation in comparison to the observed values at four regions excluding the BoFGoM region. The scatter plots for  $M_2$  constituent show that the model computed tidal elevation has remarkably improved from the Bu run. The amplitudes have improved by 50%. There is significant improvement for  $S_2$  as compared to  $N_2$  from the Bu run. The agreement in amplitude for  $S_2$  has improved especially in the Labrador and around Coastal Island of Newfoundland. For the diurnals, there is no significant change for amplitude but  $K_1$  has improved with  $O_1$  remaining the same.

In order to assess the performance of the model in reproducing the tidal elevations in comparison to the Bu experiment, we compare the error values from Table 5-1 (Bu) with error values from Table 5-3 (Ba). It is evident from both the tables that there is a significant improvement in the tidal elevations from the Ba experiment over the Bu experiment. The improvement is in the order of 40-60% for  $M_2$  constituent and around 30% for  $S_2$  and  $N_2$  constituents. The improvement is significant in the coastal regions: 70% around Newfoundland and 84% around Nova Scotia. For  $K_1$ , the improvement is more significant in phase, with the phase errors reduced by 30-40%. An improvement of 10% for  $O_1$  is observed, especially in the Scotian Shelf region. This small improvement can be attributed to the presence of an amphidromic point in that region for  $O_1$  constituent.

### **c) Comparison with North Atlantic Model**

A comparison of the error estimates of the five major semi-diurnal and diurnal constituents calculated from the Ba run (Table 5-3) and the North Atlantic model (Table D-1) shows that the mean RMS amplitude differences are smaller in all the regions

except BoFGoM, where the North Atlantic (NAt) Model performs better. Excluding the BoFGoM region, our model performs better (mean absolute error of 2.1 cm) in reproducing the  $M_2$  tidal elevations in comparison to the NAt model (mean absolute error of 2.4 cm). The mean RSS values for the five constituents excluding the BoFGoM region show a similar trend: 2.6 cm for amplitude and 3.1 cm for the Absolute Error for the Ba run; 3.3 cm for amplitude and 3.8 cm for the Absolute Error for the NAt model. In the BoFGoM region, our model was not able to calculate the resonant amplitude generated inside the Bay of Fundy. The possible reasons could be related to bathymetry and resolution of the model.

#### **d) A region by region study of the accuracy of the solution**

This section summarizes the region by region analysis of the model errors. The reader is referred to Appendix B for the maps locating the stations and Table E-1 and E-2 for a detailed study of the discrepancy between the observations and the model solution station by station, for the semi-diurnal ( $M_2$ ,  $S_2$  and  $N_2$ ) and diurnal ( $K_1$  and  $O_1$ ) constituents respectively.

For the Labrador region, the agreement is usually good for all the constituents with the absolute difference being in the range 1-5 cm for amplitude. Stations 695, 696, 697, 802, 803, 804 shows large phase deviation ( $\sim 45$  min) for  $M_2$  constituent. This is the region where the altimeter data is sparse (Figure 4-3) and is close to the Hudson Strait where  $M_2$  tide is large (over 1 m) and where the solution is changing rapidly.

For the Newfoundland area the absolute error difference in amplitude is in the range of 0.5-6 cm. At station NF-20 and NF-23, which lie close the Strait of Belle Isle, the maximum phase error (more than 20 min) is observed for the diurnal and semi-diurnal constituents respectively.

In the Bay of Fundy, the model clearly overestimates the  $M_2$  tidal signal with amplitudes errors of  $\leq 50\text{cm}$  at stations BG-5 to 11 and there is a large shift in phase. This may be related to unrealistic bottom friction or to nonlinear interactions with missing constituents.

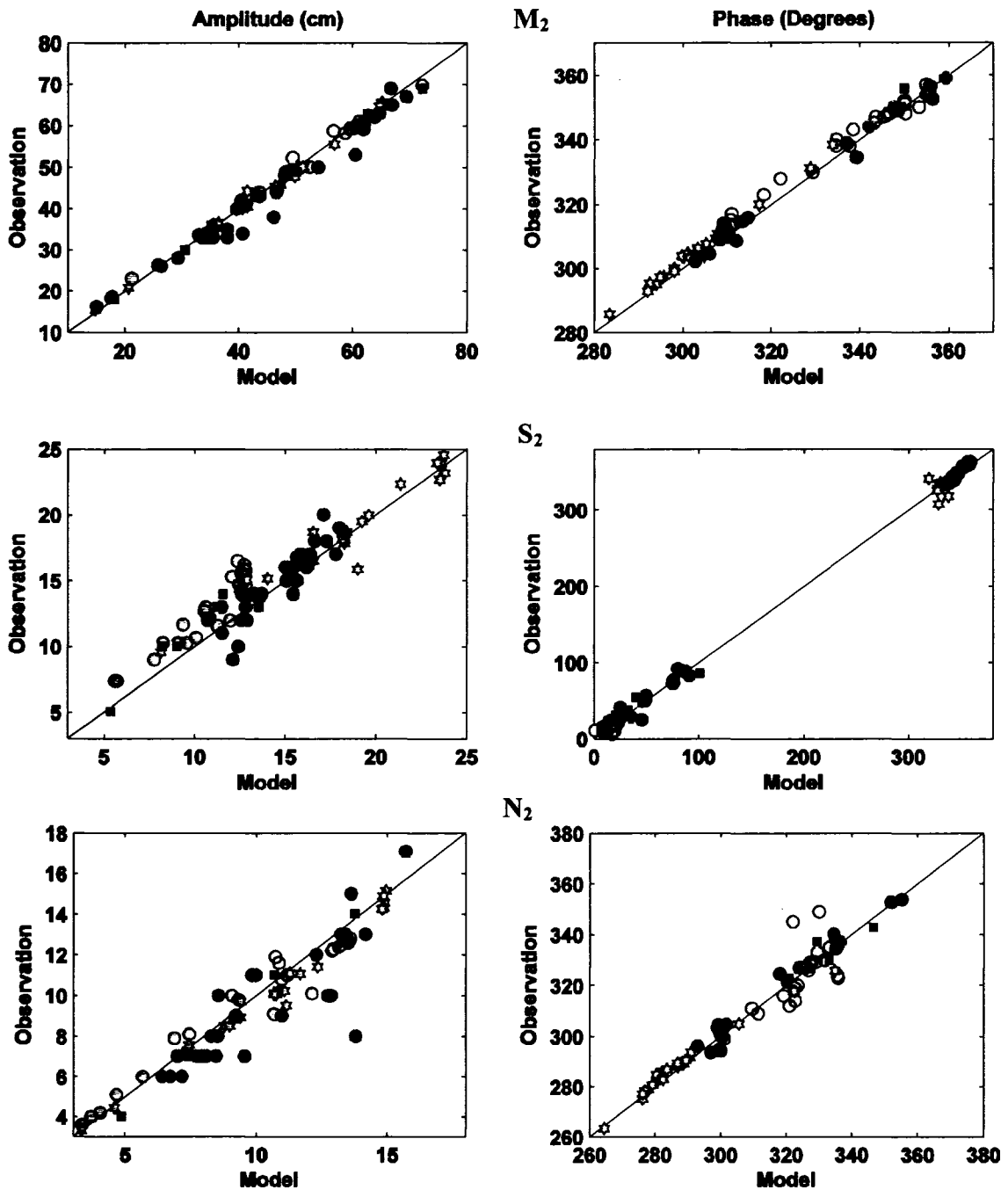


Figure 5-12. Scatter diagrams of amplitudes and phases of the model computed elevation (horizontal) and observation (vertical) for the Semi-diurnal constituents ( $M_2$ ,  $S_2$  &  $N_2$ ) from Ba run. The markers correspond to the 4 different regions, excluding BoFGoM as described in Figure 4-1. The solid line along the centre of each graph indicates where all points should lie if the agreement were perfect. Amplitudes are in centimeters and phases in degrees. The range of phases is defined from  $0^\circ$  to  $360^\circ$ .

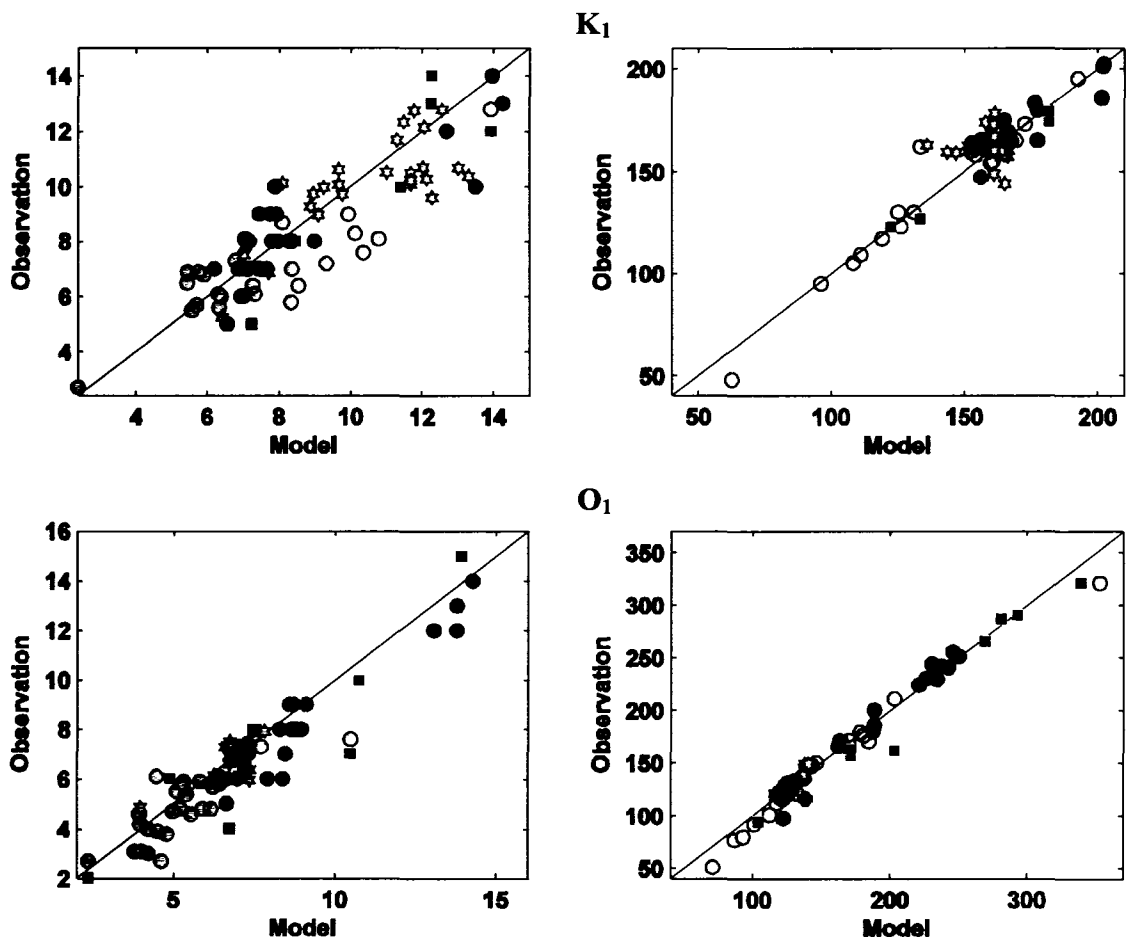


Figure 5-13. Same as Figure 5-12, but for  $K_1$  and  $O_1$ .

Table 5-3. Statistics of model computed elevation for semi-diurnal and diurnal constituents compared with observations at Tide and Bottom Pressure Gauge Sites for the Ba run. The locations are defined in Figure 4-1.

<b>Constituent</b>	<b>RMS Amplitude Difference (cm)</b>	<b>RMS Phase Difference (Degrees)</b>	<b>AbsErr (cm)</b>	<b>RelErr (%)</b>
<b>Super Stations</b>				
<b>M<sub>2</sub></b>	<b>0.9</b>	<b>2.5</b>	<b>1.5</b>	<b>3.8</b>
<b>S<sub>2</sub></b>	<b>1.9</b>	<b>5.9</b>	<b>1.8</b>	<b>13.3</b>
<b>N<sub>2</sub></b>	<b>0.8</b>	<b>4.8</b>	<b>0.8</b>	<b>9.1</b>
<b>K<sub>1</sub></b>	<b>1.1</b>	<b>6.2</b>	<b>1.0</b>	<b>15.3</b>
<b>O<sub>1</sub></b>	<b>0.7</b>	<b>9.5</b>	<b>0.8</b>	<b>17.5</b>
<b>RSS</b>	<b>2.6</b>		<b>2.8</b>	
<b>Coastal Island of Newfoundland</b>				
<b>M<sub>2</sub></b>	<b>2.3</b>	<b>2.9</b>	<b>2.6</b>	<b>6.1</b>
<b>S<sub>2</sub></b>	<b>1.1</b>	<b>5.1</b>	<b>1.3</b>	<b>9.1</b>
<b>N<sub>2</sub></b>	<b>1.2</b>	<b>5.2</b>	<b>1.1</b>	<b>13.4</b>
<b>K<sub>1</sub></b>	<b>0.9</b>	<b>6.9</b>	<b>1.0</b>	<b>12.7</b>
<b>O<sub>1</sub></b>	<b>0.8</b>	<b>5.7</b>	<b>0.8</b>	<b>12.2</b>
<b>RSS</b>	<b>3.0</b>		<b>3.4</b>	
<b>Coastal Nova Scotia</b>				
<b>M<sub>2</sub></b>	<b>1.9</b>	<b>2.7</b>	<b>2.5</b>	<b>4.2</b>
<b>S<sub>2</sub></b>	<b>2.2</b>	<b>8.6</b>	<b>2.3</b>	<b>15.9</b>
<b>N<sub>2</sub></b>	<b>0.9</b>	<b>6.6</b>	<b>1.2</b>	<b>10.8</b>
<b>K<sub>1</sub></b>	<b>1.3</b>	<b>6.0</b>	<b>1.2</b>	<b>14.0</b>
<b>O<sub>1</sub></b>	<b>1.2</b>	<b>14.2</b>	<b>1.5</b>	<b>25.6</b>
<b>RSS</b>	<b>3.5</b>		<b>4.0</b>	
<b>Labrador Sea &amp; Shelf</b>				
<b>M<sub>2</sub></b>	<b>0.8</b>	<b>2.5</b>	<b>1.7</b>	<b>3.6</b>
<b>S<sub>2</sub></b>	<b>0.9</b>	<b>3.6</b>	<b>1.2</b>	<b>7.2</b>
<b>N<sub>2</sub></b>	<b>0.5</b>	<b>2.0</b>	<b>0.4</b>	<b>4.6</b>
<b>K<sub>1</sub></b>	<b>1.0</b>	<b>8.7</b>	<b>1.4</b>	<b>14.2</b>
<b>O<sub>1</sub></b>	<b>0.5</b>	<b>2.4</b>	<b>0.4</b>	<b>6.3</b>
<b>RSS</b>	<b>1.7</b>		<b>2.6</b>	

Table 5-3. (Continued)

<b>Constituent</b>	<b>RMS Amplitude Difference (cm)</b>	<b>RMS Phase Difference (Degrees)</b>	<b>AbsErr (cm)</b>	<b>RelErr (%)</b>
<b>BoFGoM</b>				
<b>M<sub>2</sub></b>	<b>32.7</b>	<b>9.6</b>	<b>45.4</b>	<b>13.7</b>
<b>S<sub>2</sub></b>	<b>8.2</b>	<b>8.1</b>	<b>7.6</b>	<b>20.4</b>
<b>N<sub>2</sub></b>	<b>8.6</b>	<b>7.5</b>	<b>9.1</b>	<b>15.4</b>
<b>K<sub>1</sub></b>	<b>2.4</b>	<b>4.5</b>	<b>2.0</b>	<b>12.7</b>
<b>O<sub>1</sub></b>	<b>0.7</b>	<b>12.2</b>	<b>1.8</b>	<b>16.8</b>
<b>RSS</b>	<b>34.9</b>		<b>47.0</b>	
<b>Excluding BoFGoM</b>				
<b>M<sub>2</sub></b>	<b>1.5</b>	<b>2.6</b>	<b>2.1</b>	<b>4.4</b>
<b>S<sub>2</sub></b>	<b>1.5</b>	<b>5.8</b>	<b>1.6</b>	<b>11.4</b>
<b>N<sub>2</sub></b>	<b>0.8</b>	<b>4.6</b>	<b>0.9</b>	<b>9.5</b>
<b>K<sub>1</sub></b>	<b>1.1</b>	<b>6.9</b>	<b>1.2</b>	<b>14.1</b>
<b>O<sub>1</sub></b>	<b>0.8</b>	<b>7.9</b>	<b>0.9</b>	<b>15.4</b>
<b>RSS</b>	<b>2.6</b>		<b>3.1</b>	
<b>At all Locations</b>				
<b>M<sub>2</sub></b>	<b>7.7</b>	<b>4.0</b>	<b>10.7</b>	<b>6.3</b>
<b>S<sub>2</sub></b>	<b>2.8</b>	<b>6.3</b>	<b>2.8</b>	<b>13.2</b>
<b>N<sub>2</sub></b>	<b>2.4</b>	<b>5.2</b>	<b>2.5</b>	<b>10.7</b>
<b>K<sub>1</sub></b>	<b>1.3</b>	<b>6.5</b>	<b>1.3</b>	<b>13.8</b>
<b>O<sub>1</sub></b>	<b>0.8</b>	<b>8.8</b>	<b>1.1</b>	<b>15.7</b>
<b>RSS</b>	<b>8.7</b>		<b>11.5</b>	

### 5.2.2. Tidal Currents

The spatial distribution of model calculated tidal currents from the Ba run is qualitatively similar to those from the Bu experiment. Figures 5-14a,b, 5-15 and 5-16 show the tidal ellipses for  $M_2$ ,  $K_1$  and  $O_1$  constituents respectively. Tidal ellipses for  $S_2$  and  $N_2$  are not shown. The notable pattern of the tidal current ellipse distribution is that for diurnal constituents.

#### a) Tidal current ellipses

The computed  $M_2$  tidal current ellipses at the sea surface ( $\sigma = 0$ ) and the fourth level ( $\sigma = -0.95$ ) from the bottom are shown in Figure 5-15. The spatial distribution of currents is discussed region-wise for convenience and clarity.

On the Newfoundland Shelf, at the surface (Figure 5-14a) a linearly rectilinear flow is found along the coast of Avalon Peninsula. The current in the Avalon Channel is weaker and nearly rectilinear with major axis aligned along the channel. Over the Grand Banks of the Newfoundland the flow patterns are more circular. Strong tidal currents occur in the outer shelf and shelf break regions, especially in the shallow banks and shoals, where the water depth is  $>100\text{m}$ . The maximum current speed reaches 20-30 cm/s near the Southeast Shoal. The spatial pattern of the bottom tidal current ellipses is similar to that of the surface current, but the magnitude of the bottom current is significantly reduced due to bottom friction, which is approximately one-third of the surface current. The  $S_2$  and  $N_2$  (not shown) currents have similar spatial patterns to the  $M_2$  currents but with much smaller magnitudes (about one-third).

The computed  $K_1$  tidal current at the sea surface (Figure 5-15) is weak in general, compared with the  $M_2$  current. Relatively stronger currents ( $>5\text{cm/s}$ ) exist in some outer shelf and shelf break areas. The strongest tidal currents ( $>20\text{cm/s}$ ) are on the

southwestern outer shelf. The  $K_1$  current based on the Kelvin wave theory is estimated to have magnitudes of 1-2 cm/s from the computed  $K_1$  elevation amplitude (Figure 5-10). Therefore Kelvin waves, which possess relatively large surface displacements and weak currents (Lapland and Mysak, 1978), are unable to generate the localized diurnal current intensification. The  $O_1$  tidal current (Figure 5-16) is generally small in the region but significantly intensified in the southwestern and north eastern outer shelves.

On the Labrador shelf, the computed  $M_2$  tidal current is small in this region, except in the inner shelf region, especially near Hamilton Bank, where the current magnitudes are  $\sim 5$  cm/s. Computed  $K_1$  currents are stronger in the inner shelf break region with speeds of 20-25 cm/s due to localized intensification. It is evident from Figure 5-16 that for  $K_1$  constituent the model overestimates the currents by about  $\sim 10$  cm/s in the Labrador shelf region consistent with the localized maxima for tidal elevations (Figure 5-10a). Xing and Davies (1998) have reasoned that including stratification minimizes the local maxima, which are due to sharp changes in topography. The  $O_1$  tidal current is small in the region with currents of the magnitude of 5 cm/s visible at isolated shelf break locations.

In the Gulf of St. Lawrence, the  $M_2$  tidal currents show a linearly rectilinear flow in the Laurentian channel, Strait of Belle Isle & Northumberland Strait. Currents of 20 cm/s are visible south & south-west of the Magdalen Islands and west of Prince Edward Island (PEI) as expected in narrow straits where the currents can exceed 0.5 m/s (Lu et al. 2001).

In the Gulf of Maine,  $M_2$  tidal currents with speeds of  $\sim 1$  m/s are visible. On the Georges Bank the ellipses oriented along the cross-shelf direction with intensification consistent with the sharp topographic features present in the region. The maximum currents ( $> 1$  m/s) occur in the Bay of Fundy area.

On the Scotian shelf, the computed  $M_2$  tidal currents reflect the influence of the bottom topography on current magnitude, with a significant contrast between inner shelf and shallow outer banks. The amplitudes are  $\leq 5$  cm/s over the inner shelf, while those over the outer shelf can exceed 30 cm/s. The results are consistent and comparable with the results of the spring solution of Han et al. (2003). The strongest currents ( $\sim 25$  cm/s) occur west and east of Sable Island with slightly lower magnitudes on the eastern side. The currents generally elongated in the cross-shelf direction, with an eccentricity of 0.7 over the outer banks consistent with continuity and rotational effects in shallow water at midlatitude. Model  $K_1$  currents over the inner shelf are rectilinear in the alongshelf direction, with their magnitudes slightly greater than those of  $M_2$  currents. Over the outer banks the current ellipses remain oriented in the along-shelf direction but are more circular than on the inner shelf. The current magnitudes are again amplified (20-25 cm/s) over the banks, especially near Sable Island. The general intensification may be explained by the occurrence of a first-mode shelf wave at the  $K_1$  frequency (Han, 2000). The intensification is expected to be strongly dependant on the bottom topography, so high resolution of topography is expected to be crucial in obtaining accurate currents. Model  $O_1$  currents show a similar pattern close to  $K_1$ , with weaker currents close to the Great South Channel.

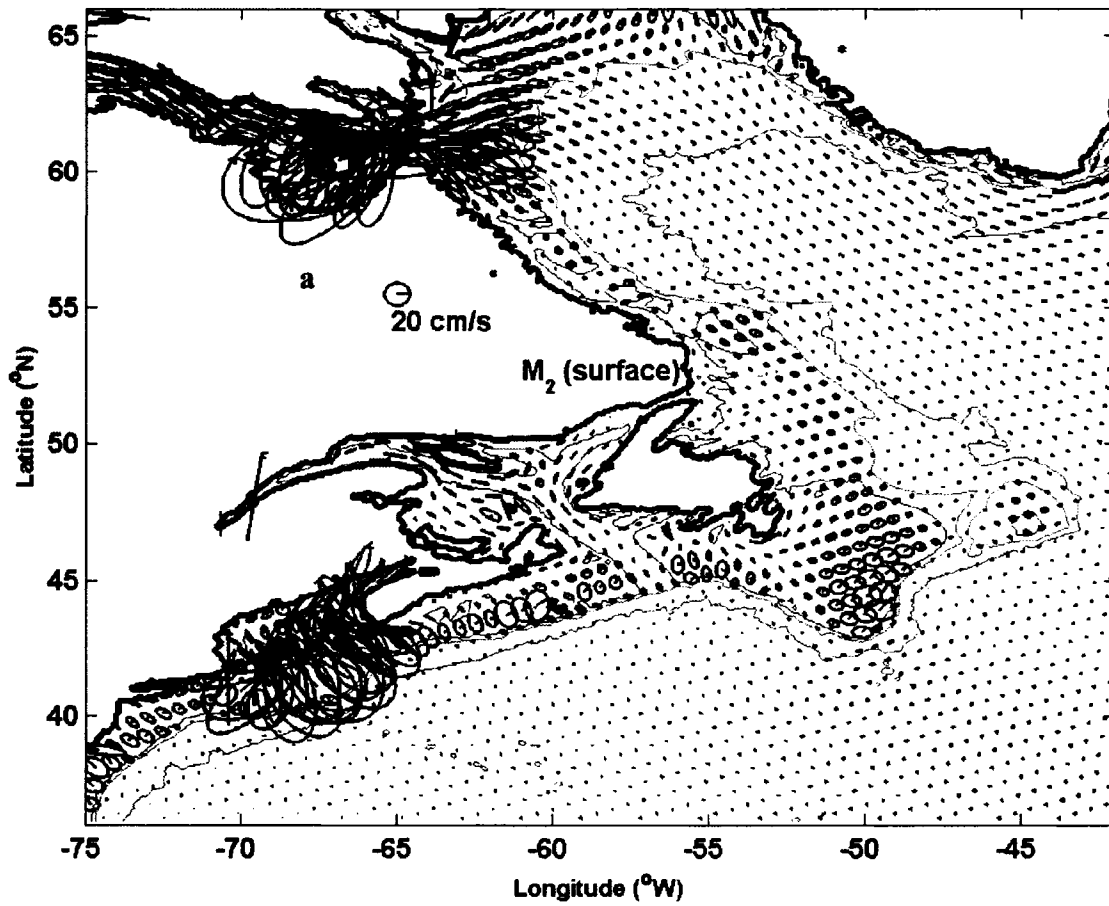


Figure 5-14. Sub-sampled  $M_2$  current ellipses (a) at the surface and (b) at a near bottom level ( $\sigma = -0.95$ ), from Ba run. The radial lines in ellipses indicate common time. The 200-, 1000- & 3000m isobaths are displayed in red, green and magenta colors respectively.

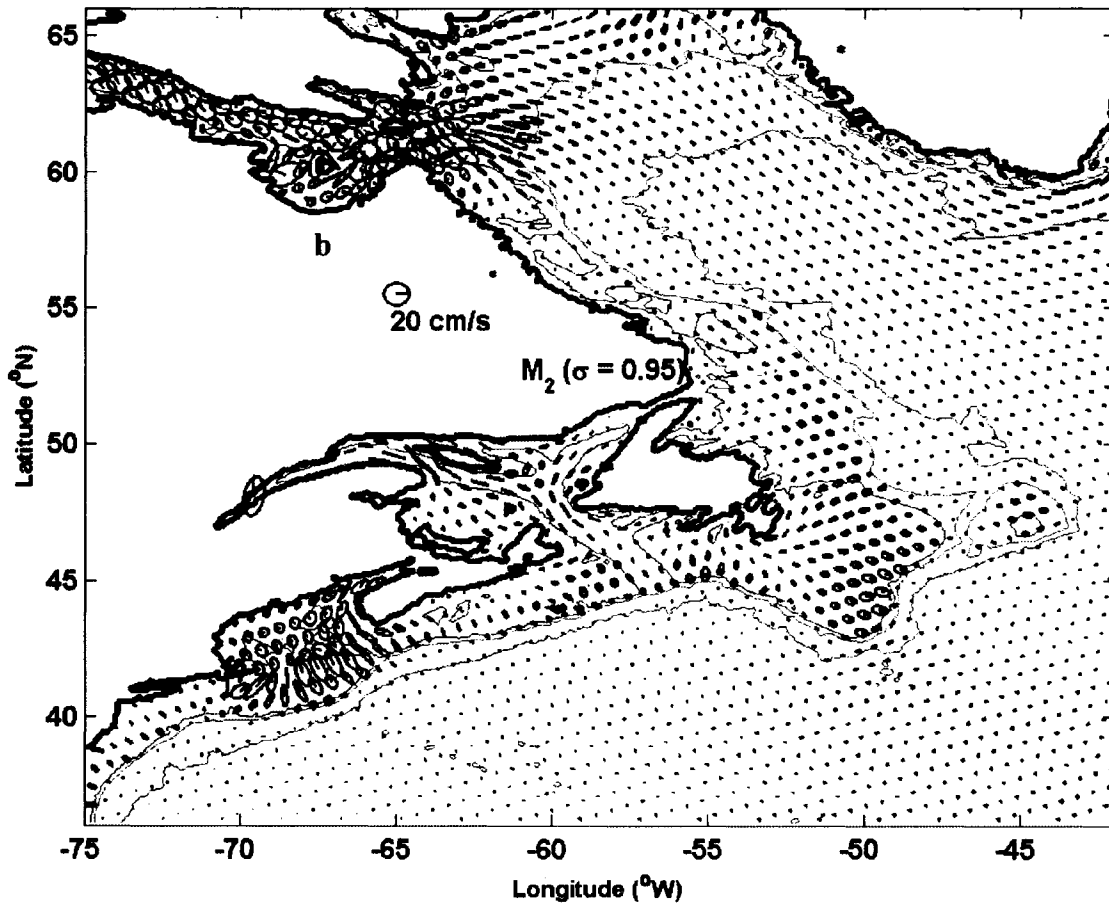


Figure 5-14. (continued)

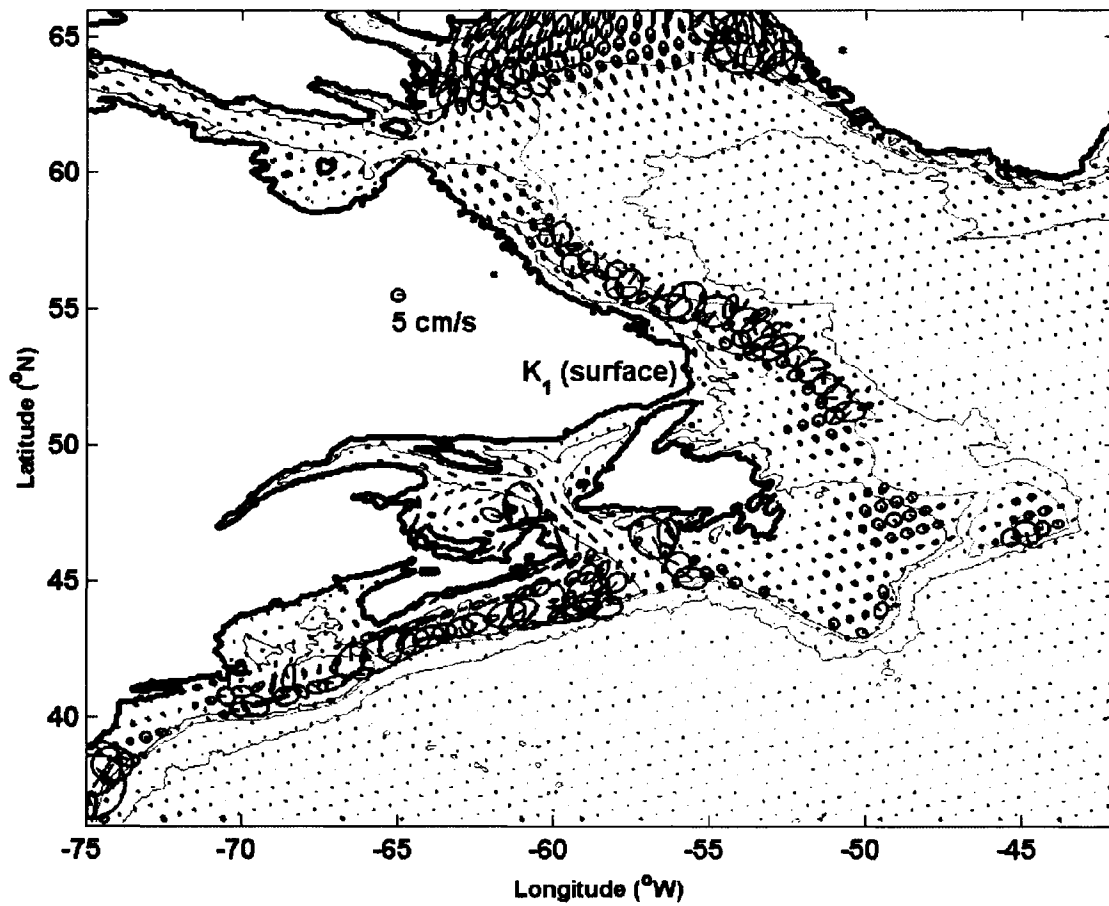


Figure 5-15. Sub-sampled  $K_1$  current ellipses at the surface, from Ba run. The radial lines in ellipses indicate common time. The 200-, 1000- & 3000m isobaths are displayed in red, green and magenta colors respectively.

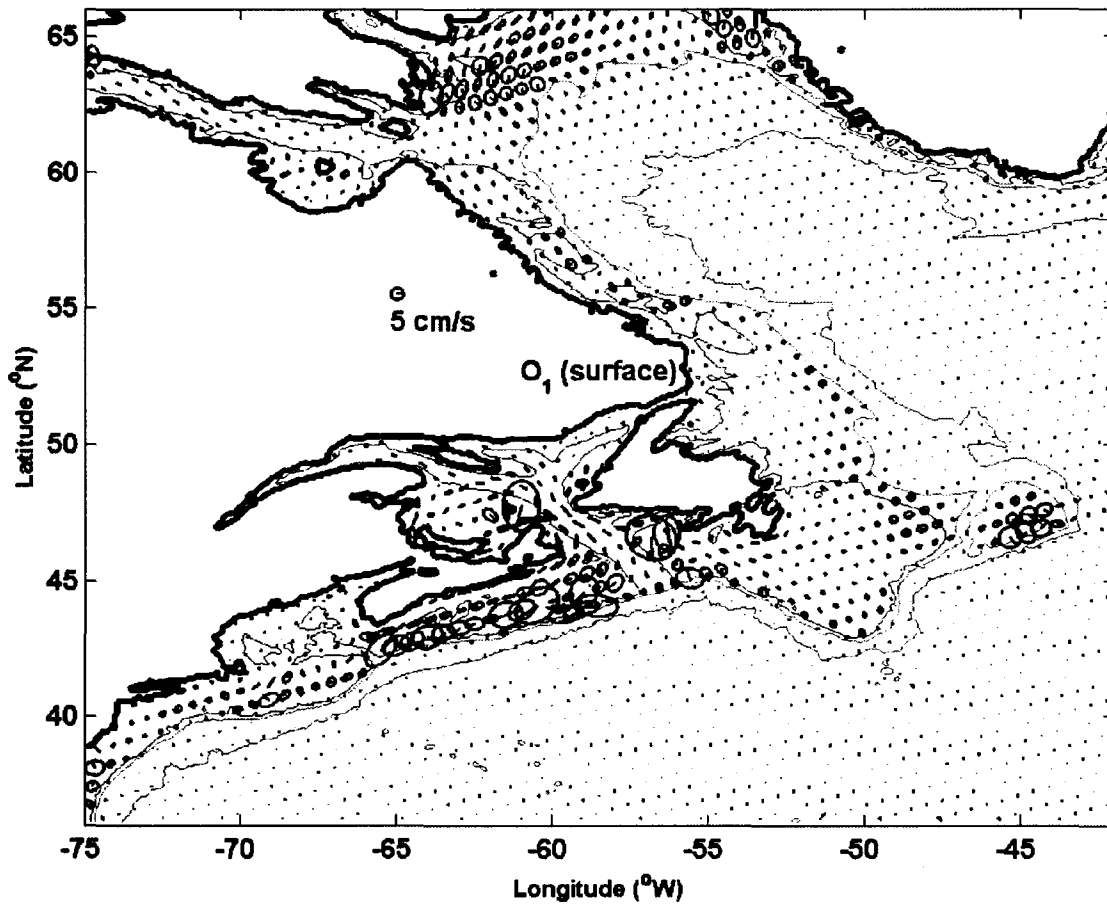


Figure 5-16. Sub-sampled  $O_1$  current ellipses at the surface, from Ba run. The radial lines in ellipses indicate common time. The 200-, 1000- & 3000m isobaths are displayed in red, green and magenta colors respectively.

## **b) Comparison with observations**

The model generated tidal currents are compared with observations for the 5 leading semidiurnal and diurnal constituents. The scatter plots for the amplitude and phase for zonal (u- velocity) and meridional (v-velocity) components are shown in Figures 5-17 ( $M_2$ ), 5-18 ( $S_2$ ), 5-19 ( $N_2$ ), 5-20 ( $K_1$ ) and 5-21 ( $O_1$ ) respectively. The scatter plots show that the model reproduces the tidal currents in better agreement with the observations for semi-diurnal constituents than for the diurnal constituents. The  $M_2$  currents are in good agreement with the observations in the Scotian Shelf region, where the currents are  $>1$  m/s. The diurnal currents are overestimated by 10-20 cm/s in the Scotian Shelf region, for currents stronger than 10 cm/s.

Table 5-5 lists the RMS errors for amplitude and phase and absolute and relative errors for the zonal and meridional components. The relative errors for model 3-D tidal currents for  $M_2$  constituent are of the order 30-60%. There is a significant improvement in the  $S_2$  tidal currents with RMS amplitude and phase errors of 2 cm/s and 46.5 deg for the zonal component and 1.5 cm/s and 51.8 deg for the meridional component. The relative errors for the meridional and zonal components are between 60-90% for the diurnal constituents and for semi-diurnals, they are between 40-70%.

Region-wise, with assimilation, the  $M_2$  tidal currents are improved by a factor of 30% in the Georges Bank and Channel. The same is true for the other semi-diurnal currents. The relative errors for these regions drop by 40% for the semidiurnal constituents and by 20% for the diurnal constituents.

Dupont et al. (2002) have also reported that their model scores well in the Georges Bank region, where the magnitudes of the tidal currents are larger than 50 cm/s. Hannah et al. (2001) found poor agreement in  $M_2$  tidal currents close to the Sable Island. According to

Xu et al. (2001), assimilating observed tidal currents as well as elevations improves significantly the velocity solution. They suggest that the velocity, being related to the elevation gradient, provides a finer scale structure to the solution. These large velocity errors seem however to be localized to a few places, suggesting that we may not resolve sufficiently the shelf or other local dynamics.

Table 5-4. Statistics of model computed currents for semi-diurnal and diurnal constituents compared with observations at moored current meter Sites for six sub regions (a-f) of the model domain and the whole model domain (g) for the Baseline run with assimilation (Ba) using multi-mission altimeter data.

**a) Bay of Fundy & Gulf of Maine**

Constituent	RMS U	RMS U	RMS V	RMS V	AbsErr U	RelErr U	AbsErr V	RelErr V
	Amp (cm/s)	Phase (Deg)	Amp (cm/s)	Phase (Deg)	(cm/s)	(%)	(cm/s)	(%)
M <sub>2</sub>	24.7	17.8	11.4	30.1	19.7	42.9	13.9	47.8
S <sub>2</sub>	3.5	42.9	1.2	36.5	3.5	67.7	1.5	46.6
N <sub>2</sub>	4.1	20.0	2.3	30.7	3.9	36.6	3.2	49.9
K <sub>1</sub>	0.6	45.8	0.4	46.5	0.7	62.3	0.5	68.0
O <sub>1</sub>	0.5	29.2	0.2	55.9	0.5	48.1	0.3	75.0

**b) Georges Bank**

Constituent	RMS U	RMS U	RMS V	RMS V	AbsErr U	RelErr U	AbsErr V	RelErr V
	Amp (cm/s)	Phase (Deg)	Amp (cm/s)	Phase (Deg)	(cm/s)	(%)	(cm/s)	(%)
M <sub>2</sub>	12.4	14.9	14.0	19.6	13.1	37.7	16.2	37.0
S <sub>2</sub>	2.4	39.2	2.5	40.5	3.6	70.5	4.2	55.8
N <sub>2</sub>	2.9	16.1	3.5	26.7	3.0	38.1	4.6	45.2
K <sub>1</sub>	1.4	31.7	1.7	14.9	1.6	54.9	1.6	48.2
O <sub>1</sub>	1.0	56.4	0.9	38.7	1.0	83.4	1.1	92.0

**c) Channel**

Constituent	RMS U	RMS U	RMS V	RMS V	AbsErr U	RelErr U	AbsErr V	RelErr V
	Amp (cm/s)	Phase (Deg)	Amp (cm/s)	Phase (Deg)	(cm/s)	(%)	(cm/s)	(%)
M <sub>2</sub>	7.7	28.0	8.0	23.0	8.5	49.9	8.7	35.7
S <sub>2</sub>	1.4	57.3	1.7	56.6	1.8	69.5	2.3	62.4
N <sub>2</sub>	1.8	36.9	2.5	27.8	2.3	52.3	2.6	44.2
K <sub>1</sub>	2.5	40.9	2.3	29.0	2.5	61.9	2.1	60.2
O <sub>1</sub>	1.5	39.4	1.5	39.2	1.5	54.3	1.3	62.6

**d) Labrador**

Constituent	RMS U	RMS U	RMS V	RMS V	AbsErr U	RelErr U	AbsErr V	RelErr V
	Amp (cm/s)	Phase (Deg)	Amp (cm/s)	Phase (Deg)	(cm/s)	(%)	(cm/s)	(%)
M <sub>2</sub>	1.4	39.1	1.6	64.3	2.2	61.5	2.7	65.0
S <sub>2</sub>	0.5	39.3	0.6	58.4	0.8	55.0	0.9	63.2
N <sub>2</sub>	0.4	41.8	0.4	61.6	0.6	64.4	0.6	63.0
K <sub>1</sub>	0.5	82.8	0.3	30.7	0.8	120.3	0.4	60.7
O <sub>1</sub>	0.4	42.9	0.4	87.2	0.4	64.0	0.5	84.4

**e) Newfoundland & North Avalon Channel**

Constituent	RMS U	RMS U	RMS V	RMS V	AbsErr U	RelErr U	AbsErr V	RelErr V
	Amp (cm/s)	Phase (Deg)	Amp (cm/s)	Phase (Deg)	(cm/s)	(%)	(cm/s)	(%)
M <sub>2</sub>	1.8	17.2	1.4	31.1	1.9	43.3	2.1	52.1
S <sub>2</sub>	1.5	42.0	1.1	51.6	2.1	95.5	2.2	79.8
N <sub>2</sub>	0.6	36.1	0.6	50.5	0.8	59.2	0.7	67.9
K <sub>1</sub>	1.3	55.0	1.0	53.2	1.5	99.8	1.5	95.1
O <sub>1</sub>	1.0	51.6	0.9	49.4	1.2	115.3	1.2	92.1

**f) Scotian Shelf**

Constituent	RMS U	RMS U	RMS V	RMS V	AbsErr U	RelErr U	AbsErr V	RelErr V
	Amp (cm/s)	Phase (Deg)	Amp (cm/s)	Phase (Deg)	(cm/s)	(%)	(cm/s)	(%)
M <sub>2</sub>	7.3	25.2	4.7	36.2	7.0	43.3	5.7	54.0
S <sub>2</sub>	2.4	49.1	1.5	53.9	2.8	65.5	2.1	69.6
N <sub>2</sub>	2.1	30.4	1.5	43.6	2.2	56.2	1.8	67.9
K <sub>1</sub>	3.0	43.1	2.2	58.0	3.5	69.5	2.8	104.4
O <sub>1</sub>	2.5	38.5	1.8	63.8	3.0	61.7	2.5	96.4

**g) At all Locations**

Constituent	RMS U	RMS U	RMS V	RMS V	AbsErr U	RelErr U	AbsErr V	RelErr V
	Amp (cm/s)	Phase (Deg)	Amp (cm/s)	Phase (Deg)	(cm/s)	(%)	(cm/s)	(%)
M <sub>2</sub>	7.0	24.4	5.4	34.6	7.0	44.9	6.5	50.9
S <sub>2</sub>	2.0	46.5	1.5	51.8	2.5	64.9	2.2	66.4
N <sub>2</sub>	1.9	31.1	1.6	42.5	2.0	54.6	2.0	62.4
K <sub>1</sub>	2.4	44.8	1.9	47.7	2.7	72.8	2.2	89.0
O <sub>1</sub>	1.9	41.6	1.4	58.3	2.2	66.7	1.9	86.7

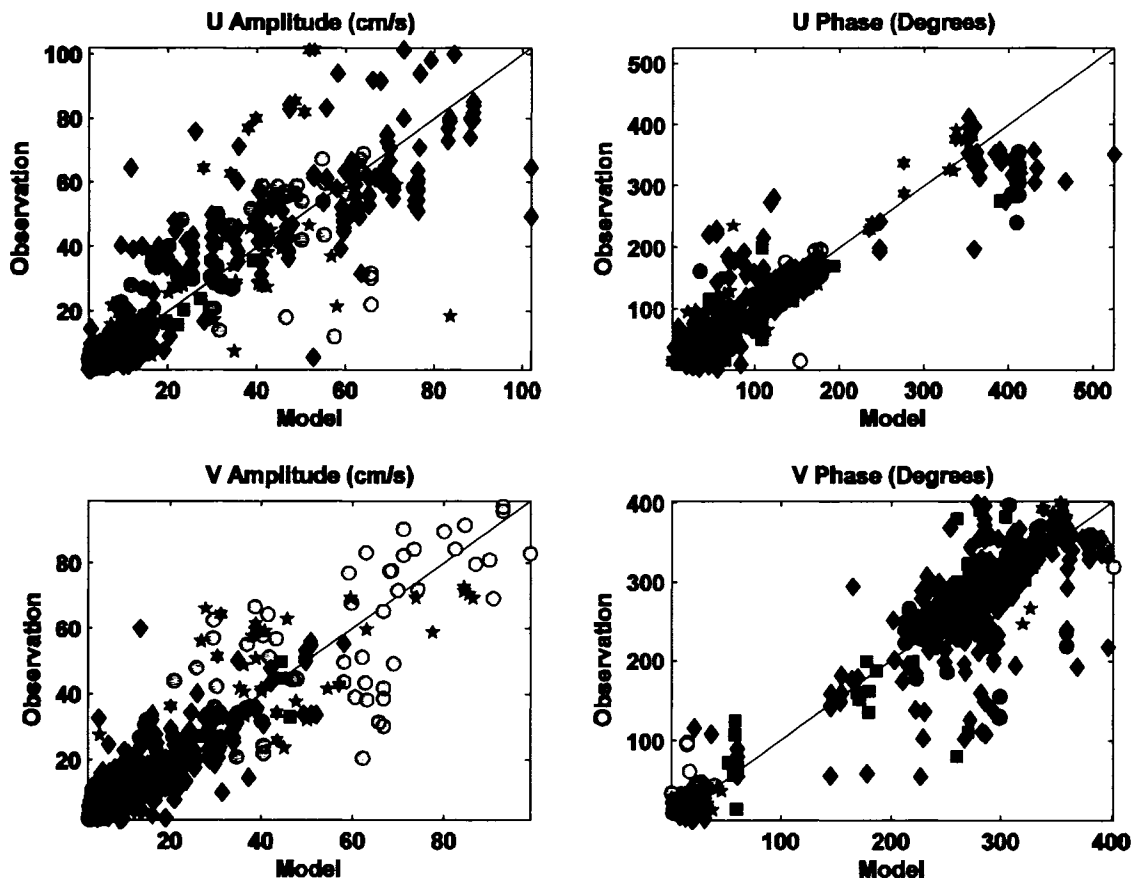


Figure 5-17. Scatter diagrams of the M<sub>2</sub> model tidal current amplitude and phase (top Panel) and the zonal (U, eastward) & meridional (V, northward) components (lower panel), from Ba run.

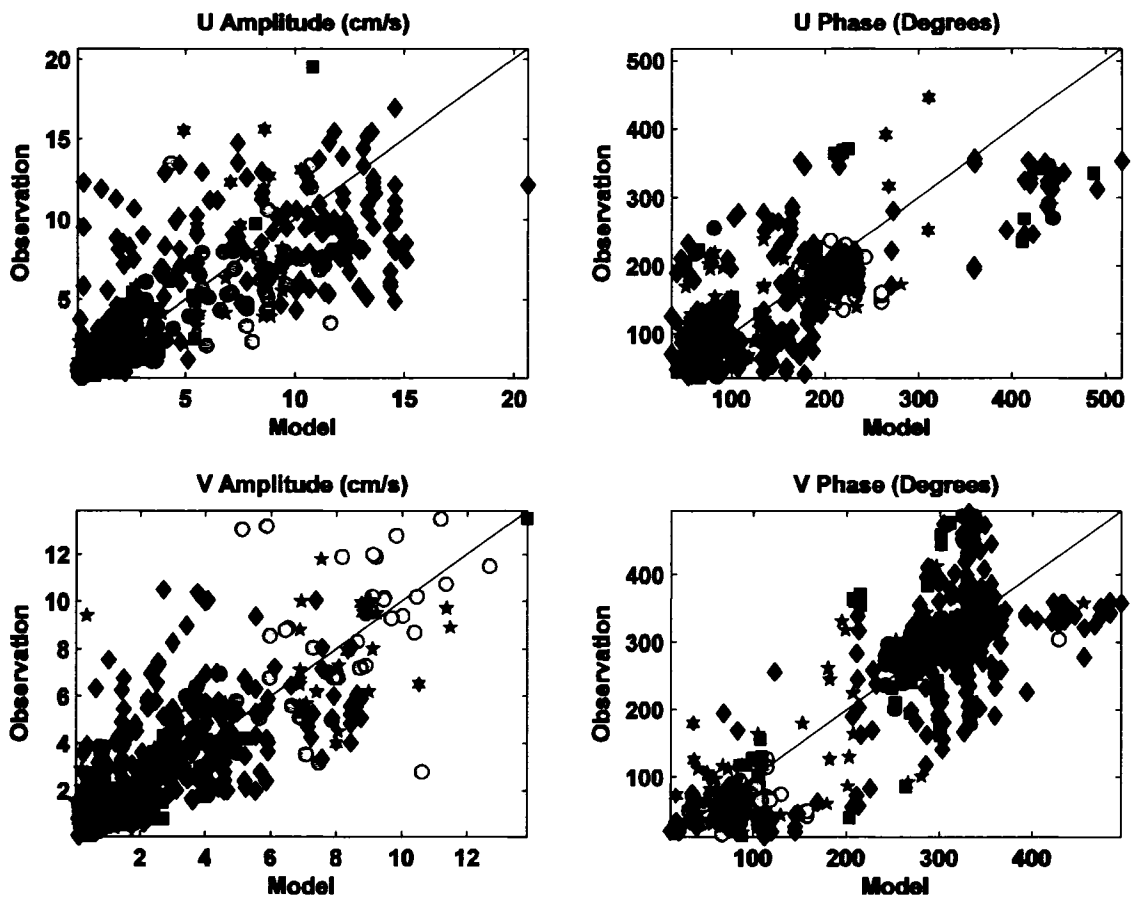


Figure 5-18. Same as Figure 5-17, but for  $S_2$ .

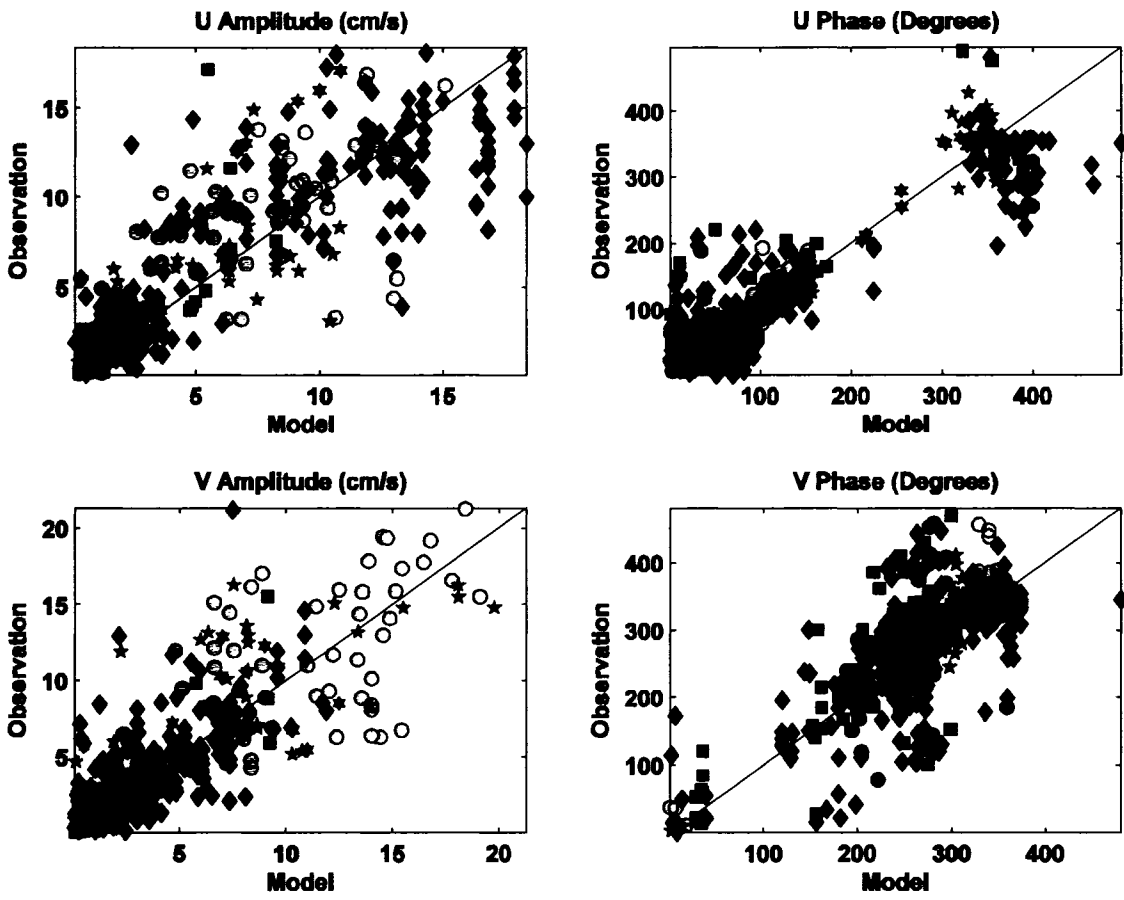


Figure 5-19. Same as Figure 5-17, but for  $N_2$ .

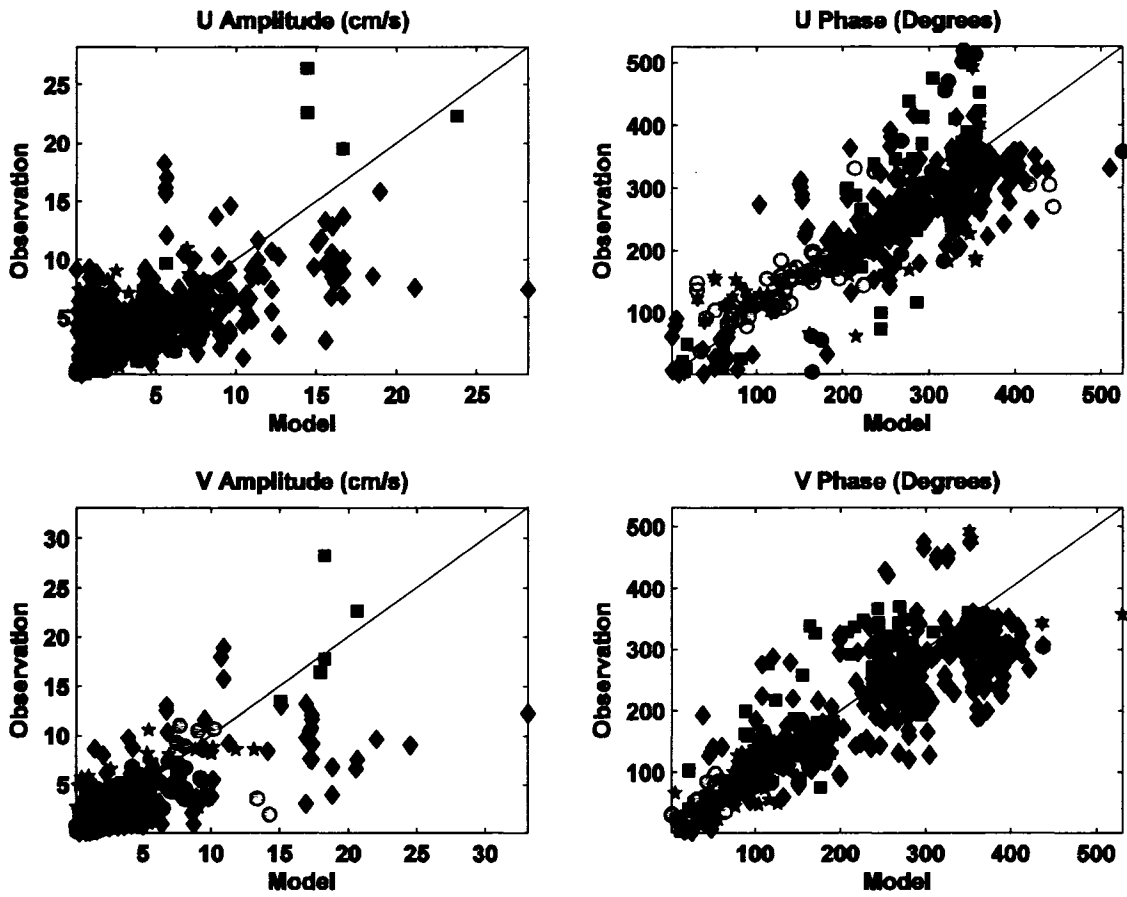


Figure 5-20. Same as Figure5-17, but for K<sub>1</sub>.

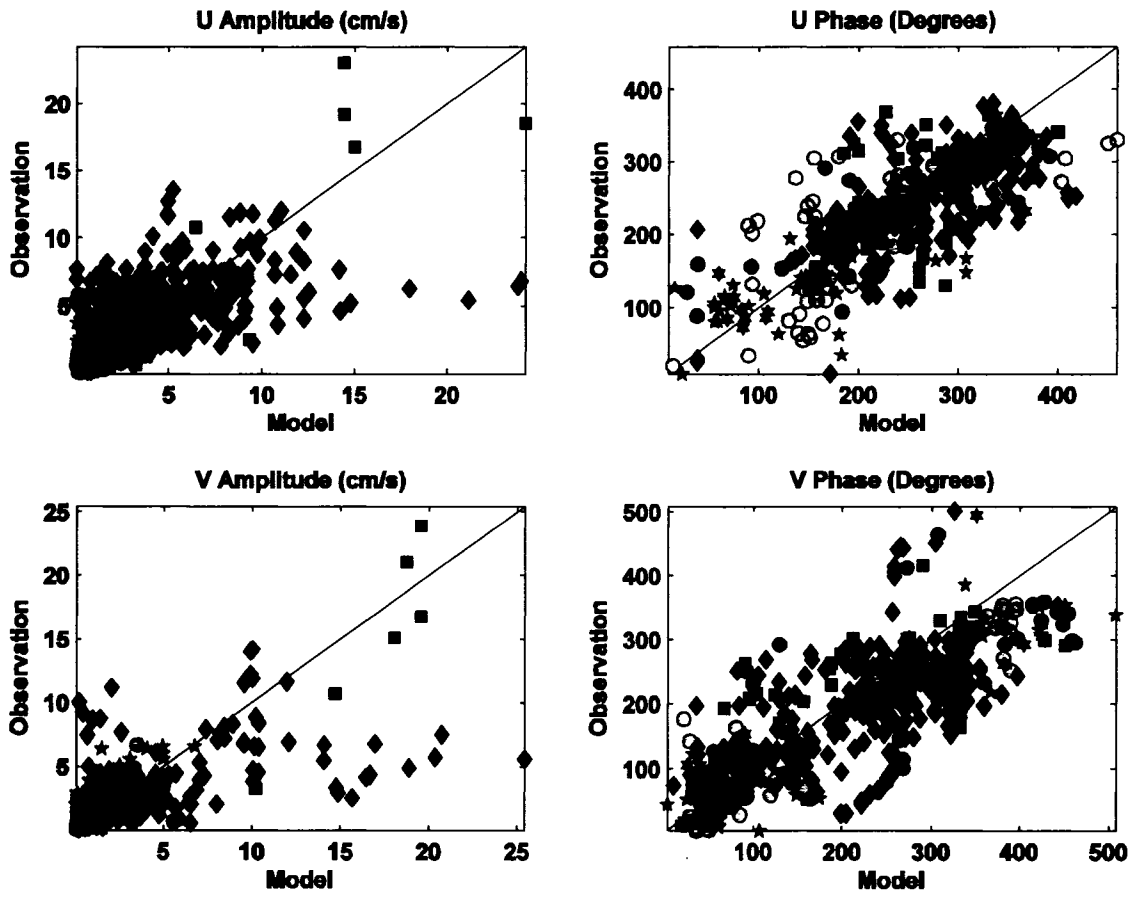


Figure 5-21. Same as Figure 5-17, but for  $O_1$ .

### 5.2.3. Vertical Structure of Model Tidal Currents

In this section we make a close examination of the vertical structure of computed tidal currents at selected individual sites to give a dynamic insight into the model results. We consider only  $M_2$  current profiles since the  $M_2$  currents dominate the tidal current variability over most of the domain.

The vertical profiles of computed  $M_2$  tidal currents are shown at selected sites S01, S02 in the Scotian Shelf, NF01, and NF02 in the Newfoundland Shelf, GB01 and GB02 in the Georges Bank (Figure 5-22). The results from the Ba (solid blue line) and Bu (dashed green line) experiment are shown together. At the shallow (62 m) site S01,  $M_2$  tidal currents are relatively large, of the order of 100cm/s, and the turbulent viscous effects are strong with a sheared boundary layer extending from the bottom to the surface. The zonal component of the current is in good agreement with the Ba experiment, while the Bu experiment overestimates by 5-10cm/s from bottom to the surface. The meridional component is overestimated by 10 cm/s in Ba and 20 cm/s in Bu. The phase for both the components is well reproduced to within <5 degrees in error. At the deeper (161m) shelf break site S02, tidal currents are weaker (15 cm/s) and the vertical current shear exists in the lower water column and near the sea bottom. The phase of the meridional component is in good agreement (within 5 degrees in error). The zonal and meridional components at depth are in good agreement (within 3 cm/s) but are overestimated at mid-depth by 4 cm/s and underestimated (7 cm/s) at the surface. At the shallow sites NF01 (56m) and NF02 (65m), located in the Grand Banks region, the currents are 15-20cm/s. The currents in the upper part of the water column are shear free and not influenced by viscous effects. The phases for both the components at both the sites are in good agreement, within an error of 2-6 degrees. The u component is within 1-2 cm/s at depth and approximately

reproduced for both the experiments at NF01 and overestimated by 5 cm/s at NF02 but the v component is overestimated by 2-3 cm/s at NF01 and approximately reproduced at NF02. Assimilation has no significant advantage in the Newfoundland shelf. The Georges Bank region is characterised by strong currents and is the region of transition into the resonant Gulf of Maine and Bay of Fundy region. The intermediate water depth location GB01 (200m) at the shelf break shows large  $M_2$  current velocities, the turbulent viscous effects are stronger. The sheared boundary layer extends from bottom to the surface. The assimilation improves the V component but degrades the U component. At GB02, the assimilated results are in better agreement with observations than the pure simulated.

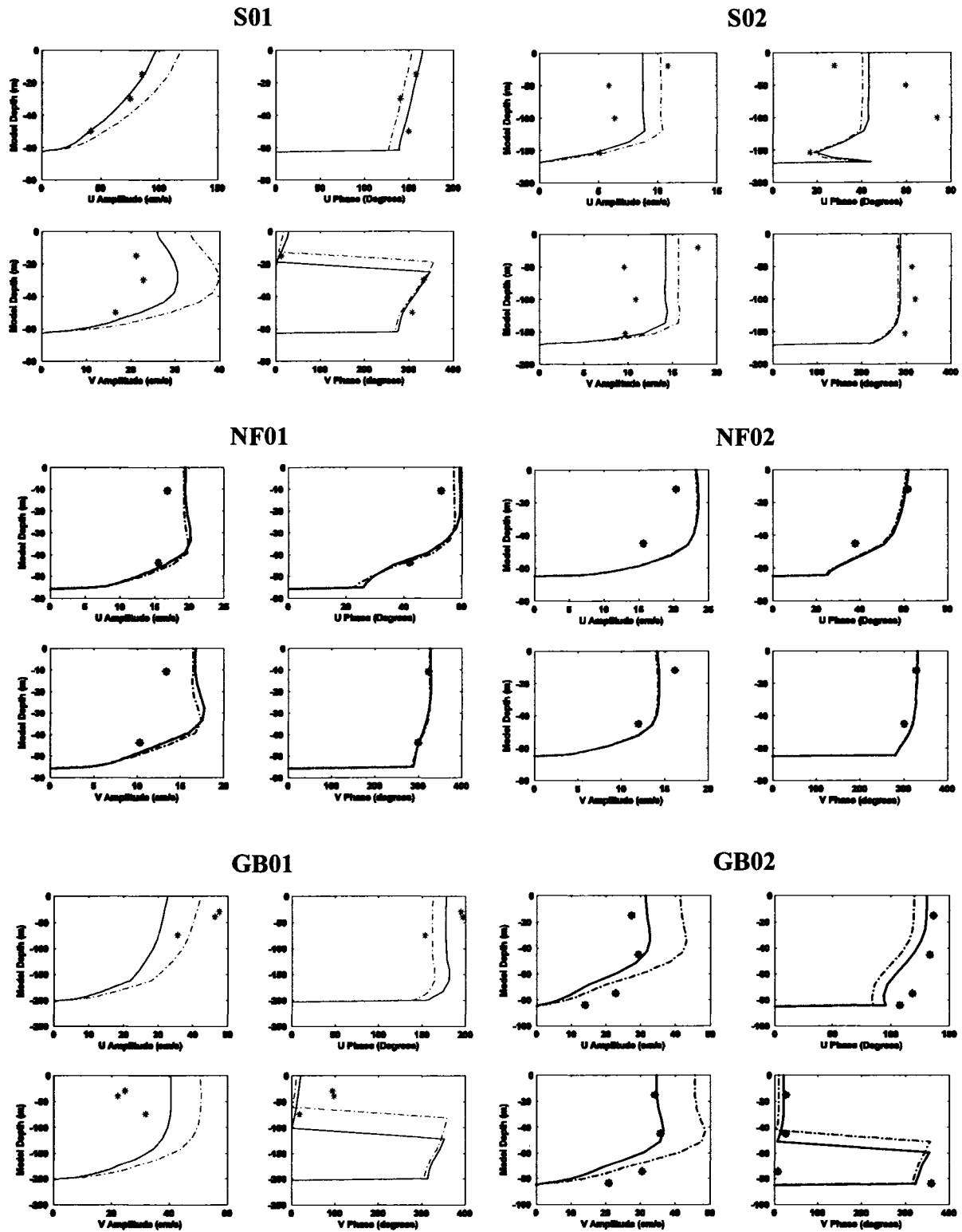


Figure 5-22. Computed vertical profiles of  $M_2$  currents at S01, S02, NF01, NF02, GB01 and GB02 for the Ba Experiment (blue solid line) and Bu experiment (green dashed line). The red asterisk (\*) are the observed values. The locations are shown in Figure 4-2.

## 6. Diagnostic Results

Water is assumed homogeneous in the vertical in Chapter 5. However, stratification does exist in the study region and evolves seasonally. In this chapter, the effects of vertical stratification on tidal currents are examined. The climatological monthly mean density field used in the computation is discussed in §4.4. A horizontally and vertically varying summer density field is specified and kept fixed during the model integration in time. As a result, no internal tides are generated. The baroclinic pressure terms in the momentum equations are turned off. The only effect of the stratification on the currents is through the buoyancy terms in the twice turbulent kinetic energy equation, in the equation for the product of the twice turbulent kinetic energy and the mixing length scale and through the stability functions.

### 6.1. Unassimilated

The results from the assimilated (Da) run only are presented. The results from the unassimilated (Du) run are not satisfactory and the variation of the vertical eddy viscosity alongwith the stability functions are unrealistically large over the shelf and shelf edge regions. The errors for elevation and currents are larger than the baseline unassimilated (Bu) run. The increase in the number of surface sigma layers has an effect on the vertical eddy viscosity formulation. Proper parameterization of the vertical eddy viscosity is necessary to improve the results in this case. However, a comparison of the vertical structure of currents is made between the Du and Da runs to investigate the effects of stratification on currents.

## **6.2. Assimilation Run**

The model results for tidal elevation and currents from the diagnostic assimilated experiment, Da, are compared with observations. A nudging method is used to assimilate the elevation data from the multi-mission altimeter data with a nudging time-period of 1 day. The vertical density profile was kept fixed throughout the model integration in time.

### **6.2.1. Tidal Elevations**

#### **b) Corange and Cophase plots**

The computed tidal elevations with vertical stratification are not significantly different from those for the homogeneous water with assimilation, Ba experiment.

#### **b) Comparison with observations**

Table 6-1 shows the statistics for the model elevations as against the observations for the five regions. It is evident from the table that there is no significant difference in the error values from the Ba experiment. Stratification does not have any significant effect on the surface elevation.

### **6.2.2. Tidal Currents**

The spatial distribution of model calculated diagnostic tidal currents with assimilation from multi-mission altimeter data is very much similar to those from the Ba experiment. For  $K_1$  constituent (Figure 6-1), the model overestimates the currents by about ~10 cm/s in the Labrador shelf region associated with the localized maxima for tidal elevations (Figure 5-2). Xing and Davies (1998) have reasoned that including stratification prognostically minimizes the local maxima, which are due to sharp changes in topography, due to the generation of internal tides.

**a) Comparison with observations**

The model generated tidal currents are compared with observations for the 5 leading semidiurnal and diurnal constituents. Table 6-2 lists the RMS errors for amplitude and phase and absolute and relative errors for the meridional and zonal components. There is no significant improvement of the model generated tidal currents from the Ba experiment except for localized improvement of absolute and relative errors. In the Newfoundland shelf the results are better than the Ba experiment with absolute errors for meridional and zonal components being 1.6 cm/s and 1.3 cm/s and 89.3% and 82.3% for the relative errors respectively.

Table 6-1. Statistics of model computed elevation for semi-diurnal and diurnal constituents compared with observations at Tide and Bottom Pressure Gauge Sites for the Diagnostic run with assimilation using multi-mission altimeter data.

Constituent	RMS Amplitude Difference (cm)	RMS Phase Difference (Degrees)	AbsErr (cm)	RelErr (%)
<b>Super Stations</b>				
M <sub>2</sub>	0.8	2.3	1.3	3.5
S <sub>2</sub>	2.0	6.4	1.8	14.0
N <sub>2</sub>	0.8	4.9	0.9	9.3
K <sub>1</sub>	1.6	5.6	1.3	19.9
O <sub>1</sub>	0.8	8.0	0.9	20.8
RSS	2.9		2.9	
<b>Coastal Island of Newfoundland</b>				
M <sub>2</sub>	1.8	2.7	2.3	5.3
S <sub>2</sub>	1.0	5.9	1.4	9.7
N <sub>2</sub>	1.1	5.2	1.1	12.6
K <sub>1</sub>	1.0	7.5	1.1	13.9
O <sub>1</sub>	0.7	5.9	0.8	11.6
RSS	2.6		3.2	
<b>Coastal Nova Scotia</b>				
M <sub>2</sub>	1.5	3.8	3.4	5.1
S <sub>2</sub>	2.3	10.4	2.6	18.1
N <sub>2</sub>	0.6	8.4	1.6	12.9
K <sub>1</sub>	1.6	7.7	1.4	22.9
O <sub>1</sub>	1.2	11.0	1.4	26.0
RSS	3.5		5.0	
<b>Labrador Sea &amp; Shelf</b>				
M <sub>2</sub>	0.9	1.6	1.3	2.8
S <sub>2</sub>	1.0	3.5	1.3	7.4
N <sub>2</sub>	0.4	1.5	0.4	4.1
K <sub>1</sub>	0.8	8.6	1.3	13.0
O <sub>1</sub>	0.5	2.5	0.4	6.6
RSS	1.6		2.3	

Table 6-1. (Continued)

<b>Constituent</b>	<b>RMS Amplitude</b>	<b>RMS Phase</b>	<b>AbsErr</b>	<b>RelErr</b>
	<b>Difference (cm)</b>	<b>Difference (Degrees)</b>	<b>(cm)</b>	<b>(%)</b>
<b>BoFGoM</b>				
<b>M<sub>2</sub></b>	<b>36.0</b>	<b>7.7</b>	<b>39.6</b>	<b>11.9</b>
<b>S<sub>2</sub></b>	<b>8.4</b>	<b>9.1</b>	<b>8.2</b>	<b>21.6</b>
<b>N<sub>2</sub></b>	<b>8.7</b>	<b>6.6</b>	<b>8.5</b>	<b>15.3</b>
<b>K<sub>1</sub></b>	<b>2.8</b>	<b>5.8</b>	<b>2.3</b>	<b>14.7</b>
<b>O<sub>1</sub></b>	<b>0.7</b>	<b>9.9</b>	<b>1.4</b>	<b>13.5</b>
<b>RSS</b>	<b>38.1</b>		<b>41.4</b>	
<b>Excluding BoFGoM</b>				
<b>M<sub>2</sub></b>	<b>1.3</b>	<b>2.6</b>	<b>2.1</b>	<b>4.2</b>
<b>S<sub>2</sub></b>	<b>1.6</b>	<b>6.5</b>	<b>1.8</b>	<b>12.3</b>
<b>N<sub>2</sub></b>	<b>0.7</b>	<b>5.0</b>	<b>1.0</b>	<b>9.7</b>
<b>K<sub>1</sub></b>	<b>1.2</b>	<b>7.4</b>	<b>1.3</b>	<b>17.4</b>
<b>O<sub>1</sub></b>	<b>0.8</b>	<b>6.9</b>	<b>0.9</b>	<b>16.3</b>
<b>RSS</b>	<b>2.6</b>		<b>3.3</b>	
<b>At all Locations</b>				
<b>M<sub>2</sub></b>	<b>8.2</b>	<b>3.6</b>	<b>9.6</b>	<b>5.7</b>
<b>S<sub>2</sub></b>	<b>2.9</b>	<b>7.0</b>	<b>3.0</b>	<b>14.2</b>
<b>N<sub>2</sub></b>	<b>2.3</b>	<b>5.3</b>	<b>2.5</b>	<b>10.8</b>
<b>K<sub>1</sub></b>	<b>1.5</b>	<b>7.0</b>	<b>1.5</b>	<b>16.9</b>
<b>O<sub>1</sub></b>	<b>0.8</b>	<b>7.5</b>	<b>1.0</b>	<b>15.7</b>
<b>RSS</b>	<b>9.2</b>		<b>10.5</b>	

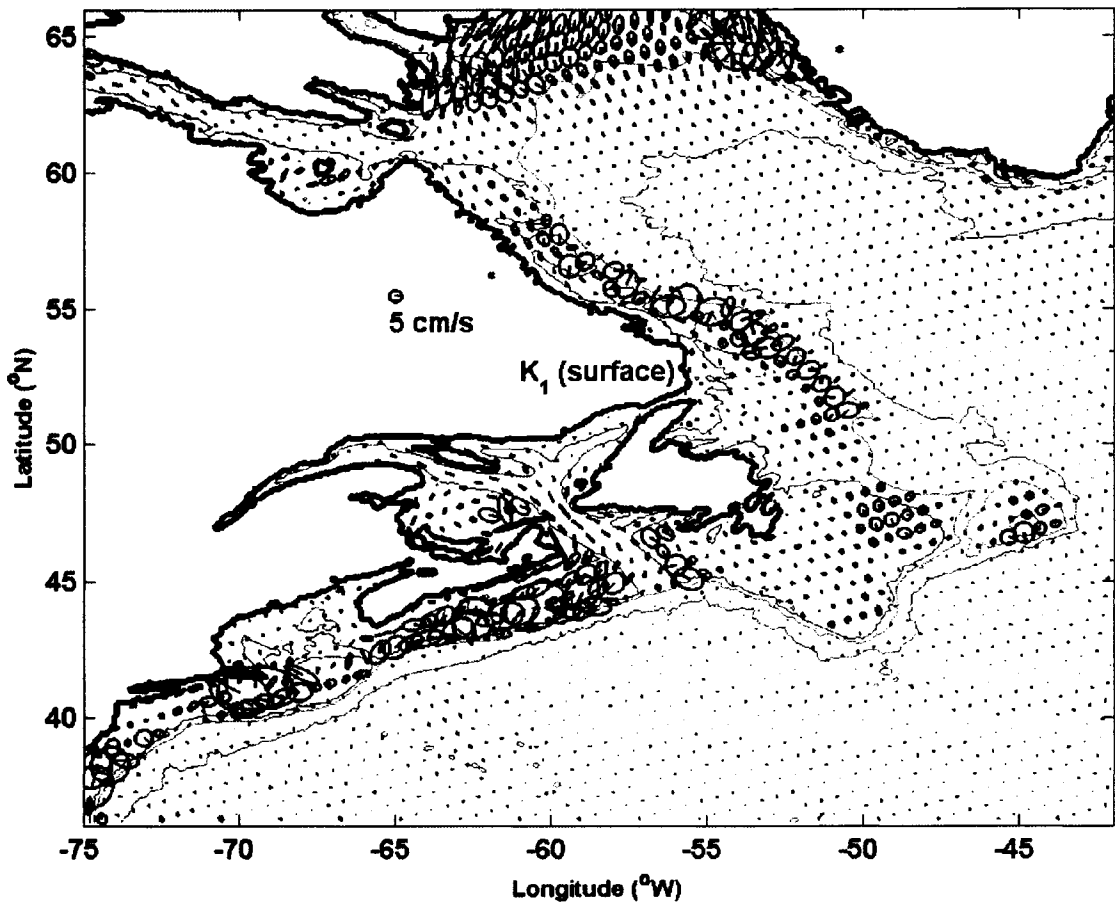


Figure 6-1. Sub-sampled  $K_1$  current ellipses at the surface, from Da run. The radial lines in ellipses indicate common time. The 200-, 1000- & 3000m isobaths are displayed in red, green and magenta colors respectively.

Table 6-2. Statistics of model computed currents for semi-diurnal and diurnal constituents compared with observations at moored current meter sites for six sub regions (a-f) of the model domain and the whole model domain (g) for the diagnostic run with assimilation (Da) using multi-mission altimeter data.

**a) Bay of Fundy & Gulf of Main**

Constituent	RMS U		RMS V		AbsErr U	RelErr U	AbsErr V	RelErr V
	Amp (cm/s)	Phase (Deg)	Amp (cm/s)	Phase (Deg)	(cm/s)	(%)	(cm/s)	(%)
M <sub>2</sub>	25.2	18.7	10.7	26.5	20.2	39.1	13.5	43.5
S <sub>2</sub>	3.6	53.7	1.6	33.9	4.0	58.1	1.7	46.7
N <sub>2</sub>	4.0	22.2	2.1	31.1	4.0	37.8	3.3	50.7
K <sub>1</sub>	0.4	51.2	0.3	43.6	0.8	76.2	0.6	69.5
O <sub>1</sub>	0.5	34.6	0.3	69.9	0.5	51.1	0.4	96.8

**b) Georges Bank**

Constituent	RMS U		RMS V		AbsErr U	RelErr U	AbsErr V	RelErr V
	Amp (cm/s)	Phase (Deg)	Amp (cm/s)	Phase (Deg)	(cm/s)	(%)	(cm/s)	(%)
M <sub>2</sub>	16.8	19.2	22.8	25.1	17.1	47.1	22.7	48.4
S <sub>2</sub>	2.6	36.7	3.3	52.1	3.7	63.5	5.8	68.3
N <sub>2</sub>	3.7	25.1	4.9	36.7	4.0	48.1	6.1	55.2
K <sub>1</sub>	1.7	67.5	2.8	29.0	1.9	65.2	2.3	51.2
O <sub>1</sub>	1.0	52.9	1.2	34.2	0.9	59.9	1.1	64.2

**c) Channel**

Constituent	RMS U		RMS V		AbsErr U	RelErr U	AbsErr V	RelErr V
	Amp (cm/s)	Phase (Deg)	Amp (cm/s)	Phase (Deg)	(cm/s)	(%)	(cm/s)	(%)
M <sub>2</sub>	13.8	31.4	13.2	34.3	12.0	66.8	12.6	50.1
S <sub>2</sub>	1.4	59.0	2.3	66.7	1.7	66.0	2.7	67.5
N <sub>2</sub>	2.7	40.6	3.5	31.6	2.8	61.5	3.2	51.6
K <sub>1</sub>	3.3	38.7	3.0	34.8	2.9	74.0	2.8	70.1
O <sub>1</sub>	1.9	38.8	1.5	46.1	1.7	60.6	1.5	62.0

**d) Labrador**

Constituent	RMS U	RMS U	RMS V	RMS V	AbsErr U	RelErr U	AbsErr V	RelErr V
	Amp (cm/s)	Phase (Deg)	Amp (cm/s)	Phase (Deg)	(cm/s)	(%)	(cm/s)	(%)
<b>M<sub>2</sub></b>	1.3	39.1	1.7	62.2	2.2	60.8	2.8	65.7
<b>S<sub>2</sub></b>	0.5	38.9	0.6	60.8	0.8	53.5	0.9	65.5
<b>N<sub>2</sub></b>	0.4	41.2	0.4	62.6	0.6	63.0	0.6	63.5
<b>K<sub>1</sub></b>	0.5	85.5	0.2	39.0	0.8	118.6	0.3	56.8
<b>O<sub>1</sub></b>	0.4	42.2	0.4	88.0	0.4	65.0	0.5	85.0

**e) Newfoundland & North Avalon Channel**

Constituent	RMS U	RMS U	RMS V	RMS V	AbsErr U	RelErr U	AbsErr V	RelErr V
	Amp (cm/s)	Phase (Deg)	Amp (cm/s)	Phase (Deg)	(cm/s)	(%)	(cm/s)	(%)
<b>M<sub>2</sub></b>	1.8	19.2	1.6	34.3	1.9	43.4	2.3	53.0
<b>S<sub>2</sub></b>	1.5	43.5	1.3	54.9	2.2	91.8	2.2	84.6
<b>N<sub>2</sub></b>	0.7	38.2	0.6	55.3	0.8	58.6	0.8	70.4
<b>K<sub>1</sub></b>	1.3	55.0	1.0	44.9	1.6	89.3	1.3	82.3
<b>O<sub>1</sub></b>	1.2	49.5	1.0	50.0	1.4	116.9	1.3	104.9

**f) Scotian Shelf**

Constituent	RMS U	RMS U	RMS V	RMS V	AbsErr U	RelErr U	AbsErr V	RelErr V
	Amp (cm/s)	Phase (Deg)	Amp (cm/s)	Phase (Deg)	(cm/s)	(%)	(cm/s)	(%)
<b>M<sub>2</sub></b>	11.5	27.4	6.6	42.1	9.8	49.9	7.1	60.0
<b>S<sub>2</sub></b>	2.8	49.3	1.6	52.2	3.0	68.2	2.1	65.8
<b>N<sub>2</sub></b>	3.1	31.0	2.0	48.4	2.8	66.5	2.1	71.5
<b>K<sub>1</sub></b>	3.5	34.4	2.2	56.2	3.4	66.3	2.5	89.7
<b>O<sub>1</sub></b>	3.5	34.4	2.2	56.2	3.4	66.3	2.5	89.7

**g) At all Locations**

Constituent	RMS U		RMS V		AbsErr U	RelErr U	AbsErr V	RelErr V
	Amp (cm/s)	Phase (Deg)	Amp (cm/s)	Phase (Deg)	(cm/s)	(%)	(cm/s)	(%)
<b>M<sub>2</sub></b>	10.6	26.7	8.0	40.1	9.4	51.2	8.4	57.1
<b>S<sub>2</sub></b>	2.3	46.9	1.7	53.7	2.7	65.3	2.4	67.4
<b>N<sub>2</sub></b>	2.6	33.0	2.1	47.3	2.5	62.1	2.3	66.5
<b>K<sub>1</sub></b>	2.8	44.0	2.1	48.2	2.8	72.4	2.2	80.2
<b>O<sub>1</sub></b>	2.4	36.4	1.6	57.8	2.2	65.7	1.8	80.5

**6.2.3. Vertical Structure of Model Tidal Currents**

In this section we make a close examination of the vertical structure of computed tidal currents at the same sites as the baseline experiment. We consider again, only M<sub>2</sub> current profiles for the same reason.

The vertical profiles of computed M<sub>2</sub> tidal currents (Figure 6-2) are shown at selected sites S01, S02 in the Scotian Shelf, NF01, and NF02 in the Newfoundland Shelf, GB01 and GB02 in the Georges Bank. The results from the Da (solid blue line) and Du (dashed green line) experiment are shown together. At the shallow (61m) site S01, M<sub>2</sub> tidal currents are relatively large, of the order of 100cm/s, and the turbulent viscous effects are strong with a sheared boundary layer extending from bottom to the surface. Stratification has reduced the currents by 2-3 cm/s in the bottom boundary layer for both the components with advancement in phase, consistent with observation near to the bottom. The Du experiment overestimates the currents by ~20 cm/s for both the components. At the S02, tidal currents are weaker and the vertical current shear exists in the lower water column and near the sea bottom. The phase of the meridional component is in good agreement near the bottom. The zonal and meridional component at depth is in good

agreement but is overestimated at mid-depth and underestimated at the surface. At the shallow sites NF01 (56m) and NF02 (64m), located in the Grand Banks region, the currents are 15-20cm/s. Stratification has important effects in the bottom boundary layer by generating a strong sheared layer, thereby reducing the currents significantly. Including stratification and assimilation has no significant advantage on the Newfoundland shelf. In the Georges Bank region, the currents are underestimated at GB01 for the u-component by 20 cm/s and are characterized by a strong vertical shear in the bottom boundary layer, where the currents are significantly reduced. The intermediate water depth location GB01 (200m) at the shelf break shows the  $M_2$  current velocities to be approximately reproduced in the middle and upper column and underestimated by 10 cm/s in the bottom boundary layer. Stratification has played a very important role in reducing the current magnitude by half as compared to the unstratified case.

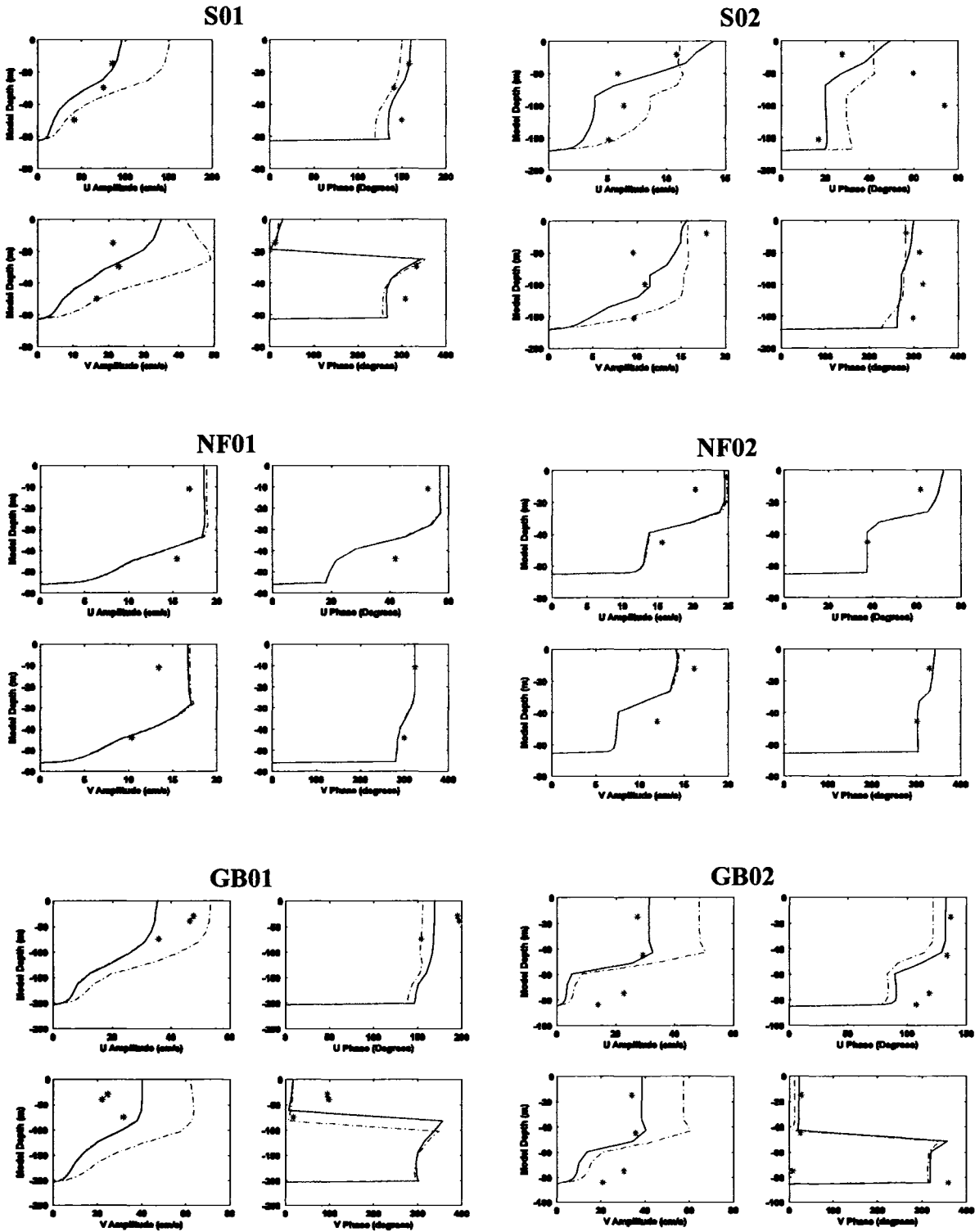


Figure 6-2. Computed vertical profiles of  $M_2$  currents at S01, S02, NF01, NF02, GB01 and GB02 for the Da Experiment (blue solid line) and Du experiment (green dashed line). The red asterisk (\*) are the observed values. The locations are shown in Figure 4-2.

## 7. Discussion and Summary

We simulated tides over the Northwest Atlantic region with a 3-D hydrodynamical, primitive equation model. Two basic configurations of the model were considered, one with homogeneous water and the second with a horizontally varying and vertically stratified fluid, representative of summer conditions, calculated diagnostically. For the Diagnostic calculations, the baroclinic pressure gradients were switched off to disallow baroclinic (internal) tides generated in the model solutions. Tidal forcing was introduced along open boundaries with eight leading constituents of the barotropic tide and depth-averaged currents of the similar constituents derived from a North Atlantic model. The influence of equilibrium, earth and load tides was incorporated into the model. Multi-mission altimeter data provided by Y. Yi and C.K Shum (PC, 2006) were assimilated into the model for the two configurations, using a simple nudging method with a nudging time period of 12.42 hrs ( $M_2$  tidal cycle) for the barotropic case and 1 day (24 hours – tidal cycle of the largest diurnal constituent  $K_1$ ) for the diagnostic case. The model does well in reproducing tidal elevations and currents for the eight leading constituents in the northwest Atlantic Ocean and assimilation of multi-mission altimeter data is the key to improving the results on tidal elevations and especially for tidal currents as is evident from the unassimilated (Bu) and assimilated (Ba & Da) runs.

Including a physically realistic horizontally and vertically varying diagnostic stratification profile has an influence upon tidally induced turbulence (Xing and Davies, 1996a; Han, 2000), in shallow waters if the thermocline coincides with a region of significant shear in the water column. However, in deep water where tidal currents are low and are only sheared in the near-bed layer, the tidally induced bottom boundary layer is close to the sea bed. And there is no significant level of turbulence in the region of the

thermocline to be suppressed by stratification effects. This is a different situation than one in which stratification evolves in a prognostic manner and internal waves with an associated shear can be produced.

## 7.1. Key Results

Preliminary calculations assuming a homogeneous sea show that the model can accurately reproduce  $M_2$ ,  $S_2$ ,  $N_2$ ,  $K_1$  and  $O_1$  tidal elevations in the region. An enhancement of the  $K_1$  and  $O_1$  tidal elevations and currents at the shelf edge in the Labrador shelf region is found in the model, qualitatively consistent with theory. However, the enhancement of diurnal tides, in particular tidal currents along the shelf edge, larger than found in the observations, with some regions of local enhancement that are not supported by observations. The calculations presented here suggest that the  $M_2$  barotropic tide can be adequately reproduced by the model, but that in any simulation of the internal tide, or shorter wavelengths, the cross-shelf grid resolutions would be refined. The  $M_2$  tidal currents dominate the tidal current variability over the northwest Atlantic, especially over the shallow shelves such as in the Scotian and Newfoundland shelf. Tidal rectification, because of resonance, is visible in the Bay of Fundy region. Strong currents reaching  $>1\text{m/s}$  are observed in the region. In the Georges Bank area, the  $M_2$  tidal currents are oriented perpendicularly.

For the stratification case, the specified time-invariant vertical stratification affects the tidal current profile only through suppressing turbulence. The diagnostic solutions indicate that the tidally induced turbulence in shallow waters is significantly reduced by a stable stratification where a sufficient density gradient coincides with a significant velocity shear in the vertical. This does not occur in the deep ocean where tidal currents

and bottom-generated turbulence is weak. Turbulence is substantially reduced in the bottom boundary layer and completely suppressed above it.

The tidal elevations are hardly influenced by the vertical stratification, but the tidal currents in shallow seas are sensitive to it. The stratification reduces the vertical current gradient in the upper and middle water column and significantly increases the gradient in the bottom boundary layer. Tidal current magnitude decreases in the log layer, increases substantially in the rest of the bottom boundary layer, and decreases above the boundary layer. The phase of the tidal currents is also subject to change, with a notable advance in the bottom boundary layer due to an increase in the frictional effect.

In the coastal zone, the tidal modeling system described here is capable of an accuracy of 2-3cm for  $M_2$  and  $<2$  cm for other constituents (outside of Gulf of Maine and Bay of Fundy). On the shelf and offshore the system is capable of an accuracy of  $<2$ cm per constituent. For Bay of Fundy and Gulf of Maine, the errors are of the order of 10 cm for  $M_2$ ,  $S_2$  &  $N_2$  and 1-3 cm for the other constituents.

The solutions in the northern part of the domain (Labrador Sea and Shelf) show prediction errors of 2.5 cm for all the constituents and  $<2$ cm for individual constituents.

The overall prediction error is of the order of 3cm for all the constituents (combined) excluding the Bay of Fundy and Gulf of Maine region. For individual constituents, the errors are about 2cm or less.

For all the locations, the prediction errors are 11.5 cm in AbsErr, for all the constituents. The model solutions in the Gulf of St. Lawrence are not analyzed, as the focus of attention is mainly on the shelf regions. With assimilation, all the semi-diurnal constituents reproduce the amphidromic point in the southern Gulf well.

The inclusion of major tidal constituents simultaneously accounted for the nonlinear effects through bottom friction and the advective momentum exchange among the major tidal constituents. Assimilating multi-mission altimeter data improves the prediction accuracy by 50 %. Further improving the prediction accuracy in the model domain, especially in the Bay of Fundy, will very likely require higher resolution, improved bathymetry and modeling of long-period tides ( $M_f$ ,  $M_m$ ,  $S_{sa}$ ).

The tidal current prediction error in terms of absolute error is the of the order of 5cm/s and 10 cm/s for the  $M_2$  constituent in the major Newfoundland and Scotian Shelf regions, respectively. The model gives the best results for the  $M_2$  constituent in the Georges Bank area where the relative error is  $\sim 30\%$ , considering that this region is the transition for resonant Bay of Fundy from the shelf region. The turbulence in the region is well represented leading to better prediction of currents. The model has underpredicted the strength of the  $M_2$  currents in the Bay of Fundy region, the absolute error being 21 cm/s and the relative error being 44 %. Overall the prediction errors for  $M_2$  currents are 10 cm/s, with RMS errors being 8.3 cm/s and phase error of 34.7 deg. For all the other constituents the absolute errors are of the order of 3-4 cm/s, with RMS amplitude difference errors of 2-2.8 cm/s and 44-59 degrees for phase.

Our goal of prediction error for  $M_2$  currents of 30-50% is achieved, though there is much scope for improvement. Assimilating multi-mission altimeter data has reduced the prediction errors by about 30%. One of the reasons for the large prediction errors could be the uncertainty about the accuracy of the depth-averaged currents employed at the open boundaries.

Including stratification (diagnostically) has had not much effect on the improvement of the prediction of diurnal currents. Prognostic calculation of currents may solve the problem of local enhancement of diurnal currents, especially in the Labrador shelf region.

## **7.2. Future Work**

There are several avenues for improvements to the modeling system. A more extensive study of the sensitivity of the model solutions to bottom friction and viscous terms will help in improving the results, especially the tidal currents. A high resolution ( $1/24 \times 1/24$  degree) and improved bathymetry would help in resolving the small scale localized effects of strong topographic features. In addition, increasing the number of vertical layers, assimilating observed tidal elevation and current data and using a curvilinear orthogonal grid would help in generating and predicting near accurate tidal currents.

Study of baroclinic currents will help in understanding the complete tidal regime in the shelf areas, in particular. A reduction in the amplitude of the diurnal currents especially at the shelf edge can be achieved by removing the areas of spurious local intensification, by including the baroclinic effects.

## References

- Anderson, O. B., 1994: Ocean tides in the northern North Atlantic and adjacent seas from ERS-1 altimetry. *J. Geophys. Res.*, 99, 22 557-22 573.
- Anonymous 1996: A collection of global ocean tide models. Pasadena, CA, United States. Jet Propulsion Laboratory Physical Oceanography Distributed Active Archive Center. CD-ROM.
- Blumberg, A.F., Mellor, G.L., 1987: A description of a three-dimensional coastal ocean circulation model. In:Heaps, N.S (Ed.), *Three-Dimensional Coastal Ocean Models* vol. 4 American Geophysical Union, Washington , DC, pp. 1-16.
- Brown , W. S. and J. A. Moody, 1987: Tides. Georges Bank, R. H. Backus and D. W. Bourne, Eds., The MIT Press, 100-107.
- Cartwright, D.E. 1978: Ocean tides. *Int. Hydrogr. Rev.*, Monaco, 60(2), 35-84.
- Cartwright, D.E., and R. D. Ray, 1990: Oceanic tides from Geosat altimetry. *J. Geophys. Res.*, 95, 3069-3090.
- Cartwright, D.E. 1993: Theory of ocean tides with application to altimetry. In *Satellite Altimetry in Geodesy & Oceanography*, pp 99-141. Springer-Verlag, Berlin/New York.
- Cartwright, D.E. 1997: Some thoughts on the spring-neap cycle of tidal dissipation. *Prog. Oceanogr.* 40, 125-133.
- Chandler, P. C. P, S. de Margerie, and J. D. Covill, 1985: Numerical modeling of tides in Hudson Strait and Ungava Bay. *Can. Contract. Rep. Hydrogr. Ocean Sci.*, No. 13, 60pp.
- Cherniawsky, J., M. G. G. Foreman, W. R. Crawford, and R. F. Henry, 2001: Ocean tides from Topex/Poseidon sea level data. *J. Atmos. Oceanic Tech.*, 18, 649–664.
- Craig, P. D., 1988: A numerical study of internal tides on the Australian North West Shelf. *J. Mar. Res.*, 46, 59-76.
- Cummins, P.F., and L.-Y. Oey, 1997: Simulation of barotropic and baroclinic tides off Northern British Columbia. *J. Phys. Oceanogr.*, 27, 762-781.
- Davies, A. M., and J. E. Jones, 1992: A three-dimensional model of the M2, S2, N2, K1 and O1 tides in the Celtic and Irish Seas. *Prog. Oceanogr.*, 29, 197-234.
- de Margerie, S., and K. Lank, 1986: Tidal circulation of the Scotian Shelf and Grand Banks. Tech. rep., Contract Rep. 08SC.FD901-5-X515, Dept. Fish. and Oceans, Ottawa, Ontario, Canada.

- Derber, J., and A. Rosati, 1989: A global oceanic data assimilative system. *J. Phys. Oceanogr.*, 19, 1333-1347.
- de Young, B., and C. L. Tang, 1990: Storm-forced baroclinic near-inertial currents on the Grand Bank. *J. Phys. Oceanogr.*, 20, 1725-1741.
- Drozdowski, A., C. G. Hannah, and J.W. Loder, 2002: The Northwest Atlantic tidal current database. Tech. rep., BIO, Department of Fisheries and Oceans, Bedford Institute of Oceanography, P.O. Box 1006, Dartmouth, NS, Canada, B2Y-4A2.
- Dupont, F., C. G. Hannah, D. A. Greenberg, J. Y. Cherniawsky and C. E. Naime. 2002: Modelling System for Tides. Can. Tech. Rep. Hydrogr. Ocean Sci. 221: vii + 72 pp.
- Easton, A. K, 1972: Tides of Hudson Strait. Bedford Institute Oceanogr. Rep. Ser., BI-R-72-6, 14pp.
- Egbert, G. D., A. F. Bennet, and M. G. G. Foreman, 1994: TOPEX/Poseidon tides estimated using a global inverse model. *J. Geophys. Res.*, 99, 24 821–24 852.
- Egbert, G. D., and S. Erofeeva, 2002: Efficient inverse modeling of barotropic ocean tides. *J. Atmos Oceanic Tech.*, 19, 183–204.
- Egbert, G. D., and S. Erofeeva, 2002: Efficient inverse modelling of barotropic Ocean tides. *J. Atmos Oceanic Tech.*, 19, 183-204.
- Farell, W. E. 1972: Deformation of the Earth by surface loads. *Review of Geophysics and Space Physics*, 10, 761-797.
- Flather, R. A., 1987: A tidal model of the northeast Pacific. *Atmos-Ocean*, 25, 22-45.
- Foreman, M. M. G., 1977: Manual for tidal heights analysis and prediction. Tech. Rep.77-10, Pacific Marine Science, Institute of Ocean Sciences, Patricia Bay.
- Foreman, M.G. G., Henry, R. F., Walters, R. A., Ballantyne, V. A., 1993: A finite element model for tides and resonance along the north coast of British Columbia. *J. Geophys. Res.*, 98, 2509-2531.
- Foreman, M. G. G., W. E. Crawford, and R.F. Marsden, 1995: De-tiding: Theory and practice. *Quantitative Skill assessment for Coastal Ocean Models*, Vol. 47, Coastal and Estuarine Studies, Amer. Geophys. Union, 203-239.
- Foreman, M. G. G., W. E. Crawford, J. Y. Cherniawsky, R. F. Henry, and M. R. Tarbotton, 2000: A high-resolution assimilating tidal model for the Northeast Pacific Ocean. *J. Geophys. Res.*, 105, 28 629–28 651.
- Francis, O., and P. Mazegga, 1990: Global charts of ocean tide loading effects. *J. Geophys. Res.*, 95, 11411-11424.

- Fu, L. L., E. J. Christensen, C. A. Yamarone Jr., M. Lefebvre, Y. Menard, M. Dorrer, and P. Escuder, 1994: TOPEX/Poseidon mission overview. *J. Geophys. Res.*, 99, 24369-24381.
- Galerpin, B., L. H. Kantha, S. Hassid, and A. Rosati, 1988: A quasi-equilibrium turbulent energy model for geophysical flows. *J. Atmos. Sci.*, 45, 55-62.
- Gelb, A., (ED.), 1988: *Applied Optimal Estimation*. MIT Press, Cambridge, MA., 374 pp.
- Geshelin, Y., J. Sheng, and R.J. Greatbatch, 1999: Monthly mean climatologies of temperature and salinity in the western North Atlantic. *Can. Tech. Rep. Hydrogr. Ocean Sci.*, 153, 62pp.
- Godin, G., 1980: *Cotidal charts for Canada*. Mar. Sci. Dir., Manuscr. Rep. Ser., 55, 93pp., Dept. Fish. And Oceans, Ottawa, Ontario, Canada.
- Greenberg, D. A., 1983: Modeling the mean barotropic circulation in the Bay of Fundy and Gulf of Maine. *J. phys. Oceanogr.*, 13, 886-904.
- Greenberg, D. A., J. W. Loder, Y. Shen, D. R. Lynch, and C. E. Naimie 1997: Spatial and temporal structure of the barotropic response of the Scotian Shelf and Gulf of Maine to surface wind stress. *J. Geophys. Res.*, 102, 20897-20915.
- Griffin, D. A. and K. R. Thompson, 1996: The adjoint method of data assimilation used operationally for shelf circulation. *J. Geophys. Res.*, 101, 3457-3477.
- Han, G., M. Ikeda, P. C. Smith, 1993: Annual variation of sea-surface slopes over the Scotian Shelf and Grand Banks from Geosat altimetry. *Atmos-Ocean*, 31(4), 591-615.
- Han, G., and M. Ikeda, 1995: Dynamical interpolation of tidal constituents derived from altimeter data. *The Abstracts of the XXI General assembly of the International association for the Physical Sciences of the Oceans*, Honolulu, Hawaii.
- Han, G., M. Ikeda, P. C. Smith, 1996: Oceanic tides over the Newfoundland and Scotian Shelves from Topex/POSEIDON altimetry, *Atmos-Ocean*, 34, 589-604.
- Han, G., C. G. Hannah, J. W. Loder and P. C. Smith, 1997: Seasonal variation of three-dimensional mean circulation over the Scotian Shelf. *J. Geophys. Res.*, 102, 1011-1025.
- Han, G., 2000: Three-dimensional modeling of tidal currents and mixing quantities over the Newfoundland Shelf, *J. Geophys. Res.*, 105, 11407-11422.
- Han, G., R. Hendry, and M. Ikeda, 2000: Assimilating Topex/Poseidon derived tides in a primitive equation model over the Newfoundland Shelf. *Contin. Shelf Res.*, 20, 84-108.

Han, G., and J. Loder, 2002: Modeling tidal currents and seasonal-mean circulation in the Scotian Gully region. Submitted to the Proceedings of the 7th International Conference on Estuarine and Coastal, ASCE.

Han, G., and J.W. Loder, 2003: Three-dimensional seasonal-mean circulation and hydrography on the eastern Scotian Shelf, *J. Geophys. Res.*, 108(C5), 1-21.

Hannah, C. G., J. W. Loder, and D. G. Wright, 1996: Seasonal variation of the baroclinic circulation in the Scotia-Maine region. *Buoyancy Effects on Coastal and Estuarine dynamics*, D. G. Aubrey and C. T. Friedrichs, Eds., Amer. Geophys. Union, 7-29.

Hannah, C. G., J. Shore, J. W. Loder, and C. E. Naimie, 2001: Seasonal circulation on the western and central Scotian Shelf. *J. Phys. Oceanogr.*, 31, 591-615.

Holloway, P.E., 1996: A numerical model of internal tides with application to the Australian north west shelf, *J. Phys. Oceanogr.*, 26, 21-37.

Kantha, K.H., 1995: Barotropic tides in the global oceans from nonlinear tidal model assimilating altimetric tides 1: Model description and results. *J. Geophys. Res.*, 100, 25283-25308.

Kantha, K.H., and C.A. Clayson, 2000: *Numerical Models of Oceans and Oceanic Processes*. Academic Press, San Diego. 940 pp.

Koblinsky, C. J., R. Ray, B. D. Beckley, Y.-M. Wang, L. Tsaoussi, A. Brenner, and R. Williamson, 1998: NASA Ocean Pathfinder Project, Report 1: Data processing handbook. Tech. Rep. NASA/TP-1998-208605, NASA, GSFC, Greenbelt, Maryland.

le Provost, C., F. Lyard, J. M. Molines, M. L. Genco, and F. Rabilloud, 1998: A hydrodynamic ocean tide model improved by assimilating a satellite altimeter-derived data set. *J. Geophys. Res.*, 103, 5513-5529.

Loder, J. W., B. Petrie, and G. Gawarkiewicz, 1998: The coastal ocean off northeastern North America: A large scale view. Ch. 5 In: *The Global coastal Ocean: Regional Studies and Synthesis*. The Sea, Vol. 11, K. H. Brink and A. R. Robinson (eds.), John Wiley and Sons, Inc., 105-133.

Lu, Y., K. R. Thompson, and D. G. Wright, 2001: Tidal currents and mixing in the Gulf of St. Lawrence: An application of the incremental approach to data assimilation. *Can. J. Fish. Aquat. Sci.*, 58, 723-735.

Lynch, D. R., D. A. Greenberg, and J. W. Loder, 1992: Diagnostic model for baroclinic, wind-driven and tidal circulation in shallow seas. *Cont. Shelf Res.*, 12(1), 37-64.

Lynch, D. R., and C. E. Naimie, 1993: The M2 tide and its residual on the outer banks of the Gulf of Maine. *J. Phys. Oceanogr.*, 23, 2222-2253.

- Lynch, D. R., C. E. Naimie, and C. G. Hannah, 1998: Hindcasting the Georges Bank circulation, Part I: Detiding. *Cont. Shelf Res.*, 18, 607–639.
- Ma, X. C., C. K. Shum, R. J. Eanes, and B. D. Tapley, 1994: Determination of the ocean tides from the first year of TOPEX/Poseidon altimeter measurements. *J. Geophys. Res.*, 99, 24809- 24820.
- Madala, R. V., and S. A. Piacsek, 1977: A semi-implicit numerical model for baroclinic oceans, *J. Comput. Phys.*, 23, 167-178.
- Matsumoto, K., M. Ooe, T. Sato, and J. Segawa, 1995: Ocean tide model obtained from TOPEX/Poseidon altimetry data. *J. Geophys. Res.* 100, C12, 25 319-25 330.
- Matsuyama, M., 1985: Numerical experiments of internal tides in Suruga Bay, *J. Oceanogr. Soc. Japan*, 41, 145-156.
- Mazegga, P., and M. Berge. 1994: Ocean tides in the Asian semienclosed seas from TOPEX/Poseidon. *J. Geophys. Res.*, 99, 24867-24881.
- Mellor, G. L., and T. Yamada, 1974: A hierarchy of turbulence closure models for planetary boundary layers. *J. Atmos. Sci.*, 31, 1791-1806.
- Mellor, G. L., and T. Yamada, 1982: Development of a turbulence closure model for geophysical fluid problems. *Rev. Geophys.*, 20, 851-875.
- Mellor, G. L, T. Ezer, and L. -Y. Oey, 1994: The pressure gradient conundrum of sigma coordinate ocean models. *J. Atmos. Ocean. Tech.*, 11, 1126-1134.
- Moody, J., B. Butman, R. C. Beardsley, W. S. Brown, P. Daifuku, J. D. Irish, D.A Mayer, H. O. Mofjeld, B. Petrie, S. Ramp, P. Smith and W. R. Wright, 1984: Atlas of tidal elevation and current observations on the Northeast American Continental Shelf and Slope. *U.S. Geol. Surv. Bull.*, 1611, 122 pp.
- Oey, L. -Y, G. L. Mellor, and R. I Hires, 1985a: A three-dimensional simulation of the Hudson-Raitan estuary. Part I: Description of the model and model simulations. *J. Phys. Oceanogr.*, 15, 1676-1692.
- Oey, L. -Y, G. L. Mellor, and R. I Hires, 1985b: A three-dimensional simulation of the Hudson-Raitan estuary. Part I: Comparison with observations. *J. Phys. Oceanogr.*, 15, 1693-1709.
- Osborn, T. R., P. H. LeBlond, and D. O. Hodgins., 1978: Analysis of ocean currents, Davis Strait, 1977. Vols. I and II, APOA Rep. 138., Arctic Petroleum Operators Association, Calgary, Alta.
- Pawlowicz, R., B. Beardsley, and S. Lentz, 2002: "Classical Tidal "Harmonic Analysis including Error Estimates in MATLAB using T\_TIDE", *Computers and Geosciences*.

- Petrie, B Lank, K. D., de Margerie, S., 1987: Tides on the Newfoundland Grand Banks, *Atmos-Ocean*, 25, 10-21.
- Ray, R., 1998: Ocean self-attraction and loading in numerical tidal models. *Marine Geodesy*, 21, 181-192.
- Saucier, F., and J. Chass'e, 2000: Tidal circulation and buoyancy effects in the St. Lawrence Estuary. *Atmosphere-Ocean*, 38, 1-52.
- Schwiderski, E. W., 1980a: On charting global ocean tides. *Rev. of Geophys.*, 18, 243-268.
- Schwiderski, E. W., 1980b: Ocean tides. I. Global ocean tidal equations. *Marine Geodesy*, 3, 161-217.
- Schwing, F. B., 1992: Subtidal response of Scotian Shelf circulation to local and remote forcing. Part I: Observations. *J. Phys. Oceanogr.*, 22, 523-541.
- Sheng, J., and K. R. Thompson, 1996: A robust method for diagnosing regional shelf circulation from density profiles. *J. Geophys. Res.*, 101, 25647- 25659.
- Sherwin, T. J., and N. K. Taylor, 1990: Numerical investigation of internal tide generation in the Rockall Trough, *Deep-Sea Res.*, 37, 1595-1618.
- Simons, T. J., 1974: Verification of numerical models of Lake Ontario. Part I, circulation in spring and early summer, *J. Phys. Oceanogr.*, 4, 507-523.
- Smagorinsky, J., S. Manabe, and J. L. Holloway, 1965: Numerical results from a nine-level general circulation model of the atmosphere. *Mon. Weather Rev.*, 93, 727-768.
- Sutcliffe, W. H., R. H. Loucks, and K. F. Drinkwater, 1976: Coastal circulation and physical oceanography of the Scotian Shelf and Gulf of Maine. *J. Fish. Res. Board Can.*, 33, 98-115.
- Tee, K. T., P. C. Smith, and D. Lefaivre, 1993: Topographic upwelling off southwest Nova Scotia. *J. Phys. Oceanogr.*, 1703-1726.
- Thacker, W. C., and R. B. Long, 1987: Fitting dynamics to data. *J. Geophys. Res.*, 93, 1227-1240.
- Wahr, J.M., 1981: Body tides on an elliptical, rotating, elastic and oceanless earth. *Geophysical Journal of Research of the Astronomical Society*, 64, 677-703.
- Wang, D. P., 1989: Mean of mean and tidal flows in the Strait of Gibraltar. *Deep-Sea Res.*, 36, 1535-1548.

White, W.B., Tai, C.K., Holland, W.R., 1990: Continuous assimilation of simulated Geosat sea level into an eddy-resolving numerical ocean model, 1, Sea level differences. *J. Geophys. Res.*, 95, 3219-3234.

Woodworth, P. L., and J. P. Thomas, 1990: Determination of the major semidiurnal tides of the northwest European continental shelf from Geosat altimetry. *J. Geophys. Res.*, 95, 3061-3068.

Wright, D. G., J. Lazier, and W. Armstrong, 1988: Moored current and pressure data from the Labrador/Newfoundland Shelf, June 1985-1987. *Can. Data Rep. Hydrogr. Ocean Sci.*, No. 62, x + 258 pp.

Wright, D. G., J. Lazier, and M.J. Graca, 1991: Current meter and pressure data between Hamilton Bank and OWS Bravo, July 1997-August 1998. *Can. Data Rep. Hydrogr. Ocean Sci.*, No. 96, vii + 101 pp.

Xing, J., and A. M. Davies, 1998: Influence of stratification upon diurnal currents in shelf edge regions. *J. Phys. Oceanogr.*, 28, 1803-1831.

Xu, Z., 1998: A direct inverse method for inferring open boundary conditions of a finite element linear harmonic ocean circulation model. *J. Atmos. Oceanic Tech.*, 15, 1379-1399.

Xu, Z., R. Hendry, and J. Loder, 2001: Application of a direct inverse data assimilation method to the M2 tide on the Newfoundland and southern Labrador Shelves. *J. Atmos. Oceanic Tech.*, 18, 665-690.

## Appendix

### A. Names and locations of Tide and Bottom Pressure Gauges

This sections lists locations (longitude and latitude) of the tide and bottom pressure gauges, with the assigned station numbers that are used for station by station comparison collected from various sources, as described in §2-1.

Table A-1. List of Tide and Bottom pressure gauge locations including the length of the record used for comparing the model elevation solutions.

Station Name	St. No	No of of Days	Longitude	Latitude
<b>Coastal Nova Scotia</b>				
'FLAT ISLAND'	SS-1	29	-66	43.5
'SEAL ISLAND'	SS-2	44	-66	43.48
'LOCKEPORT'	SS-3	29	-65.11	43.7
'HALIFAX'	SS-4	365	-63.45	44.55
'SABLE ISLAND'	SS-5	47	-59.8	43.96
'LA POINTE'	SS-6	29	-61.05	46.6
'LOUISBOURG'	SS-7	146	-59.96	45.87
'NORTH SYDNEY'	SS-8	362	-60.2	46.35
'ST. PAUL ISLAND'	SS-9	369	-60.15	47.2
<b>BoFGoM</b>				
'OUTER WOOD ISLAND'	BG-1	29	-66.8	44.6
'SEAL COVE'	BG-2	52	-66.85	44.65
'GANNET ROCK'	BG-3	125	-66.78	44.51
'SAINT JOHN'	BG-4	365	-66.06	45.2
'ST. MARTINS'	BG-5	29	-65.53	45.35
'CAPE ENRAGE'	BG-6	29	-64.78	45.6
'CAPE CAPSTAN'	BG-7	29	-64.85	45.46
'WEST ADVOCATE'	BG-8	29	-64.81	45.35
'CAPE D OR'	BG-9	197	-64.76	45.28
'ILE HAUTE'	BG-10	90	-64.96	45.25
'MARGRETSVILLE'	BG-11	62	-65.06	45.05
'CENTREVILLE'	BG-12	113	-66.03	44.55
'SANDY COVE'	BG-13	79	-66.1	44.5
'EAST SANDY COVE'	BG-14	55	-66.08	44.48

'TIVERTON'	BG-15	29	-66.21	44.38
'TIVERTON (BOAR'S HD)'	BG-16	31	-66.21	44.4
'WEST NARROWS'	BG-17	81	-66.21	44.4
'WESTPORT'	BG-18	87	-66.35	44.26
'LIGHTHOUSE COVE'	BG-19	29	-66.4	44.25
'PORT MAITLAND'	BG-20	29	-66.15	43.98
<b>Coastal Island of Newfoundland</b>				
'GRAND BAY'	NF-1	49	-59.36	47.53
'PORT AUX BASQUES'	NF-2	362	-59.15	47.58
'ISLE AUX MORTS'	NF-3	40	-58.96	47.56
'PUSHTHROUGH'	NF-4	29	-56.17	47.58
'HERMITAGE'	NF-5	29	-55.92	47.45
'HARBOUR BRETON'	NF-6	29	-55.83	47.42
'BELLEORAM'	NF-7	33	-55.41	47.53
'TACKS BEACH'	NF-8	29	-54.2	47.58
'ARGENTIA'	NF-9	362	-53.98	47.3
'LANCE COVE'	NF-10	76	-52.83	47.08
'GULL ISLAND'	NF-11	83	-52.78	47.26
'MIDDLE COVE'	NF-12	68	-52.7	47.66
'Longpond- Nfld.'	NF-13	37	-53	47.6
'BONAVISTA- NFLD'	NF-14	66	-53.11	48.73
'Fogo Hbr (Seal Cove)'	NF-15	61	-54.28	49.73
'Twillingate- Nfld.'	NF-16	128	-54.76	49.65
'Bridgeport NF'	NF-17	143	-54.88	49.55
'SOP S ISLAND'	NF-18	29	-56.76	49.83
'ST. ANTHONY'	NF-19	119	-55.54	51.3
'SHIP COVE'	NF-20	110	-55.63	51.63
'SAVAGE COVE'	NF-21	343	-56.7	51.33
'FLOWERS COVE'	NF-22	54	-56.73	51.3
'PORT SAUNDERS'	NF-23	29	-57.3	50.65
'LARK HARBOUR'	NF-24	369	-58.36	49.2
'FOX ISLAND'	NF-25	29	-58.75	48.75
'PORT HARMON'	NF-26	60	-58.53	48.51
<b>Labrador Shelf &amp; Sea</b>				
	836	194	-55.46	53.74
	837	1000	-54.01	55.08
	838	2500	-53.76	55.35
	840	3560	-51.65	56.96
	697	203	-60.31	56.55

	802	201	-60.33	56.54
	696	174	-59.26	56.95
	803	157	-59.3	56.94
	695	570	-58.96	57.05
	804	570	-58.95	57.03
	795	200	-55.44	54.46
	691	109	-55.74	53.63
	793	80	-55.83	53.63
	789	200	-55.45	53.73
	692	145	-55.18	53.84
	794	153	-55.18	53.84
	693	200	-53.61	53.73
	792	200	-53.62	53.73
	694	600	-52.85	54.01
	791	1007	-52.13	54.03
	790	2480	-52.13	54.17
	796	360	-52.99	51.67
<b>Super Stations</b>				
St. John's	ST-1		-52.7	47.57
2	ST-2		-56.16	46.8
3	ST-3		-60.22	45.7
4	ST-4		-62.62	44.79
5	ST-5		-61	45.33
6	ST-6		-65.11	43.7
7	ST-7		-51.5	47
8	ST-8	146	-48.85	46.77
9 (Hibernia)	ST-9	171	-50.5	45.33
10	ST-10	122	-51	48.95
11	ST-11	174	-48.27	48.03
12	ST-12	173	-47.38	46.27
13	ST-13	171	-49.02	44.67
14	ST-14	199	-54.48	45
15	ST-15	166	-63.06	44.55
16	ST-16		-62.86	44.15
17	ST-17		-62.74	43.95
18	ST-18		-63.25	44.36
19	ST-19		-62.52	44.6
20	ST-20		-61.86	44.79

21	ST-21		-57.68	44.58
22	ST-22		-63.2	42.82
23	ST-23		-63.98	42.78
24	ST-24		-64.37	42.62

### B. Station by Station Comparison

The model domain under study is divided into 5 different regions (Super stations, Coastal Island of Newfoundland, Coastal Nova Scotia, Labrador Sea and Shelf and Bay of Fundy & Gulf of Maine). This section lists the detailed locations of each region separately with station numbers used for comparing the model solutions.

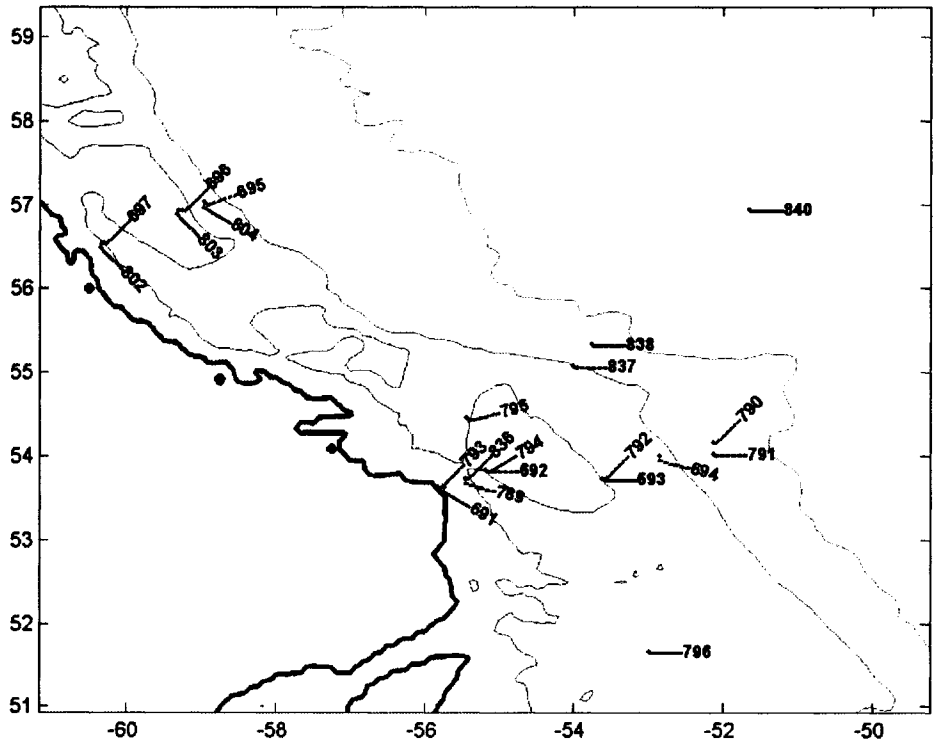


Figure B-1. Location of assigned Station Numbers of Bottom Pressure gauges in the Labrador Sea & Shelf

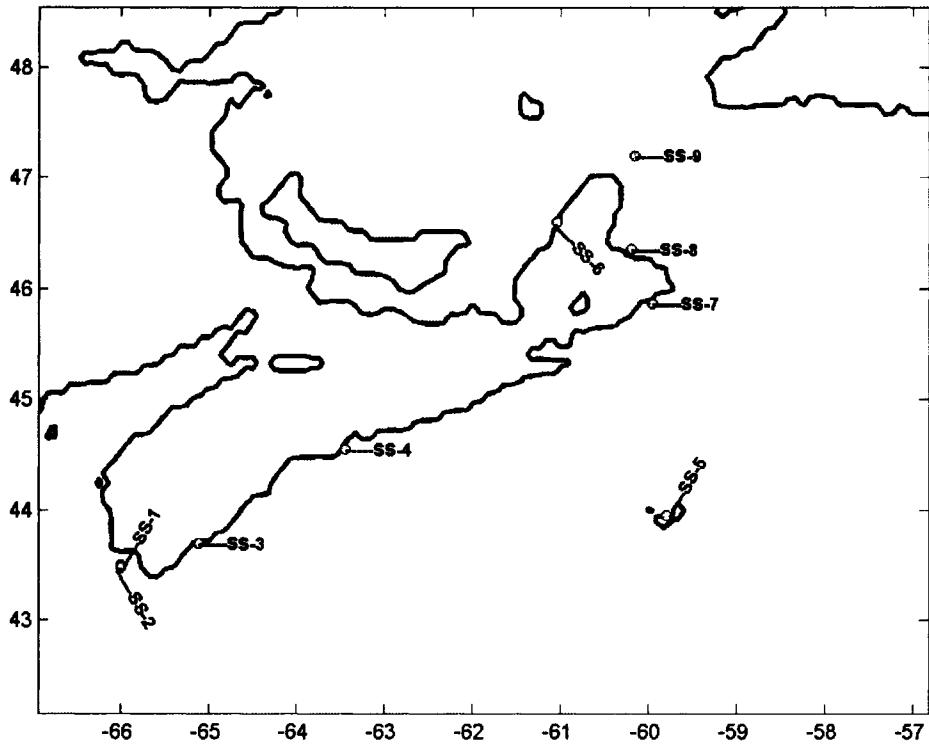


Figure B-2. Location of assigned Station Numbers of tide gauges in the Coastal Nova Scotia

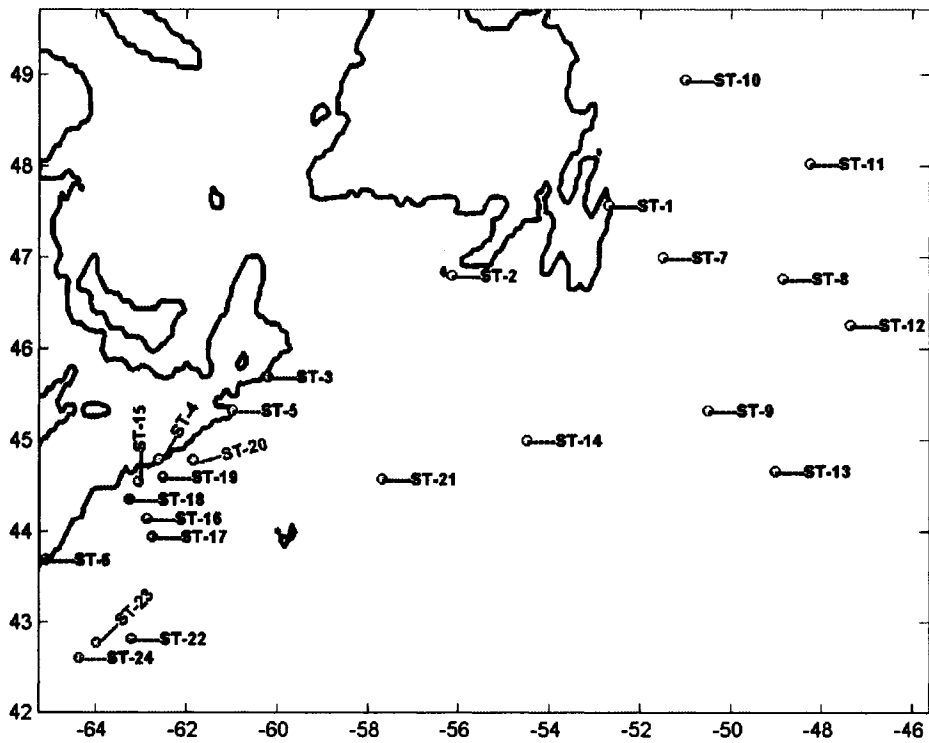


Figure B-3. Location of assigned Station Numbers of tide and bottom pressure gauges in the Super Stations.

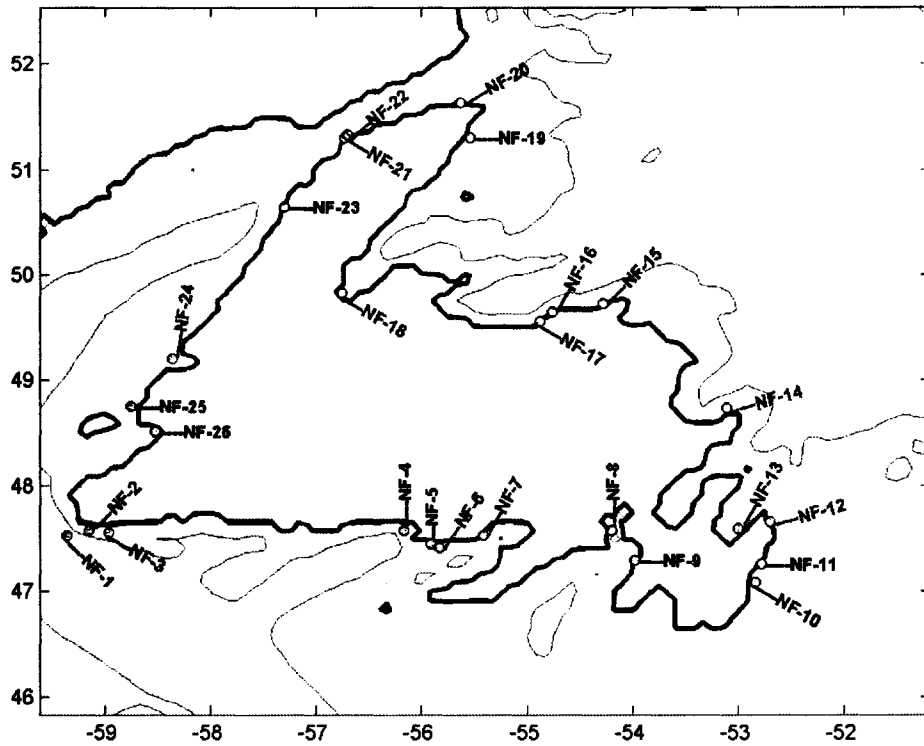


Figure B-4. Location of assigned Station Numbers of tide gauges in the Coastal Island of Newfoundland

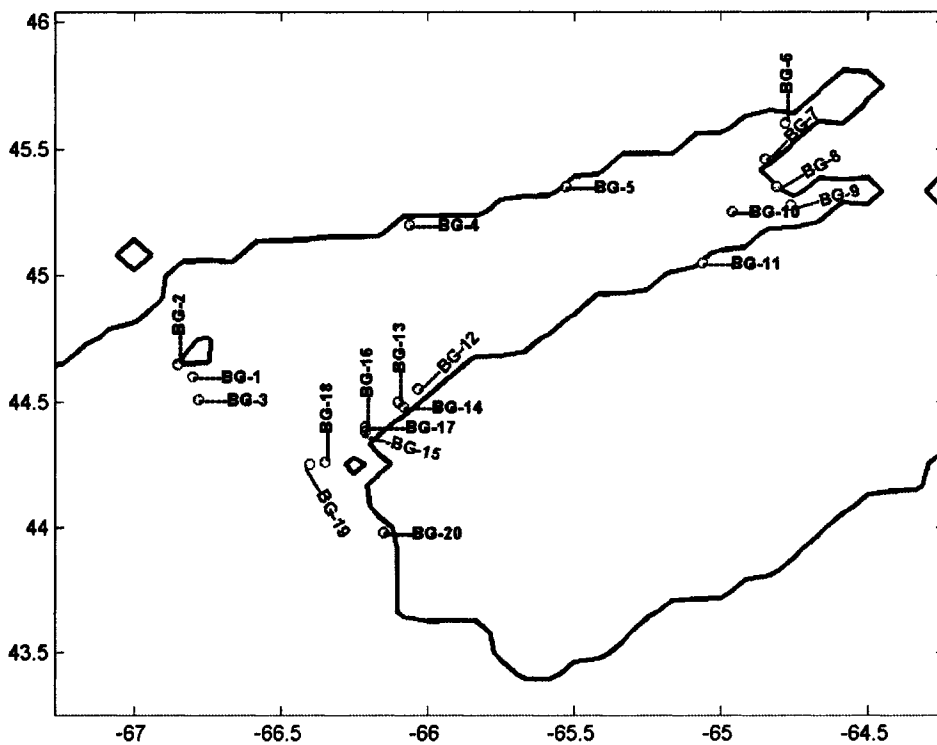


Figure B-5. Location of assigned Station Numbers of tide gauges in the Bay of Fundy & Gulf of Maine

### **C. Co-range and Co-phase charts of Equilibrium, Earth & Load Tides**

In this section, the co-range and co-phase charts of the 5 major semidiurnal ( $M_2$ ,  $S_2$  &  $N_2$ ) and diurnal ( $K_1$  &  $O_1$ ) constituents for the equilibrium, earth and load tides are presented, that have been incorporated into the model. The method for calculating them is described in §2.7.

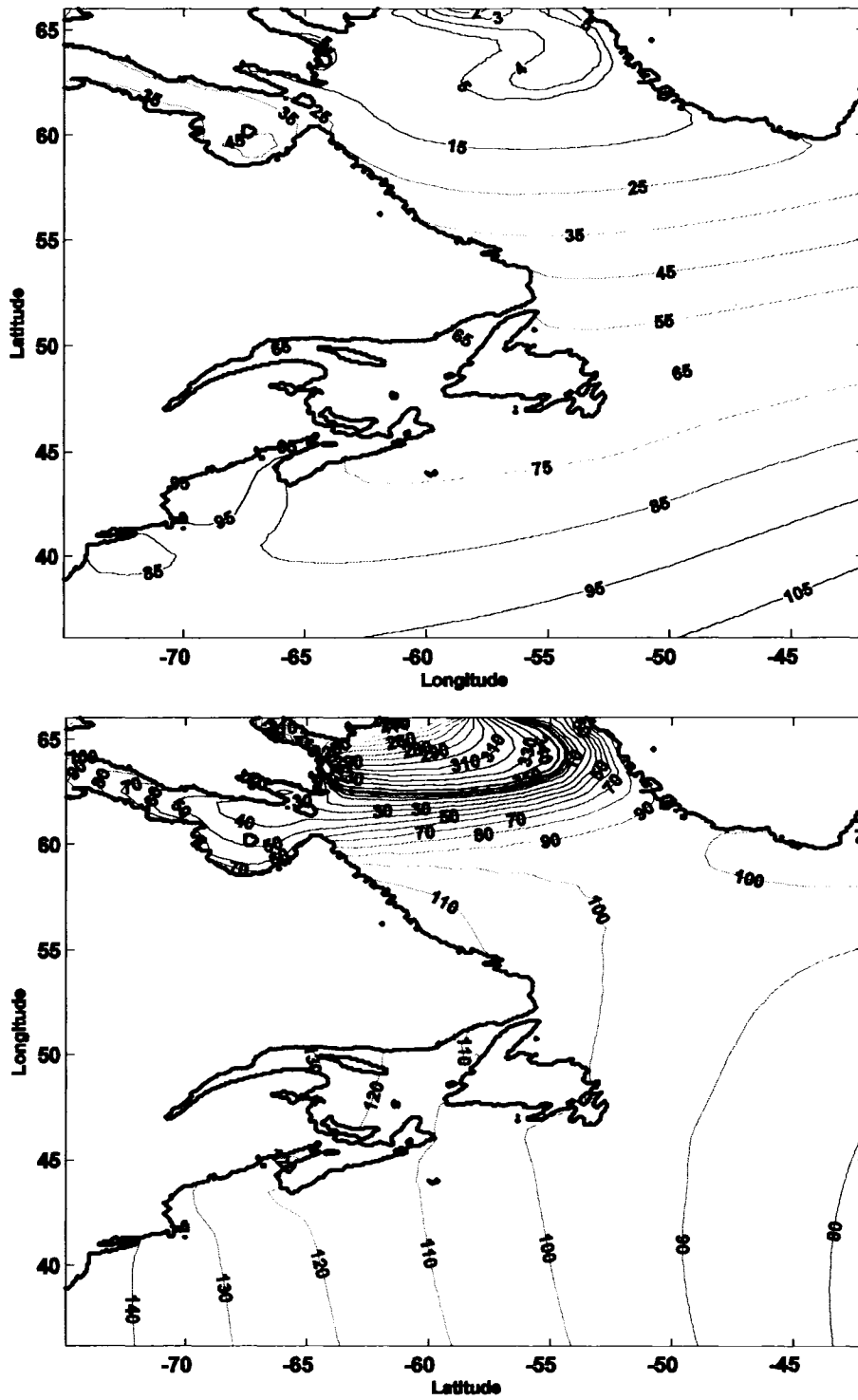


Figure C-1. Co-range (top) and Co-phase (bottom) charts for  $M_2$  equilibrium, earth & load tide. The amplitude is in mm and phases are in degrees. The contours are scaled to show proper distribution of amplitude and phase respectively.

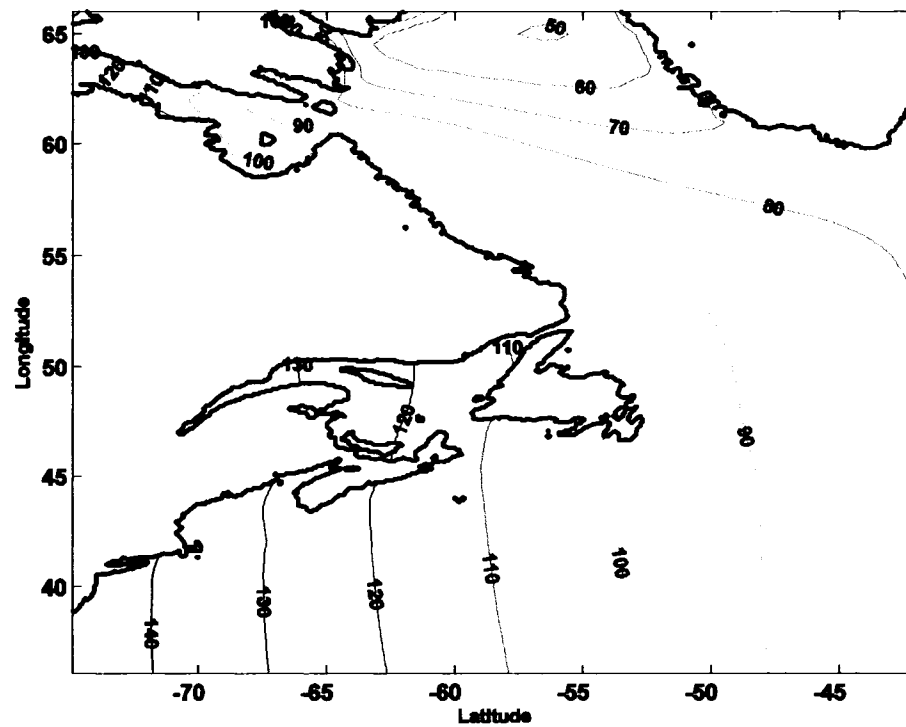
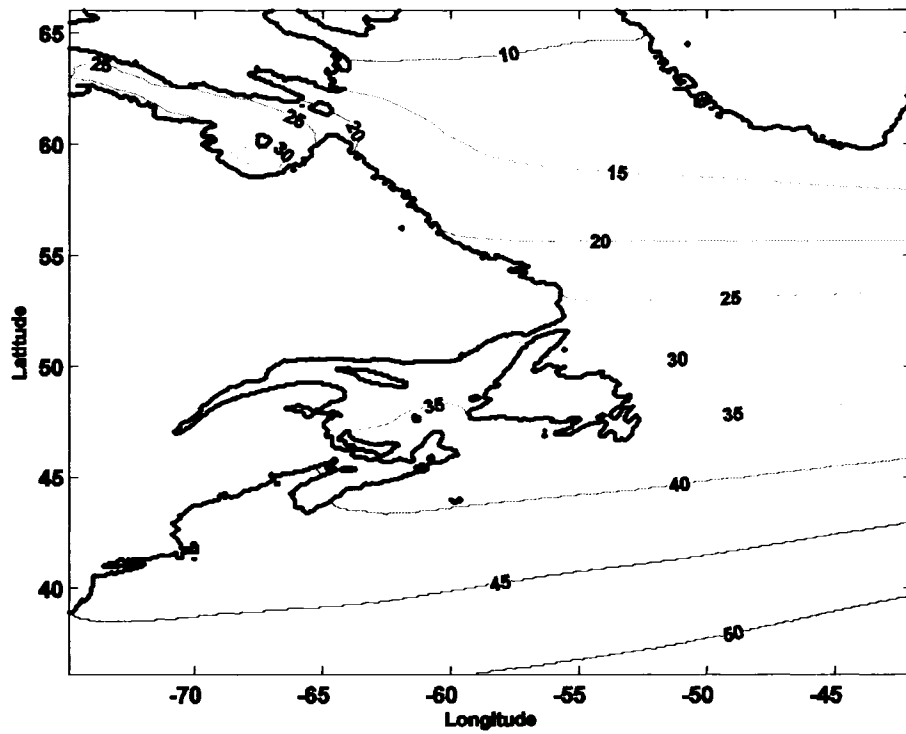


Figure C-2. Co-range (top) and Co-phase (bottom) charts for  $S_2$  equilibrium, earth & load tide. The amplitude is in mm and phases are in degrees. The contours are scaled to show proper distribution of amplitude and phase respectively.

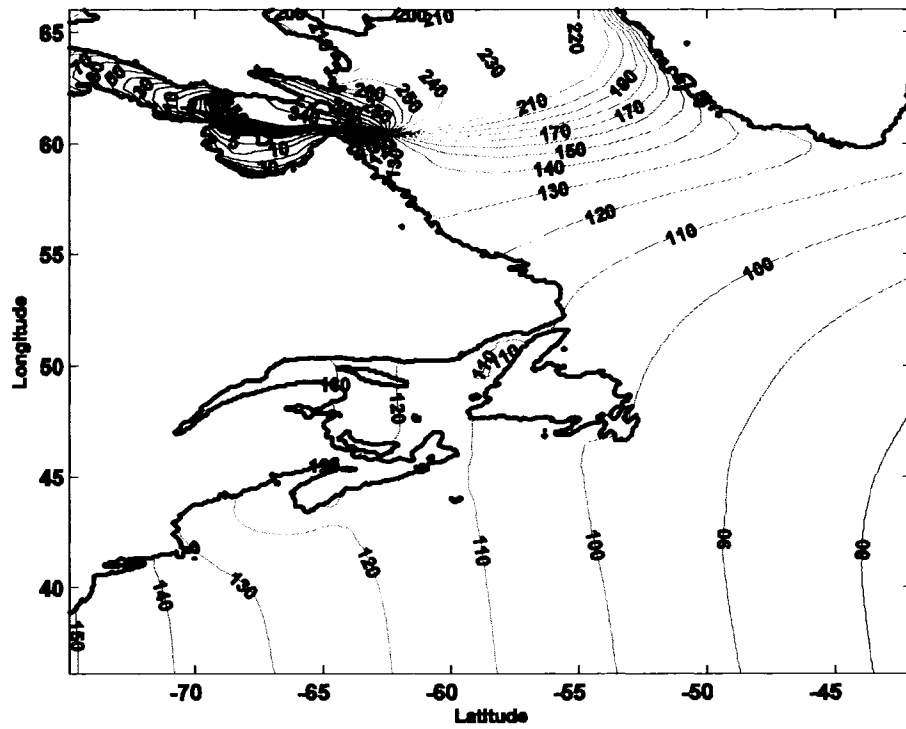
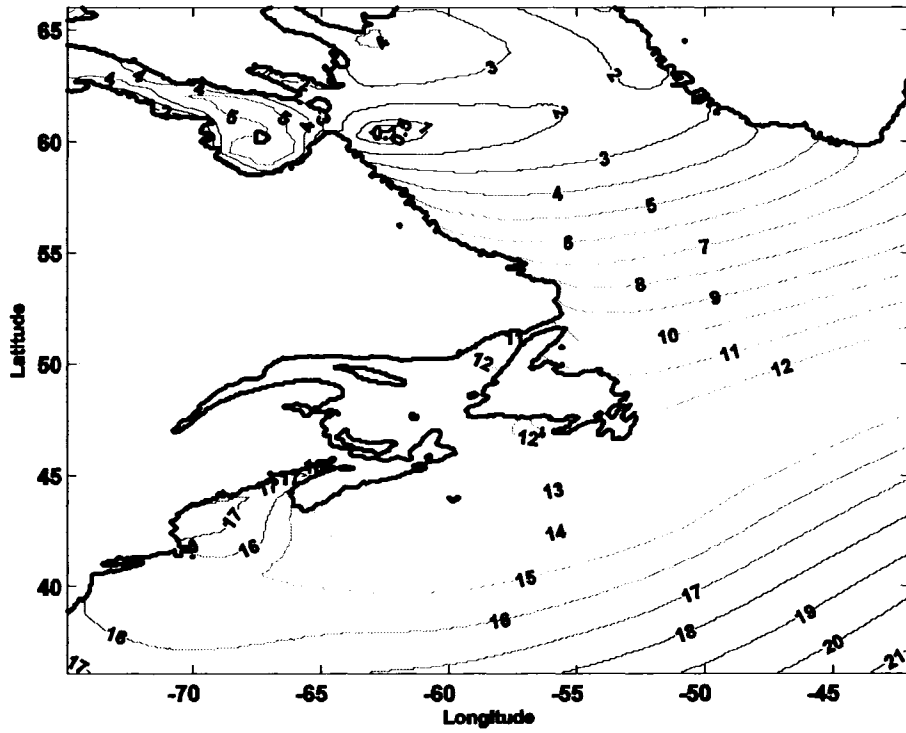


Figure C-3. Co-range (top) and Co-phase (bottom) charts for  $N_2$  equilibrium, earth & load tide. The amplitude is in mm and phases are in degrees. The contours are scaled to show proper distribution of amplitude and phase respectively.



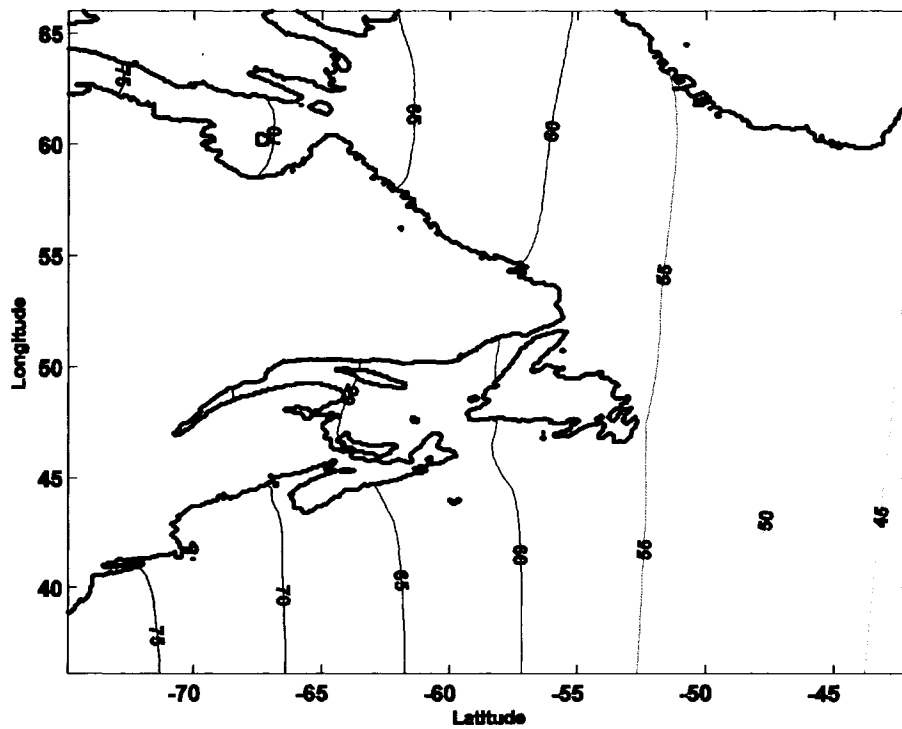
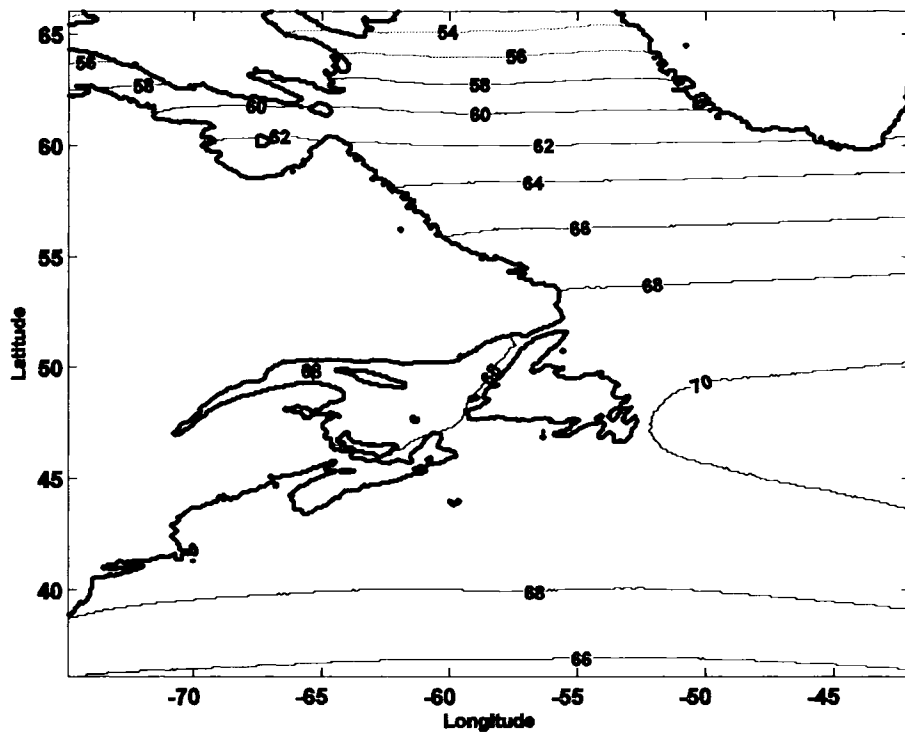


Figure C-5. Co-range (top) and Co-phase (bottom) charts for  $O_1$  equilibrium, earth & load tide. The amplitude is in mm and phases are in degrees. The contours are scaled to show proper distribution of amplitude and phase respectively.

## D. Elevation data for the North Atlantic Model

The tidal elevations for 5 major semidiurnal and diurnal constituents from the North Atlantic model are compared against the observations from tide and bottom pressure gauge data for same number of regions and the statistics are calculated.

Table D-1. Statistics of model computed elevation for semi-diurnal and diurnal constituents compared with observations at Tide and Bottom Pressure Gauge Sites for the North Atlantic Model.

<b>Constituent</b>	<b>RMS Amplitude</b>	<b>RMS Phase</b>	<b>AbsErr</b>	<b>RelErr</b>
	<b>Difference (cm)</b>	<b>Difference (Degrees)</b>	<b>(cm)</b>	<b>(%)</b>
<b>Super Stations</b>				
<b>M<sub>2</sub></b>	<b>1.1</b>	<b>2.2</b>	<b>1.4</b>	<b>3.6</b>
<b>S<sub>2</sub></b>	<b>1.8</b>	<b>8.9</b>	<b>2.0</b>	<b>14.5</b>
<b>N<sub>2</sub></b>	<b>1.1</b>	<b>6.4</b>	<b>1.2</b>	<b>12.9</b>
<b>K<sub>1</sub></b>	<b>1.7</b>	<b>8.3</b>	<b>1.5</b>	<b>22.2</b>
<b>O<sub>1</sub></b>	<b>0.5</b>	<b>8.5</b>	<b>0.6</b>	<b>14.0</b>
<b>RSS</b>	<b>3.0</b>		<b>3.2</b>	
<b>Coastal Island of Newfoundland</b>				
<b>M<sub>2</sub></b>	<b>3.5</b>	<b>4.9</b>	<b>4.0</b>	<b>9.2</b>
<b>S<sub>2</sub></b>	<b>3.7</b>	<b>11.7</b>	<b>3.0</b>	<b>22.4</b>
<b>N<sub>2</sub></b>	<b>1.4</b>	<b>11.1</b>	<b>1.7</b>	<b>20.4</b>
<b>K<sub>1</sub></b>	<b>1.5</b>	<b>6.6</b>	<b>1.4</b>	<b>17.0</b>
<b>O<sub>1</sub></b>	<b>0.8</b>	<b>6.8</b>	<b>0.9</b>	<b>13.3</b>
<b>RSS</b>	<b>5.6</b>		<b>5.6</b>	
<b>Coastal Nova Scotia</b>				
<b>M<sub>2</sub></b>	<b>2.2</b>	<b>2.2</b>	<b>2.8</b>	<b>4.7</b>
<b>S<sub>2</sub></b>	<b>1.2</b>	<b>8.5</b>	<b>2.0</b>	<b>14.1</b>
<b>N<sub>2</sub></b>	<b>2.1</b>	<b>7.9</b>	<b>2.3</b>	<b>14.3</b>
<b>K<sub>1</sub></b>	<b>1.5</b>	<b>15.5</b>	<b>2.0</b>	<b>28.9</b>
<b>O<sub>1</sub></b>	<b>1.2</b>	<b>10.9</b>	<b>1.2</b>	<b>23.2</b>
<b>RSS</b>	<b>3.8</b>		<b>4.8</b>	

Table D-1. (Continued)

<b>Constituent</b>	<b>RMS Amplitude</b>	<b>RMS Phase</b>	<b>AbsErr</b>	<b>RelErr</b>
	<b>Difference (cm)</b>	<b>Difference (Degrees)</b>	<b>(cm)</b>	<b>(%)</b>
<b>Labrador Sea &amp; Shelf</b>				
<b>M<sub>2</sub></b>	<b>0.9</b>	<b>1.6</b>	<b>1.1</b>	<b>2.8</b>
<b>S<sub>2</sub></b>	<b>0.7</b>	<b>4.6</b>	<b>1.3</b>	<b>7.5</b>
<b>N<sub>2</sub></b>	<b>0.3</b>	<b>1.9</b>	<b>0.3</b>	<b>3.5</b>
<b>K<sub>1</sub></b>	<b>0.7</b>	<b>4.2</b>	<b>0.8</b>	<b>8.0</b>
<b>O<sub>1</sub></b>	<b>0.3</b>	<b>2.5</b>	<b>0.4</b>	<b>5.2</b>
<b>RSS</b>	<b>1.5</b>		<b>2.0</b>	
<b>BoFGoM</b>				
<b>M<sub>2</sub></b>	<b>16.2</b>	<b>8.3</b>	<b>40.0</b>	<b>12.5</b>
<b>S<sub>2</sub></b>	<b>18.5</b>	<b>11.1</b>	<b>14.2</b>	<b>30.4</b>
<b>N<sub>2</sub></b>	<b>20.3</b>	<b>6.3</b>	<b>15.9</b>	<b>29.8</b>
<b>K<sub>1</sub></b>	<b>1.4</b>	<b>6.5</b>	<b>1.7</b>	<b>11.1</b>
<b>O<sub>1</sub></b>	<b>1.5</b>	<b>5.4</b>	<b>1.3</b>	<b>12.9</b>
<b>RSS</b>	<b>32.0</b>		<b>45.4</b>	
<b>Excluding BoFGoM</b>				
<b>M<sub>2</sub></b>	<b>1.9</b>	<b>2.7</b>	<b>2.4</b>	<b>5.1</b>
<b>S<sub>2</sub></b>	<b>1.8</b>	<b>8.4</b>	<b>2.1</b>	<b>14.6</b>
<b>N<sub>2</sub></b>	<b>1.3</b>	<b>6.8</b>	<b>1.4</b>	<b>12.8</b>
<b>K<sub>1</sub></b>	<b>1.4</b>	<b>8.6</b>	<b>1.4</b>	<b>19.0</b>
<b>O<sub>1</sub></b>	<b>0.7</b>	<b>7.2</b>	<b>0.8</b>	<b>13.9</b>
<b>RSS</b>	<b>3.3</b>		<b>3.8</b>	
<b>At all Locations</b>				
<b>M<sub>2</sub></b>	<b>4.8</b>	<b>3.8</b>	<b>9.9</b>	<b>6.6</b>
<b>S<sub>2</sub></b>	<b>5.2</b>	<b>9.0</b>	<b>4.5</b>	<b>17.8</b>
<b>N<sub>2</sub></b>	<b>5.1</b>	<b>6.7</b>	<b>4.3</b>	<b>16.2</b>
<b>K<sub>1</sub></b>	<b>1.4</b>	<b>8.2</b>	<b>1.5</b>	<b>17.5</b>
<b>O<sub>1</sub></b>	<b>0.9</b>	<b>6.8</b>	<b>0.9</b>	<b>13.7</b>
<b>RSS</b>	<b>8.8</b>		<b>11.8</b>	

Table D-2. Summary of observed and computed semidiurnal tidal elevations at Tide and Bottom Pressure gauge sites for the North Atlantic Model. AO, amplitude (cm) observed; PO, phase (degree) observed; AMO, difference of model amplitudes from observations; PMO, model-observation phase difference.

St. No.	M <sub>2</sub>				S <sub>2</sub>				N <sub>2</sub>			
	S <sub>2</sub>	PO	AMO	PMO	AO	PO	AMO	PMO	AO	PO	AMO	PMO
ST-1	N <sub>2</sub>	317.0	-1.1	0.0	14.7	363.0	2.5	-3.6	7.1	300.0	0.3	-11.9
ST-2	K <sub>1</sub>	348.0	-2.2	0.0	16.8	28.0	2.7	5.1	10.0	349.0	3.3	-22.2
ST-3	O <sub>1</sub>	344.0	2.9	1.0	12.0	24.0	0.6	10.7	11.0	312.0	0.7	8.3
ST-4	61.1	348.0	0.9	2.0	15.8	6.0	-4.0	22.5	12.7	327.0	1.3	1.2
ST-5	58.8	347.0	0.0	0.3	14.0	20.0	-1.7	15.4	10.1	345.0	3.0	-21.7
ST-6	69.8	359.0	0.4	3.0	13.7	29.0	-1.7	-9.3	17.1	337.0	-0.2	8.5
ST-7	36.0	328.0	-2.0	-0.9	14.7	11.0	1.8	-0.2	8.1	311.0	-0.2	-1.9
ST-8	23.1	330.0	-0.9	-6.0	10.3	9.0	-0.2	7.6	5.1	314.0	-0.9	4.7
ST-9	33.6	338.0	-0.1	1.1	13.0	16.0	-0.6	6.5	7.9	319.0	-0.9	17.2
ST-10	26.3	315.0	-0.6	-2.5	12.2	355.0	0.2	-2.5	6.0	299.0	-0.7	-4.1
ST-11	18.6	323.0	-0.9	-8.2	9.0	361.0	-0.2	-3.4	4.2	309.0	-0.8	-5.0
ST-12	16.2	340.0	-0.7	-6.5	7.4	19.0	-1.8	-1.9	3.6	323.0	-0.5	16.7
ST-13	18.3	343.0	-0.7	-4.5	7.4	24.0	-1.6	-1.8	4.0	324.0	-0.6	14.3
ST-14	43.2	338.0	0.9	-0.1	12.7	14.0	-1.1	-6.5	10.0	316.0	-1.6	-0.5
ST-15	60.6	350.0	1.9	1.0	15.5	10.0	-3.7	16.1	12.8	327.0	1.4	2.8
ST-16	59.3	349.0	1.9	2.1	16.5	11.0	-4.4	14.8	12.4	326.0	1.4	4.4
ST-17	58.3	350.0	1.8	1.1	15.3	9.0	-3.1	16.2	12.2	329.0	1.2	1.6
ST-18	60.4	350.0	1.8	1.7	15.6	10.0	-3.7	15.2	12.6	328.0	1.5	3.0
ST-19	60.0	348.0	1.8	2.1	15.9	8.0	-3.9	20.3	12.5	327.0	1.4	1.5
ST-20	59.4	347.0	1.9	2.2	16.2	8.0	-3.9	22.9	12.3	327.0	1.3	-0.2
ST-21	44.1	345.0	-0.8	-1.7	10.7	23.0	0.1	-6.5	9.8	320.0	-0.5	1.8
ST-22	48.2	351.0	-0.2	-1.6	10.3	22.0	0.1	-3.1	11.9	329.0	-1.1	0.1
ST-23	49.2	350.0	-0.2	2.6	11.7	20.0	-1.2	2.1	10.8	330.0	0.2	2.4
ST-24	49.0	357.0	-0.6	-2.8	10.3	23.0	-0.1	1.7	11.6	335.0	-0.7	-1.8
NF-1	42.0	19.7	-3.6	-7.8	12.0	56.8	0.1	-4.6	10.0	382.4	-1.8	-31.0
NF-2	43.0	14.3	-1.7	-2.9	13.0	50.4	-0.2	1.5	9.0	353.8	-0.1	-3.1
NF-3	44.0	4.1	-0.5	4.9	9.0	24.8	4.6	25.4	11.0	352.7	-1.5	-4.7
NF-4	59.0	352.4	-29.8	1.1	17.0	33.0	-7.5	5.0	10.0	335.5	-3.4	-3.9
NF-5	62.0	356.4	-1.5	-3.9	17.0	29.0	3.0	8.9	13.0	334.5	0.6	-3.8
NF-6	63.0	354.9	-1.7	-2.7	18.0	30.2	2.4	7.6	13.0	338.0	0.8	-7.6
NF-7	65.0	353.7	-2.0	-1.8	18.0	40.9	3.0	-4.0	8.0	340.2	6.1	-10.1

<b>NF-9</b>	69.0	338.8	-6.3	-1.4	20.0	15.8	2.5	4.5	15.0	324.5	-0.2	-9.4
<b>NF-10</b>	41.0	315.9	-2.6	6.4	14.0	3.4	4.7	1.6	8.0	304.7	0.8	-11.5
<b>NF-11</b>	40.0	314.6	-2.9	7.0	14.0	2.7	4.3	1.2	7.0	303.8	1.5	-11.5
<b>NF-12</b>	34.0	310.9	-0.2	6.0	14.0	358.9	2.9	0.0	6.0	301.3	1.2	-12.7
<b>NF-13</b>	33.0	313.1	-1.0	1.6	13.0	358.4	3.4	-3.2	7.0	294.9	-0.5	-6.9
<b>NF-14</b>	28.0	308.8	1.8	3.2	12.0	356.9	2.5	-6.1	6.0	304.5	-0.2	-13.1
<b>NF-15</b>	34.0	309.7	1.4	0.8	15.0	347.8	1.3	2.2	7.0	294.2	0.2	1.5
<b>NF-16</b>	35.0	314.0	1.8	-5.1	16.0	349.2	0.8	-0.2	7.0	303.3	0.4	-8.8
<b>NF-17</b>	33.0	312.1	3.7	-3.4	14.0	347.0	2.8	1.6	7.0	303.5	0.4	-9.0
<b>NF-19</b>	33.0	302.1	2.8	0.7	16.0	334.9	0.1	6.6	7.0	296.1	0.4	-5.0
<b>NF-20</b>	26.0	308.5	0.5	8.8	14.0	338.9	-1.2	6.2	6.0	303.5	-0.1	10.7
<b>NF-21</b>	35.0	56.2	3.9	13.2	11.0	72.8	-10.6	62.2	7.0	27.0	3.5	24.3
<b>NF-22</b>	34.0	59.7	7.1	10.2	10.0	72.8	-8.9	65.7	8.0	29.5	2.9	22.7
<b>NF-23</b>	53.0	56.9	5.5	11.2	17.0	83.0	-9.6	40.6	12.0	28.5	2.5	21.6
<b>NF-24</b>	50.0	60.4	0.7	-1.1	15.0	88.3	-6.0	14.4	9.0	37.9	3.3	3.8
<b>NF-25</b>	49.0	57.9	-0.7	-2.8	14.0	92.0	-4.6	3.3	11.0	29.5	0.5	8.0
<b>NF-26</b>	38.0	47.0	0.6	-10.2	12.0	76.7	-1.1	-3.9	7.0	41.7	1.6	-21.5
<b>SS-1</b>	130.0	48.9	-9.8	-1.6	18.0	86.0	-0.1	-21.5	25.0	14.7	8.2	17.8
<b>SS-2</b>	120.0	51.9	0.2	-4.6	21.0	86.0	-3.1	-21.5	25.0	23.7	8.2	8.8
<b>SS-3</b>	69.0	358.9	1.2	-357.0	13.0	29.0	-1.0	-9.3	17.0	336.7	-0.1	8.8
<b>SS-4</b>	63.0	350.3	-0.1	1.3	13.0	22.5	-1.3	3.2	14.0	326.8	0.4	3.8
<b>SS-5</b>	50.0	355.8	2.6	-2.5	13.0	30.9	-1.1	3.7	11.0	337.2	0.5	-7.5
<b>SS-6</b>	18.0	5.9	3.2	2.8	5.0	54.0	1.5	-2.3	4.0	361.7	0.8	-18.1
<b>SS-7</b>	49.0	344.2	1.9	0.3	14.0	24.6	-1.4	10.5	11.0	322.7	0.2	-3.3
<b>SS-8</b>	36.0	352.9	0.1	1.6	10.0	37.2	1.2	4.7	7.0	330.0	0.6	-2.0
<b>SS-9</b>	30.0	5.9	0.7	-1.8	10.0	47.0	0.0	-0.1	6.0	342.7	0.2	-1.4
<b>836</b>	45.0	307.5	1.1	-0.3	17.8	318.3	0.9	21.7	10.2	289.2	-0.1	1.9
<b>837</b>	47.8	297.5	1.5	0.0	15.8	336.0	3.1	-4.8	9.5	278.7	1.0	2.1
<b>838</b>	50.3	294.9	-0.2	1.0	19.5	308.1	-0.3	21.6	11.1	275.1	-0.4	3.8
<b>840</b>	55.5	285.6	1.0	0.0	22.4	341.3	-0.8	-20.2	11.4	263.3	0.6	3.3
<b>697</b>	65.6	304.7	-2.0	-2.6	23.2	334.3	0.4	-0.3	15.1	283.5	-1.2	2.2
<b>802</b>	65.5	304.7	-1.9	-2.5	24.5	334.6	-1.0	-0.5	14.6	285.9	-0.7	-0.2
<b>696</b>	64.6	303.7	-0.8	-1.2	22.7	333.5	0.5	1.5	14.9	282.3	-0.7	2.8
<b>803</b>	64.5	303.5	-0.6	-1.0	23.9	333.8	-0.7	1.2	14.3	284.4	-0.1	0.7
<b>695</b>	64.8	303.6	-0.6	-1.2	22.7	333.7	0.5	1.4	14.9	282.3	-0.6	2.4
<b>804</b>	64.6	303.8	-0.8	-1.5	23.9	334.3	-0.8	0.8	14.3	284.8	0.0	-0.2
<b>795</b>	50.1	304.7	0.6	-1.3	20.0	334.8	0.0	1.8	11.1	286.9	-0.1	-0.4
<b>691</b>	45.3	309.3	1.0	0.2	18.1	340.1	0.7	1.8	10.3	291.6	0.0	1.6

<b>793</b>	45.8	310.7	1.1	-0.8	18.7	338.8	0.3	3.3	10.2	293.6	0.1	-0.2
<b>789</b>	45.1	303.6	0.7	3.1	18.6	335.7	0.1	4.0	10.0	289.7	0.0	1.0
<b>692</b>	45.3	305.7	0.6	-0.6	18.1	337.7	0.5	0.8	10.1	287.9	-0.1	1.3
<b>794</b>	45.4	306.3	0.5	-1.2	18.7	335.9	-0.1	2.6	10.1	289.4	0.0	-0.2
<b>693</b>	40.5	299.9	1.2	-0.2	16.5	333.6	0.4	0.7	8.9	283.2	0.0	0.8
<b>792</b>	44.3	299.0	-2.7	0.7	18.7	330.4	-1.8	3.9	9.7	282.8	-0.7	1.2
<b>694</b>	40.1	297.2	0.6	-0.4	16.1	331.7	0.2	-0.7	8.8	280.5	-0.1	0.2
<b>791</b>	39.8	295.3	-0.3	-0.9	16.5	328.0	-0.6	1.0	8.5	278.4	-0.2	-0.1
<b>790</b>	40.2	292.8	0.1	1.2	16.7	325.6	-0.5	3.0	8.5	277.1	0.0	0.6
<b>796</b>	32.8	303.3	1.4	-0.9	15.2	337.0	-0.2	3.3	7.0	290.3	0.1	-2.1
<b>BG-1</b>	201.0	83.9	59.2	-11.9	41.0	146.0	29.2	-0.9	25.0	70.7	25.1	-25.0
<b>BG-2</b>	202.0	93.2	67.7	-20.2	29.0	129.4	44.1	16.5	47.0	60.2	4.9	-13.5
<b>BG-3</b>	208.0	90.2	45.9	-20.2	30.0	124.0	38.0	19.3	46.0	61.1	2.9	-17.5
<b>BG-4</b>	301.0	98.0	24.0	-24.1	48.0	137.5	41.3	9.2	59.0	67.5	3.1	-19.8
<b>BG-5</b>	368.0	101.6	7.2	-25.5	58.0	148.2	47.1	0.5	90.0	68.3	-18.8	-18.1
<b>BG-6</b>	436.0	105.9	-25.1	-29.8	77.0	148.0	39.3	0.6	95.0	66.7	-17.3	-16.5
<b>BG-7</b>	413.0	102.9	-5.5	-27.0	66.0	142.0	49.3	6.4	78.0	71.7	-0.9	-21.7
<b>BG-8</b>	408.0	97.7	-8.5	-21.9	67.0	145.7	45.4	2.8	88.0	64.5	-12.4	-14.7
<b>BG-9</b>	434.0	102.0	-31.1	-24.4	68.0	141.8	45.3	9.1	91.0	73.2	-15.0	-21.8
<b>BG-10</b>	415.0	99.2	-18.4	-24.5	53.0	145.8	58.6	1.7	74.0	60.8	1.1	-12.0
<b>BG-11</b>	386.0	92.9	1.9	-20.1	41.0	142.8	68.0	2.6	106.0	59.5	-32.5	-12.7
<b>BG-12</b>	265.0	90.3	33.0	-23.9	41.0	134.0	40.0	5.2	65.0	71.3	-7.9	-31.0
<b>BG-13</b>	221.0	73.3	66.9	-7.4	35.0	112.8	43.1	25.9	37.0	44.1	18.2	-4.3
<b>BG-14</b>	214.0	74.5	73.9	-8.6	31.0	110.7	47.1	28.0	46.0	39.4	9.2	0.4
<b>BG-15</b>	208.0	75.6	66.1	-10.0	33.0	108.8	41.0	29.7	46.0	43.9	6.7	-4.4
<b>BG-16</b>	233.0	77.7	41.1	-12.1	36.0	112.2	38.0	26.3	55.0	44.9	-2.3	-5.4
<b>BG-17</b>	223.0	78.1	51.1	-12.5	33.0	122.0	41.0	16.5	44.0	46.4	8.7	-6.9
<b>BG-18</b>	219.0	80.2	35.4	-17.0	33.0	118.8	35.2	17.3	48.0	47.5	1.0	-10.4
<b>BG-19</b>	215.0	80.9	36.2	-17.0	34.0	117.0	33.1	19.8	45.0	50.7	3.5	-13.0
<b>BG-20</b>	185.0	65.6	37.2	-9.6	29.0	101.1	29.3	28.0	38.0	47.0	5.0	-17.2

Table D-3. Same as Table D-2, but for diurnal constituents.

St. No.	K <sub>1</sub>				O <sub>1</sub>			
	AO	PO	AMO	PMO	AO	PO	AMO	PMO
ST-1	8.1	162	-1.3	-19.2	7.3	128	-0.8	2.1
ST-2	6	195	1.3	-6.4	7.3	177	0.1	5.5
ST-3	6.1	24	1.8	9.3	6.1	321	0.3	20
ST-4	7.6	105	3.5	-3.5	4.6	77	2	-7.8
ST-5	6.4	48	2.8	5.6	2.7	335	3.8	29.5
ST-6	12.8	147	2.1	6.2	7.6	116	4.3	15.4
ST-7	7.3	163	-0.3	-16.4	5.9	134	-0.4	0.6
ST-8	7	163	0.5	-3.1	5.5	135	-0.5	1.7
ST-9	5.7	160	0.1	-4.1	4	150	0.1	-3.5
ST-10	8.7	158	-0.6	-4.1	6.1	125	0.2	2.6
ST-11	9	161	0.8	-2.6	5.8	125	0.6	-3
ST-12	5.6	155	0.7	5.1	4.6	148	-0.8	-7.4
ST-13	6.1	154	0.2	4.6	4.2	147	-0.4	-4.6
ST-14	6.5	165	-1.2	5.1	4.8	171	0.5	-3.2
ST-15	8.1	117	3.4	-4.2	4.8	92	2.2	-6.6
ST-16	7	130	1.7	-10.9	3.9	112	0.7	-11.5
ST-17	6.4	130	1.1	-4.8	3.1	121	0.6	-3.9
ST-18	8.3	123	2.4	-2.6	4.8	101	1.7	-3.5
ST-19	7.2	109	2.7	-4.7	3.8	80	1.7	-6
ST-20	5.8	95	3.1	-6.4	3.1	51	1.7	-2.4
ST-21	5.5	162	0	-2.2	4.7	166	0.2	-0.9
ST-22	6.9	173	-1.5	1.2	5.7	170	0.7	16.2
ST-23	6.9	172	-1.3	-11.7	5.9	176	-0.7	6.4
ST-24	6.8	170	-1	-11.1	5.4	179	-0.2	0.2
NF-1	9	252.4	-0.1	0.3	9	229.7	0.9	5.1
NF-2	8	252	1.3	-9.3	9	230.4	1.1	-3.5
NF-3	7	242.8	1.8	-6.7	8	224.3	1.6	-2.4
NF-4	5	185.7	2.7	12.5	6	183.8	1.7	4.7
NF-5	7	213.7	1	-15.4	8	185.8	0.1	2.6
NF-6	6	202	2.1	-3.5	6	199.9	2.2	-11.5
NF-7	6	201	2.2	-3.1	7	180.3	1.2	7.3
NF-8	9	179.7	-0.2	-10.7	8	170.8	0.1	-8.9
NF-9	7	183.2	1.6	-14.5	9	165.4	-1.1	-3.7
NF-10	7	162.8	0.2	-20.5	7	133	-0.3	1
NF-11	7	162.2	0.1	-20.1	7	132.3	-0.4	0.4
NF-12	7	162.1	-0.2	-19	6	128.5	0.5	0.9

<b>NF-13</b>	8	163.5	-1.3	-18.7	7	129.6	-0.5	-1.2
<b>NF-14</b>	8	165.2	-1.6	-11.6	6	118.1	0.3	9.5
<b>NF-15</b>	9	164.9	-1.8	6.3	6	121.3	0.8	6.7
<b>NF-16</b>	10	169.4	-2.6	1.4	6	119.2	0.9	8.4
<b>NF-17</b>	9	166.1	-1.6	4.6	5	120.8	1.9	6.7
<b>NF-18</b>	8	174.7	-0.2	-4.3	7	130.8	0.1	-4
<b>NF-19</b>	8	164.2	-0.2	7.6	6	115.2	0.8	8.6
<b>NF-20</b>	7	164.9	-0.4	19.7	3	97.3	1.3	28
<b>NF-21</b>	8	259.1	2.1	-4.4	8	251	1.7	-5
<b>NF-22</b>	8	265	2.7	-13.8	8	255.3	2	-13.8
<b>NF-23</b>	14	263.2	2.1	-7.7	12	240.8	3.3	-2.7
<b>NF-24</b>	13	262.5	3.5	-10	14	242.1	1.8	-8.3
<b>NF-25</b>	10	280.2	5.7	-32.1	13	234.8	2.2	-5.4
<b>NF-26</b>	12	267.9	2.8	-21	12	243.9	2.5	-15.8
<b>SS-1</b>	14	174.2	-0.9	4.7	10	156.8	2.1	13.9
<b>SS-2</b>	13	179.2	0.1	-0.3	10	162.8	2.1	7.9
<b>SS-3</b>	12	147.2	2.9	6	7	115.8	4.9	15.6
<b>SS-4</b>	10	123	2.2	-6.6	4	94.5	3.7	-5
<b>SS-5</b>	2	127	-0.1	7	2	161.8	0.5	49.1
<b>SS-6</b>	13	322.2	5.4	-6.8	15	290.8	2.4	-2.1
<b>SS-7</b>	5	16.9	2.9	3.7	6	321.5	1	8.6
<b>SS-8</b>	7	324.7	1.8	-12.9	8	287.3	1.5	-8.1
<b>SS-9</b>	8	295.2	2.2	-1.2	9	265.8	2.1	2
<b>836</b>	9.6	143.8	3	21.4	6.2	120.5	1.1	-2.6
<b>837</b>	12.8	178	-0.2	-19.6	7.5	127.5	-0.3	1
<b>838</b>	10.1	148.4	1.5	10.7	7.4	124	-0.3	4.1
<b>840</b>	10.7	173.6	1.3	-16.1	7.1	120.1	0	3.7
<b>697</b>	9.8	170.6	-0.6	-7.3	7.3	148.4	-1	-7.5
<b>802</b>	9.3	172.6	-0.2	-10.3	7.3	145.3	-1.1	-4.4
<b>696</b>	12.3	163.8	-1.3	-5.1	7.8	128.3	-0.3	-0.5
<b>803</b>	11.7	165	-0.8	-5.4	7.7	127.9	-0.3	0.9
<b>695</b>	12.8	162.4	-1.6	-2.3	7.9	125.2	-0.3	0.9
<b>804</b>	12.1	164	-0.7	-6.5	7.9	125	-0.2	0.5
<b>795</b>	10.5	160.5	0.6	1.3	7	123	0.2	0
<b>691</b>	10.7	159.7	2.7	6.2	5.9	117.9	1.6	-2.4
<b>793</b>	10.4	157	3.4	8.9	6.4	120.6	1.2	-5.9
<b>789</b>	10.3	157.8	2.2	6.6	6.5	121.1	0.8	-2.8
<b>692</b>	10.5	161.9	1.4	1.6	6.2	122.1	1	-2.4
<b>794</b>	10.2	159.4	1.7	4.1	6.7	122.8	0.5	-3.1
<b>693</b>	10.1	162.4	-0.4	-12.1	6.6	126.4	0	-2.4

<b>792</b>	10.6	159.5	-1	-9.2	7.5	125.6	-0.9	-1.6
<b>694</b>	10.1	162.7	-2.3	-28.9	6.9	127.1	-0.2	-3.9
<b>791</b>	9.7	159	0	-17	7.3	125.3	-0.7	-0.5
<b>790</b>	10	158.8	-0.8	-13.2	6.9	123.6	-0.3	1
<b>796</b>	8.9	159.9	0.1	0.1	6	126.3	0.5	-1.8
<b>BG-1</b>	12	176.2	1.7	13.9	9	149.8	3.6	33.6
<b>BG-2</b>	14	194.7	-0.2	-3.9	11	174.3	1.7	9.7
<b>BG-3</b>	13	190.3	0.5	-1.1	11	171.6	1.5	11.1
<b>BG-4</b>	15	196.4	-0.5	-6.1	11	173.5	2.1	11
<b>BG-5</b>	16	194.8	-1.3	-4.5	12	176.1	1.3	10
<b>BG-6</b>	18	194.6	-3.1	-2.6	12	173.2	1.6	13.9
<b>BG-7</b>	18	194.2	-3.1	-3.3	10	180.8	3.5	6
<b>BG-8</b>	17	182.6	-2.2	8.7	10	160.4	3.5	26.3
<b>BG-9</b>	17	197	-2	-4	12	171.4	1.4	16
<b>BG-10</b>	18	197.4	-2.9	-6.8	12	175	1.5	10.6
<b>BG-11</b>	15	187.8	0.2	2	12	170.4	1.5	14.1
<b>BG-12</b>	15	190.1	-0.9	-3.8	11	168.8	1.8	12.3
<b>BG-13</b>	13	183.6	0.9	2.7	10	165.3	2.7	15.7
<b>BG-14</b>	14	183.3	-0.1	3	11	169.5	1.7	11.5
<b>BG-15</b>	13	186.1	0.8	0.3	10	171.8	2.7	9.1
<b>BG-16</b>	15	183.3	-1.2	3.1	11	161.1	1.7	19.8
<b>BG-17</b>	14	190.1	-0.2	-3.7	11	164.9	1.7	16
<b>BG-18</b>	14	183.8	-0.3	1.3	11	166.2	1.4	13.3
<b>BG-19</b>	16	184.2	-2.4	1.7	10	168.8	2.4	11.1
<b>BG-20</b>	15	182.9	-1.8	0.5	10	167	2.3	10

## E. Station-wise error estimates of tidal elevations for the barotropic runs

Table E-1. Summary of observed and computed semidiurnal tidal elevations at Tide and Bottom Pressure gauge sites from Ba experiment. AO, amplitude (cm) observed; PO, phase (degree) observed; AMO, difference of model amplitudes from observations; PMO, model-observation phase difference.

St. No.	M <sub>2</sub>				S <sub>2</sub>				N <sub>2</sub>			
	AO	PO	AMO	PMO	AO	PO	AMO	PMO	AO	PO	AMO	PMO
ST-1	35.6	317.0	0.1	-6.0	14.7	3.0	-1.9	353.2	7.1	300.0	0.2	0.2
ST-2	60.3	348.0	1.0	2.3	16.8	28.0	-1.2	-6.7	10.0	349.0	2.7	-19.1
ST-3	50.2	344.0	2.2	-1.9	12.0	24.0	-0.1	-8.6	11.0	312.0	0.2	8.8
ST-4	61.1	348.0	0.1	-1.6	15.8	6.0	-3.0	11.2	12.7	327.0	0.7	-2.3
ST-5	58.8	347.0	-2.2	-3.5	14.0	20.0	-1.4	-3.9	10.1	345.0	2.0	-23.0
ST-6	69.8	359.0	2.4	0.3	13.7	29.0	-0.2	6.4	17.1	337.0	-1.4	-0.6
ST-7	36.0	328.0	-0.4	-6.0	14.7	11.0	-2.2	-10.0	8.1	311.0	-0.7	-1.5
ST-8	23.1	330.0	-1.9	-0.7	10.3	9.0	-2.0	0.0	5.1	314.0	-0.4	8.6
ST-9	33.6	338.0	-0.6	-3.3	13.0	16.0	-2.4	-5.2	7.9	319.0	-1.0	3.4
ST-10	26.3	315.0	-0.4	-4.2	12.2	355.0	-1.4	-4.0	6.0	299.0	-0.3	2.0
ST-11	18.6	323.0	-0.9	-4.8	9.0	1.0	-1.2	356.5	4.2	309.0	-0.2	2.4
ST-12	16.2	340.0	-1.2	-5.3	7.4	19.0	-1.8	-0.9	3.6	323.0	-0.3	12.8
ST-13	18.3	343.0	-0.8	-4.5	7.4	24.0	-1.6	-0.9	4.0	324.0	-0.3	11.6
ST-14	43.2	338.0	-0.1	-0.3	12.7	14.0	-2.1	-5.2	10.0	316.0	-0.9	3.1
ST-15	60.6	350.0	1.3	-2.2	15.5	10.0	-2.7	8.6	12.8	327.0	0.8	-1.0
ST-16	59.3	349.0	0.7	-0.7	16.5	11.0	-4.1	7.7	12.4	326.0	0.8	0.7
ST-17	58.3	350.0	0.4	-1.4	15.3	9.0	-3.2	9.7	12.2	329.0	0.7	-2.0
ST-18	60.4	350.0	1.1	-1.2	15.6	10.0	-3.0	9.6	12.6	328.0	0.9	-0.9
ST-19	60.0	348.0	0.6	-1.3	15.9	8.0	-3.2	9.4	12.5	327.0	0.8	-1.9
ST-20	59.4	347.0	0.1	-1.5	16.2	8.0	-3.5	8.4	12.3	327.0	0.6	-3.1
ST-21	44.1	345.0	-0.5	-1.9	10.7	23.0	-0.6	-8.5	9.8	320.0	-0.5	3.5
ST-22	48.2	351.0	-0.1	-1.0	10.3	22.0	-0.7	-3.0	11.9	329.0	-1.2	-0.3
ST-23	49.2	350.0	-0.3	3.3	11.7	20.0	-2.3	2.2	10.8	330.0	0.2	1.6
ST-24	49.0	357.0	-0.8	-2.1	10.3	23.0	-1.2	0.4	11.6	335.0	-0.8	-2.0
NF-1	42.0	19.7	-1.6	-2.9	12.0	56.8	-1.3	-6.9	10.0	382.4	-1.5	-27.7
NF-2	43.0	14.3	0.6	2.9	13.0	50.4	-1.5	-0.8	9.0	353.8	0.2	1.5
NF-3	44.0	4.1	2.6	9.6	9.0	24.8	3.1	20.9	11.0	352.7	-1.2	-0.7
NF-4	59.0	352.4	2.9	4.0	17.0	33.0	-1.2	-6.0	10.0	335.5	2.9	0.2
NF-5	62.0	356.4	1.8	-0.5	17.0	29.0	-0.6	-2.6	13.0	334.5	0.2	0.7
NF-6	63.0	354.9	1.7	0.8	18.0	30.2	-1.4	-4.0	13.0	338.0	0.4	-2.9

<b>NF-7</b>	65.0	353.7	1.8	1.3	18.0	40.9	-0.7	-15.6	8.0	340.2	5.8	-5.7
<b>NF-8</b>	67.0	334.4	2.4	4.9	19.0	14.0	-1.0	-2.7	13.0	321.5	1.2	-1.1
<b>NF-9</b>	69.0	338.8	-2.3	-1.7	20.0	15.8	-2.9	-6.8	15.0	324.5	-1.4	-6.4
<b>NF-10</b>	41.0	315.9	0.2	-1.1	14.0	3.4	-0.7	355.0	8.0	304.7	0.3	-2.9
<b>NF-11</b>	40.0	314.6	-0.4	-1.1	14.0	2.7	-0.9	355.0	7.0	303.8	1.0	-2.7
<b>NF-12</b>	34.0	310.9	0.7	-0.6	14.0	358.9	-1.3	-3.2	6.0	301.3	1.1	-1.4
<b>NF-13</b>	33.0	313.1	0.6	-3.8	13.0	358.4	-0.2	-3.5	7.0	294.9	0.0	4.8
<b>NF-14</b>	28.0	308.8	1.3	-0.4	12.0	356.9	0.6	-5.9	6.0	304.5	0.4	-5.2
<b>NF-15</b>	34.0	309.7	0.3	0.5	15.0	347.8	0.1	-0.9	7.0	294.2	0.7	5.8
<b>NF-16</b>	35.0	314.0	0.3	-4.7	16.0	349.2	-0.6	-3.5	7.0	303.3	0.9	-4.1
<b>NF-17</b>	33.0	312.1	2.4	-3.1	14.0	347.0	1.4	-1.6	7.0	303.5	0.9	-4.5
<b>NF-18</b>	33.0	304.4	4.9	1.6	16.0	344.0	0.2	-2.2	7.0	293.5	1.5	3.6
<b>NF-19</b>	33.0	302.1	1.7	0.7	16.0	334.9	-1.0	3.8	7.0	296.1	1.1	-3.1
<b>NF-20</b>	26.0	308.5	0.4	3.6	14.0	338.9	-1.3	4.5	6.0	303.5	0.7	-2.7
<b>NF-21</b>	35.0	56.2	3.0	6.1	11.0	72.8	0.5	2.4	7.0	27.0	0.9	8.0
<b>NF-22</b>	34.0	59.7	6.7	1.8	10.0	72.8	2.4	3.4	8.0	29.5	0.5	5.4
<b>NF-23</b>	53.0	56.9	7.5	11.0	17.0	83.0	0.8	8.3	12.0	28.5	0.3	16.2
<b>NF-24</b>	50.0	60.4	4.0	0.6	15.0	88.3	0.6	-1.1	9.0	37.9	2.0	0.8
<b>NF-25</b>	49.0	57.9	-0.4	-5.6	14.0	92.0	-0.3	-11.6	11.0	29.5	-1.0	0.7
<b>NF-26</b>	38.0	47.0	8.1	-0.3	12.0	76.7	0.9	-0.7	7.0	41.7	2.5	-17.0
<b>SS-1</b>	130.0	48.9	-0.8	1.8	18.0	86.0	7.2	15.1	25.0	14.7	2.0	12.1
<b>SS-2</b>	120.0	51.9	9.2	-1.2	21.0	86.0	4.2	15.1	25.0	23.7	2.0	3.1
<b>SS-3</b>	69.0	358.9	3.2	0.4	13.0	29.0	0.5	6.4	17.0	336.7	-1.3	-0.3
<b>SS-4</b>	63.0	350.3	-0.5	-1.9	13.0	22.5	-0.2	-3.0	14.0	326.8	-0.3	-0.1
<b>SS-5</b>	50.0	355.8	-0.6	-5.8	13.0	30.9	-1.8	-9.6	11.0	337.2	-0.3	-8.0
<b>SS-6</b>	18.0	5.9	0.2	-4.7	5.0	54.0	0.3	-13.7	4.0	361.7	0.8	-26.7
<b>SS-7</b>	49.0	344.2	1.1	-2.2	14.0	24.6	-2.4	-8.7	11.0	322.7	-0.3	-1.9
<b>SS-8</b>	36.0	352.9	-0.9	2.3	10.0	37.2	-1.0	-4.7	7.0	330.0	0.5	3.0
<b>SS-9</b>	30.0	5.9	0.5	3.7	10.0	47.0	-1.8	-1.0	6.0	342.7	0.6	3.9
<b>836.0</b>	45.0	307.5	1.8	-2.1	17.8	318.3	0.4	19.6	10.2	289.2	0.6	-0.5
<b>837.0</b>	47.8	297.5	2.0	-1.8	15.8	336.0	3.2	-5.9	9.5	278.7	1.7	-0.7
<b>838.0</b>	50.3	294.9	0.2	-0.8	19.5	308.1	-0.3	20.5	11.1	275.1	0.2	1.2
<b>840.0</b>	55.5	285.6	1.2	-2.2	22.4	341.3	-1.0	-22.1	11.4	263.3	0.9	1.2
<b>697.0</b>	65.6	304.7	-0.4	-3.6	23.2	334.3	0.6	-0.6	15.1	283.5	-0.2	-1.5
<b>802.0</b>	65.5	304.7	-0.4	-3.5	24.5	334.6	-0.8	-0.8	14.6	285.9	0.3	-3.8
<b>696.0</b>	64.6	303.7	0.2	-3.5	22.7	333.5	0.9	-0.2	14.9	282.3	0.0	-1.4
<b>803.0</b>	64.5	303.5	0.4	-3.2	23.9	333.8	-0.3	-0.5	14.3	284.4	0.6	-3.4
<b>695.0</b>	64.8	303.6	0.2	-3.7	22.7	333.7	0.8	-0.4	14.9	282.3	0.0	-1.8
<b>804.0</b>	64.6	303.8	0.0	-3.9	23.9	334.3	-0.6	-1.2	14.3	284.8	0.5	-4.3
<b>795.0</b>	50.1	304.7	1.1	-3.5	20.0	334.8	-0.4	-0.3	11.1	286.9	0.6	-3.3

<b>691.0</b>	45.3	309.3	1.6	-1.9	18.1	340.1	0.2	-0.6	10.3	291.6	0.7	-1.0
<b>793.0</b>	45.8	310.7	1.6	-2.7	18.7	338.8	-0.3	1.1	10.2	293.6	0.8	-2.6
<b>789.0</b>	45.1	303.6	1.4	1.4	18.6	335.7	-0.4	1.9	10.0	289.7	0.7	-1.3
<b>692.0</b>	45.3	305.7	1.1	-2.2	18.1	337.7	0.0	-1.3	10.1	287.9	0.6	-1.0
<b>794.0</b>	45.4	306.3	1.0	-2.8	18.7	335.9	-0.5	0.5	10.1	289.4	0.6	-2.5
<b>693.0</b>	40.5	299.9	1.0	-1.8	16.5	333.6	0.1	-1.1	8.9	283.2	0.5	-0.7
<b>792.0</b>	44.3	299.0	-2.8	-0.9	18.7	330.4	-2.1	2.1	9.7	282.8	-0.3	-0.3
<b>694.0</b>	40.1	297.2	0.5	-2.3	16.1	331.7	0.2	-1.7	8.8	280.5	0.3	-1.3
<b>791.0</b>	39.8	295.3	-0.3	-2.7	16.5	328.0	-0.8	0.2	8.5	278.4	0.3	-1.5
<b>790.0</b>	40.2	292.8	0.2	-0.7	16.7	325.6	-0.6	2.0	8.5	277.1	0.5	-0.9
<b>796.0</b>	32.8	303.3	0.6	-1.8	15.2	337.0	-1.1	0.8	7.0	290.3	0.5	-0.9
<b>BG-1</b>	201.0	83.9	13.8	-1.6	41.0	146.0	-0.6	-11.7	25.0	70.7	21.1	-12.5
<b>BG-2</b>	202.0	93.2	22.0	-9.9	29.0	129.4	13.1	6.2	47.0	60.2	1.3	-1.0
<b>BG-3</b>	208.0	90.2	0.5	-10.3	30.0	124.0	8.8	8.5	46.0	61.1	-1.6	-5.7
<b>BG-4</b>	301.0	98.0	-24.7	-14.8	48.0	137.5	3.7	1.8	59.0	67.5	1.7	-9.7
<b>BG-5</b>	368.0	101.6	-45.9	-16.6	58.0	148.2	5.3	-4.5	90.0	68.3	-18.1	-9.1
<b>BG-6</b>	436.0	105.9	-81.5	-21.0	77.0	148.0	-6.2	-3.9	95.0	66.7	-16.2	-7.7
<b>BG-7</b>	413.0	102.9	-61.8	-18.3	66.0	142.0	4.2	2.0	78.0	71.7	0.1	-13.0
<b>BG-8</b>	408.0	97.7	-66.0	-13.7	67.0	145.7	1.0	-1.8	88.0	64.5	-12.1	-6.6
<b>BG-9</b>	434.0	102.0	-91.5	-16.6	68.0	141.8	-0.3	4.3	91.0	73.2	-15.4	-14.1
<b>BG-10</b>	415.0	99.2	-75.8	-16.0	53.0	145.8	14.5	-2.6	74.0	60.8	1.3	-3.6
<b>BG-11</b>	386.0	92.9	-55.1	-11.5	41.0	142.8	25.2	-1.6	106.0	59.5	-32.8	-4.3
<b>BG-12</b>	265.0	90.3	-16.7	-14.8	41.0	134.0	7.0	-3.6	65.0	71.3	-11.9	-21.1
<b>BG-13</b>	221.0	73.3	18.0	1.7	35.0	112.8	11.2	16.6	37.0	44.1	14.0	5.9
<b>BG-14</b>	214.0	74.5	25.0	0.5	31.0	110.7	15.2	18.7	46.0	39.4	5.0	10.6
<b>BG-15</b>	208.0	75.6	18.4	-0.7	33.0	108.8	10.6	19.7	46.0	43.9	2.2	6.1
<b>BG-16</b>	233.0	77.7	-6.6	-2.8	36.0	112.2	7.6	16.3	55.0	44.9	-6.8	5.1
<b>BG-17</b>	223.0	78.1	3.4	-3.2	33.0	122.0	10.6	6.5	44.0	46.4	4.2	3.6
<b>BG-18</b>	219.0	80.2	-10.9	-7.8	33.0	118.8	7.5	6.6	48.0	47.5	-4.0	0.3
<b>BG-19</b>	215.0	80.9	-9.6	-7.8	34.0	117.0	5.5	8.7	45.0	50.7	-1.5	-2.2
<b>BG-20</b>	185.0	65.6	-6.7	-1.1	29.0	101.1	6.0	16.5	38.0	47.0	-0.9	-6.9

Table E-2. Same as Table E-1, but for diurnal constituents

St. No.	K <sub>1</sub>				O <sub>1</sub>			
	AO	PO	AMO	PMO	AO	PO	AMO	PMO
ST-1	8.1	162.0	-1.0	-9.1	7.3	128.0	-0.3	-1.1
ST-2	6.0	195.0	0.4	-2.4	7.3	177.0	0.4	4.4
ST-3	6.1	24.0	1.2	19.1	6.1	321.0	-1.6	31.5
ST-4	7.6	105.0	2.8	3.2	4.6	77.0	1.0	9.9
ST-5	6.4	48.0	2.2	14.7	2.7	335.0	1.9	-315.4
ST-6	12.8	147.0	1.1	9.4	7.6	116.0	2.9	22.5
ST-7	7.3	163.0	-0.5	-9.8	5.9	134.0	-0.1	-0.4
ST-8	7.0	163.0	0.5	-1.8	5.5	135.0	-0.4	2.6
ST-9	5.7	160.0	0.0	-0.2	4.0	150.0	0.2	-3.3
ST-10	8.7	158.0	-0.6	-3.6	6.1	125.0	0.3	3.2
ST-11	9.0	161.0	0.9	-3.3	5.8	125.0	0.6	-2.3
ST-12	5.6	155.0	0.7	5.9	4.6	148.0	-0.7	-7.3
ST-13	6.1	154.0	0.2	6.1	4.2	147.0	-0.2	-4.3
ST-14	6.5	165.0	-1.1	4.4	4.8	171.0	0.4	-1.2
ST-15	8.1	117.0	2.7	2.0	4.8	92.0	1.4	9.1
ST-16	7.0	130.0	1.4	-4.8	3.9	112.0	0.6	5.5
ST-17	6.4	130.0	0.9	1.0	3.1	121.0	0.9	11.3
ST-18	8.3	123.0	1.8	3.1	4.8	101.0	1.1	11.4
ST-19	7.2	109.0	2.1	2.1	3.8	80.0	1.0	13.1
ST-20	5.8	95.0	2.5	1.2	3.1	51.0	0.7	19.7
ST-21	5.5	162.0	0.1	-0.4	4.7	166.0	0.3	-0.4
ST-22	6.9	173.0	-1.4	-0.1	5.7	170.0	0.5	14.2
ST-23	6.9	172.0	-1.2	-10.4	5.9	176.0	-0.6	4.4
ST-24	6.8	170.0	-0.9	-9.1	5.4	179.0	0.0	-1.0
NF-1	9.0	252.4	-1.6	6.2	9.0	229.7	-0.3	4.6
NF-2	8.0	252.0	-0.2	-3.8	9.0	230.4	0.1	-3.8
NF-3	7.0	242.8	0.4	-1.5	8.0	224.3	0.8	-3.0
NF-4	5.0	185.7	1.6	16.2	6.0	183.8	1.9	4.4
NF-5	7.0	213.7	-0.1	-11.4	8.0	185.8	0.3	2.6
NF-6	6.0	202.0	0.9	0.5	6.0	199.9	2.4	-11.4
NF-7	6.0	201.0	1.0	1.1	7.0	180.3	1.5	7.5
NF-8	9.0	179.7	-1.2	-1.8	8.0	170.8	0.6	-7.3
NF-9	7.0	183.2	0.7	-6.4	9.0	165.4	-0.4	-3.0
NF-10	7.0	162.8	0.1	-9.3	7.0	133.0	0.3	-1.5
NF-11	7.0	162.2	0.1	-9.2	7.0	132.3	0.2	-2.3
NF-12	7.0	162.1	0.1	-9.1	6.0	128.5	1.0	-2.5

<b>NF-13</b>	8.0	163.5	-0.9	-10.4	7.0	129.6	-0.1	-5.0
<b>NF-14</b>	8.0	165.2	-0.8	-8.3	6.0	118.1	0.4	5.7
<b>NF-15</b>	9.0	164.9	-1.2	2.1	6.0	121.3	0.6	4.3
<b>NF-16</b>	10.0	169.4	-2.1	-2.9	6.0	119.2	0.6	6.1
<b>NF-17</b>	9.0	166.1	-1.1	0.2	5.0	120.8	1.6	4.4
<b>NF-18</b>	8.0	174.7	0.3	-9.4	7.0	130.8	-0.1	-5.5
<b>NF-19</b>	8.0	164.2	0.0	3.6	6.0	115.2	0.6	7.0
<b>NF-20</b>	7.0	164.9	-0.8	12.9	3.0	97.3	1.2	25.4
<b>NF-21</b>	8.0	259.1	0.4	3.0	8.0	251.0	0.6	-0.5
<b>NF-22</b>	8.0	265.0	1.0	-6.9	8.0	255.3	0.9	-9.5
<b>NF-23</b>	14.0	263.2	0.0	-0.4	12.0	240.8	1.8	1.9
<b>NF-24</b>	13.0	262.5	1.3	-3.4	14.0	242.1	0.3	-4.6
<b>NF-25</b>	10.0	280.2	3.5	-25.7	13.0	234.8	0.8	-2.4
<b>NF-26</b>	12.0	267.9	0.7	-14.7	12.0	243.9	1.1	-13.2
<b>SS-1</b>	14.0	174.2	-1.7	7.8	10.0	156.8	0.7	15.0
<b>SS-2</b>	13.0	179.2	-0.7	2.8	10.0	162.8	0.7	9.0
<b>SS-3</b>	12.0	147.2	1.9	9.2	7.0	115.8	3.5	22.7
<b>SS-4</b>	10.0	123.0	1.4	-0.6	4.0	94.5	2.7	9.8
<b>SS-5</b>	2.0	127.0	0.4	6.5	2.0	161.8	0.3	41.3
<b>SS-6</b>	13.0	322.2	2.1	2.0	15.0	290.8	-1.1	2.4
<b>SS-7</b>	5.0	16.9	2.2	13.9	6.0	321.5	-1.1	17.8
<b>SS-8</b>	7.0	324.7	0.4	-4.2	8.0	287.3	-0.6	-5.9
<b>SS-9</b>	8.0	295.2	0.5	6.8	9.0	265.8	0.0	3.7
<b>836.0</b>	9.6	143.8	2.7	21.7	6.2	120.5	1.0	-1.5
<b>837.0</b>	12.8	178.0	-0.2	-16.2	7.5	127.5	-0.2	0.1
<b>838.0</b>	10.1	148.4	1.6	13.0	7.4	124.0	-0.2	3.1
<b>840.0</b>	10.7	173.6	1.3	-15.3	7.1	120.1	0.1	3.2
<b>697.0</b>	9.8	170.6	-0.8	-8.1	7.3	148.4	-0.7	-9.9
<b>802.0</b>	9.3	172.6	-0.4	-11.2	7.3	145.3	-0.7	-6.9
<b>696.0</b>	12.3	163.8	-0.8	-4.0	7.8	128.3	-0.3	-0.8
<b>803.0</b>	11.7	165.0	-0.4	-4.5	7.7	127.9	-0.2	0.4
<b>695.0</b>	12.8	162.4	-1.0	-1.6	7.9	125.2	-0.2	0.8
<b>804.0</b>	12.1	164.0	-0.1	-5.0	7.9	125.0	-0.1	0.6
<b>795.0</b>	10.5	160.5	0.5	1.8	7.0	123.0	0.2	0.1
<b>691.0</b>	10.7	159.7	2.4	7.1	5.9	117.9	1.4	-0.8
<b>793.0</b>	10.4	157.0	2.9	9.6	6.4	120.6	1.0	-4.3
<b>789.0</b>	10.3	157.8	1.9	7.4	6.5	121.1	0.7	-1.7
<b>692.0</b>	10.5	161.9	1.2	2.2	6.2	122.1	0.9	-1.7
<b>794.0</b>	10.2	159.4	1.5	4.7	6.7	122.8	0.4	-2.4
<b>693.0</b>	10.1	162.4	-0.4	-10.8	6.6	126.4	0.2	-2.2

<b>792.0</b>	10.6	159.5	-0.9	-7.9	7.5	125.6	-0.8	-1.4
<b>694.0</b>	10.1	162.7	-2.0	-26.5	6.9	127.1	0.1	-3.3
<b>791.0</b>	9.7	159.0	0.1	-15.2	7.3	125.3	-0.5	-0.5
<b>790.0</b>	10.0	158.8	-0.7	-11.8	6.9	123.6	-0.2	0.8
<b>796.0</b>	8.9	159.9	0.2	0.3	6.0	126.3	0.4	-1.9
<b>BG-1</b>	12.0	176.2	0.6	15.9	9.0	149.8	2.3	31.8
<b>BG-2</b>	14.0	194.7	-1.3	-2.0	11.0	174.3	0.4	7.8
<b>BG-3</b>	13.0	190.3	-0.5	1.1	11.0	171.6	0.2	9.4
<b>BG-4</b>	15.0	196.4	-1.9	-3.9	11.0	173.5	0.6	8.7
<b>BG-5</b>	16.0	194.8	-2.8	-2.6	12.0	176.1	-0.2	7.2
<b>BG-6</b>	18.0	194.6	-5.0	-3.1	12.0	173.2	-0.1	10.7
<b>BG-7</b>	18.0	194.2	-4.9	-2.6	10.0	180.8	1.9	2.9
<b>BG-8</b>	17.0	182.6	-4.1	9.0	10.0	160.4	1.8	23.4
<b>BG-9</b>	17.0	197.0	-4.1	-4.8	12.0	171.4	-0.3	12.6
<b>BG-10</b>	18.0	197.4	-5.0	-5.8	12.0	175.0	-0.1	8.3
<b>BG-11</b>	15.0	187.8	-2.1	3.2	12.0	170.4	-0.1	12.1
<b>BG-12</b>	15.0	190.1	-2.3	-0.6	11.0	168.8	0.3	10.9
<b>BG-13</b>	13.0	183.6	-0.4	5.9	10.0	165.3	1.3	14.4
<b>BG-14</b>	14.0	183.3	-1.4	6.2	11.0	169.5	0.3	10.2
<b>BG-15</b>	13.0	186.1	-0.4	3.4	10.0	171.8	1.2	7.7
<b>BG-16</b>	15.0	183.3	-2.4	6.2	11.0	161.1	0.3	18.4
<b>BG-17</b>	14.0	190.1	-1.4	-0.6	11.0	164.9	0.3	14.6
<b>BG-18</b>	14.0	183.8	-1.5	4.4	11.0	166.2	0.1	12.1
<b>BG-19</b>	16.0	184.2	-3.5	4.6	10.0	168.8	1.1	9.9
<b>BG-20</b>	15.0	182.9	-2.9	3.5	10.0	167.0	0.9	9.9

Table E-3. Summary of observed and computed  $M_2$  and  $K_1$  tidal elevations at Tide and Bottom Pressure gauge sites from Bu experiment. AO, amplitude (cm) observed; PO, phase (degree) observed; AMO, difference of model amplitudes from observations; PMO, model-observation phase difference.

St. No.	$M_2$				$K_1$			
	AO	PO	AMO	PMO	AO	PO	AMO	PMO
ST-1	35.6	317.0	1.1	-9.2	8.1	162.0	-1.3	-19.2
ST-2	60.3	348.0	4.3	3.0	6.0	195.0	1.3	-6.4
ST-3	50.2	344.0	1.3	-0.9	6.1	24.0	1.8	9.3
ST-4	61.1	348.0	1.1	-3.3	7.6	105.0	3.5	-3.5
ST-5	58.8	347.0	-2.8	-3.8	6.4	48.0	2.8	5.6
ST-6	69.8	359.0	9.7	-3.0	12.8	147.0	2.1	6.2
ST-7	36.0	328.0	0.1	-8.4	7.3	163.0	-0.3	-16.4
ST-8	23.1	330.0	-1.8	-2.6	7.0	163.0	0.5	-3.1
ST-9	33.6	338.0	-0.4	-4.6	5.7	160.0	0.1	-4.1
ST-10	26.3	315.0	-0.3	-8.2	8.7	158.0	-0.6	-4.1
ST-11	18.6	323.0	-0.7	-7.7	9.0	161.0	0.8	-2.6
ST-12	16.2	340.0	-1.2	-6.1	5.6	155.0	0.7	5.1
ST-13	18.3	343.0	-0.7	-4.8	6.1	154.0	0.2	4.6
ST-14	43.2	338.0	0.6	-0.6	6.5	165.0	-1.2	5.1
ST-15	60.6	350.0	2.9	-4.2	8.1	117.0	3.4	-4.2
ST-16	59.3	349.0	2.3	-2.2	7.0	130.0	1.7	-10.9
ST-17	58.3	350.0	2.1	-2.7	6.4	130.0	1.1	-4.8
ST-18	60.4	350.0	3.0	-3.1	8.3	123.0	2.4	-2.6
ST-19	60.0	348.0	1.7	-2.8	7.2	109.0	2.7	-4.7
ST-20	59.4	347.0	0.6	-2.7	5.8	95.0	3.1	-6.4
ST-21	44.1	345.0	0.0	-1.6	5.5	162.0	0.0	-2.2
ST-22	48.2	351.0	1.6	-1.2	6.9	173.0	-1.5	1.2
ST-23	49.2	350.0	2.1	3.2	6.9	172.0	-1.3	-11.7
ST-24	49.0	357.0	1.8	-2.0	6.8	170.0	-1.0	-11.1
NF-1	42.0	19.7	4.3	1.0	9.0	252.4	-0.1	0.3
NF-2	43.0	14.3	6.6	6.0	8.0	252.0	1.3	-9.3
NF-3	44.0	4.1	8.2	12.4	7.0	242.8	1.8	-6.7
NF-4	59.0	352.4	7.0	5.2	5.0	185.7	2.7	12.5
NF-5	62.0	356.4	6.1	0.5	7.0	213.7	1.0	-15.4
NF-6	63.0	354.9	6.0	1.7	6.0	202.0	2.1	-3.5
NF-7	65.0	353.7	6.3	2.1	6.0	201.0	2.2	-3.1
NF-8	67.0	334.4	5.0	2.3	9.0	179.7	-0.2	-10.7
NF-9	69.0	338.8	-0.1	-2.5	7.0	183.2	1.6	-14.5

<b>NF-10</b>	41.0	315.9	1.3	-3.4	7.0	162.8	0.2	-20.5
<b>NF-11</b>	40.0	314.6	0.7	-3.6	7.0	162.2	0.1	-20.1
<b>NF-12</b>	34.0	310.9	1.7	-3.9	7.0	162.1	-0.2	-19.0
<b>NF-13</b>	33.0	313.1	1.6	-7.5	8.0	163.5	-1.3	-18.7
<b>NF-14</b>	28.0	308.8	1.6	-5.6	8.0	165.2	-1.6	-11.6
<b>NF-15</b>	34.0	309.7	-0.4	-6.2	9.0	164.9	-1.8	6.3
<b>NF-16</b>	35.0	314.0	-0.5	-11.5	10.0	169.4	-2.6	1.4
<b>NF-17</b>	33.0	312.1	1.6	-9.9	9.0	166.1	-1.6	4.6
<b>NF-18</b>	33.0	304.4	3.7	-5.5	8.0	174.7	-0.2	-4.3
<b>NF-19</b>	33.0	302.1	0.3	-6.0	8.0	164.2	-0.2	7.6
<b>NF-20</b>	26.0	308.5	-3.1	2.4	7.0	164.9	-0.4	19.7
<b>NF-21</b>	35.0	56.2	18.5	4.1	8.0	259.1	2.1	-4.4
<b>NF-22</b>	34.0	59.7	22.7	-0.6	8.0	265.0	2.7	-13.8
<b>NF-23</b>	53.0	56.9	27.3	5.4	14.0	263.2	2.1	-7.7
<b>NF-24</b>	50.0	60.4	19.7	-4.5	13.0	262.5	3.5	-10.0
<b>NF-25</b>	49.0	57.9	12.4	-9.3	10.0	280.2	5.7	-32.1
<b>NF-26</b>	38.0	47.0	19.6	-2.9	12.0	267.9	2.8	-21.0
<b>SS-1</b>	130.0	48.9	32.2	-5.7	14.0	174.2	-0.9	4.7
<b>SS-2</b>	120.0	51.9	42.2	-8.7	13.0	179.2	0.1	-0.3
<b>SS-3</b>	69.0	358.9	10.5	-2.9	12.0	147.2	2.9	6.0
<b>SS-4</b>	63.0	350.3	1.4	-4.0	10.0	123.0	2.2	-6.6
<b>SS-5</b>	50.0	355.8	-0.2	-5.7	2.0	127.0	-0.1	7.0
<b>SS-6</b>	18.0	5.9	-8.7	30.6	13.0	322.2	5.4	-6.8
<b>SS-7</b>	49.0	344.2	0.2	-0.3	5.0	16.9	2.9	3.7
<b>SS-8</b>	36.0	352.9	1.6	10.1	7.0	324.7	1.8	-12.9
<b>SS-9</b>	30.0	5.9	4.8	11.7	8.0	295.2	2.2	-1.2
<b>836</b>	45.0	307.5	-2.7	-7.9	9.6	143.8	3.0	21.4
<b>837</b>	47.8	297.5	-2.7	-5.1	12.8	178.0	-0.2	-19.6
<b>838</b>	50.3	294.9	-4.5	-3.9	10.1	148.4	1.5	10.7
<b>840</b>	55.5	285.6	-3.4	-3.4	10.7	173.6	1.3	-16.1
<b>697</b>	65.6	304.7	-9.9	-6.3	9.8	170.6	-0.6	-7.3
<b>802</b>	65.5	304.7	-9.9	-6.3	9.3	172.6	-0.2	-10.3
<b>696</b>	64.6	303.7	-9.1	-5.7	12.3	163.8	-1.3	-5.1
<b>803</b>	64.5	303.5	-8.9	-5.4	11.7	165.0	-0.8	-5.4
<b>695</b>	64.8	303.6	-9.1	-5.6	12.8	162.4	-1.6	-2.3
<b>804</b>	64.6	303.8	-9.1	-5.9	12.1	164.0	-0.7	-6.5
<b>795</b>	50.1	304.7	-4.3	-7.8	10.5	160.5	0.6	1.3
<b>691</b>	45.3	309.3	-3.2	-8.1	10.7	159.7	2.7	6.2
<b>793</b>	45.8	310.7	-3.4	-9.0	10.4	157.0	3.4	8.9

<b>789</b>	45.1	303.6	-3.1	-4.3	10.3	157.8	2.2	6.6
<b>692</b>	45.3	305.7	-3.2	-7.6	10.5	161.9	1.4	1.6
<b>794</b>	45.4	306.3	-3.3	-8.2	10.2	159.4	1.7	4.1
<b>693</b>	40.5	299.9	-1.9	-6.4	10.1	162.4	-0.4	-12.1
<b>792</b>	44.3	299.0	-5.8	-5.5	10.6	159.5	-1.0	-9.2
<b>694</b>	40.1	297.2	-2.2	-6.5	10.1	162.7	-2.3	-28.9
<b>791</b>	39.8	295.3	-2.7	-6.6	9.7	159.0	0.0	-17.0
<b>790</b>	40.2	292.8	-2.4	-4.4	10.0	158.8	-0.8	-13.2
<b>796</b>	32.8	303.3	-0.6	-7.0	8.9	159.9	0.1	0.1
<b>BG-1</b>	201.0	83.9	59.2	-11.9	12.0	176.2	1.7	13.9
<b>BG-2</b>	202.0	93.2	67.7	-20.2	14.0	194.7	-0.2	-3.9
<b>BG-3</b>	208.0	90.2	45.9	-20.2	13.0	190.3	0.5	-1.1
<b>BG-4</b>	301.0	98.0	24.0	-24.1	15.0	196.4	-0.5	-6.1
<b>BG-5</b>	368.0	101.6	7.2	-25.5	16.0	194.8	-1.3	-4.5
<b>BG-6</b>	436.0	105.9	-25.1	-29.8	18.0	194.6	-3.1	-2.6
<b>BG-7</b>	413.0	102.9	-5.5	-27.0	18.0	194.2	-3.1	-3.3
<b>BG-8</b>	408.0	97.7	-8.5	-21.9	17.0	182.6	-2.2	8.7
<b>BG-9</b>	434.0	102.0	-31.1	-24.4	17.0	197.0	-2.0	-4.0
<b>BG-10</b>	415.0	99.2	-18.4	-24.5	18.0	197.4	-2.9	-6.8
<b>BG-11</b>	386.0	92.9	1.9	-20.1	15.0	187.8	0.2	2.0
<b>BG-12</b>	265.0	90.3	33.0	-23.9	15.0	190.1	-0.9	-3.8
<b>BG-13</b>	221.0	73.3	66.9	-7.4	13.0	183.6	0.9	2.7
<b>BG-14</b>	214.0	74.5	73.9	-8.6	14.0	183.3	-0.1	3.0
<b>BG-15</b>	208.0	75.6	66.1	-10.0	13.0	186.1	0.8	0.3
<b>BG-16</b>	233.0	77.7	41.1	-12.1	15.0	183.3	-1.2	3.1
<b>BG-17</b>	223.0	78.1	51.1	-12.5	14.0	190.1	-0.2	-3.7
<b>BG-18</b>	219.0	80.2	35.4	-17.0	14.0	183.8	-0.3	1.3
<b>BG-19</b>	215.0	80.9	36.2	-17.0	16.0	184.2	-2.4	1.7
<b>BG-20</b>	185.0	65.6	37.2	-9.6	15.0	182.9	-1.8	0.5

## **F. Co-range and co-phase charts for $M_2$ constituent from a single constituent run.**

In this section, the co-range and co-phase charts of the  $M_2$  constituent from a single constituent unassimilated run are presented with bathymetry derived from the North Atlantic Model (Egbert and Erofeeva, 2002) in the Gulf of St. Lawrence. The presence of an amphidromic point is clearly seen which is shifted to the west of the Gulf of St. Lawrence.

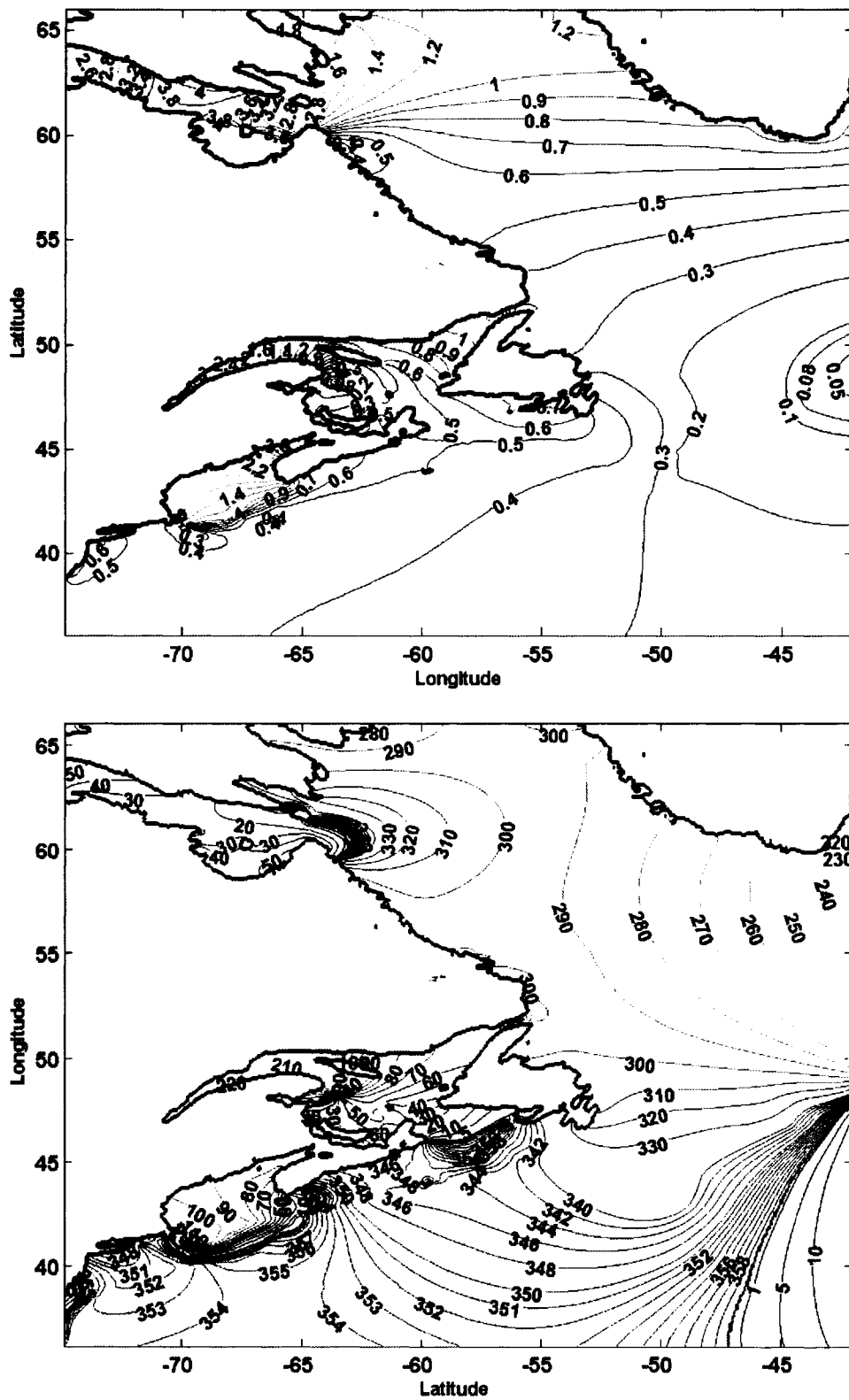


Figure F-1. Model computed Co-range (top) and Co-phase (bottom) charts for  $M_2$  constituent from single constituent unassimilated run. The amplitude is in m and phases are in degrees. The contours are co-range (top) and co-phase (bottom) lines scaled to show the proper distribution of amplitude and phase respectively.







